Elementary Processes in Layers of Electron Transporting Donor-Acceptor Copolymers:

Investigation of Charge Transport and Application to Organic Solar Cells

Kumulative Dissertation
zur Erlangung des akademischen Grades
***doctor rerum naturalium* (Dr. rer. nat.)**
in der Wissenschaftsdisziplin Experimentalphysik

Eingereicht an der
Mathematisch-Naturwissenschaftlichen Fakultät
der Universität Potsdam

von

Marcel Schubert

Potsdam, im Januar 2014

Für meinen Vater.

Published online at the
Institutional Repository of the University of Potsdam:
URL http://opus.kobv.de/ubp/volltexte/2014/7079/
URN urn:nbn:de:kobv:517-opus-70791
http://nbn-resolving.de/urn:nbn:de:kobv:517-opus-70791

Abstract

Donor-acceptor (D-A) copolymers have revolutionized the field of organic electronics over the last decade. Comprised of a electron rich and an electron deficient molecular unit, these copolymers facilitate the systematic modification of the material's optoelectronic properties. The ability to tune the optical band gap and to optimize the molecular frontier orbitals as well as the manifold of structural sites that enable chemical modifications has created a tremendous variety of copolymer structures. Today, these materials reach or even exceed the performance of amorphous inorganic semiconductors. Most impressively, the charge carrier mobility of D-A copolymers has been pushed to the technologically important value of 10 $cm^2V^{-1}s^{-1}$. Furthermore, owed to their enormous variability they are the material of choice for the donor component in organic solar cells, which have recently surpassed the efficiency threshold of 10%.

Because of the great number of available D-A copolymers* and due to their fast chemical evolution, there is a significant lack of understanding of the fundamental physical properties of these materials. Furthermore, the complex chemical and electronic structure of D-A copolymers in combination with their semi-crystalline morphology impede a straightforward identification of the microscopic origin of their superior performance. In this thesis, two aspects of prototype D-A copolymers were analyzed. These are the investigation of electron transport in several copolymers and the application of low band gap copolymers as acceptor component in organic solar cells.

In the first part, the investigation of a series of chemically modified fluorene-based copolymers is presented. The charge carrier mobility varies strongly between the different derivatives, although only moderate structural changes on the copolymers structure were made. Furthermore, rather unusual photocurrent transients were observed for one of the copolymers. Numerical simulations of the experimental results reveal that this behavior arises from a severe trapping of electrons in an exponential distribution of trap states. Based on the comparison of simulation and experiment, the general impact of charge carrier trapping on the shape of photo-CELIV and time-of-flight transients is discussed.

* For 2013, Thomson Reuters database *Web of Knowledge* lists 309 publications for the search term: copolymer *and* ("donor-acceptor" *or* "D-A" *or* "Push-Pull" *or* "low-bandgap") (at Oct. 30th 2013). Thus, on average their is about one paper per day published on that topic, with the majority describing the synthesis of new D-A copolymers.

In addition, the high performance naphthalenediimide (NDI)-based copolymer P(NDI2OD-T2) was characterized. It is shown that the copolymer posses one of the highest electron mobilities reported so far, which makes it attractive to be used as the electron accepting component in organic photovoltaic cells.

Solar cells were prepared from two NDI-containing copolymers, blended with the hole transporting polymer P3HT. I demonstrate that the use of appropriate, high boiling point solvents can significantly increase the power conversion efficiency of these devices. Spectroscopic studies reveal that the pre-aggregation of the copolymers is suppressed in these solvents, which has a strong impact on the blend morphology.

Finally, a systematic study of P3HT:P(NDI2OD-T2) blends is presented, which quantifies the processes that limit the efficiency of devices. The major loss channel for excited states was determined by transient and steady state spectroscopic investigations: the majority of initially generated electron-hole pairs is annihilated by an ultrafast geminate recombination process. Furthermore, exciton self-trapping in P(NDI2OD-T2) domains account for an additional reduction of the efficiency. The correlation of the photocurrent to microscopic morphology parameters was used to disclose the factors that limit the charge generation efficiency. Our results suggest that the orientation of the donor and acceptor crystallites relative to each other represents the main factor that determines the free charge carrier yield in this material system. This provides an explanation for the overall low efficiencies that are generally observed in all-polymer solar cells.

Contents

1

Introduction

Organic semiconducting materials promise an unique and superior combination of mechanical and electronic properties. Within the last decade, conjugated molecules and polymers have taken important technological hurdles and are going to find their way into main consumer electronic applications in the form of, for instance, organic light emitting diodes (OLED), organic field-effect transistors (OFET) and organic photovoltaic (OPV) cells. In general, any application of organic materials in functional devices and complex circuitry is related to their ability to transport electrical charges. The best measure of the charge transport capability is the charge carrier mobility which directly affects many processes and properties of the devices.

Unless in singly crystals, the OFET mobility of organic semiconductors has long been far below the technologically important value of 1 $cm^2V^{-1}s^{-1}$, which is set by the mobility of amorphous silicon. Due to intensive material development, this threshold has been overcome and current record values of solution processed polymers are exceeding values of 10 $cm^2V^{-1}s^{-1}$.[1–3] Furthermore, several of the new high mobility polymers are ambipolar, meaning that they possess comparable hole and electron mobilities.[4–6]

This great improvement can be attributed to the development of so called *donor-acceptor (D-A) copolymers*, where the backbone repeat unit typically combines an electron rich (donor) and an electron deficient (acceptor) unit. The energies of the HOMO and LUMO orbitals of the donor and acceptor fragments are displayed in Fig. 1.1. Upon covalent binding, hybridization of these orbitals creates new molecular orbitals.[7] Most important, the band gap of the copolymer is defined by the energy difference between the HOMO of

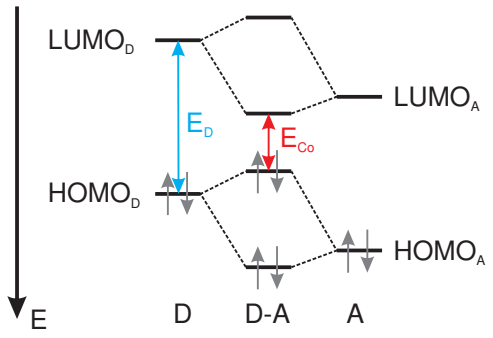

Figure 1.1: Illustration of the band gap lowering in donor-acceptor copolymers by covalent binding of an electron deficient acceptor (A) unit with a electron rich donor (D) fragment. Hybridization of the frontier molecular orbitals leads to a copolymer with an strongly reduced band gap E_{Co}, which is roughly given by the energy difference between the HOMO of the donor and the LUMO of the acceptor.

the donor and the LUMO of the acceptor fragment, which is significantly lower compared to the band gap of the single fragments. Fig. 1.1 illustrates that with this concept, the band gap as well as the energetic position of the frontier orbitals can be strongly varied just by exchanging the donor or acceptor units.

An important factor for the good charge transporting performance of D-A copolymers is their ability to form highly ordered, crystalline domains. These are separated by less ordered regions, and the film morphology is therefore usually semi-crystalline. Within the self-organized polymer crystals the polymer chains planarize and a close π-π packing enables an efficient *inter*molecular transfer of charge carriers. An important example is the electron transporting polymer P(NDI2OD-T2). In 2009, this polymer set a new record for the electron mobility of 0.85 $cm^2V^{-1}s^{-1}$, measured in an printed OFET in air.[8] Due to this outstanding performance, P(NDI2OD-T2) soon became a reference system to investigate the interplay of microscopic structure and charge transport properties. By applying wide-angle X-ray scattering (WAXS), *Rivnay* and coworkers investigated the packing of P(NDI2OD-T2) within the crystalline domains and disclosed an unconventional face-on orientation of the polymer with respect to the substrate, shown in Fig. 1.2.[9] The exceptional OFET properties were explained by the formation of large crystalline grains and the efficient transport along the π–stacking direction of the polymer.

The complex semi-crystalline structure on the other hand may also have negative impact on the charge transport. *Rivnay* and coworkers report the formation of exponential band tails, depending on the degree of disorder within the crystal.[11] These additional states extends into the band gap and effectively work as charge carrier traps. Similar to that, *Tretiak* investigated the interplay of molecular structure and the distribution of energy

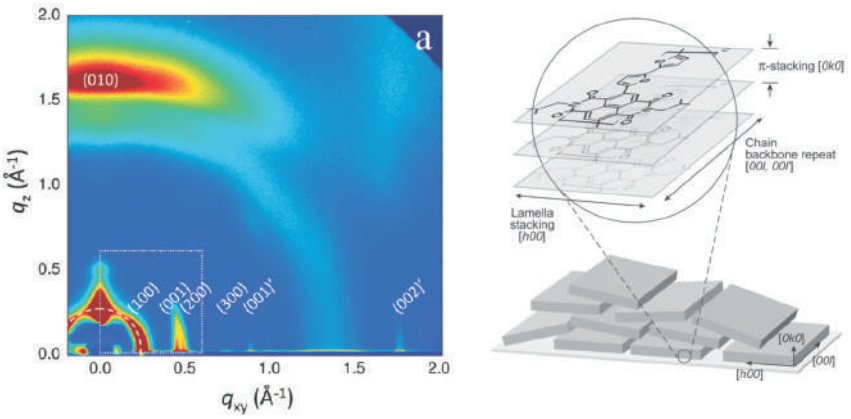

Figure 1.2: (*left*) Grazing incidence wide-angle X-ray scattering of a spin-coated film of the D-A copolymer P(NDI2OD-T2). Reprinted with permission from Ref. [10]. Copyright (2011) American Chemical Society. (*right*) Proposed packing and orientation of the polymer crystallites with respect to the substrate. Reprinted with permission from Ref. [9]. Copyright (2010) John Wiley and Sons.

sites. For two weakly ordered conjugated polymers the formation of trap states due to the interaction of the conjugated systems is reported. To which extend the proposed mechanisms influence the charge transport and how this is related to the polymers structure is only poorly understood. This renders fundamental charge transport investigations for the growing number of D-A copolymers important for their further improvement.

D-A copolymers have also contributed to the tremendous increase of the efficiency of organic solar cells, which recently surpassed the 10% efficiency value (see Fig. 1.3).[12] These devices comprise a hole and electron transporting material. D-A copolymers were so far mainly used as the donor component, while the acceptor component almost exclusively consist of fullerene molecules. The success of D-A copolymers as donors is governed by tailoring of their optical and electrical properties, which enabled the following improvements:

1. Lowering of the optical band gap to absorb a broader fraction of the solar spectrum.

2. Decreasing the ionization energy of the donor to increase the open circuit voltage.

3. Increasing the charge carrier mobility to reduce the recombination of free charges.

It is expected that organic solar cells will further benefit from the large variability of D-A copolymers when they are incorporated also as the acceptor component. Beside the advantageous properties of the copolymers themself, the morphology of polymer:polymer blends is supposed to be more stable than those based on polymer:fullerene mixtures. However, while the power conversion efficiency of polymer:fullerene solar cells has increased steadily from about 2 to 10% over the last decade, solar cells with polymeric acceptors were

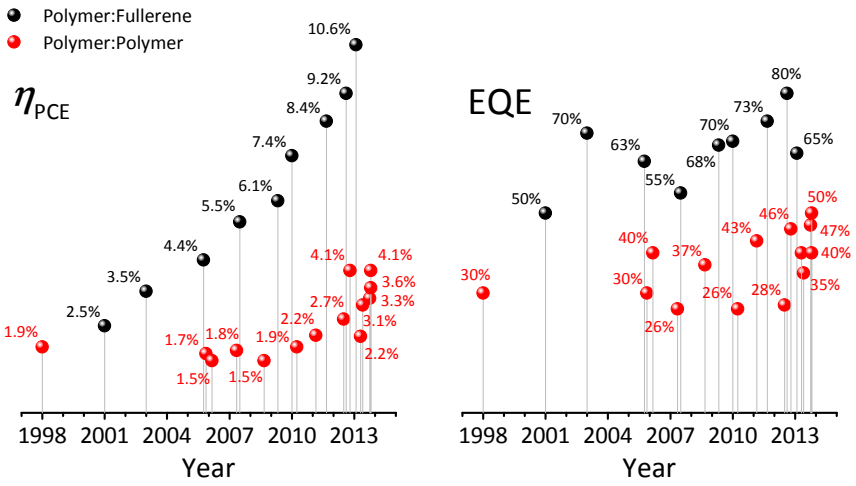

Figure 1.3: Power conversion efficiency (*left*) and external quantum efficiency (*right*) of selected polymer:fullerene[13–21] (black spheres) and polymer:polymer solar cells[22–34] (red spheres). Only research solar cells were considered.

not able to surpass the 2% value until 2011. From then, it increased to the actual record of 4.1%.§ This is illustrated in Fig. 1.3 for selected record solar cells, where also the external quantum efficiencies (EQE) of these cells are shown. A comparison between fullerene- and polymer-based cells makes clear that the difference in power conversion efficiency can be related to a surprisingly general trend in the EQE, where the polymer:polymer solar cells reach only about half the EQE of the polymer:fullerene cells.

This is shown in more detail for solar cells that incorporate the high-mobility D-A copolymer P(NDI2OD-T2). In Fig. 1.4, the power conversion efficiency of P(NDI2OD-T2)-based cells is compared to cells based on the fullerene derivative phenyl-C_{60}-buteric-acid-methyl-ester (PCBM) for three different donor polymers. Even after extensive morphology optimizations, and in spite of the large amount of data available on charge transport, crystal structure and film morphology, the performance of the P(NDI2OD-T2)-based cells lacks significantly behind the PCBM-based counterparts. With respect to a further improvement of organic solar cells, understanding the origin of the low EQE of polymeric acceptors is of great importance and P(NDI2OD-T2) is currently the most relevant polymer for these studies.

It is the goal of this thesis to investigate fundamental processes in layers of electron transporting D-A copolymers relevant to their application as acceptors in organic solar cells, including the charge transport, the change of the structural conformation from solution

§ I mention here a certified efficiency of 6.4% for a polymer:polymer solar cell, published by the Polyera corporation in beginning of 2013. However, since no further information are given for this cell, it is not displayed in Fig. 1.3.

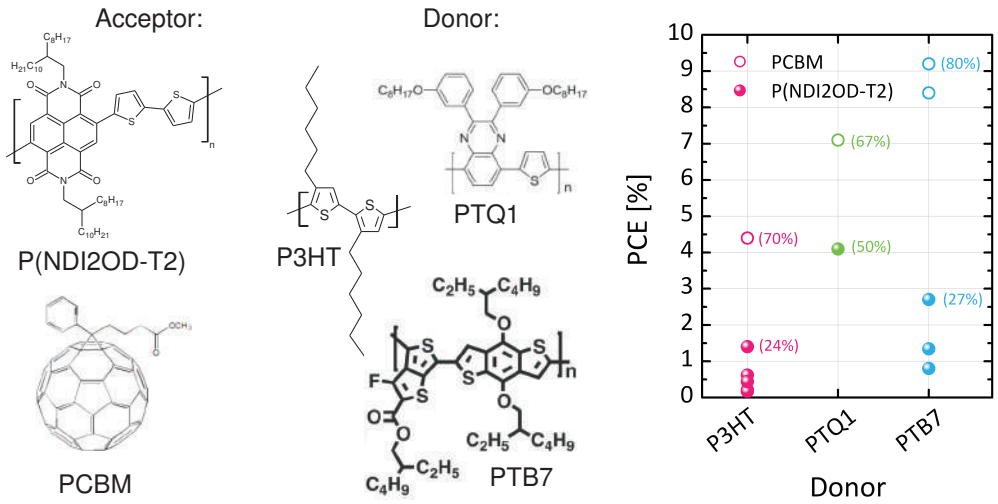

Figure 1.4: Comparison of the power conversion efficiency of P(NDI2OD-T2)-based (spheres) and PCBM-based (open circles) solar cells, with the donor polymers P3HT[34–39], PTQ1[33,40] and PTB7[19,20,34,41]. The numbers in brackets denote the maximum external quantum efficiency of the best cells. The chemical structures of the polymers and of PCBM are also shown.

to the film as well as understanding the impact of the polymer microstructure on the photocurrent generation.

In the first part of this thesis, transient and steady-state charge transport measurements, conducted on the prototype donor-acceptor copolymers PFTBTT and P(NDI2OD-T2), will be presented. PFTBTT has been chosen as it was one of the first D-A copolymers that has been designed for the use in organic solar cells, and which displayed also promising preliminary results. On the other hand, P(NDI2OD-T2) represents the state-of-the art electron transporting material with excellent optical and electrical properties. With respect to their use as potential acceptors in organic solar cells, the electron transport properties were characterized. Transient photocurrent measurements on a series of PFTBTT copolymers are presented in Sec. 4.1. The anomalous shape of the photocurrent transients in octyl-substituted PFTBTT is correlated to strong trapping of electrons. The general effect of trapping on photo-CELIV and ToF experiments is analyzed with a Monte Carlo computer simulations. The origin of the electron traps is traced back to the molecular structure through the comparison of structurally modified copolymers. In Sec. 4.2, we characterize the bulk electron transport in P(NDI2OD-T2), which reveals an exceptional high electron mobility. We also identify a severe barrier for the injection of electrons from the contact into the P(NDI2OD-T2).

In the second part of this thesis, I present a detailed study on the optimization and characterization of all-polymer solar cells comprised of the donor P3HT and two low band gap acceptor copolymers. In Sec. 4.3, the optimization of the solar cells is presented, which was realized by adjusting the pre-aggregation of the acceptor polymers in solution. These cells were then further analyzed in Sec. 4.4 to investigate the relevant pathways of photo-generated excited states. Furthermore, through investigation of the blend domain structure and crystal orientation, a correlation between the photocurrent and the orientation distribution of the polymer crystals is identified. Based on the findings of this thesis, a microscopic model is proposed, that provides a framework to understand the overall low performance of polymeric acceptors.

2

Fundamental properties of organic semiconductors

2.1 Conjugation in organic molecules

The semiconducting properties of organic compounds are based on the ability of carbon atoms to form molecules with extended, delocalized molecular orbitals, so called π-conjugated electron systems. The origin of conjugation in an organic molecule is the sp^2-hybridization of carbon atoms, where three sp-hybrid and one p_z-orbital mediate the chemical binding. The overlap of the sp-hybrid orbitals, which all lay in a common plane, leads to σ-orbitals that built up the molecules skeleton. Perpendicular to this plane, the p_z-orbitals overlap and create molecular π-orbitals. Fig. 2.1 displays the formation of a π-orbital in case of the aromatic molecule benzene. The π-orbitals are delocalized over the molecule as long as the sp^2-binding pattern of the carbon atoms is conserved. Of special importance are the highest occupied molecular orbital (HOMO) and the lowest unoccupied molecular orbital (LUMO) of a molecule in the ground state. The energy difference between the HOMO and LUMO is defined as the single charge band gap E_g. The length of the conjugated system directly affects the energy of the molecular orbitals, which decrease in energy with increasing size of the conjugated system. Consequently, also E_g decreases with increasing conjugation length.

Conjugation can also be realized in polymers, macromolecules built up by the repeated covalent binding of one or several structural units. However, due to the large number of repeat units $\left(\text{usually } 10^2 - 10^5\right)$ polymer chains don't form linear or elongated structures but adopt a coiled and rather disordered conformation. Fig. 2.1 shows this scenario. It

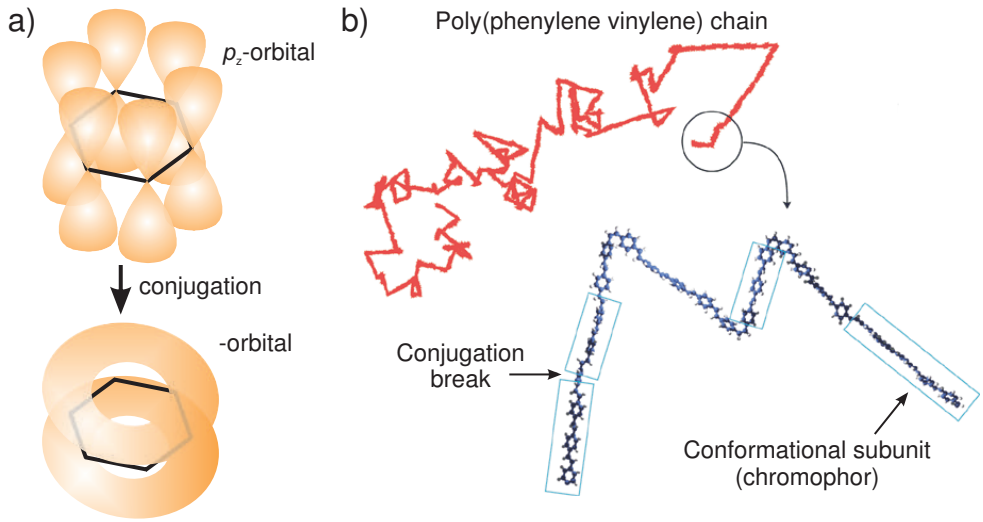

Figure 2.1: *a)* Formation of a π-conjugated system in benzene through overlap of the p_z-orbitals. *b)* Schematic representation of a single polymer chain, demonstrating the formation of conjugated subunits (chromophores). Subfigure *b)* is reprinted with permission from Ref. [42]. Copyright (2006) Macmillan Publishers Ltd.

becomes visible that strong kinks in the backbone lead to a break in conjugation. As a consequence the polymer chain is divided into conformational subunits (*chromophores*), each with a different conjugation length, energy levels and band gap. Excitation of a molecule to a higher energy state is possible through absorption of light with an energy larger than the optical band gap. This process transfers an electron from the HOMO into the LUMO and creates a so called exciton, a bound electron-hole pair. Excitons, as well as positive or negative charge carriers, who occupy the HOMO or LUMO, respectively, are restricted in space by the length of the chromophore.

The various conformations of conjugated materials also control their energetic structure. While single chromophores have well defined, discrete energy levels, averaging over all possible conformations yields a broad distribution of energy values. Based on the statistical nature of the conjugation length distribution it is reasonable to assume that the energy levels adopt a Gaussian distribution, which sum up to form a continuous density of states distribution. The optical and energetic properties of organic semiconductors are further influenced by the *inter*molecular coupling of chromophores, as it is often observed for aggregated or crystallized organic molecules.

2.2 The semi-crystalline structure of conjugated polymers

The disordered conformation of long polymer chains, their polydispersity and complex molecular design may not impede the formation of highly ordered structures. The structure formation is based on the self-organization of individual segments and whole chains during the transition from solution or melt to the solid state and is driven by strong Van-der-Waals interactions between the highly polarizable aromatic systems that build up the backbone of conjugated polymers.

Organic molecules can be tailored to promote self-organization. Most common are methods that focus on assisting the inter- as well as intramolecular ordering of the polymers by decreasing the disorder along the chains. Prominent examples are the chemical bridging of monomers as in ladder-type polymers, the hydrogen bond assisted planarization of the backbone or the control of the regio-regularity.[43,44] The latter describes the controlled coupling of monomer units to obtain a uniform orientation of the side-chains along the polymer, which has been found to improve the ordering and electronic properties of many classes of conjugated polymers, including PPV*-, rylene†-, and polythiophene-based materials.[31,35,45,46] Another way to introduce order is the increase of the intermolecular interactions by using molecules with large and symmetric aromatic segments. This principle is used in many industrial and natural dyes, as in e.g. phthalocyanines or perylenes.

Although self-assembling promotes structure formation, the remaining conformational disorder and the preparation of the active layer from solution, in which polymers adopt a coiled conformation, creates a rather inhomogeneous film morphology. Thus, it is necessary to discriminate between different types of structures according to the degree of molecular ordering. The most obvious structure that a polymer chain will adopt in a film is the coiled and disordered conformation resembled from the structure in solution. After evaporation of the solvent, the polymer chains form a network of entangled chains, with a random orientation of the neighboring segments and the absence of any short or long range order. At room temperature, this network is kinetically trapped in a glassy state and is called ***amorphous***. Disregarding solvent-induced shifts (solvatochromism), amorphous polymers have film absorption spectra similar to their absorption in solution.

When the intermolecular interactions are strong enough to induce self-assembling, aggregation of polymer chains starts. Fig. 2.2 displays the molecular packing of ***aggregated*** regioregular poly(3-hexylthiophene) (P3HT). The interchain alignment planarizes the backbone and promotes the stacking of π-orbitals on top of each other. Optical spectroscopy has proven to be a sensitive tool to study aggregation phenomena in organic materials. For

* Abbreviation of poly(phenylene-vinylene).
† Rylenes are a homologeous series of condensed naphthalene molecules.

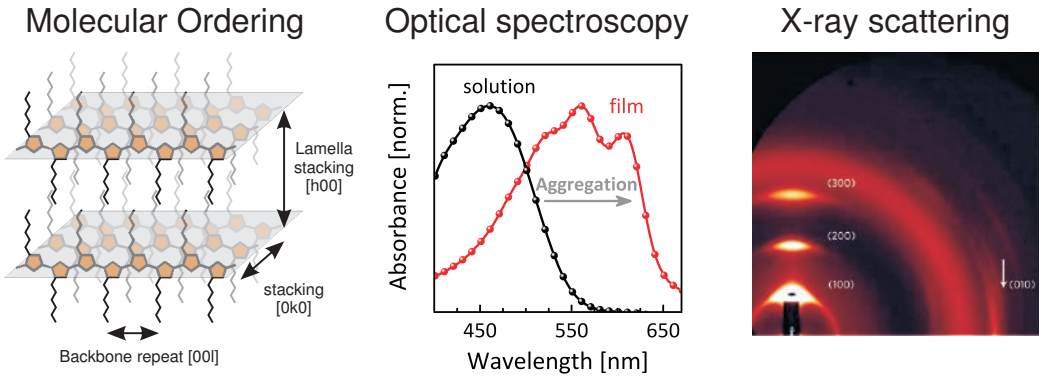

Figure 2.2: (*left*) Schematic drawing of the packing structure of aggregated P3HT chains. (*middle*) Effect or ordering on the optical absorption of P3HT by the transition from disordered chains in solution (black spheres) to ordered crystals in a mesithylene-cast film (red spheres). (*right*) X-ray scattering of P3HT crystals in a spin-coated film. This subfigure is reprinted with permission from Ref. [50]. Copyright (2012) Macmillan Publishers Ltd.

instance, planarization of the polymer backbone strongly enhances the conjugation along the chain, which lowers the optical band gap.[47] For P3HT, this shift is about 0.35 eV (see Fig. 2.2). Furthermore, due to the small distance of adjacent π-orbitals of aggregated chromophores (typically 4 Å) and the alignment of the transition dipole moments, the electronic *inter*molecular coupling leads to the formation of *H*- or *J*-aggregates.[48] This changes the absorption and emission profiles which are for individual chains defined by the Franck-Condon progression.[49] Therefore, the optical absorption of conjugated polymers can provide a direct proof for the formation of ordered domains.

If the precise arrangement of molecules and chains is preserved over larger distances, diffraction of X-rays occurs due to the high symmetry of the structures. The structure and size of such ***crystalline*** domains are directly obtained from the position and shape of the scattering peaks, respectively. The ability to diffract X-rays also distinguishes aggregates from crystals. As it is usually very difficult to obtain the absolute degree of crystallinity, the degree of aggregated molecules, as determined from the analysis of optical properties, can serve as an upper boundary to estimate the number of molecules in the crystalline domains.

In practice, most conjugated polymers comprise a large range of disordered and ordered structures and are described more generally as ***semi-crystalline*** materials. The composition can be strongly altered by the processing and manufacturing conditions that are applied during or after film formation.

2.3 Charge transport models

The semi-crystalline morphology of organic semiconductors has a severe impact on the transport of electrical charges. On the molecular scale, a charge carrier is constraint to conjugated segments and can delocalize over larger distances only within the crystalline domains. Thus, charge carriers in organic semiconductors are constraint in space, and transport of charges over large distances requires charge carrier hopping between transport sites. Generally, the Miller-Abrahams rate ν is used to describe the hopping from site i to site j:

$$\nu \propto \exp(-2\gamma r_{ij}) \begin{cases} \exp\left(-\frac{\epsilon_j - \epsilon_i}{k_B T}\right) & \text{if } \epsilon_j > \epsilon_i \\ 1 & \text{else} \end{cases} \tag{2.1}$$

where r_{ij} is the distance between the transport sites, ϵ_i and ϵ_j are the site energies, $k_B T$ is thermal energy, and γ is the inverse localization radius, a measure of the electronic wave function overlap. From this equation it appears that the hopping transport is strongly temperature activated, which explains the strong temperature dependence of the mobility in organic materials.

Because the energy of the hopping sites enters Eq. 2.1, the shape of the density of states (DOS), which represents the distribution of transport states in energy, dictates the properties of charge transport. A Gaussian distribution is commonly used to describe the DOS of disordered systems. The solution of the percolation problem by numerical modeling created a large set of transport models from which the Gaussian disorder model (GDM) has been confirmed in many experiments.[51] Based on Monte Carlo-type computer simulations, Bässler and coworker modeled the temporal evolution of a charge distribution as function of time.[52] After excitation within the center of the DOS, charge carriers relax to the mean equilibrium energy $\epsilon_{00} = \sigma^2/k_B T$, where σ denotes the width of the Gaussian distribution. The time the carrier needs for thermalization is given by the relaxation time t_{rel}, which can be estimated by:[52]

$$t_{\text{rel}} = 10 \cdot t_0 \cdot \exp\left[1.07 \cdot (\sigma/k_B T)\right]^2, \tag{2.2}$$

were t_0 is the dwell time of a charge in an iso-energetic lattice, which defines the time-scale in the simulation. If the charge transport is probed on time scales smaller than t_{rel} it becomes strongly dispersive and the charge carrier mobility will decrease with time. When the equilibrium has established, the mobility is time-independent and an empirical formula can be used that describes the field and temperature dependence of the mobility.[52]

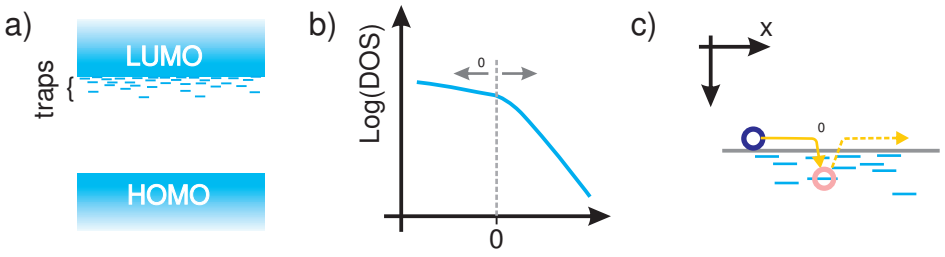

Figure 2.3: a) Energy diagram with electron traps close to the LUMO. **b)** Exponential density of trap states, following the definition of Eq. 2.3. **c)** Schematic represenation of the transport and trapping mechanism of the MTM.

Although the GDM has been widely used for many material systems, including pristine conjugated polymers, molecular glasses or molecularly doped polymers, it was developed under the assumption of spatially isotropic media. In contrast to this, semi-crystalline organic semiconductors posses a rather inhomogeneous micro structure, which introduces effects that are not adequately described by the GDM. Within the crystalline domains charge transport proceeds via delocalized orbitals, rendering the mobility to be orders of magnitude faster than in the disordered domains. In addition, charge transport is highly anisotropic for the different crystallographic directions, while distortions of the crystal structure can introduce exponentially distributed tail states, which act as trapping sites for charge carriers.[11] This situation is represented by the multiple trapping and release model (MTM), where transport within ordered (crystalline) domains is with a constant mobility while traps immobilize the carriers for a given time.[53–56]

In the MTM, the mobility is controlled by the statistics of trapping and detrapping. It assumes the existence of a defined energy that separates mobile states in the transport band from trap states, which are lower in energy. It is common to assume an exponentially decaying trap state distribution

$$N_{\mathrm{t}}(\epsilon) = N_0 \cdot exp\left(-\frac{\epsilon}{\epsilon_T}\right) \ , \tag{2.3}$$

which is characterized by the number of states at the band edge N_0 and the characteristic energy ϵ_T, often expressed by the characteristic temperature T_0 via $\epsilon_T = k_B T_0$, which defines the slope of the exponential tail states. However, other DOS distributions have be used and the choice of the distribution determines the general transport characteristics. An exponential distribution and a schematic of the transport mechanism are depicted in Fig. 2.3. In the band-like states, a charge carrier can move freely with a constant mobility μ_0, while a trapped carrier is immobile, e.g. it has zero mobility, and needs to be thermally excited to the transport band to contribute to the current. Hopping between trap states

is not taken into account. Under these conditions, a reasonable definition of the average mobility is obtained by multiplying μ_0 with the fraction of free charge carriers ϕ:

$$\mu_{\text{eff}} = \phi \cdot \mu_0 = \frac{N_{\text{mobile}}}{N_{\text{mobile}} + N_{\text{trapped}}} \cdot \mu_0. \tag{2.4}$$

This so called effective mobility μ_{eff} represents the average over the whole carrier population by counting only the mobile carriers. Note that as time elapses, the average energy of trapped carriers in an exponential trap distribution steadily decreases,[53] which increases their dwell time. As a result, the number of trapped carriers (N_{trapped}) continuously increases at the expense of mobile carriers (N_{mobile}). Consequently, the effective mobility becomes time-dependent (see Eq. 2.4).

2.4 Organic solar cells

Charge carrier generation

A characteristic property of organic semiconductors is the strong binding energy of photogenerated excitons. The energy of an photon that is absorbed is stored in the form of chemical energy in the excited organic molecule and can be transfered into electrical energy, when the exciton splits into individual charge carriers which are then extracted from the photoactive material and allowed to flow through an external circuit. This is the principle of a photovoltaic cell. However, the strong binding of the electron-hole-pair renders the direct conversion inefficient and so the great majority of the excitons will recombine. Before the exciton relaxes to it's ground state, it diffuses through the film. This movement is essential for the dissociation of excitons into free charge carriers.

Tang discovered that the combination of two semiconductors with different electron affinities and ionization energies largely promotes the generation of free charge carriers.[57] Following the usual convention, the material with the higher LUMO is called *donor*, as it donates an electron to the material with the lower LUMO energy, which is called (electron) *acceptor* (see Fig. 2.4). Excitons that reach the donor/acceptor (D/A)‡ heterojunction are quenched due to the charge transfer of either the hole or electron. The single steps that lead to the photocurrent generation are displayed in Fig. 2.4.

With the donor/acceptor concept a conversion efficiency of excitons to free charge carriers of nearly 100% has been realized.[17] This is surprising, given that the low dielectric constant of organic materials permits the attractive interaction of opposite charges over a

‡ The abbreviation *D/A* is used whenever the physical contact of a donor with an acceptor compound is meant, which should not be mistaken for the D-A copolymers.

large distance. Moreover, several physical properties of the dissociation process challenges the picture where free charge carrier generation proceeds via strongly bound electron hole pairs. One of these observations is the ultrafast dissociation of excitons in D/A mixtures. Transient absorption spectroscopy studies reveal that excitons are quenched within less than 1 ps in the most efficient solar cells, several orders in time faster than the typical lifetime of excitons.[58,59] Furthermore, it is found that the free charge carrier yield can be independent of the electric field.[60,61] Finally, for a small number of D/A pairs it was demonstrated that the dissociation process is a quasi barrierless process which requires no temperature activation.[62–65] In their entirety, these observations provide a detailed physical description of the free charge carrier generation at organic D/A interfaces. Unfortunately, they don't provide an explanation why these high yields can be reached despite the weak screening of charges in organic materials. To elucidate this problem a deeper understanding of the microscopic processes at the heterojunction and of the role of the anisotropic and inhomogeneous micro structure of the organic materials is strongly needed.

Charge-transfer states at the D/A heterojunction

One of the most promising approach to investigate the processes directly at the D/A interface is to explore the nature and properties of the intermoelcular *charge-transfer state* (CTS).[61,66] Such state is enabled by the physical contact of a donor and acceptor and characterized by a partial charge transfer between the molecules. The electronic structure and energy of a CTS is different from that of the pure components. Via a charge-transfer (CT) transition, e.g. by absorption of a photon, an electron (hole) on the donor (acceptor) can be directly transferred to the acceptor (donor), which generates an excited CTS. An additional absorption band in D/A mixtures, that is not observed in the pristine materials, is a direct proof for the CT transition.[67,68] Fig. 2.4.a shows that the band gap of the CT transition is always lower than the band gap of the donor and acceptor, causing the new band appearing as so-called sub-band gap absorption. The detection of this band requires very sensitive techniques due to the low oscillator strength of the intermolecular CT transition.[67,68] Since the excited CTS is always coupled to the electronic ground state, it is also possible to detect the radiative CTS recombination in the form of photo- or electroluminescence.[69,70] The spectral signatures of CTS have been found for a great number of D/A combinations, allowing to correlate their properties to the device performance.

Vandewal and coworkers found that the energy of the CTS is directly connected to the open circuit voltage of the solar cell.[68,71] Furthermore, it is believed that excited CTS are precursors to free charge carriers in organic solar cells. Several authors propose that

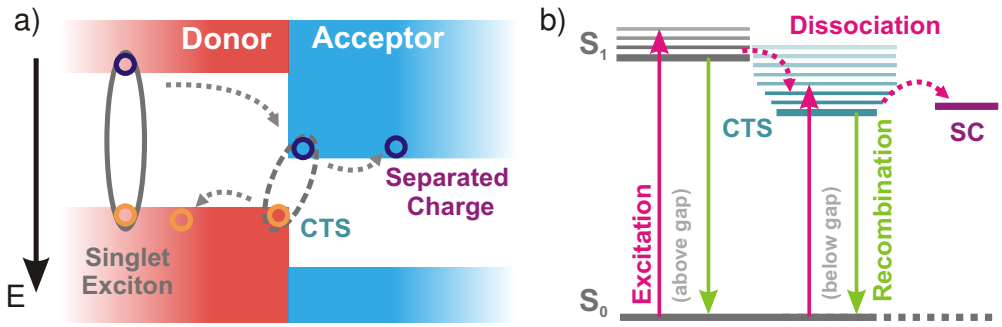

Figure 2.4: *a)* Schematic band diagram of the donor/acceptor heterojunction. *b)* Free energy diagram of the states that are involved in the photocurrent generation process. Upon absorption of a photon, a singlet exciton is generated and diffuses to the heterojunction. There, it is proposed that the exciton quenching first yields a charge-transfer state (CTS), which than dissociates into separated charge carriers (SC). Thick and thin horizontal lines represent energetic and vibrational states, respectively. The graph is adapted from Ref. [66].

CTS dissociation is more efficient from an excited CTS with additional vibronic and/or electronic excitation energy.[66,72] The probability to populate these so-called *hot* CTS depends mainly on the LUMO/LUMO or HOMO/HOMO energy gap at the heterojunction, and the photon energy in case of below gap excitation (see Fig. 2.4). On the other hand, *Vandewal* recently demonstrated that splitting of the lowest-lying, relaxed CTS is as efficient as the dissociation of excitons, suggesting that excess energy is not needed to reach a high internal quantum efficiency.[61] Based on the close relation of CTS and solar cell properties it has been suggested that free charge carrier generation is solely based on the CTS dissociation. In this picture, any exciton would first generate a CTS which than dictates the efficiency of the electron-hole separation. However, although the directly excited CTS can dissociate efficiently, there are also arguments that questions this picture, which will be discussed in the following paragraph.

Theoretical description of the exciton dissociation process

The current understanding of the high efficiency of exciton dissociation in organic solar cells is mainly based on the experimental investigation of the dissociation process itself. On the other hand, what is still missing is a comprehensive theoretical model of the charge carrier generation process. The lack of understanding is the sore spot in the field of organic photovoltaics that also impedes the systematic optimization of the organic molecules, as it its not clear which molecular property drives the charge separation.

First attempts to explain the free carrier formation were based on kinetical models, which describe the dissociation process as a diffusive motion of oppositely charged particles in

presence of their Coulomb attraction and an external field.[73] However, even under consideration of a CTS,[74,75] these models cannot explain the aforementioned properties of the charge carrier generation, given that realistic and experimentally determined parameters were used. Instead, computer simulations have become the main source for the theoretical description of the dissociation process. Monte Carlo simulations (MCS), similar to those used to model the charge transport in disordered organic systems, are able to investigate the influence of various parameters of organic solar cells, especially those of the complex domain structure of bulk heterojunction blends.[76–78] Furthermore, effects related to the energetic disorder can be modeled. In particular, it has been proposed that charge carrier dissociation is assisted by e.g. a large difference between the electron and hole mobilities in the acceptor and donor, respectively, or by a large energetic disorder.[79–81] Recently, also attempts were made to include the effect of delocalization of charges and excitons.[81,82] Unfortunately, MCS use discrete grid points to represent the molecular sites. Thus, they can hardly provide a direct correlation of the molecular structure and orientation to the fundamental properties of charge carrier separation. Consequently, processes related to the CTS can not be well described by a MCS.

Recently, molecular dynamics and quantum dynamical simulations based on density functional theory (DFT) calculations became able to describe systems with a large number of molecules, enabling the investigation of microscopic processes at extended donor/acceptor interfaces. The ability to simulate large molecule clusters is a prerequisite when the influence of the semi-crystalline nature of organic semiconductors wants to be taken into account. This becomes particular important since many experimental studies suggested that the delocalized nature of excited states and charges in the crystalline domains are the key to understand the CTS dissociation.[35,65,66,83]

In a series of publications *Tamura and Burghardt* provided a detailed picture of the influence of charge delocalization on lowering the potential barrier for charge separation. For the model system consisting of the crystalline, π–stacked donor P3HT and the fullerene acceptor C_{60}, they first demonstrated that the potential barrier decreases with increasing π–conjugation of the P3HT.[84] By modeling the charge delocalization between adjacent fullerene molecules,[85] the collective properties of electron and hole delocalization were analyzed.[86] The authors find that the efficient delocalization of the electron in crystalline fullerene clusters further decreases the potential barrier for charge separation, which enables ultrafast dissociation of excitons within tens of femtoseconds. The modeled fullerene clusters and the corresponding potential energy curves of an electron-hole pair are displayed in Fig. 2.5. These simulations show that the energy a CTS needs to overcome in order to dissociate into free carriers is only in the order of 50 meV for the system with the largest delocalization, which is reached when the hole has traveled a distance of just about 4 nm away from the interface.

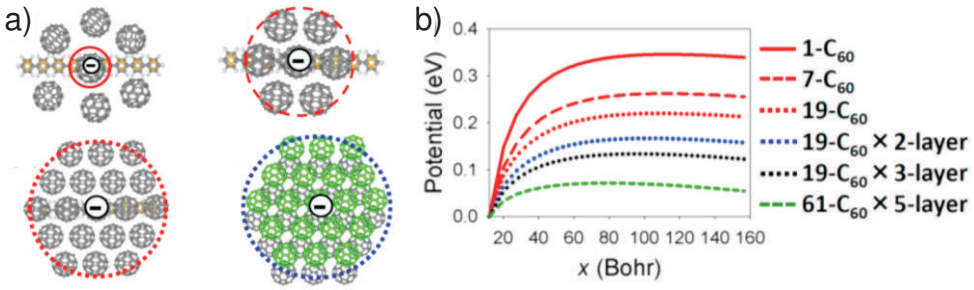

Figure 2.5: a) Molecular arrangement of π–stacked P3HT oligomers in contact with, a disordered C_{60} condensate where one C_{60} molecule interacts with the donor, and a hexagonal closed packed C_{60} cluster with either one layer that contains 7 or 19, or two layers with 19 C_{60} molecules. **b)** Potential energy curves for different cluster sizes as function of the electron-hole distance x. Figure a) and b) are reprinted with permission from Ref. [86]. Copyright (2013) American Chemical Society.

An alternative model is presented by *Troisi* and coworkers, who first investigated the distortion of the crystalline donor domains at the heterojunction. Here, the model system P3HT and PCBM is investigated. The increased dihedral angle between thiophene rings in the outermost layers of a polymer crystal decreases the conjugation and increases the band gap (see Sec. 2.1). Thus, the band gap is largest directly at the heterojunction and decreases by about 150 meV within the more ordered regions, as it is depicted in Fig. 2.6.b.[87] The resulting energy gradient can strongly promote the dissociation of excited CTS by driving the hole away from the heterojunction. This effect may becomes even stronger when the crystalline polymer is embedded in an amorphous polymer matrix. However, before the CTS can dissociate, it must first be populated from an excitonic state in the bulk of the material, which is the dominating initial photoexcited species. Unfortunately, the increased band gap at the D/A interface repels excitons, making it unlikely that they will be able to reach the heterojunction. Although the energy gradient theory provides an reasonable mechanism for the efficient splitting of CTS, it needs further expansions to explain how these states can be populated or an alternative model for the long-range separation of electron-hole pairs.

In order to facilitate exciton quenching in systems with a large energy gradient at the heterojuncion, charge carriers must be transferred over several nanometers.[87,88] *Troisi* proposed that this transfer is mediated by tunneling through the potential well, which results in a spatially separated electron-hole pair with reduced binding energy. The distance over which the rate for exciton dissociation exceeds the recombination rate is critically depending on the electronic coupling between neighboring hopping sites, which is orders of magnitude larger along the polymer backbone and pi-stacking direction than in the lamella-stacking direction.[88] Although this model aims for a realistic description of the D/A interface it remains open if the discussed exciton dissociation mechanisms describes the relevant processes.

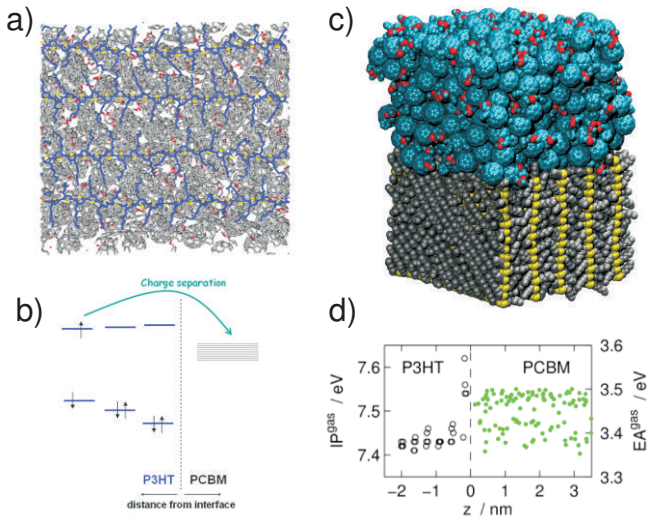

Figure 2.6: a) Snapshot of the P3HT:PCBM interface, modeled by *Troisi.*[87] **b)** Schematic energy diagram at the D/A interface. The increasing band gap at the heterojunction is caused by the larger disorder of P3HT chains close to the heterojunction. **c)** Snapshot of an equilibrium structure of stacked P3HT chains in contact with an amorphous PCBM domain, simulated by *Castet and Beljonne.*[89] **d)** Ionization potential (IP) and electron affinity (EA) of P3HT and PCBM, respectively, calculated for the molecular geometries of several 2D model clusters. Sub-figure a) and b) are reprinted with permission from Ref. [87]. Copyright (2011) American Chemical Society. Figure c) and d) are reprinted with permission from Ref. [89]. Copyright (2013) American Chemical Society.

A last example of the numerous models that arise from the microscopic modelling of organic solar cells is a recent study from *Castet and Beljonne.*[89] Similar to the simulations of Troisi, the molecular geometry of a P3HT crystal in contact to an amorphous PCBM and C_{60} domain was first geometrically optimized. It is found that again the P3HT interface layer is strongly disordered compared to the crystalline bulk. In a next step, the electrostatic energy is calculated and it is shown that the ionization potential increases by about 120 meV at the heterojunction. Furthermore, the energy for holes and electrons is calculated by considering the influence of the polarization of the molecular orbitals. It is found that beside the energy gradient, the electronic polarization provides a second major contribution to overcome the Coulombic interaction between electrons and holes, because it stabilizes the charges in the bulk of the material. Comparable to the results of Tamura and Burkhard an electron-hole capture radius (the distance at which opposite charges can be considered as free) of only 5 nm is found, which results in a quantitative yield of free charge carriers. Again, this model does not involve a CTS as a procursor for the free charge generation and corroborates the picture that excitons can hardly reach the heterojunction via a diffusive motion.

In summary, the presented simulations propose several different mechanisms as explanation for the efficient carrier dissociation in organic solar cells. Thus, it is necessary to gain a deeper understanding of the interplay of microscopic and energetic structure close to the heterojunction to prove or disprove the different theories.

3

Experimental and computational methods

3.1 Transient charge transport measurements

The most common quantity to describe the quality of charge transport in a certain material is the charge carrier *mobility* (μ), which is a measure of how fast a charge carrier can move under a given electric field $v = \mu \cdot E$. However, the mobility is a complex function of the electric field, temperature, charge carrier density and eventually also time. Transient photocurrent methods are able to investigate these dependencies and so they have been widely applied to study the charge transport in organic semiconductors.

A simple method to determine the mobility is the time-of-flight (TOF) technique. Here, free charge carriers are generated by a short laser pulse in a narrow sheet at one side of the device. Under a constant electric field $E = V/d$ these charges travel through the film of thickness d until they arrive at the counter electrode. The extraction of charges causes an abrupt change of the photocurrent, from which the transit time t_{tr} is obtained. The mobility is then calculated from:

$$\mu_{\mathrm{TOF}} = \frac{d}{E \cdot t_{\mathrm{tr}}} = \frac{d^2}{V \cdot t_{\mathrm{tr}}}. \tag{3.1}$$

Variation of the electric field and temperature is commonly used to obtain a data set that allows to extract characteristic material parameters, of which the energetic disorder is the most important one.[52] Furthermore, hole and electron mobilities can be determined separately. However, TOF requires a layer thickness of about 10 times the optical

absorption length to create a thin charge carrier sheet. Typically, thicknesses in excess of 1 µm are needed, much larger than the active layers used in OLEDs or solar cells. Due to the different preparation conditions that are applied to prepare such thick films, it is questionable if the determined values are reliable also for thin films. To apply the TOF technique to relevant film thicknesses of only several hundred nanometer, the so-called charge generation layer (CGL) concept can be used.

A CGL device incorporates an additional thin layer of a semiconducting material.[90] The CGL and the investigated material should be combined in a way that they form a working photovoltaic heterojunction (see Fig. 2.4) at which photoexcited excitons can be splitted with superior efficiency. Free carriers are than generated mostly within a narrow sheet at the heterojunction. Moreover, the charge carrier type depends on the relative energy levels of the CGL

As alternative to CGL TOF, the photo-CELIV technique has established as a powerful tool to investigate charge transport and recombination in films of a typical thickness of 100 nm. The working principle relies on the extraction of photogenerated charges by a linearly increasing voltage pulse. The time between excitation and extraction, denoted as delay time t_{del}, can be varied over several orders in time to uncover time-dependent processes. Due to the small layer thickness and the microcavity effect, free charges are usually generated over the whole layer thickness. Fig. 3.1 displays the device structure, charge generation profile, as well as the voltage pulse and theoretical current response of the conventional CELIV experiment (denoted as "bulk"). Application of the extraction voltage pulse causes a characteristic photocurrent signal that reaches a maximum at time t_{max}, from which the mobility of the charge carrier is obtained:[91]

$$\mu = \frac{2d^2}{3A' t_{\mathrm{max}}^2}. \tag{3.2}$$

Here, d and A' are the active layer thickness and voltage rise speed, respectively. Superimposed with the photocurrent signal is the constant dark current $j_0 = \epsilon_0 \epsilon_{\mathrm{r}} \frac{A'}{d}$, that arises due to the capacitive charging of the electrodes. The dark current is separately measured and subtracted from the light induced transient. Eq. 3.2 is valid in the limit of low conductivity and carrier concentration ($J_{\mathrm{light}} - J_{\mathrm{dark}} \ll j_0$). It is experimentally reached by adjusting the incident laser power or A'.

In general, the analytic description of the CELIV experiment does not consider ambipolar transport ($\mu_e \approx \mu_h$).[92] More seriously, from CELIV transients it is not possible to distinguish whether holes or electrons dominate the current. To avoid these difficulties and to access selective choice over the charge carrier type a CGL can be implemented in the photo-CELIV experiment. Fig. 3.1 displays the structure of a CGL device and the

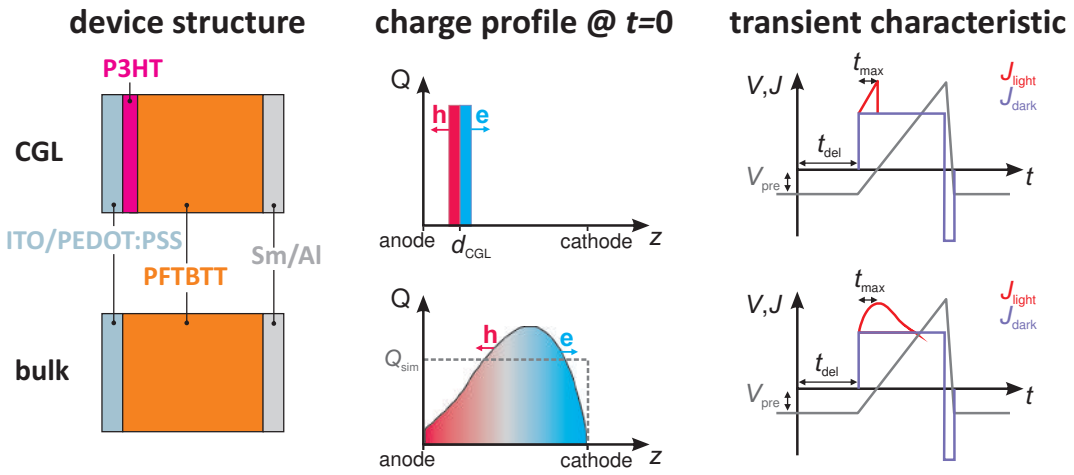

Figure 3.1: Comparison of the device structure (*left*), profile of the photogenerated charge carriers (*middle*) and transient photocurrent characteristics (*right*) of a charge generation layer (CGL) device (*top*) and a bulk device (*bottom*). The device structures correspond to the data discussed in Sec. 4.1. The charge profiles schematically display the position of maximum charge carrier generation. For the simulation of the bulk device a constant density (dashed line) is used.

difference to the bulk device with respect to the charge carrier profile and shape of the current transient. Due to the difference in the charge generation profiles, Eq. 3.2 can not be applied to analyze the photocurrent of a CGL device. A modified expression for μ is obtained from the extraction depth of the charge carriers $s(t) = \int v(t')dt' = \mu \int E(t')dt'$, assuming that charges are generated at one side of the device (at the CGL) and accelerated by the linear increasing field $E(t) = A't/d$. The time to reach the maximum is equal to the time charges need to travel through the active layer ($s(t_{\max}) = d$). Substitution of the field and integrating from zero to $t_{\max}$ gives:

$$\mu_{\mathrm{CGL}} = \frac{2d^2}{A'\, t_{\max}^2}, \tag{3.3}$$

which differs only by a factor of 1/3 from the case of a constant initial carrier density profile. A more general description of photo-CELIV transients under varying illumination profiles and intensities can be found in a recent paper by *Juska* and coworkers.[92] A further difficulty of the CELIV experiment arises from the non-constant extraction field. In particular, it might be difficult to discriminate the field-dependence of the mobility from other effects, as e.g. from carrier density- or time-dependent processes.[93]

Finally, it should be remembered that photogenerated charge carriers will reach the thermodynamic equilibrium only when the relaxation time (see Eq. 2.2 in Sec. 2.3) is faster

than the transit time. Otherwise, the mobility decreases with time as long as charges continue to relax within the density of states. In a TOF experiment, this effect is visible by strongly dispersive transients, meaning that the current continuously decreases with time, which complicates the definition and identification of a transit time. To study the effect of time-dependent mobilities, a rectangular extraction voltage pulse can be applied to the CGL sample after an adjustable delay time. This *time-delayed time-of-flight* (td-TOF) merges advantages of photo-CELIV (pulsed extraction after a defined delay) and TOF (constant extraction field). To the best of my knowledge, it is the first time that transport dynamics have been investigated with the td-TOF technique.

For the photocurrent experiments an optical parametric oscillator fed by the third harmonic of a neodymium-doped yttrium aluminum garnet laser working at 500 Hz (Ekspla, NT series) provided short excitation pulses. The excitation wavelength was 600 nm, and the pulse width was 6 ns. Samples were mounted in a homemade sample holder or in a closed-cycle He cryostat. Currents were amplified by a Femto DLH current amplifier and recorded by a Yakagawa 500 MHz storage Oscilloscope. The intensity was adjusted to keep the photogenerated charge <10% of the capacitive charge to exclude a redistribution of the internal field due to the photogenerated charge or any effect of bimolecular recombination.[93] In all transient measurements, the internal electric field was corrected by the built-in voltage. A value of 1.2 eV was found, determined as the voltage at which no photocurrent flows during the delay. The active area of the devices was 1 mm^2.

3.2 Simulation of photocurrent transients

Simulations of optoelectronic devices have proven as a essential tool to rationalize experimental results and to obtain important physical parameters which are not directly accessible. Numerical drift-diffusion simulations (DDS) have established as the most common technique to model charge transport in organic materials. Their success is based on their ability to perform virtual experiments with exact physics and controllable degree of complexity. However, this approach requires a relatively large set of input parameters. On the other hand, for percolation problems numerical methods like the master equation approach or Monte Carlo simulations (MCS) has established, which provide an alternative way to parametrize the charge carrier mobility.[94,95]

The DDS used for the simulations in this thesis is a complete device simulation that was written by Dr. Sebastian Bange.[96] It has been formerly applied to model charge transport experiments of several materiel systems and to study the effect of bimolecular recombination in the photo-CELIV experiment.[60,93,97]

To model the transient experiments under the influence of severe charge trapping, a one dimensional MCS instead of the DDS was used. The MCS was written by Dr. James Blakesley during his post-doctoral research at the University of Potsdam. The program measures the transit time of a single particle that is subject to multiple trapping and detrapping events. Current characteristics are obtained by averaging over usually 10^5 runs. Compared to the DDS the MCS is faster and allows to implement an exponential distribution of trap states. However, owing to the simplicity of the underlying model it can not capture density dependent effects like diffusion of charge carriers.

Four parameters (μ_0, ϵ_T, N_{eff} and t_{trap}) are necessary to describe the multiple trapping and release process that is simulated by the MCS. Here, we assume an exponential density of trap states (DOTS) directly below the conduction band (see Eq. 2.3). The simulation starts with an initially free charge that has a constant free carrier mobility μ_0. The time until a charge carrier is trapped, is randomly sampled from an exponential distribution with mean time t_{trap}. Once a carrier is trapped, it has zero mobility and the energy of the trap ϵ is sampled at random from the exponential DOTS with mean trap energy ϵ_T. After that, the immobilization or dwell time the carrier remains trapped is determined by detailed balance, which yields an exponential distribution with mean time $t_{\text{trap}} N_{\text{eff}}^{-1} e^{\left(\frac{\epsilon}{k_B T}\right)}$. The effective trap density $N_{\text{eff}} = N_{\text{trap}}/N_{\text{free}}$ is defined as the ratio of the concentration of trap and conduction band states. This routine is repeated until the carrier has traveled a distance that equals the thickness of the active layer d. In this definition, the inverse of t_{trap} is identical to the often used attempt-to-release rate ν. It was shown that the multiple trapping and release model yields an time-dependent effective mobility μ_{eff} (Eq. 2.4) that can reproduce the characteristic current decay seen in many TOF experiments[53]:

$$I \propto \mu_{\text{eff}} \propto t^{\alpha-1}. \tag{3.4}$$

Thus, the decrease of the current is caused by the temporal mobility relaxation, and the slope m in the double logarithmic representation depends only on the characteristic temperature $\alpha = T/T_0$.

3.3 Device preparation

For the experiments presented in this thesis several device structures were implemented and analyzed and more detailed descriptions are given in the original publications. Solar cell devices were prepared on pre-structured indium tin oxid (ITO)-covered glass substrates. In the standard device configuration, PEDOT:PSS (AI4083, 30 nm) and Samarium (20 nm)/Aluminium (100 nm) were used as hole (bottom) and electron (top) collecting

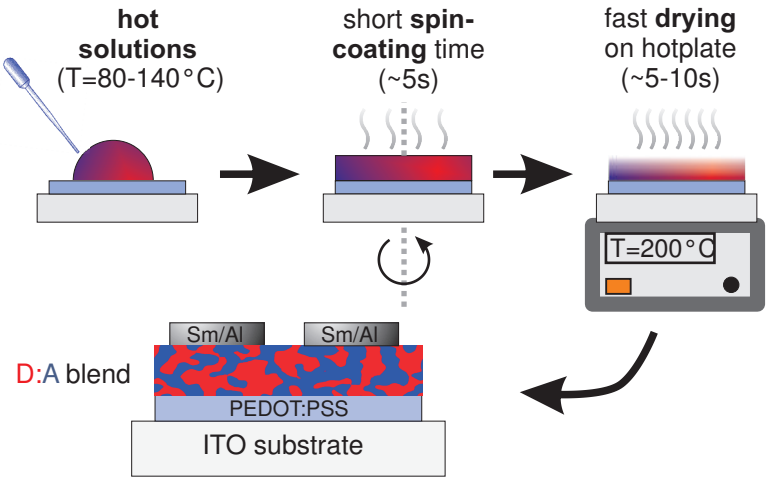

Figure 3.2: Preparation of bulk-heterojunction solar cells from high boiling point solvents. The temperature of the drying step is found to be a crucial parameter for device optimization (see Fig. 4.18.b).

contacts, respectively. The final structure of the cells was glass/ITO/PEDOT:PSS/active layer/Sm/Al and the active area of the cells 16 mm^2. Device preparation, transport and measurements were performed under inert atmosphere. Inverted devices were realized by preparing a thin (20 nm) TiO_x or ZnO layer (from a sol-gel precursor)[98,99] on top of ITO, which served as electron extracting contact. For the top contact 7 nm MoO_3 covered with 100 nm Al was used. The active layer thickness was determined with a Dektak profilometer.

The optimization of the polymer:polymer solar cells in Sec. 4.3 required the use of the high boiling point solvent 1-chloronaphthalene (CN, $T_{evap} = 260\,°C$). The, preparation of active layers from CN can result in a fast dewetting of the films after spin coating, due to residual solvent which didn't evaporate. Therefore, a preparation routine was developed that allows the preparation of homogeneous films. The single steps are displayed in Fig. 3.2. For the solar cells shown in this thesis, hot solutions ($T > 80\,°C$) were spin-coated for a short time. After that, the substrates were transferred immediately onto a hot plate. At a typical drying temperature of 200 °C, the films dry within 5–10 s, which is fast enough to form a continuous and homogeneous film.

For charge transport measurements, ultrathin layers of conjugated polymers were used as charge generation layer (CGL). Here, the polymer was spin coated on top of PEDOT:PSS and thermally annealed (typically at 180 °C for 10 min). Through interaction with the PEDOT:PSS, a several nanometer thick insoluble polymer layer forms.[100] The polymer that is not immobilized is removed by washing the layer three times with a good solvent. The thickness of the CGL was determined from the optical density, which was measured by a Varian Cary 5000 spectrometer.

3.4 Solar cell characterization

To evaluate the power conversion efficiency (η_{PCE}) of a solar cell, the current-voltage characteristic is measured under standardized conditions. Through extraction of the short-circuit current density (J_{SC}), the open circuit voltage (V_{OC}) and the fill factor (FF), the PCE is calculated from:

$$\eta_{\mathrm{PCE}} = \frac{P_{\mathrm{max}}}{P_{\mathrm{L}}} = \frac{V_{\mathrm{OC}}\, J_{\mathrm{SC}}\, FF}{I_0}, \tag{3.5}$$

where, I_0 is the intensity of the incoming light. The fraction of photons that can be converted into electrical charges is known as the *external quantum efficiency* (η_{EQE}), which is measured as function of wavelength. It can be further divided into the efficiency for absorption of a photon (η_{abs}) and the *internal quantum efficiency* (η_{IQE}), which represents the probability that an absorbed photon is converted into an electrical charge carrier. The IQE than depends on the efficiency for exciton quenching (η_{quen}), geminate electron-hole pair dissociation (η_{diss}) and charge carrier collection (η_{coll}), which finally yields:

$$\eta_{\mathrm{EQE}} = \frac{\#\,\text{charge carriers}}{\#\,\text{photons}} = \eta_{\mathrm{abs}} \cdot \eta_{\mathrm{IQE}} = \eta_{\mathrm{abs}} \cdot \eta_{\mathrm{quen}} \cdot \eta_{\mathrm{diss}} \cdot \eta_{\mathrm{coll}}\ . \tag{3.6}$$

From a measured EQE spectrum, the short circuit current density can be calculated from:

$$J_{\mathrm{SC}} = \frac{q}{hc} \int \lambda \cdot \eta_{\mathrm{EQE}}(\lambda) \cdot S(\lambda) d\lambda\ , \tag{3.7}$$

where S is the spectral irradiance of the incoming light. With a known absorption spectrum of the solar cell (η_{abs}) and with an estimated IQE, the maximum J_{SC} of the solar cell can be calculated. Furthermore, to check the correct calibration of the solar simulator, the measured J_{SC} can be compared to the theoretical value under AM 1.5G standard illumination conditions.

Solar cells where characterized under simulated sunlight of a Newport Oriel Sol2A solar simulator. Calibration of the setup was done with a KG5 filtered reference silicon solar cell (calibrated by Fraunhofer ISE) and the intensity was set to 100 mW/cm^2. The irradiance of the solar simulator was monitored before each measurement by a calibrated KG5 filtered Si photo diode, which is directly integrated into the home build, temperature controlled sample holder, with the temperature set to 20 °C. Current-voltage characteristics were measured with a source-measure-unit (Keithley 2400).

For EQE measurements, light from a 100 W quartz halogen lamp (Philips 7724) was time-modulated by a mechanical chopper ($\nu = 90 - 140$ Hz) and focused into a Cornerstone 260 1/4m monochromator (model 74100). The monochromatic output was focused onto

a fibre to transfer the light into the glovebox. The modulated photocurrent from the solar cell was detected over the input resistor of a lock-in amplifier (Princeton Research Instruments). To increase the sensitivity of the setup, an input resistance of 1 kΩ was used. The setup covers the spectral range from 300 to 1200 nm and an EQE as small as 0.0001% can be measured. No background illumination was applied.

3.5 Photoluminescence quenching

The Photoluminescence quantum yield (QY) Φ is an important parameter displaying the efficiency that an absorbed photon is re-emitted through fluorescence. An integrating sphere setup is used to measure the QY of pristine and blended films with high precision. The standard measuring procedure is displayed in Fig. 3.3. First, the spectral photon flux of the empty sphere is measured, which yields the reference spectrum of the excitation light. After the sample is placed in the sphere, the measurement is repeated. The number of absorbed photons (N_{abs}) can be calculated from the reduction of the excitation intensity by integrating the difference spectra over the wavelength region of the excitation light. The number of emitted photons (N_{em}) is obtained by integrating over the whole emission spectra. The QY is than given by $\Phi = N_{\mathrm{em}}/N_{\mathrm{abs}}$.

To measure the low QY of D/A blends, optical density (OD) filters were used to increase the dynamic range of the setup. The working principle is shown in Fig. 3.3. During the measurement of the excitation intensity (gray line), an OD filter is placed in front of the monochromator input, which reduces the excitation intensity and increases the integration time. After the reference measurement, the filter is removed and the sample (orange line) is excited with a higher intensity than for the reference. As a result, the fluorescence intensity increases which finally allows to measure signals that would be otherwise too small. However, to determine the number of absorbed photons correctly, the true excitation intensity I_0 (light gray line) must be calculated from the measured reference intensity I_{ref} via $I_0 = I_{\mathrm{ref}} \cdot 10^{\mathrm{OD}}$. This requires the knowledge of the *exact* optical density of the filter at the excitation wavelength. For this, the standard measurement procedure can be applied (taking the filter as sample), which directly yields the reduction of the intensity at the excitation wavelength, from which the OD of the filter is obtained. This procedure can be applied as long as the intensity at the excitation wavelength does not saturate. OD filters between 0.8 and 1.3 were found to give best results, enhancing the signal by up to a factor of 20, which allows to measure QYs as low as 0.01% .

With respect to the internal processes of an organic solar cell (Eq. 3.6) not only the absolute QY of a material is important but also its change upon blending with another material,

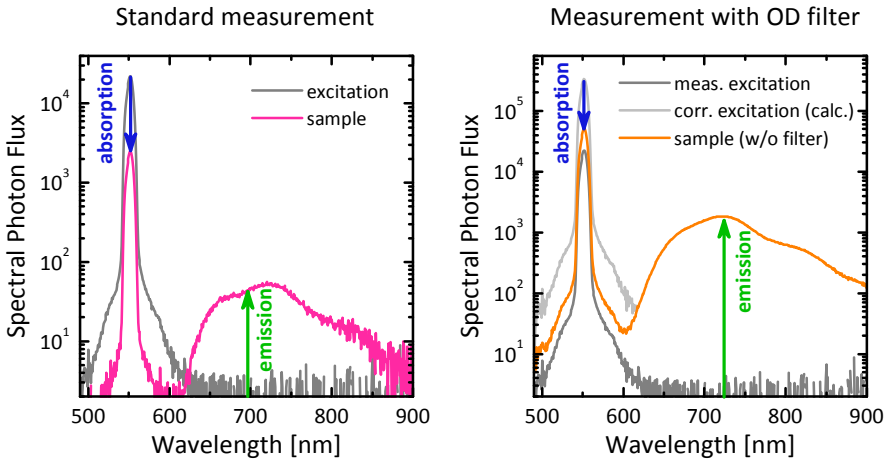

Figure 3.3: *(left)* Working principle of the standard quantum yield measurement used for samples with high quantum yield (above 1%). The gray and pink line displays the measurement of the excitation light at 550 nm and of the sample (pristine P3HT on PEDOT:PSS with a QY of 4.5%), respectively. *(right)* QY measurement with enhanced dynamic range. The reference measurement (gray line) of the excitation is performed with an OD filter in front of the monochromator, while the filter is removed during the measurement of the sample (orange line, pristine P3HT on glass with a QY of 7.8%). The corrected intensity (light gray line) is also given. The blue and green arrows indicate the spectral regions were the number of absorbed and emitted photons are calculated, respectively.

given that the later is able to deactivate excited states. A material that works in this sense is called *quencher*, and the reduction of the QY is termed *quenching*, which is a direct measure of how many excitons where transferred to (via energy transfer) or quenched by (via charge transfer) the quencher molecules. The relative decrease of the QY, the PL quenching efficiency (PQE), is calculated by comparing the QY of the pristine material (either donor or acceptor) to the QY of the same material in the blend:

$$\mathrm{PQE} = 1 - \frac{\Phi_{\mathrm{blend}}}{\Phi_{\mathrm{pristine}}}. \tag{3.8}$$

Due to the sensitivity of Φ on the preparation conditions (e.g. drying temperature, solvents) each blend sample should be compared to a pristine reference sample that was prepared following the same recipe. Note that the PQE can be used to determine η_{quen} in Eq. 3.6.

Films for PL quenching measurements were prepared on uncovered glass slices. Functional layers between the substrate and sample, such as PEDOT:PSS or PSS, significantly reduce the QY of the sample and were not implemented. All steps, including film preparation, sample transport and measurement with an integrating sphere setup (Hamamatsu C9920-02, A10094, C10027) were performed under inert atmosphere, as it is found that films which have been exposed to air show strongly reduced QYs (up to a factor of 2). For monochromatic excitation, the EQE setup (see above) was used.

4

Summarized presentation

This chapter contains a compact presentation of work that has been published in, or that is submitted to peer reviewed journals. Each section corresponds to a paper of the same title. Within one section, the text follows mainly the structure of the original publication. However, the results are viewed in the latest state of knowledge and may contain additional discussions. A detailed description of the author contributions is given in Sec. 6.1 and the original publications are reprinted in the Appendix.

4.1 Mobility relaxation and electron trapping in a donor-acceptor copolymer*

Over the last decade, the development of D-A copolymers was the main driving force for the improvement of the charge transporting and photovoltaic performance of conjugated polymers, as it was already outlined in the *Introduction*. However, the influence of the molecular structure of D-A copolymers on their charge transport is so far only poorly understood. Furthermore, Sec. 2.4 summarizes that it is expected that the electronic properties of conjugated polymers (mobility, energetic disorder, HOMO/LUMO energy, delocalization) play an important role in the primary charge carrier generation process of organic solar cells. This motivated the synthesis of several derivatives of a model-type D-A copolymer with the aim to correlate the charge transport properties to the corresponding structure of the copolymers.

Material system

For our studies, we chose a model copolymer with fluorene (F) as donor and thieno-benzothiadiazole-thieno (TBTT) as acceptor unit. The corresponding copolymer PFTBTT‡ was one of the first D-A copolymers that has been systematically designed as donor for bulk heterojunction solar cells.[101] It has a low HOMO energy of about −5.5 eV and a moderate optical band gap of 1.88 eV. In addition, it showed good hole transport, and so several chemically modified PFTBTT copolymers exist.[102–104] Beside the use as donor it has been soon realized that PFTBTT copolymers are ambipolar materials, with nearly equal electron and hole mobilities.[25] Consequently, it has been also used as acceptor in organic solar cells.[25,29,30] In combination with the donor P3HT, PFTBTT copolymers showed a PCE of up to 2.7 %, whereas the increase of the molecular weight and the exchange of side-chains played an important role in the optimization process.[25,29]

In this study, the effect of two distinct structural modifications is investigated. First, a regularly alternating (alt) PFTBTT with linear octyl side chains (named alt-PF8TBTT), and a derivative with longer and branched octyldodecyl side chains (alt-PF8/12TBTT) has been synthesized by the group of Prof. Scherf in Wuppertal. From each of these two polymers a second derivative is obtained where the alternation of the donor/acceptor units is partially disrupted. These so called partially (part) alternating copolymers carry, with a probability of about 5 %, blocks of several, directly connected TBTT units, which

* This section is based on M. Schubert, E. Preis, J. C. Blakesley, P. Pingel, U. Scherf, D. Neher, "Mobility relaxation and electron trapping in a donor-acceptor copolymer", Physical Review B **87**, 024203 (2013).

‡ The full name is poly[2,7-(9,9-dialkylfluorene)-alt-5,5-(4',7'-di-2-thienyl-2',1',3'-benzothiadiazole)]

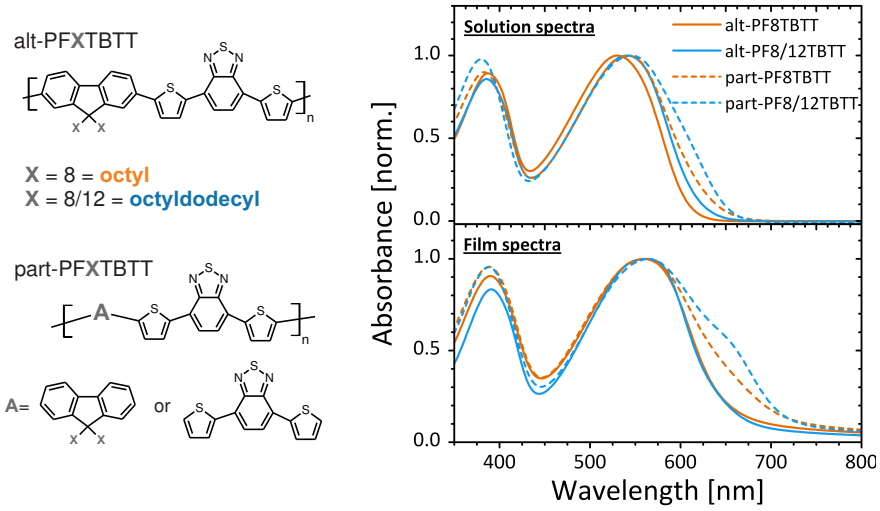

Figure 4.1: *(left)* Molecular structure of alternating (alt-) and partially alternating (part-) PFTBTT copolymers. *(right)* Optical absorbance in solution (0.1 g/l, chloroform) and of thin films.

breaks the otherwise regular D-A alternation. The molecular structures of the different copolymers are shown in Fig. 4.1. Also shown are the optical absorption spectra in solution and in a thin film. Compared to the alternating copolymers, the absorption of the partially alternating moieties reveal a pronounced shoulder at about 650 nm and a concomitant decrease of the optical band gap by about 0.15 eV. These spectral features are typical assigned to the aggregation or crystallization of conjugated polymers, a consequence of the improved planarization and extended conjugation (see Sec. 2.2).[47,48,104,105] However, the absence of the red-edge absorbance suggest that both alternating copolymers have a rather amorphous structure, which is consistent with the absence of X-ray diffraction features described in literature for octyl-substituted PFTBTT.[30,104] For the partially alternating copolymers, aggregation might be driven by the presence of blocks of the TBTT acceptor unit. Alternatively, these blocks will have a different LUMO energy, which might also affect the intermolecular charge transfer transition.[106]

Transient photocurrent experiments on alt-PF8TBTT

To investigate the potential of the different PFTBTT copolymers as electron transporting components, the mobilities were determined with transient photocurrent experiments. In these experiments, one of the copolymers (alt-PF8TBTT) showed rather unusual current transients, which impedes a direct comparison of the copolymers. Thus, this section is focused mainly on the investigation of the origin of the anomalous transport characteristics of alt-PF8TBTT, while the results of the other copolymers are discussed at the end.

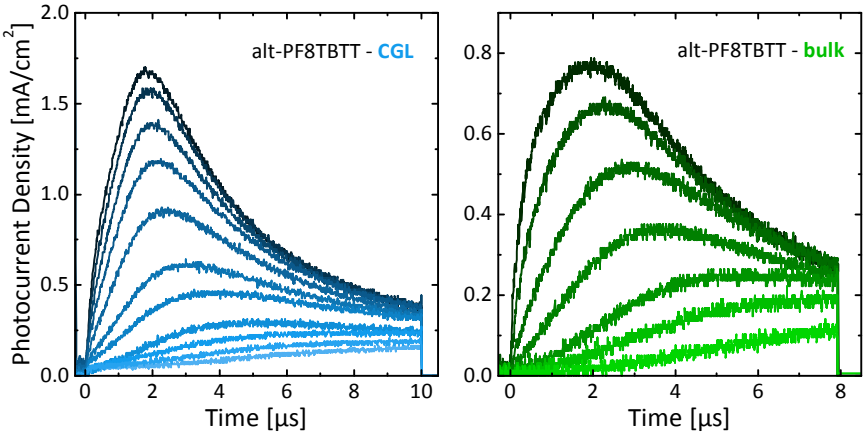

Figure 4.2: Photo-CELIV current transients of alt-PF8TBTT for increasing delay time between charge generation and extraction. *(left)* Data from a CGL device with 3 nm P3HT sensing layer and 170 nm alt-PF8TBTT or *(right)* from a 205 nm thick bulk device. The current decreases with increasing t_{del}, which was varied from 100 ns (black line) to 100 µs. The graph displays photocurrents only (dark current has been subtracted). All transients were shifted in time to set $t = 0$ as the beginning of the extraction pulse. Excitation was at 500 nm and A' was 1.09 and 0.86 V/µs for CGL and bulk device, respectively.

In Fig. 4.2 the delay-time dependence of alt-PF8TBTT photo-CELIV transients is shown. Two device structures (bulk and CGL, see Fig. 3.1 in Sec. 3.1) were investigated. In both devices the current decreases with increasing delay and a distinct change of the transients shape from a well defined maximum at short delay time to a steadily increasing current at 100 µs delay is observed. This similarity allows the assumption that the same carrier type (either holes or electrons) dominates the current in both device structures. We can use the CGL device to examine which charge carrier species is dominating. P3HT is known to effectively work as donor in combination with PFTBTT.[25] Thus, in the CGL device electrons and holes travel separately through alt-PF8TBTT and P3HT, respectively. However, due to the small layer thickness of the P3HT CGL (3 nm), and the high bulk mobility for regio-regular P3HT of about 1×10^{-4} cm^{2}V^{-1}s^{-1},[107] the transit time of holes is relatively short and the estimated t_{max} is only 40 ns, about two orders of magnitudes faster than the observed 2 µs at the shortest t_{del}. Consequently, the photocurrent in the CGL and in the bulk device must be dominated by the transport of electrons.

From the transients in Fig. 4.2, the electron mobility (μ_{e}) is directly obtained from Eq. 3.2 (bulk device) or Eq. 3.3 (CGL device). They are displayed in Fig. 4.3. The absolute difference between both device structures is assigned mainly to the strong approximation of a constant carrier density, made for the bulk sample, which leads to an underestimation of the mobility.[92] More important, both devices display a continuous decrease of the mobility with increasing delay time, suggesting that μ_e is explicitly depending on the time

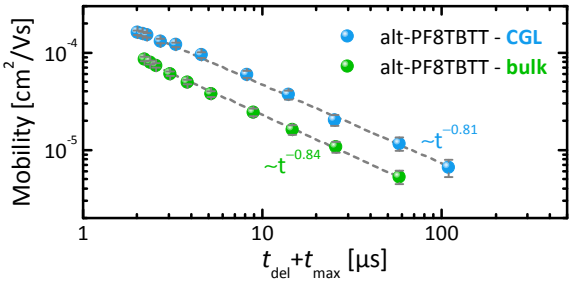

Figure 4.3: Calculated electron mobility for the CGL and bulk devices from the transients displayed in Fig. 4.2. Dashed lines show a linear fit to the data and the corresponding power laws are also given. The error is estimated from the uncertainty of t_{max}, which increases with increasing delay from 2 to 10%.

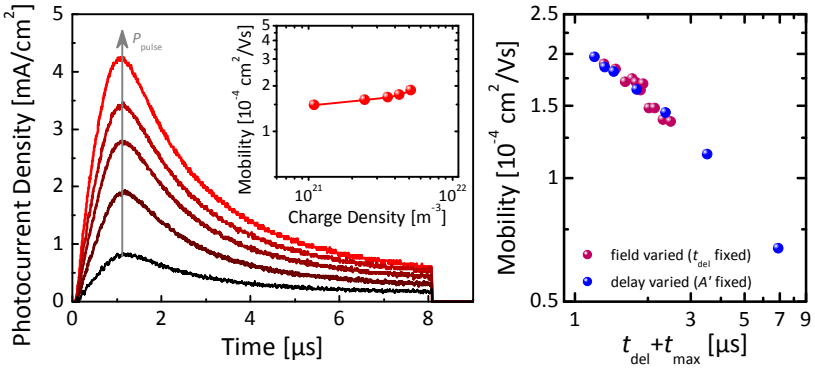

Figure 4.4: *(left)* Photo-CELIV transients of a CGL device with a 100 nm thick alt-PF8TBTT layer after 500 ns delay for increasing pulse fluences P_{pulse}. Inset: Calculated electron mobilities over charge carrier density, extracted by integration of the photocurrent. *(right)* Purple and blue spheres show mobilities for the same device measured either at a fixed delay of 500 ns and varying voltage rise speed (A' =0.4 to 3.5 V/µs) or at a fixed A' of 1 V/µs and varying t_{del}, respectively.

between generation and extraction (which is the sum of t_{del} and t_{max}). The mobility decay follows a power law behavior with comparable dynamics in both devices. Although time-dependent mobilities have been described in the literature in rare cases,[108–111] it is a uncommon and poorly understood phenomenon. Hence, we performed a detailed analysis of this process.

Recombination of non-equilibrium charges is a common source of erroneous mobilities, which can introduce an artificial time dependence of the mobility.[92,93] However, as bimolecular recombination is depending quadratically on the carrier density, the transients shape and t_{max} will change under different light intensities in the recombination dominated regime.[92,93] Transients under varying illumination conditions are displayed in Fig. 4.4. No change of the mobility and the transients on the whole is observed, verifying that recombination of free charges during extraction is negligible and that the experiments presented so far were indeed performed in the limit of low carrier concentrations. Finally,

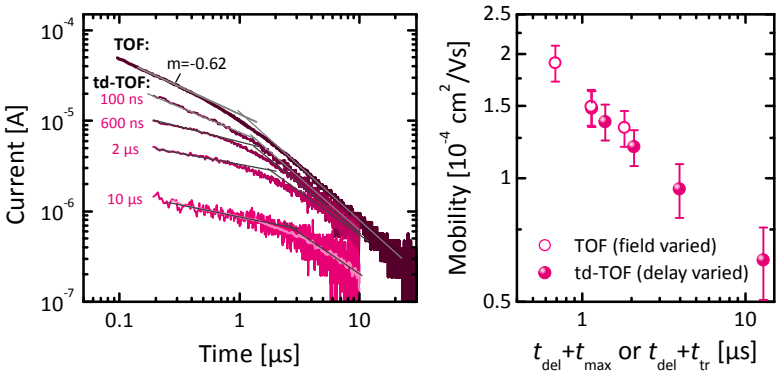

Figure 4.5: (*left*) TOF transient under a constantly applied voltage of -0.5 V and td-TOF transients measured with a 10 µs long voltage pulse with -0.5 V extraction voltage and 1.2 V offset voltage. The delay time is indicated in the graph. Measurements were performed in a CGL device with 170 nm thick alt-PF8TBTT. Transit times t_{tr} are extracted from the crossing of the two linear regimes, marked by the gray lines. The 10 µs delay data was averaged (pink line). Dark currents have been subtracted for all transients. (*right*) Calculated mobility values from TOF transients (open circles) measured under different electric fields ($V_{int} = 1.2, 1.7$ and 2.2 V) and td-TOF transients (purple spheres) obtained under the same field ($V_{int} = 1.7$ V) but varied delay.

we note that the delay experiment in Fig. 4.2 is measured at a fixed voltage rise speed A'. Hence, the mobility relaxation does not originate from a potential field dependence of the mobility, but it might be affected by that. This is due to the linearly increasing extraction voltage which means that for a sample with lower μ (higher $t_{del} + t_{max}$), extraction is at a higher field. To estimate if the dynamics are affected by the electric field dependence of the mobility, photo-CELIV transients were measured by changing either A' (at fixed t_{del}) or t_{del} (at fixed A'). Fig. 4.4 shows that both experiments yield identical mobilities when they are plotted over the sum of t_{del} and t_{max}, indicating that the electron mobility in alt-PF8TBTT is field-independent. To confirm this assumption, a second transient photocurrent measurement was performed.

The use of the P3HT charge generation layer also allows to perform time-of-flight experiments on the same devices at which photo-CELIV has been measured on. The advantage of TOF is that during illumination and extraction of the free charges a constant electric field is applied to the device. The TOF transient of the 170 nm thick alt-PF8TBTT device is shown in Fig. 4.5. The initial current decay follows a strict power-law dependence $j(t) \propto t^m$, followed by a transition to a faster power-law regime. The change of the slopes denotes the transit time (t_{tr}) of charges that traveled through the device of thickness d, and allows to estimate the mobility from Eq. 3.1. In a TOF experiment, the change of the extraction voltage provides an easy way to study the field dependence of the carrier mobility. However, the constantly applied voltage permits the direct investigation of their temporal evolution. Therefore, a pulsed TOF experiment was designed in which a rectangular shaped voltage pulse rather than a voltage ramp is applied to extract photo-excited

charge carriers. The technique allows to study the dynamics of the mobility under a static electric field and is identical to the recently developed time-delayed collection field experiment (TDCF),[60] with the only difference that charge generation is not in the whole bulk but only within a thin layer. To make this difference clear, it is named time-delayed time-of-flight (td-TOF).

With TOF and td-TOF the impact of the electric field on the mobility can be studied. In analogy with CELIV, two measurements were performed. One is the variation of the extraction voltage ($V_{\mathrm{app}} = 0$, -0.5 and -1 V) using regular TOF ($t_{\mathrm{del}} = 0$) and the other is changing t_{del} at a fixed extraction voltage (-0.5 V) using td-TOF. The transients which were measured at the same V_{app} are shown in Fig. 4.5 and mobilities are extracted from interpolated t_{tr}. Both experiments reveal a similar mobility relaxation, which is now purely based on the time dependence of the mobility. Again, this implies that the field dependence of the mobility of alt-PF8TBTT is rather small compared to the strong relaxation in time.

We conclude that the results from the photo-CELIV and td-TOF experiments reveal a distinct time dependence of the electron mobility in the prototype polymer alt-PF8TBTT. Examining the effects of delay time, charge carrier density and electric field reveals that *time is the mobility determining variable*. The origin of the mobility relaxation will be discussed in the next section together with the various effects that this time-dependence introduces on the interpretation and evaluation of transient experiments in general.

Simulation of current transients: The effect of trapping

To understand the origin of the mobility relaxation in alt-PF8TBTT, a drift-diffusion (DDS) and Monte Carlo simulation (MCS) were applied (see Sec. 3.2). The green line in Fig. 4.6 shows a DDS-obtained photo-CELIV transient, together with the measured response of a bulk device. The only free parameter in this simulation was the electron mobility, which was treated as field- and density-independent, in accordance to the findings of the former subsection. Setting the mobility to 1×10^{-4} cm^{2}V^{-1}s^{-1} yields a narrow and slightly asymmetric photocurrent peak with a comparable t_{max} but less than half the width of the measured photo-CELIV peak. In the simulation, all electrons can be extracted within 3.5 µs while in the experiment a large current flows under high internal fields at the end of the extraction pulse. It is reasonable that this current originates from charge carriers that are trapped inside the copolymer and gradually released by the increasing field. To simulate the effect of trapping, an MCS was written which can handle exponential trap distributions.

In Sec. 2.3, it was discussed that the multiple trapping and detrapping of charge carriers in an exponential density of trap states continuously decreases their average mobility.

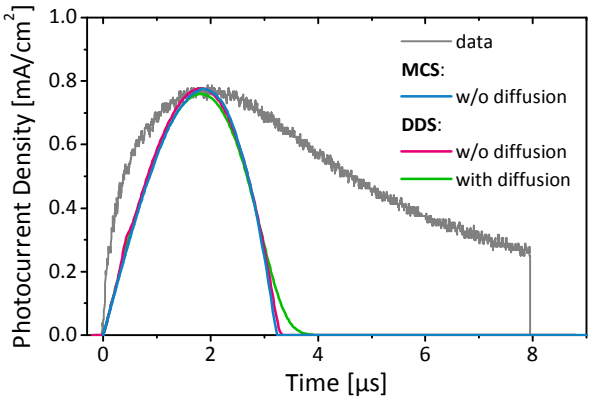

Figure 4.6: Comparison between MCS and DDS in the ideal trap-free case. The blue (MCS) and pink line (DDS) display simulated transients without the influence of trapping and diffusion. The green line shows a DDS transient with enabled diffusion. A homogeneous charge carrier concentration is assumed. For comparison, the photo-CELIV transient of the 205 nm thick alt-PF8TBTT bulk device after 150 ns delay is given (grey line).

This introduces a power-law decay of the photocurrent that follows photoexcitation, as it is observed in Fig. 4.5.[53] To verify that the MCS yields physically correct transients and to evaluate the influence of diffusion under ideal, *trap-free* conditions, photo-CELIV transients were simulated considering only the drift of charges with a constant mobility of 1×10^{-4} $\mathrm{cm^2V^{-1}s^{-1}}$. It should be noted that MCS-calculated photocurrents has no absolute physical dimension because they represent the average over many virtual single particle experiments. Thus, the height was scaled to match the measured data. The comparison between MCS and DDS in Fig. 4.6 demonstrates that both simulations yield nearly identical transients. Furthermore, the influence of diffusion is negligible small and can't account for the overall strong deviation of the simulated from the measured photo-CELIV transients which must have a different physical origin. We will now use the MCS to examine the influence of charge carrier trapping.

In the multiple-trapping and release model, the initial decay of the photocurrent in the TOF experiment is directly connected to the trap energy ϵ_T via $m = \alpha - 1 = k_B T/\epsilon_T - 1$ (see Eq. 3.4 in Sec. 3.2), which provides a way to determine the trap distribution experimentally. For the data in Fig. 4.5 a value of $\alpha = 0.38$ is calculated which yields a trap energy of $\epsilon_T = 67$ meV ($T_0 = 776$ K). The other MCS parameters were optimized to match the measured TOF transient. The result is shown in Fig. 4.7 together with simulated td-TOF transients, where only a delay between excitation and extraction was introduced in the simulation. Both techniques are well described by the MCS with a single set of parameters. Deviations exist for simulated td-TOF transients at large delay which will be discussed below. In addition, a second CGL device with 100 nm alt-PF8TBTT layer

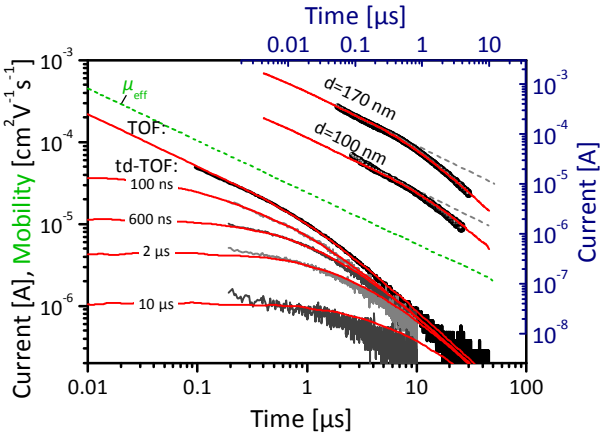

Figure 4.7: (*lower left*) TOF and td-TOF data (black lines) from Fig. 4.5 together with MCS simulation results (red lines). The effective mobility from the simulated TOF experiment (no delay) is displayed as green dotted line. The parameters were $\mu_0 = 2.3 \times 10^{-3}$ cm^{2}V^{-1}s^{-1}, $\epsilon_T = 67$ meV, $t_{\text{trap}} = 0.5$ ns and $N_{\text{eff}} = 0.05$. td-TOF transients are shifted in time and $t = 0$ denotes the beginning of the extraction pulse. (*upper right*) Measured (black spheres) and simulated (red lines) TOF transients from two CGL devices with 100 and 170 nm alt-PF8TBTT.

thickness can be well described with the same parameter set. This demonstrates that the initial current decay in the TOF experiment is independent of the internal field and thickness but depends purely on ϵ_T. Also displayed in Fig. 4.7 is the effective mobility μ_{eff} (see Eq. 2.4 in Sec. 2.3) in the TOF experiment, which continuously decreases with time. This illustrates that at times shorter than the transit time, where the number of charges in the device is constant, the current decay is controlled by the mobility relaxation only.

We now want to address the effect of the time-dependent mobility on the appearance of td-TOF transients. A first effect of the ongoing relaxation of the mobility during the delay is the decreasing height of the photocurrent (see Fig. 4.5), which is directly proportional to μ_{eff}. Also, plotted on the time scale of the extraction pulse (with $t = 0$ denoting the beginning) the slope of the initial current m decreases for increasing t_{del}, which might suggests a time-dependent trap energy since $m \propto T/T_0$. However, the transients have been calculated with a constant ϵ_T. Obviously, the decreased slope is a result of the shift of the current transients along the time-axis, due to the subtraction of the delay time. It appears because the absolute change of the mobility per unit time decreases as t_{del} increases. This yields a constant current for extraction times much smaller than the delay time. As a consequence, it is not meaningful to estimate the transit time from transients which are plotted on the time scale of the extraction pulse. The simulated transients clearly demonstrate that there is no characteristic change of the slopes which could unveil a transit time. Alternatively, td-TOF data should be plotted on a absolute time scale, with its origin at the moment of charge generation. Finally, we note that the expected constant

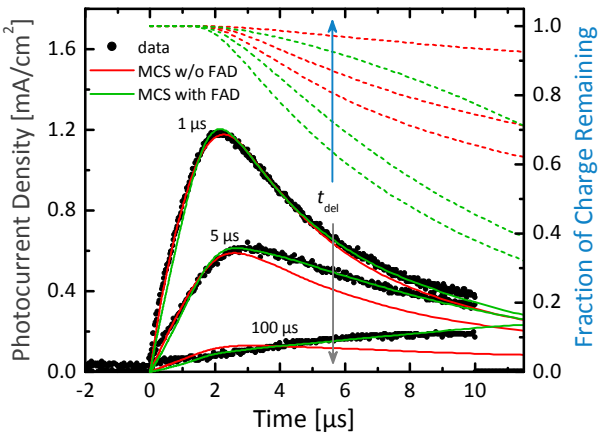

Figure 4.8: Influence of field-assisted detrapping (FAD) on photo-CELIV transients from Fig. 4.2. (*left axis*) Simulations without FAD (red lines) were performed with the same parameters as used in Fig. 4.7 for the TOF experiments, while the mobility was adjusted to $\mu_0 = 2.8 \times 10^{-3}$ cm^{2}V^{-1}s^{-1} with enabled FAD (green lines). A field activation length of 1.1 nm was used. Arrows point in the direction of increasing delay time. (*right axis*) Fraction of charges remaining (dotted lines) in the device as function of time ($t = 0$ at the beginning of the CELIV pulse) for all simulated transients.

initial current at high t_{del} is not observed in the experiment (e.g. for the 10 µs-delay transient). We propose that the remaining slope is an measuring artifact, introduced by the subtraction of the large capacitive loading current.

In a next step, the parameters from the TOF experiment were used to simulate photo-CELIV transients. Compared to the trap-free transient in Fig. 4.6, the simulated photocurrent peak in Fig. 4.8 becomes strongly asymmetric by the introduction of the trapping mechanism. For short delays, the MCS is in agreement with the measured data, reproducing the maximum as well as the pronounced tail of the current. This changes for larger t_{del}. At a delay of 100 µs the measured current increases continuously, while the simulated reaches a maximum at about 3 µs. Obviously, the simulation underestimates the current when most of the extracted charges stem from deep traps (at the end of the extraction pulse). Furthermore, the discrepancy between measured and simulated transients increases with increasing internal field. Due to the linear increasing extraction voltage of the CELIV experiment, the internal voltage exceeds 11 V at the end of the extraction pulse, which is significantly higher than the 1.7 V constantly applied in the TOF experiment. However, the simulation so far neglected the effect of the field on the trapping or detrapping. Assuming that the electric field lowers the energetic barrier by a value $a \cdot E$ but leaves the cross section of a trap unaffected, the probability for the release of a trapped charge carrier (detrapping) increases and becomes field-dependent, while the trapping remains unchanged. The *field activation length* (a) is a measure of the average hopping distance between a trap and free carrier state. This *field-assisted detrapping* (FAD) process was implemented

into the simulation by reducing the dwell time, which is proportional to $\exp(\epsilon/k_\mathrm{B}T)$, by a factor $\exp(-a\cdot E(t)/k_\mathrm{B}T)$ (up to $a\cdot E = \epsilon$). In this approximation the increasing extraction field continuously decreases the dwell time.

Fig. 4.8 displays the simulated transients with field-assisted detrapping, using a field-activation length of 1.1 nm. With a slight increase of μ_0 to 2.8×10^{-3} $\mathrm{cm^2V^{-1}s^{-1}}$ and leaving the other parameters unchanged, the experimental data is well described over the entire delay range. The origin of the improved simulation becomes clear when the number of charges that remain in the device is analyzed. For $t_\mathrm{del} = 1$ µs, the FAD reduces the charges in the device at the end of the extraction pulse from about 65% to 35%, due to the increased detrapping rate. Under these conditions, the peak of the photocurrent do not simply represent the transit time of the charge carriers. This also explains the faster decay of the CELIV mobility ($\mu \propto t^{-0.81}$) compared to the effective mobility ($\mu \propto t^{-0.62}$). Field-assisted detrapping is thus an important process in photo-CELIV experiments that are subject to pronounced charge carrier trapping. On the other hand TOF transients are not affected by the increased detrapping rate due to the relatively small electric field.

In summary, it is demonstrated that a simple one-dimensional Monte Carlo simulation is able to describe three photocurrent experiments—TOF, td-TOF and photo-CELIV—under several experimental conditions. The dominating process is found to be the trapping of charges in an exponential DOS, a process that was suggested also by the strong dispersion of the TOF transients. Compared to ideal, trap-free conditions, trapping of charges strongly broadens the photocurrent maximum in photo-CELIV experiments. To fully describe the delay dependence, field-assisted detrapping was introduced which has not been implemented in the analysis of CELIV transients before.

Origin of electron traps

The observation of electron traps in alt-PF8TBTT, raises the question about the origin of these trap states. In an attempt to identify chemical impurities, two new batches of the copolymer were synthesized independently by two laboratories, and the effect of an additional purification of the polymer after the synthesis was analyzed. However, we could not observe any change in the transient photocurrent characteristics. Furthermore, in contrast to the results obtained for the alt-PF8TBTT, photo-CELIV transients of the copolymers alt-PF8/12TBTT , part-PF8/12TBTT and part-PF8TBTT (chemical structures shown in Fig. 4.1) do not display a mobility relaxation. For all three polymers, a distinct current maximum can be observed even for high delay times. Furthermore, the maxima do not shift with increasing delay time (Fig. 4.9), except for alt-PF8/12TBTT, where a slight increase of t_max is observed, which might be due to a very weak trapping of electrons.

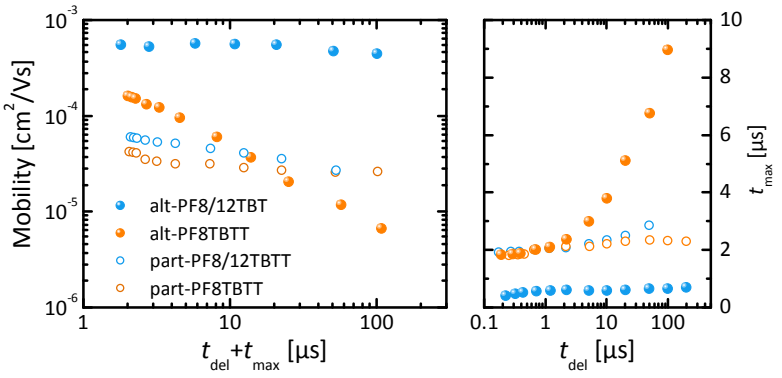

Figure 4.9: (*left*) Electron mobility of different PFTBTT copolymers, shown in Fig. 4.1, all measured in the CGL device structure. (*right*) Change of t_{max} as function of t_{del}.

These results demonstrate that rather small changes of the molecular structure of either the side chains or the backbone of the PFTBTT copolymer strongly alter the charge transport characteristics. First, the change from the alternating to the partially alternating structure reduces the mobility for the octyldodecyl-substituted copolymers by one order of magnitude. This trend is also visible in the octyl-substituted copolymers but in addition, the transport changes from being completely trap-dominated to trap-free. Given that the device preparation and measurements were carried out under the same conditions, we propose that it is unlikely that the electron traps are originating from doping, chemical defects, or impurities,[112,113] and that they must be related to the microscopic morphology or the molecular design of the copolymer itself. It was recently noted that solar cells which incorporate the high-performance donor copolymer PCDTBT (which has a chemical structure similar to alt-PF8TBTT) may suffer from significant intrinsic trapping of free charge carriers, introduced by morphological changes of the PCDTBT phase.[114,115]

An explanation for the observed effect arises from work by *Dieckmann* et al., who showed that the electrostatic interactions of transport sites and randomly oriented dipoles can cause a significant broadening of the DOS.[116] Such permanent dipoles might be created via intermolecular Coulombic interactions between the electron-attracting and electron-withdrawing group of neighboring chains. Recently, a combined molecular dynamics and density functional theory study by *Kilina* and coworkers investigated the influence of the side chain substitution on the energetic structure of amorphous aggregates of poly(fluorene).[117] Here, substitution with octyl side chains increases the conformational disorder, which finally creates highly localized and energetically deep trap states.

Conclusions

In this work, several transient photocurrent techniques have been applied to study the charge transport in PFTBTT copolymers. An uncommon mobility relaxation was observed for alt-PF8TBTT in bulk and CGL devices. This phenomenon was so far mainly observed in D/A blends and by using photo-CELIV.[109,118,119] In pure materials, a mobility relaxation has been seen on the ps–µs time scale by Devizis[110,111], and by Österbacka in regio-random poly(3-hexylthiophene) on the millisecond time scale, and was assigned to the intrinsic relaxation of charges in a Gaussian DOS.[108] However, the GDM predicts that the mobility attains a constant value at sufficiently long time, which was not observed by these authors. To understand the temporal change of the current transients measured in alt-PF8TBTT, a numerical simulation was used, which revealed that the time dependent mobility is caused be the trapping of charge carriers in an exponential density of trap states. Furthermore, the FAD mechanism was described for the first time. This allowed us to present for the first time a detailed description of photo-CELIV transients which are subject to severe charge carrier trapping.

Moreover, the comparison of the different PFTBTT copolymers gives some important information: First, it was demonstrated that the disruption of the alternating structure of D-A copolymers strongly reduces the charge carrier mobility. Second, trapping of charge carriers might be introduced intrinsically by the chemical structure of the copolymer. Our results illustrate the complex interplay between molecular structure and charge transport properties of D-A copolymers. However, a detailed investigation of the morphology of the different copolymers in the solid state would be necessary to identify the origin of the electron traps in alt-PF8TBTT on the molecular scale.

4.2 Bulk electron transport and charge injection in a high mobility n-type semiconducting polymer*

Compared to the continuously increasing hole mobility of organic semiconductors, the mobility of negative charge carriers has been unexplainable low for a long time. In 2005, *Chua* and coworkers discovered that interface traps in the commonly used SiO_2 gate dielectric inhibited the observation of electron transport in OFETs.[120] However, for the break through of n-type polymers further improvements in the device design and the development of D-A copolymers was needed. In 2009, the novel copolymer P(NDI2OD-T2), comprised of the strong electron-accepting naphthalene-diimide (NDI) core and a di-thiophene donor unit, exhibited an exceptional high electron mobility of 0.85 $cm^2V^{-1}s^{-1}$ in printed OFETs.[8] In addition, the copolymer shows a low LUMO energy of -3.96 eV, an optical band gap of only 1.45 eV and is stable in air. Several studies on the charge transport, film morphology, as well as of the energetic and optical properties followed. Due to the rather unique combination of excellent electron transport, low LUMO and small band gap, P(NDI2OD-T2) is supposed to be a potential acceptor for organic solar cells.

In OFETs, charge carriers are accumulated within a narrow sheet close to the gate dielectric. The charge transport is therefore quasi two-dimensional and at very high charge carrier densities, which strongly increases the mobility.[95,121] In contrast, the bulk heterojunction structure of D/A blends used in solar cells requires efficient three dimensional transport at significantly lower densities. Furthermore, charge carrier traps which strongly hamper charge transport, as it has been demonstrated in the former section, can be permanently occupied and deactivated at higher carrier densities. Consequently, a mobility that has been determined in an OFET might differ significantly from the value measured in the bulk, where transport occurs throughout the entire film thickness and at relevant carrier densities. However, only if the good charge transport properties of P(NDI2OD-T2) are retained in the bulk of the film it can be considered to be used as electron acceptor. Here, the commonly used fullerene acceptors demonstrate bulk mobilities of about $10^{-4} - 10^{-3}$ $cm^2V^{-1}s^{-1}$.[122,123]

Space charge-limited current-voltage measurements have established as a standard tool to investigate the bulk charge transport of organic semiconductors. The method is based on the injection of excess charge carriers of a single carrier type into the semiconductor and the subsequent transport of these charges through the film. Furthermore, ohmic charge injection is assumed, where the density of charges at the contact is much higher than in

* This section is based on Robert Steyrleuthner, Marcel Schubert, Frank Jaiser, James C. Blakesley, Zhihua Chen, Antonio Facchetti, and Dieter Neher, "Bulk electron transport and charge injection in a high mobility n-type semiconducting polymer", Advanced Materials **25**, 2799 (2010).

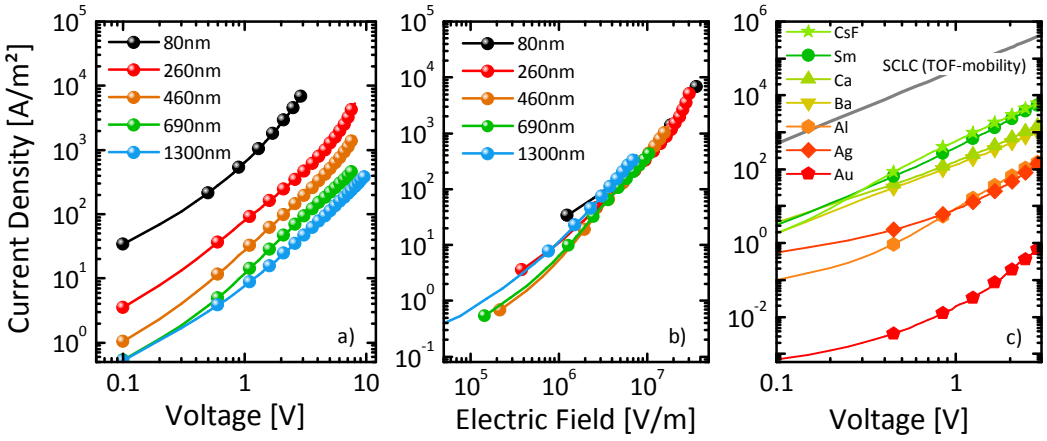

Figure 4.10: *a)* J-V characteristics of electron-only devices with varying P(NDI2OD-T2) thickness. The device structure comprises a flat aluminum bottom contact and a barium top contact. *b)* Same characteristics as in *a)* but plotted over the electric field. *c)* J-V characteristics of electron-only devices with 85 nm thick P(NDI2OD-T2) with different electron-injecting top contacts. The theoretical SCL current (grey line) is calculated from Eq. 4.1 by using the measured TOF mobility. All films were spin coated from chlorobenzene solution.

the bulk (the electric field at the injecting contact is zero). Charges will than adopt a characteristic profile in the device. In the absence of traps, the space charge-limited (SCL) current is described by the Mott-Gurney law:

$$J_{\mathrm{SCL}} = (9/8)\, \mu_{\mathrm{SCL}}\, \epsilon_0\, \epsilon_r\, \frac{V^2}{d^3}, \tag{4.1}$$

and depends on the applied voltage V, the film thickness d and the mobility μ_{SCL}. Current-voltage characteristics of electron-only devices with the thickness of the P(NDI2OD-T2) varying between 80 and 1300 nm are shown in Fig. 4.10.a. The current increases superlinearly with the voltage and approaches a slope of two at high voltages. This it expected from Eq. 4.1 for space charge-limited current, but has been also observed for devices that are limited by injection of charge carriers. It is therefore also necessary to control the correct scaling of the current with film thickness. Here, Eq. 4.1 is often rewritten as function of the electric field ($E = V/d$) and the characteristic scaling is:

$$J_{\mathrm{SCL}}(E) \propto d^{-1}\ . \tag{4.2}$$

Fig. 4.10.b displays the current for the different layer thicknesses as a function of E. The current of all devices falls onto a single line, demonstrating that the current is clearly not space charge-limited. In contrast, current injection rates into organic semiconductors are commonly described to depend explicitly on E but not on the thickness.[124,125] Thus, the current in thin P(NDI2OD-T2) layers is not determined by the mobility but seems

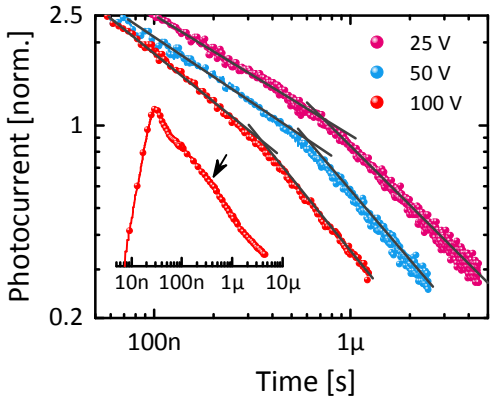

Figure 4.11: Time-of-flight photocurrent transients (normalized to the current at the inflection point) of a 5.2 µm thick P(NDI2OD-T2) layer for various applied voltages. A thin polymer interlayer (PFB) was incorporated into the device structure (ITO/PEDOT/PFB/P(NDI2OD-T2)/Ba/Al) tu suppress the dark current. Thin grey lines indicate the two linear regimes. The inset shows the complete 100 V current transient. The arrow indicates the transit time.

to depend on the efficiency for the injection of electrons into the polymer. In order to overcome the injection limitations, the material of the electron injecting top contact was varied. Materials with work functions between about 5.0 eV (gold) and 2.7 eV (samarium) were tested. For metals with a work function of 3 eV and below (samarium (Sm), barium, calcium), ohmic injection is expected, given that the LUMO energy of P(NDI2OD-T2) is about -4 eV.[126] J-V characteristics in Fig. 4.10.c display that the current scales according to the work function of the cathode and increases by 4 orders of magnitude. However, compared to the injection-limited Ba devices, the current can be improved by only a factor of 5 for Sm and cesium fluoride (CsF)-based devices, leaving it open if the space charge-limited regime is reached or not.

Due to the strong sensitivity of the injection current on the electrode material, transient photocurrent measurements were applied, which do not rely on electrically injected charge carriers. Time-of-flight (TOF) experiments were performed on thick P(NDI2OD-T2) layers and the transients are shown in Fig. 4.11. Mobilities were calculated from Eq. 3.1, while the transit time was taken at the time where the photocurrent has decreased to half of the value at the inflection point (the so called $t_{1/2}$ time).[127] The electron transport appears dispersive and the mobilty ranges from 6×10^{-3} $\mathrm{cm^2V^{-1}s^{-1}}$ (@ 25 V) to 4.5×10^{-3} $\mathrm{cm^2V^{-1}s^{-1}}$ (@ 100 V). These are among the highest room temperature electron mobilities reported for conjugated polymers and comparable to the bulk electron mobility of fullerene molecules. In analogy to Sec. 4.1, the dispersion of the transients imply a trapping of electrons. However, in contrast to the transport in alt-PF8TBTT, the decay of the current yields a characteristic energy (Eq. 2.3) of only 45 eV, which is in agreement with the low degree of energetic disorder that has been reported for P(NDI2OD-T2).[128,129]

The knowledge of the electron mobility allows us to calculate the electron current under SCL conditions (Eq. 4.1). The grey line in Fig. 4.10.c shows that the predicted transport-limited current is almost two orders of magnitude larger than the current measured for the best injecting devices. This suggest the presence of severe injection barriers for all cathode materials used in this study, which is in contradiction to the low LUMO energy of P(NDI2OD-T2), and the observed band-bending at the Al/P(NDI2OD-T2) interface.[128]

Recently, *Schuettfort* reported that the P(NDI2OD-T2) chains adopt a preferential edge-on orientation at the top surface of the film.[130] The orientation is found to be independent of the preparation method and of the resulting surface and bulk morphology. Furthermore, *Fabiano* and coworker investigated the injection of electrons from Au bottom contacts into spin coated and face-on-oriented layers of P(NDI2OD-T2) and into films with an edge-on orientation prepared with the Langmuir-Blodgett technique.[131] It is found that the electron injection barrier increases from 0.4 eV to 0.9 eV when the orientation is changed from face- to edge-on, which demonstrates the importance of the backbone orientation for the injection of electrons into P(NDI2OD-T2). We propose that the origin of this orientation dependent charge injection stems from the molecular structure of the P(NDI2OD-T2) polymer chains. In particular, the polymer contains very long and bulky *octyldodecyl* side chains, which are attached to the NDI units (see Fig. 4.12 for molecular structure). Given that the NDI units adopt an edge-on surface orientation,[130] these side chains must stick out of the film. Thus, the metal/organic interface is dominated by the insulating side chains and charge carrier injection requires the hopping (or tunneling) of electrons through a relatively large energetic barrier. Alternatively an internal barrier might be generated slightly below the top-surface due to the change of the backbone orientation from edge-on (at the surface) to face-on (in the bulk). The existence of such an internal barrier was suggested by numerical simulations of temperature-dependent J-V characteristics.[132]

In summary, a characterization of the bulk electron transport in P(NDI2OD-T2) is presented. The mobility was determined from transient photocurrent measurements and is among the highest ever reported for a conjugated polymer. Furthermore it is comparable to the mobility of fullerene molecules, which represent the state-of the art electron transporters so far. This important results suggest that P(NDI2OD-T2) can be applied as the electron accepting component in organic solar cells. A surprising result is found for charge injection-based current-voltage measurements, which revealed the presence of a severe injection barrier for a wide range of electrode materials. It is proposed that the long alkyl chains which promote the solubilization of the polymer in solution, in combination with a distinct surface orientation is responsible for the injection limited electron currents.

4.3 Influence of aggregation on the performance of all-polymer solar cells containing low-bandgap naphthalenediimide copolymers*

The excellent charge transport properties of the naphthalenediimide-based D-A copolymer P(NDI2OD-T2) motivated several studies on the photovoltaic properties. Surprisingly, first bulk-heterojunction solar cells comprising blends of the donor polymer P3HT and P(NDI2OD-T2) as the acceptor showed rather disappointing efficiencies of 0.2%, irrespective of the casting solvent or thermal treatment of the blend layers, which normally has a large impact of the solar cell performance.[38,39] By performing steady state and transient optical spectroscopy in combination with scanning X-ray transmission microscopy (SXTM) studies, *Moore et al.* came to the conclusion that the studied P3HT:P(NDI2OD-T2) systems exhibit a hierarchical blend morphology, consisting of strongly phase separated but impure donor-rich and acceptor-rich domains.[38] It was further proposed that the high degree of intermixing within these domains causes the localization of charges on individual chains, which facilitates geminate recombination and reduces the probability to generate free charge carriers. By adjusting the donor/acceptor weight fraction and by usind xylene as the solvent, the efficiency could be increased to 0.6% by *Fabiano* and coworkers.[37] P3HT is known to self-assemble in the form of ribbon-like crystals in dilute solutions of poor solvents such as cyclohexanone or p-xylene,[133,134] and the better performance of the xylene-coated blend was attributed to the formation of an interpenetrating network of well-crystallized P3HT nanofibers, embedded into the P(NDI2OD-T2) phase. These results suggest that the aggregation of the polymers may play a vital role with respect to the purity and structure of the phase separated polymer domains, which will be investigated systematically in this section.[37]

Here, we investigate the photovoltaic performance of the NDI-based acceptor copolymers P(NDI2OD-T2) and P(NDI-TCPDTT)‡, which were synthesized by Zhihua Chen at the Polyera Corporation and by Daniel Dolfen at the University of Wuppertal, respectively. The chemical formulas and the solid state absorption of the two acceptors and the donor P3HT are shown in Fig. 4.12. An important aspect of a further optimization of organic solar cells is the spectral match of the OSC absorption with the solar spectrum (see Fig. 4.12). An optimum band gap of about 1.4 eV was estimated to ideally match

* This section is based on M. Schubert, D. Dolfen, J. Frisch, S. Roland, R. Steyrleuthner, B. Stiller, Z. H. Chen, U. Scherf, N. Koch, A. Facchetti, D. Neher, "Influence of aggregation on the performance of all-polymer solar cells containing Low-bandgap naphthalenediimide copolymers", Advanced Energy Materials **2**, 369 (2012).

‡ The full name is poly[N,N´-bis(2-octyldodecyl)-2,6-bis(thieno-2-yl)naphthalene-1,4,5,8-tetracarboxylic-diimide-5´,5´´-diyl-alt-4,4-bis(2-ethylhexyl)-4H-cyclopenta(1,2-b:5,4-b´)dithiophene-2,6-diyl)].

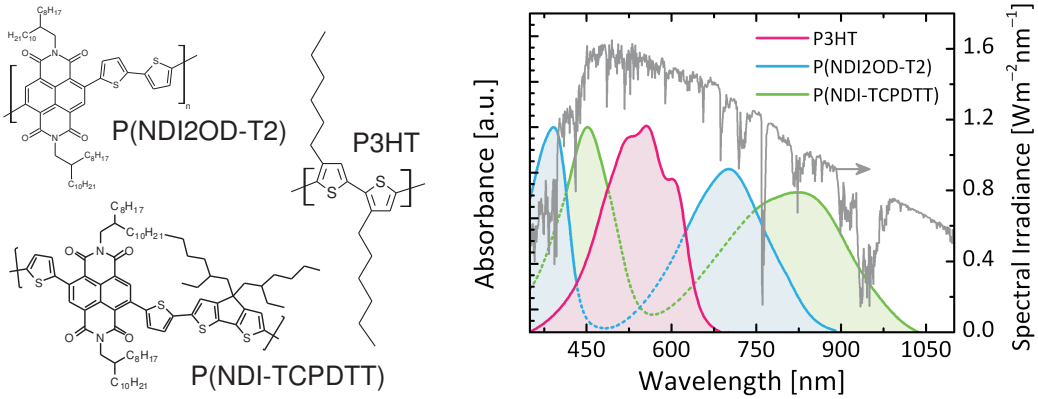

Figure 4.12: Molecular structure of P(NDI2OD-T2), P(NDI-TCPDTT) and P3HT. The right figure shows the normalized solid state absorption of the polymers (left axis) and the AM 1.5G solar spectrum (right axis).

the trade-off between generating maximum photocurrent while still providing a sufficient open circuit voltage.[135] With about 1.45 eV and 1.25 eV for P(NDI2OD-T2) and P(NDI-TCPDTT), respectively, both acceptor polymers have close to ideal band gaps and can significantly enhance the spectral sensitivity of the solar cells.

Preaggregation of pristine copolymers in solution

Perylene- and naphthalenediimide molecules are extensively used as dye materials providing a unique variability in structure and a widely tuneable color. The origin of their great versatility relies on the strong tendency to aggregate and the related formation of intermolecular excitations, a result of strong noncovalent interactions between the large conjugated cores of these molecules. A well-established approach to investigate the aggregation of small molecules or polymer chains is to study their absorption in different solvents.[136] Fig. 4.13.a and c display the absorption spectra of P(NDI2OD-T2) and P(NDI-TCPDTT) in various organic solvents including p-xylene (Xy), chloroform (CF), toluene (Tol), chloro- (CB), dichloro- (DCB) and trichlorobenzene (TCB), as well as 1-chloronaphthalene (CN) and tetralin (Tet). For a better comparison Fig. 4.13.b and d display only the CN and the film spectra. Solved in CN, the polymers reveal unstructured spectra with two absorption maxima. The high and low energy peak can be assigned to the $\pi - \pi^*$ and the *intra*molecular charge-transfer transition, respectively, typical for D-A copolymers.[105,106] In contrast, the film spectrum is more structured and strongly red-shifted. Compared to the CN solution, the onset of absorption of P(NDI2OD-T2) and P(NDI-TCPDTT) in the solid state shifts by 0.3 eV and 0.2 eV in energy, respectively, due to the appearance of new

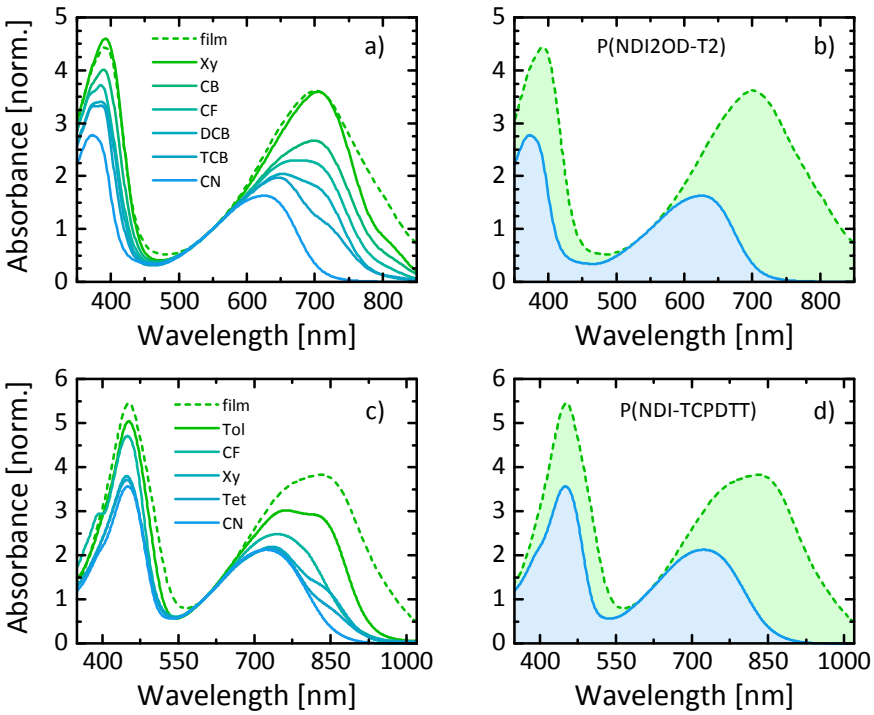

Figure 4.13: *a)* and *c)* Absorption spectra of P(NDI2OD-T2) and P(NDI-TCPDTT), respectively, in several organic solvents. Film spectra are displayed as dashed lines. *b)* and *d)* Absorption spectra of P(NDI2OD-T2) and P(NDI-TCPDTT), respectively, in CN solution (solid blue line) and of a spin-coated film (dashed green line). All spectra are normalized to the absorption of the amorphous P(NDI2OD-T2) and P(NDI-TCPDTDT) content at 550 and 600 nm, respectively, to visualize the contribution of the amorphous and aggregated phase.

absorption bands. These are typically observed in semi-crystalline organic semiconductors and are related to the formation of intermolecular aggregates with planarized backbones (Sec. 2.2).[48,49]

Structure analysis of thin P(NDI2OD-T2) layers by Rivnay et al.[9,10,137] and Schuettfort et al.[138] revealed that spin-coated films of P(NDI2OD-T2) contain a significant amount of crystalline domains, which makes it reasonable to assign the change of the absorption spectrum to the transition from the free, non-aggregated chain (measured in CN) to the strongly aggregated or crystalline conformation adopted in spin coated films. The close correspondence of film and Xy solution spectra also allows us to conclude that a high proportion of the P(NDI2OD-T2) polymer chains is pre-aggregated in Xy solution. More details of the pre-aggregation behavior of P(NDI2OD-T2) can be found in a recent publication of our group.[105] On the other hand, chain aggregation in CN is apparently rather weak or even absent, whereas a weakly aggregated state prevail in some other solvents. Here, we conclude, that solvent molecules with large and highly polarizable naphthalene units (such as CN and Tet) tend to suppress the aggregation of the copolymers in solution, due to the screening of the strong interactions between the NDI units.

Bulk-heterojunction solar cells

We now investigate the influence of the degree of pre-aggregation on the solar cell performance. BHJ solar cells from P3HT:P(NDI2OD-T2) showed very low efficiencies and photocurrents when the active layer was deposited from the commonly used solvents CB, Xy, DCB, or CF.[37–39] However, as demonstrated in the previous section, these solvents induce a strong pre-aggregation of the P(NDI2OD-T2) chains in solution. Thus, the degree of pre-aggregation was systematically tuned from a strongly aggregated (as in Xy) to a more and more non-aggregated conformation (as in CN). Fig. 4.14.a displays the evolution of the *J*-*V* characteristics of solar cells prepared from Xy:CN solvent mixtures with increasing CN content (see also Tab. 4.1). The Xy-cast device shows a high fill factor (FF), but the power conversion efficiency (PCE) is only 0.24%, and limited by the very small short-circuit current density (J_{SC}) of only 0.8 mA cm^{-2}. The addition of CN results in a marked improvement of all photovoltaic parameters, but the largest effect is on J_{SC}. The best performing cell is found for a 1:1 mixture (by volume) of Xy and CN, giving a PCE of 1.4%. Here, the pre-aggregation of the P(NDI2OD-T2) is completely suppressed and higher CN fractions do not significantly improve the solar cell performance further. The obtained efficiency is still one of the highest reported for PDI- or NDI-based acceptor polymers in combination with regio-regular P3HT. We note that BHJ layers are rather difficult to fabricate from solvent mixtures with high CN content, due to a facile dewetting of the solution from the anode. Interestingly we found that the temperature of drying directly after spin-coating (for details of the film preparation see Sec. 3.3) had a strong influence on solar cell performance (see also Fig. 4.18), while an additional thermal annealing step performed thereafter neither improved nor degraded the P3HT:P(NDI2OD-T2) BHJ solar cell properties. This implies that the drying process introduces a (meta-)stable blend morphology which cannot be further altered by thermal annealing.

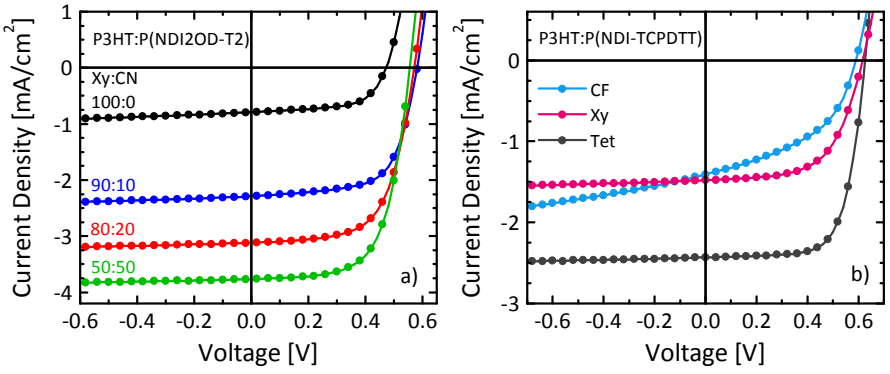

Figure 4.14: *J*-*V* characteristics of *a)* P3HT:P(NDI2OD-T2) (1:0.75) and *b)* P3HT:P(NDI-TCPDTT) (1:1.5) solar cells for various casting solvents, measured under simulated sun light at 100 mW cm^{-2}.

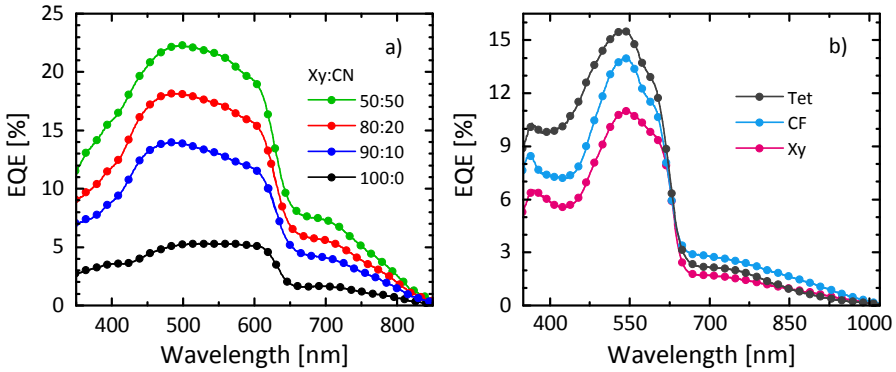

Figure 4.15: External quantum efficiency of *a)* P3HT:P(NDI2OD-T2) and *b)* P3HT:P(NDI-TCPDTT) solar cells from Fig. 4.14 (with the same color code).

For the P3HT:P(NDI-TCPDTT) blend, we, again observe an improvement in the device performance when adding CN to Xy (see Tab. 4.1), but the effect is weaker than for P(NDI2OD-T2)-based blends. On the other hand, we found rather different device characteristics when comparing blends spin-coated from CF, Xy, or Tet, despite a similar degree of pre-aggregation of P(NDI-TCPDTT) in these three solvents (see Fig. 4.13.d). *J-V* characteristics are displayed in Fig. 4.14.b. While the cells from CF and Xy have similar J_{SC} of 1.5 mA cm^{-2}, cells coated from Tet show a strongly improved photocurrent and a PCE of 1.1%. Most notably, the fill factor in this cell reaches 70%, the highest value ever observed for all-polymer solar cells. This fill factor has been reached for an active layer thickness of 410 nm, which implies that carrier extraction must be very efficient and that the generation of free charge carriers does not involve an appreciable electric field, as it is commonly observed for the best performing fullerene devices.

The increase in the photocurrent parallels systematic changes of the EQE spectra, which are shown in Fig. 4.15. For the P3HT:P(NDI2OD-T2) solar cells, the highest EQE (23%) is measured for the 1:1 Xy:CN solvent mixture. The comparison of the EQE spectra with the absorption spectra in Fig. 4.12 shows that the P3HT phase contributes strongest to the photocurrent, with the vibronic structure of P3HT still visible in the EQE spectrum. The composition of the EQE spectra of the P3HT:P(NDI-TCPDTT) solar cells is comparable between the different solvents and similar to that of the P(NDI2OD-T2)-based cells. However, the maximum EQE in the P3HT region is about 5–6 times larger than the EQE in the P(NDI-TCPDTT) region, demonstrating that the acceptor contributes only marginally to the photocurrent.

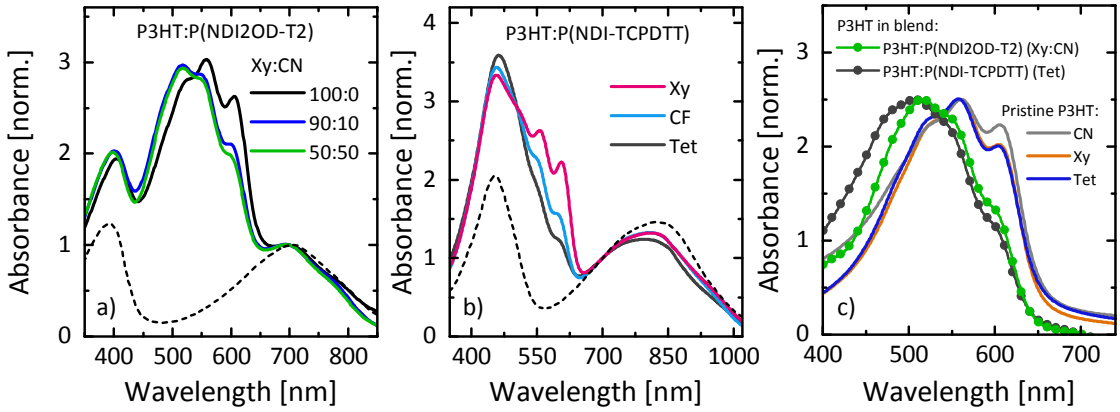

Figure 4.16: Absorption spectra of *a)* P3HT:P(NDI2OD-T2) and *b)* P3HT:P(NDI-TCPDTT) blends from the solar cells shown in Fig. 4.14 (with the same color code). Dashed lines show the pristine acceptor film spectrum from Fig. 4.13. *c)* Absorption spectra of pristine P3HT films (solid lines) spin coated from various solvents. Also shown is the P3HT absorption in the best performing solar cells, which was obtained by subtracting the acceptor absorption from the blend spectrum.

Chain aggregation in blend layers

The results presented in the previous section demonstrate that suppression of pre-aggregation in solution leads to significant improvement of the J_{SC} and EQE. This raises the question about the origin of the marked improvement and motivates a more detailed investigation of the optical and morphological properties of the blends. Fig. 4.16 displays the absorption of the BHJ solar cells from Fig. 4.14. The complementary absorption of P3HT and P(NDI2OD-T2) allows the direct probing of the aggregation of both polymers. Compared to the pristine P(NDI2OD-T2) layer, the absorption spectrum of P(NDI2OD-T2) in the blend layer shows only negligible differences. Hence, neither the addition of CN nor the presence of the P3HT is able to prevent aggregation of the P(NDI2OD-T2) chains in the blend during film formation. On the other hand, the spectral contributions attributed to the P3HT phase change largely with increasing CN content. The blend spin-coated from Xy shows a strongly aggregated P3HT spectrum with pronounced 0–0 and 0–1 vibronic progressions at 610 nm and 560 nm. Addition of CN clearly suppresses the 0–0 transition while the 0–2 peak at 510 nm becomes more pronounced. According to the model by Spano and co-workers,[48,136] the relative strength of the 0–0 vibronic transition is a direct measure of the intermolecular coupling strength, which is further related to the conjugation length and intrachain order of the interacting chains in P3HT aggregates. Thus, the addition of CN does not primarily prevent the aggregation of the polymers in the film but leads to more ill-defined donor aggregates. Presumably, the presence of non-aggregated P(NDI2OD-T2) chains in the drying solution prevents large-scale phase separation.

Table 4.1: Solar cell parameters for the devices shown in Fig. 4.14.

P3HT:**P(NDI2OD-T2)** (1:0.75)					P3HT:**P(NDI-TCPDTT)** (1:1.5)				
Xy:CN	J_{SC}	FF	V_{OC}	PCE	Solvent	J_{SC}	FF	V_{OC}	PCE
100:0	0.79	61	0.47	0.2	CF	1.41	46	0.59	0.4
90:10	2.29	65	0.58	0.9	Xy	1.48	60	0.62	0.6
80:20	3.12	63	0.57	1.2	Xy:CN (1:1)	2.04	71	0.59	0.9
50:50	3.77	65	0.56	1.4	Tet	2.43	70	0.63	1.1

A similar correlation between optical and photovoltaic properties is seen for the P3HT: P(NDI-TCPDTT) blends in Fig. 4.16.b., where only small changes in the P(NDI-TCPDTT) aggregate-related absorption band above 650 nm are visible, whereas the P3HT features are highly sensitive to the film preparation. As for the P(NDI2OD-T2)-based cells, the best performing blend shows the weakest P3HT aggregate absorption. The comparison of the P3HT spectrum in the blend* to the spectrum of pristine P3HT films prepared from CN, Xy and Tet, shown in Fig. 4.16.c, demonstrates that the reduced P3HT aggregation must be caused by the interaction with the acceptor in the blend layers and not by a different solvent-related film formation. The clear anti correlation between the presence of large and well-ordered P3HT aggregates in the blend layer and the device efficiency for both acceptor polymers, is in clear contrast to the well-established properties of P3HT:PCBM blends, where the formation of needle-like P3HT nanofibers with high intra- and interchain order was proven to be a major prerequisite for high short-circuit currents.[139,140]

Morphology

Scanning near-field optical microscopy (SNOM) measurements were performed to investigate the morphology of the blend films. Here, monochromatic illumination through an optical fibre with an aperture of about 100 nm is used to visualize either P3HT or the acceptor copolymer. SNOM images of the P3HT:P(NDI2OD-T2) solar cells from Fig. 4.14 spun from Xy and 1:1 Xy:CN are presented in Fig. 4.17. The P3HT and P(NDI2OD-T2) domains are probed at 500 nm and 690 nm, respectively (see Fig. 4.12). For both wavelengths, the films cast from pure Xy exhibits a high contrast in the optical density due to the strong

* This was obtained by subtracting a film spectrum of the pristine acceptor copolymer from the blend spectrum.

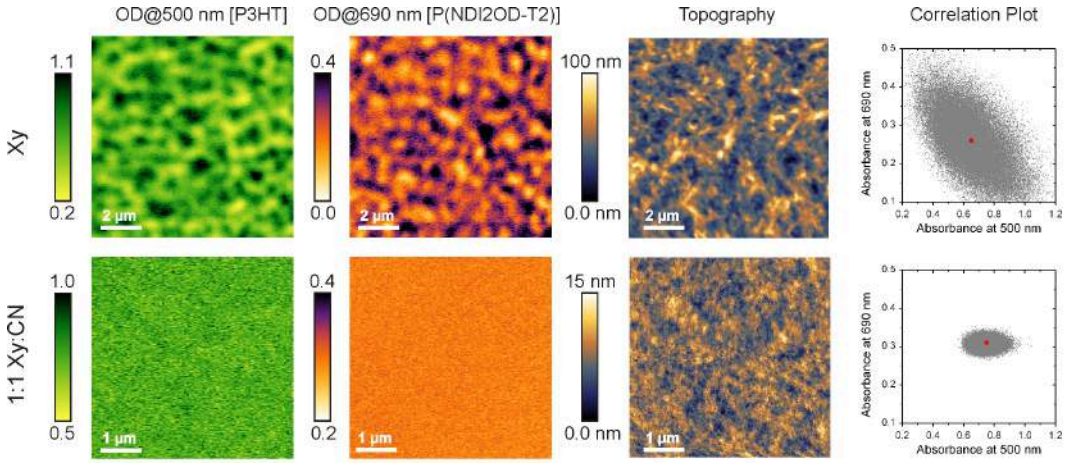

Figure 4.17: SNOM images of the P3HT:P(NDI2OD-T2) blends from Fig. 4.14.a fabricated from Xy (top) and 1:1 Xy:CN (bottom). Images taken at 500 and 690 nm visualize the optical density ($OD = -\text{Log}_{10}(I/I_0)$, where I_0 is the incident and I the transmitted photon flux) of P3HT and P(NDI2OD-T2), respectively. The topography is obtained by independent atomic force microscopy (AFM) measurements. Red dots in the correlation plots represent average OD values at the respective wavelength obtained by averaging over the whole SNOM image.

phase separation of both polymers at a length scale of about 1 µm. Furthermore, AFM height images recorded in parallel to each SNOM image revealed that the morphology of the Xy-cast blend consists of a network of elevated P(NDI2OD-T2)-rich domains, while P3HT-rich domains fill up the valleys in loosely connected islands.

Addition of CN to Xy solution has a strong effect on the nanoscale morphology of the resulting films. Firstly, images of films spun from a 1:1 Xy:CN mixture are much more homogeneous and lack a pronounced domain structure in the SNOM images. Also, we see no evidence for a pronounced anti-correlation between the absorption at 500 and 690 nm. Both observations indicate a homogeneously intermixed blend morphology, which can be directly related to the strong increase in photocurrent observed for this blend. However, we note that a phase separation may still be present with the size of the domains being too small (below 100 nm) to be resolved by our SNOM setup.

Large domains are also visible in the SNOM images of the Xy-cast P3HT:P(NDI-TCPDTT) blends. Smaller domains are visible in the best performing Tet-cast sample and the measurements imply the presence of a mixed donor:acceptor phase, which could explain the reduced aggregation of the P3HT upon mixing with the acceptor. However, the resolution of the SNOM setup turned out to be to small to resolve the relevant domain structures.

Conclusions

In this study it was shown for the first time that NDI-based D-A copolymers can serve as efficient electron acceptors. Solar cells with a peak PCE of 1.4% were demonstrated, which is significantly larger than in any other study of the same system and still one of the highest efficiencies for P3HT based all-polymer solar cells. Analysis of the absorption spectra of the corresponding BHJ solar cells reveals an anti-correlation between the solar cell performance and the quality of the P3HT aggregates. For P3HT blended with P(NDI2OD-T2), the highest efficiency is observed for layers coated from a 1:1 Xy:CN solvent mixture, where the pre-aggregation of the acceptor chains is completely suppressed. The analysis of the optical spectra indicates that addition of CN to Xy does not suppress the aggregation of the donor and acceptor chains in the final solid layer, but that it prevents the formation of large and well-ordered donor aggregates. Note that all low-efficiency P3HT:P(NDI2OD-T2) blends reported in the literature displayed a very aggregated P3HT spectrum in the blend, probably a result of the strong phase separation of both components.[37,38] The high fill factors and the strong improvement of the PCE upon changing device preparation conditions imply that a further optimization of NDI-based solar cells is possible. This was recently proven by several authors, who combined different D-A-type donor copolymers with NDI-based acceptors,[33,34,41] yielding an actual record efficiency for all-polymer solar cells of 4.1%.[33]

4.4 Correlated donor/acceptor crystal orientation and geminate recombination controls photocurrent generation in all-polymer solar cells*

The current status of all-polymer solar cells in general and the detailed optimization of the photovoltaic performance of P3HT:P(NDI2OD-T2) devices has been discussed in Sec. 1 and Sec. 4.3 of this thesis, respectively. It was shown that the efficiency limiting factor is generally the low external quantum efficiency (EQE) observed in all-polymer solar cells (see also Fig. 1.3) , which has not yet exceeded the 50% value. In blends of conjugated polymers, previous work has assigned geminate recombination via interfacial charge transfer states (CTS) as the dominant pathway for the decay of photo-induced excitations.[69,141,142] This suggests that geminate recombination is a surprisingly common and dominant process in polymer-polymer blends. Unfortunately, it is not understood how photogenerated charge carriers are able to overcome their Coulombic interactions. Thus, fullerenes keep up their mysterious role as the only universal class of organic molecules that can work as efficient electron acceptors.

In order to gain inside in the microscopic properties that govern free charge carrier generation, several recent studies suggest that it is controlled by the extent of charge delocalization on the donor or acceptor.[65,66,83] This is supported by computer simulations,[81,82,86] but also other models are discussed intensively (see also Sec. 4.4).[87,89,143] However, the specific microscopic structure or electronic processes that assist exciton dissociation remains unresolved.

With a moderate EQE of about 20%, blends of P3HT and P(NDI2OD-T2) display a typical all-polymer combination. Furthermore, we showed in the previous section, that the device efficiency is dominated by the photocurrent, while the fill factor remains high in all devices, suggesting that the transport and extraction of charges must be very efficient and that the low EQE lies on the ability to generate of free charge carriers. Thus it represents an ideal material combination to investigate the complex interplay of microscopic structure, film morphology and charge carrier generation.

* This section is based on Marcel Schubert, Brian A. Collins, Hannah Mangold, Ian A. Howard, Koen Vandewal, Wolfram Schindler, Steffen Roland, Jan Behrends, Felix Kraffert, Robert Steyrleuthner, Zhihua Chen, Konstantinos Fostiropoulos, Robert Bittl, Alberto Salleo, Antonio Facchetti, Frédéric Laquai, Harald Ade, and Dieter Neher, "Correlated donor/acceptor crystal orientation and geminate recombination controls photocurrent generation in all-polymer solar cells", submitted to Advanced Functional Materials.

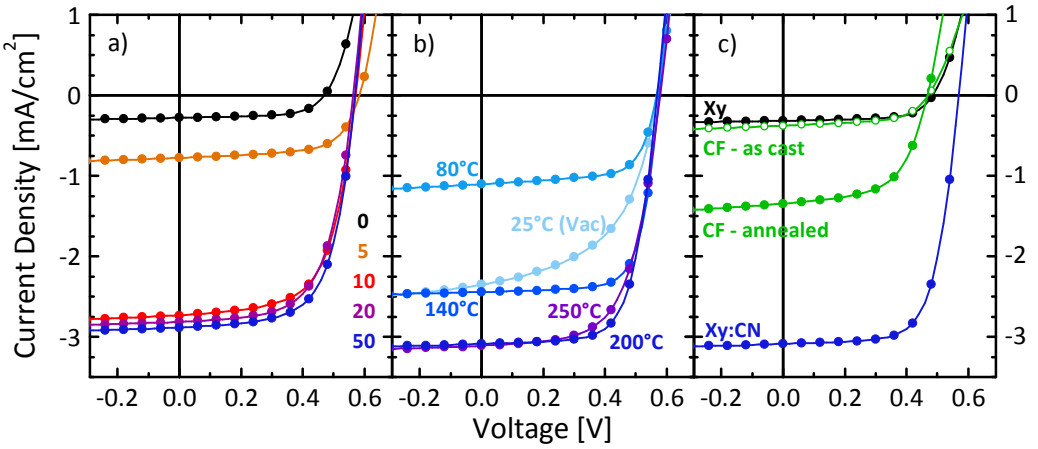

Figure 4.18: *J-V* characteristics of P3HT:P(NDI2OD-T2) BHJ solar cells prepared from *a)* different Xy:CN solvent mixtures, where the CN volume concentration is indicated in the graph. The active layers have a thickness of 300 nm and were dried at 200 °C. *b)* Solar cells prepared from a 1:1 Xy:CN solution for various drying temperatures and *c)* from different solvents. Annealing of the CF-cast device was at 160 °C. The weight ratio of P3HT to P(NDI2OD-T2) is held constant at 1:0.75 for all devices.

Variation of the photocurrent in BHJ solar cells

To identify the efficiency limiting processes, we first established protocols to prepare devices with a large variation of the photocurrent, which will be than correlated to the evolution of morphological parameters. Fig. 4.18.a displays *J-V* characteristics of P3HT:P(NDI2OD-T2) solar cells, prepared from different Xy:CN solvent mixtures, as it is also shown in Fig. 4.14.a. Note that the current of the solar cells investigated in this study is slightly lower and saturates at lower CN fractions than in the previously presented devices, which we attributed to the change of the polymer batches. However, every device series in Fig. 4.18 has been reproduced 5–10 times, and the variations of the currents within these experiments is below 10%. Fig. 4.18.b, shows the effect of the drying temperature on the solar cell performance. The photocurrent saturates at a temperature of 200 °C and decreases to about one third of the maximum current at 80 °C. For lower temperatures the current than increases again but at the same time the fill factor decreases strongly. The influence of different solvents on the photocurrent is displayed in Fig. 4.18.c, which shows that the performance of the solar cells prepared from CF can be increased by thermal annealing but stays below that of the Xy:CN-cast device. The devices from Fig. 4.18 were used for a thorough investigation of the morphology and the evolution of the excited states. It turned out that the CN series from Fig. 4.18.a provides the best insight into the microscopic processes that control the photocurrent generation, while the analysis of the drying temperature series and of the CF-cast devices is not yet finished. Thus, the following investigations will concentrate on the CN series only.

Table 4.2: Solar cell parameters[a] for the P3HT:P(NDI2OD-T2) devices shown in Fig. 4.18.

Solvent	Prep.[b]	J_{SC} [mA/cm^2]	FF [%]	V_{OC} [V]	PCE [%]	PQE[c] P/N [%]	d[d] [nm]
Xy:CN (**CN series**)							
100:0	as cast	0.27(1)	62(1)	0.47(1)	0.08(1)	91.9/44.7	300
95:5	dry@200 °C	0.77(6)	64(1)	0.58(1)	0.29(2)	91.5/-	300
90:10	''	2.8(1)	63(1)	0.57(1)	0.99(3)	94.9/-	295
80:20	''	2.9(2)	62(1)	0.56(1)	1.00(6)	95.6/-	300
50:50	''	2.9(2)	65(1)	0.57(1)	1.07(8)	96.2/54.8	300
Xy:CN (**Drying series**)							
50:50	dry@300 °C	3.0(3)	62(7)	0.56(3)	0.9(2)	96.0/-	300
50:50	dry@250 °C	3.2(3)	62(6)	0.57(1)	1.2(1)	95.5/55.4	300
50:50	dry@200 °C	3.0(2)	66(4)	0.57(1)	1.2(1)	96.2/54.8	300
50:50	dry@140 °C	2.3(2)	71(1)	0.57(1)	1.0(1)	94.8/53.9	300
50:50	dry@80 °C	1.09(5)	67(3)	0.57(1)	0.43(3)	94.5/48.2	300
50:50	dry@25 °C	2.39(4)	44(1)	0.54(1)	0.60(1)	-/-	300
50:50	dry@25 °C (Vac)	2.30(8)	49(2)	0.57(1)	0.66(6)	94.5/56.2	300
Solvent series							
Xy:CN 1:1	dry@200 °C	2.9(2)	65(1)	0.57(1)	1.07(8)	96.2/54.8	300
Xy	as cast	0.32(3)	63(1)	0.48(1)	0.10(1)	91.9/44.7	175
CF	as cast	0.40(3)	56(3)	0.50(4)	0.11(1)	99.4/93.5	150
CF	ann.@160 °C	1.4(8)	57(5)	0.47(1)	0.39(4)	97.1/85.7	150

[a] Obtained from 2–8 independent devices, each with 6 individual solar cells. The number in parentheses denotes the statistical uncertainty in the last digit. [b] This column denotes the active layer preparation (Prep.). "*dry@*" refers to films spin cast from CN-containing solutions, which were dried at the given temperature according to the recipe displayed in Fig. 3.2. Films from Xy and CF were spin coated until the film dried completely ("*as cast*"), where some have been annealed ("*ann.*") at elevated temperatures before deposition of the top-electrode. [c] Photoluminescence quenching efficiency (PQE) of P3HT (P) and P(NDI2OD-T2) (N) measured in films that were prepared according to the recipe of the corresponding solar cells (same D/A ratio, film preparation, etc.) [d] Typical active layer thickness measured with a surface profilometer.

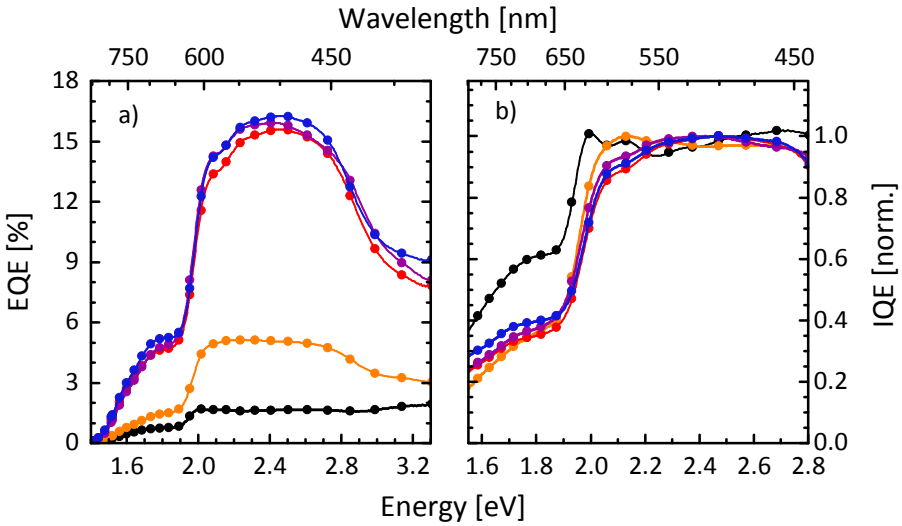

Figure 4.19: *a)* EQE and *b)* normalized IQE spectra of the solar cell devices from the CN series shown in Fig. 4.18.a.

The EQE of the CN series is displayed in Fig. 4.19.a. All spectra have a similar shape and composition. The maximum is reached between 2.0 and 2.8 eV, the range where P3HT constitutes the maximum absorption. In the range where predominantly P(NDI2OD-T2) absorbs, from 1.6 eV to 1.9 eV, the EQE drops significantly to about one third of the maximum value. Due to the high absorption of the active layers, also the internal quantum efficiency (IQE), which is the EQE corrected by the fraction of photons absorbed in the active layer (see Eq. 3.6), do not exceed the 20% value. Thus, we make a first conclusion that the low IQE of the P3HT:P(NDI2OD-T2) solar cells is responsible for the low photocurrents and represents the device limiting process. Normalized IQE spectra are shown in Fig. 4.19.b. They reveal a significantly reduced IQE of the P(NDI2OD-T2) phase, which is only between 40% (in the CN-cast devices) and 60% (in the Xy-cast device) of the value measured in the P3HT range. Thus, an additional process further lowers the free charge carrier yield of excitons absorbed by the acceptor polymer as compared to excitations absorbed by P3HT.

Blend Morphology

To elucidate the influence of CN on the film morphology, energy-filtered transmission electron microscopy (EF-TEM) measurements were performed, which shows enhanced chemical contrast compared to conventional TEM. We analyzed the electron energy loss spectrum at the sulphur ionization edge (165 eV), where the interaction of the transmitted electrons with the sulphur containing thiophene units reduces their kinetic energy. Due

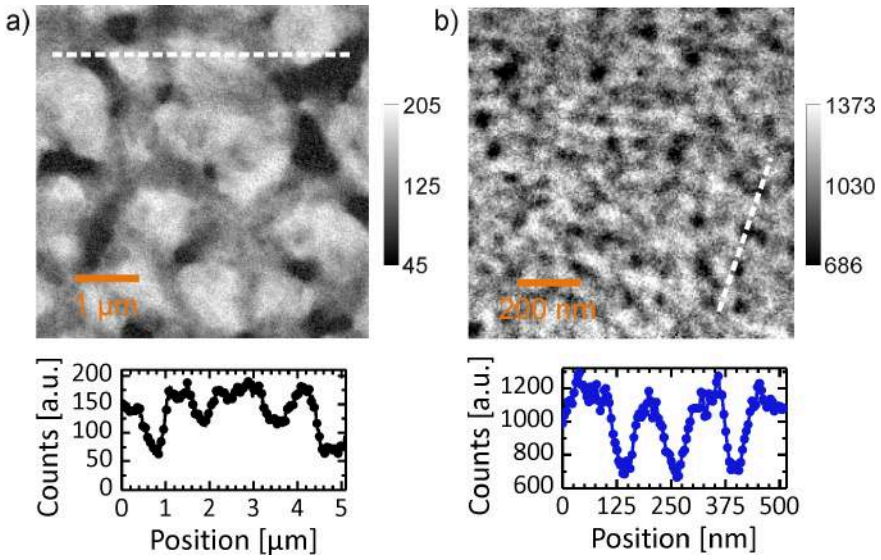

Figure 4.20: EF-TEM sulphur maps of *a)* Xy-cast and *b)* 50:50 Xy:CN-cast P3HT:P(NDI2OD-T2) blends. The signal is expressed in sulphur counts, where bright and dark areas correspond to P3HT- and P(NDI2OD-T2)-rich domains, respectively. The thickness of the film in a) and b) is 170 nm and 145 nm, respectively. Dashed lines indicate line scans shown below the images.

to the three times larger sulphur density in P3HT than in P(NDI2OD-T2), energy filtering provides sufficient chemical contrast between both polymers. The EF-TEM sulphur maps of a Xy-cast blend film is given in Fig. 4.20.a. It displays a strongly phase separated morphology comprised of irregular shaped P3HT domains with a typical diameter of 1 µm, and a network of P(NDI2OD-T2) fibrils, which have a width of 0.5-1 µm. Additional scanning transmission X-ray microscopy (STXM) measurements reveal that the darkest regions in EF-TEM sulphur maps are regions of pure P(NDI2OD-T2) and that the P(NDI2OD-T2) fibers are embedded within a matrix of P3HT. Donor domains that do not overlap with P(NDI2OD-T2) fibers, visible as the brightest domains in the sulphur maps, show an average P3HT concentration between 80 and 90%, indicating that these domains are impure and contain a significant fraction of P(NDI2OD-T2). The observation of a large phase separation in the Xy-cast film is consistent with the results of the SNOM measurements (Fig. 4.17). Furthermore, the high resolution of the EF-TEM also allows to visualize the domain structure in the best performing solar cells. Fig. 4.20.b reveals that P(NDI2OD-T2) arranges in circular domains in the 50:50 Xy:CN-cast film. Embedded in a P3HT matrix, these domains have a typical diameter between 30 and 50 nm, rather independent of the active layer thickness (see Fig. A.1 in App. A.1).

To obtain a statistical average of the domain structure over a large sample area, additional X-ray scattering measurements were performed on the complete CN series. The transition of the morphology within the series is probed by resonant soft X-ray scatter-

ing (R-SoXS) and small-angle X-ray scattering (SAXS) experiments.[144] Fig. 4.21.a shows profiles acquired at an energy of 285.3 eV, where the maximum chemical contrast between both polymers is observed.[144,145] Profiles acquired at 270 eV are also shown. These correspond to the non-resonant conditions in conventional SAXS and are more sensitive to mass density fluctuations. For the Xy-cast film, the intensity exhibits a maximum at $q = 0.0045$ nm^{-1} and a shoulder at $q = 0.014$ nm^{-1}. The corresponding characteristic lengths ($l_c = 2\pi/q$) of 1.4 and 0.44 µm can be retraced in the EF-TEM sulphur maps as the spacings between the P3HT domains and the mesh width of the P(NDI2OD-T2) network, respectively.

In stark contrast to the Xy-cast film, the R-SoXS profile of the 50 vol.% CN-cast sample shows a broad feature at $q = 0.08 - 0.09$ nm^{-1} ($l_c = 70$ nm) and a shoulder at $q = 0.2$ nm^{-1} ($l_c = 35$ *nm*), which we attribute to particle-like scattering from the circularly shaped domains seen in the EF-TEM sulphur maps. Furthermore, an additional shoulder is identified in the pattern at $q = 0.056$ nm^{-1} ($l_c = 112$ nm), reflecting the typical spacing of the P(NDI2OD-T2) domains seen in EF-TEM. The two high-q features, caused by scattering from the smaller circularly shaped P(NDI2OD-T2) domains, are common in all films with any amount of CN, linking the formation of these domains to the presence of the CN. In contrast, the position of the low-q feature, interpreted as dominant domain spacing, changes with CN-concentration. Starting with $l_c = 1.4$ µm at 0 vol.%, the feature moves to $l_c = 690$ nm with 5 vol.%, and $l_c = 123$ nm with 10 vol.%. At higher CN concentration, the change in position stops, with the dominant domain spacing for 20 vol.% and 50 vol.% equal to each other at $l_c = 112$ nm. Thus from the scattering profiles, it is likely that the mesoscale structural changes in the film largely saturate between 10 and 20 vol.% CN.

In Fig. 4.21.b also the total scattering intensity (TSI) is displayed, which is obtained through integration of each profile. As a function of CN concentration, the TSI increases strongly upon addition of 5 vol.% CN and then remains the same for higher CN concentrations. This indicates that the CN-induced domains have a higher purity than those cast from Xy. Since the STXM analysis in Xy-cast films showed pure fibers of P(NDI2OD-T2) but impure P3HT domains, the CN concentration dependence of the TSI suggests that mainly the purity of the P3HT domains increases upon addition of CN. Consequently, the smaller P(NDI2OD-T2) domains in the CN-cast blends are similarly pure. This conclusion is supported by the large contrast in the EF-TEM maps, which can be seen more clearly in the line scans in Fig. 4.20.

Polymer crystallinity

It has been presumed that the generation of free charge carriers is dictated by the microscopic structure of the donor and acceptor at the heterojunction. P3HT and

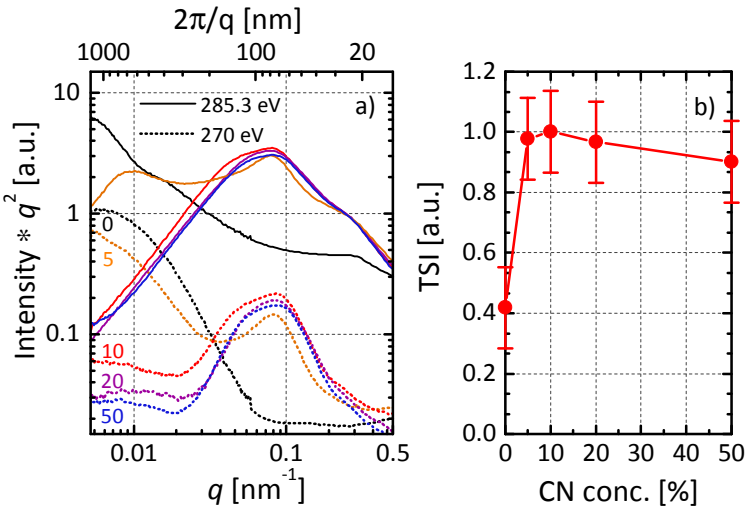

Figure 4.21: *a)* R-SoXS and SAXS profiles of blend layers with 300 nm thickness, measured at the $C_{1s}-\pi^*$ transition energy (285.3 eV, solid lines) and at non-resonant energy (270 eV, dashed lines). The CN concentration of the Xy:CN casting solution is indicated in the graph. The upper scale represents l_c. *b)* Calculated total scattering intensity (TSI) from the R-SoXS profiles shown in a).

P(NDI2OD-T2) are semi-crystalline materials, which comprise well ordered aggregated or crystalline, as well as disordered amorphous fractions. While ordered regions are associated with better charge transport and larger exciton and charge delocalization, it is generally unknown which role they play in the exciton dissociation process.

Grazing-incidence wide-angle X-ray scattering (GIWAXS) measurements have been used to study the micro structure of the crystalline domains. The different molecular structure of both polymers gives rise to a relatively large number of well separated scattering peaks, which allows the extraction of the molecular packing structure, the size and orientation of the P3HT and P(NDI2OD-T2) crystallites. Fig. 4.22 displays 2D detector plots as well as sector averaged GIWAXS profiles of the Xy- and Xy:CN-cast blends. According to the usual convention, the crystal directions were labeled as lamella stacking [h00], π-π stacking [0k0] and backbone repeat [00l], while the letter P and N of the peak labels stands for P3HT and P(NDI2OD-T2), respectively. From the position of the peak the real space repeat distances are obtained, which are in accordance with formerly published values,[9] while the coherence of P3HT and P(NDI2OD-T2) crystallites is obtained from a Scheerer analysis of the first order peak width. Furthermore, we use the intense [100] lamella stacking peak to probe the orientation of the crystals relative to the substrate.

We start with a quantitative description of the orientation distribution of the polymer crystals. From the two-dimensional GIWAXS data, pole figures were constructed following previously published routines.[146,147] A pole figure displays the distribution of crystals as function of the polar angle ω, defined as the angle between the substrate's surface normal

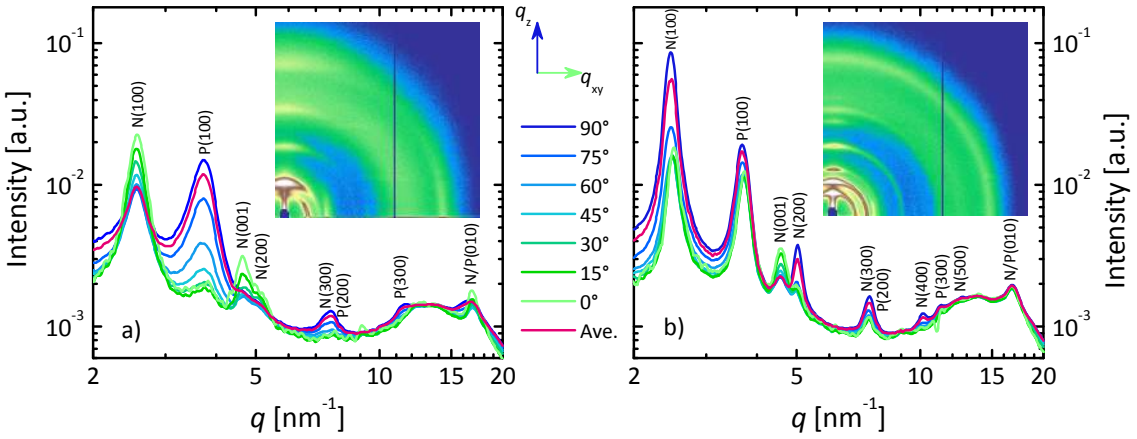

Figure 4.22: Sector averaged GIWAXS scattering intensity of P3HT:P(NDI2OD-T2) films cast from *a)* Xy or *b)* 50:50 Xy:CN. The 2D detector images are shown as inset. The peaks were labeled in accordance to earlier publications.[9]

and the [100] lamella stacking direction. Fig. 4.23 shows the orientation distribution of the P3HT and P(NDI2OD-T2) crystals. In the Xy-cast blend, P3HT crystals adopt a preferential edge-on orientation where the majority of crystals are oriented within an polar angle of 25°, while P(NDI2OD-T2) crystals are oriented diametrical opposed, adopting a face-on preference with the P(NDI2OD-T2) backbone lying parallel to the substrate.

Starting from this situation, CN introduces two distinct changes to these distributions, with the strongest change being the reorientation of the P(NDI2OD-T2) crystals from face- to edge-on. This transition clearly starts in the blend processed from 5% CN. Here a large face-on population of P(NDI2OD-T2) with a maximum at about 75° coexists with an edge-on population. With increasing CN concentration, the edge-on population further grows and saturates at about 20% CN, while the amount of edge-on crystals continuously decreases. The close coincidence of the structural changes with increasing CN concentration seen in the R-SoXS (see Fig. 4.21) and GIWAXS experiment reveals a close conjunction of domain structure and crystal orientation. Since P(NDI2OD-T2) forms a fiber network in Xy-cast films that is still present in the 5% CN-cast blend but disappear for 10% and larger CN concentrations, it is clear that the fibrils contain P(NDI2OD-T2) crystals with face-on orientation. On the other hand P(NDI2OD-T2) crystals are oriented edge-on in the circular domains which dominate the structure in the optimized blends. For P3HT, higher CN concentrations also introduce a significant fraction of randomly oriented crystals, while the edge-on preference is conserved. We note that the amount of face-on oriented crystals is actually larger than it is implied by Fig. 4.23, which can be seen after performing a geometrically correction of the raw pole figures. However, the same conclusion can be drawn from these corrected pole figures, that in the optimized blends, P3HT

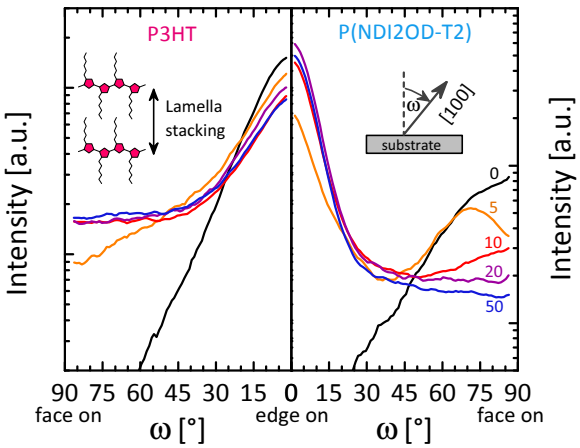

Figure 4.23: Pole figures of the [100] lamella stacking of P3HT (*left*) and P(NDI2OD-T2) (*right*) crystals in the blend films. The CN concentration is indicated in the right figure. The definition of the polar angle ω and a sketch of the lamella stacking are given as insets.

and P(NDI2OD-T2) crystals adopt the same preferential edge-on orientation distribution, while they are almost perpendicularly oriented in the Xy-cast blend.

Not only the orientation but also the crystal coherence (a measure of the crystal size and quality)[148] and the relative degree of crystallinity (DoC) are influenced by the formulation of the casting solution (see Fig. A.2 in App. A.1). However, the abrupt change of the coherence of both polymers and the DOC of P3HT do not follow the changes in device performance, which indicates that it is neither the size nor the amount of crystals that determine the current in the presented devices.

Exciton quenching

From the investigation of the morphology, we know turn to analyze the dynamics and yields of the excited states in the solar cells. The quenching of excitons at the heterojunction stands at the beginning of the cascade of elementary processes which leads to the generation of the photocurrent. The quenching (by charge-transfer) of excitons created after photon absorption in competition to their recombination to the ground state, is simply probed by measuring the decrease of the PL of the donor (acceptor) in presence of an acceptor (donor). For the blends from Fig. 4.18.a the photoluminescence quenching efficiency (PQE), defined in Eq. 3.8, is given in Tab. 4.2. For P3HT, the singlet exciton quenching is almost complete and ranges from 92% to 96%. The high P3HT quenching for the micrometer large domains of the Xy-coated film is consistent with the observed low domain purity in the STXM experiment, while we assign the increased quenching in the Xy:CN-processed films to the strongly reduced domain size. Determining the P(NDI2OD-T2) PQE is much more

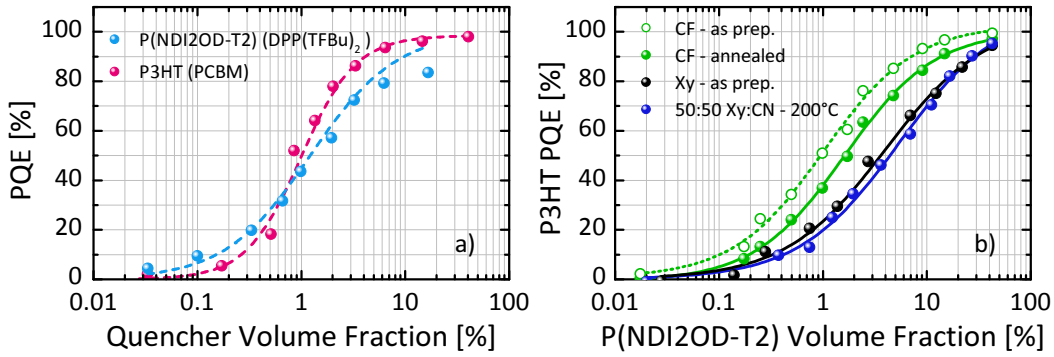

Figure 4.24: *a)* PQE of P3HT and P(NDI2OD-T2) as function of the volume concentration of the quencher molecules PCBM and $DPP(TFBu)_2$. *b)* PQE of P3HT, quenched by P(NDI2OD-T2). The layers were prepared from different solvents, according to the recipes used for the solar cells shown in Fig. 4.18.c. The volume fraction and the mass fraction of the quencher are assumed to be the same. Lines are a guide to the eye.

challenging due to the very low PL quantum efficiency of pure P(NDI2OD-T2), which we find is only about 0.14%. In the 50:50 Xy:CN-cast blend only 55% of the excitons can be quenched, while in the Xy-cast film the PQE is even lower and reaches 45%. The incomplete quenching of excitons formed on the acceptor therefore represents a direct and significant loss channel. Furthermore, we can safely state that the decreased IQE for photons absorbed in the acceptor is mainly caused by the incomplete quenching of the primary-excited excitons in P(NDI2OD-T2).

We consider two possible explanations for the low PQE of P(NDI2OD-T2) compared to P3HT: a morphology in which the P(NDI2OD-T2) domains are purer than the P3HT domains, or a significantly reduced exciton mobility in P(NDI2OD-T2). With regard to the second hypothesis, *Mikhnenko* and co-workers recently designed an experiment to determine the exciton diffusion length from PQE measurements using a series of concentrations of well dispersed quenchers.[149] We adopted this technique to compare the exciton diffusion length in the donor and acceptor materials. To ensure efficient intermixing, small conjugated molecules were used as quencher (PCBM for P3HT and DPP(TFBu)2 for P(NDI2OD-T2)). At a quencher volume concentration of about 1% the PQE is equivalent for P3HT and P(NDI2OD-T2), suggesting that both have a comparable diffusion length. Thus, the difference in quenching efficiency does not stem from a poorer exciton diffusion in the acceptor but likely originate from a dissimilar composition of the donor and acceptor domains.

We observed in the last section that the P3HT-rich domains are larger than the P(NDI2OD-T2) domains in both the Xy- and 50:50 Xy:CN-cast films but the PL quenching of P3HT is about twice that of P(NDI2OD-T2). Furthermore, we demonstrated that both polymers have a comparable exciton diffusion length. This implies that the P3HT

domains are impure, as already suggested by STXM and R-SoXS. On the other hand the poor quenching of P(NDI2OD-T2) even in the small domains of the 50:50 Xy:CN-cast blend, leads us to conclude that they are relatively pure; that the miscibility of P3HT in the P(NDI2OD-T2) phase is rather low. This could be a consequence of the strong aggregation of P(NDI2OD-T2) during the transition from solution to the solid state,[36,105] tending to exclude P3HT from the domains. Thus, the reduced IQE of the acceptor polymer is a result of the high domain purity and the incomplete quenching of excitons in the P(NDI2OD-T2) domains.

Concentration-dependent PL quenching might be also a powerful tool to investigate the domain purity of D/A blends. As example, Fig. 4.24.b displays the PQE of P3HT as it is gradually mixed with P(NDI2OD-T2). The films were prepared according to the recipes used for the solar cells shown in Fig. 4.18.c. First, the lowest quenching is observed for the 50 vol.% CN-cast recipe, for which we suggested a high domain purity. Interestingly, the quenching profile of the Xy-cast blends is nearly identical, despite a stronger phase separation (Fig. 4.20.a). We showed that the purity of the P3HT domains in the Xy-cast blend is significantly lower than in the CN-cast samples, demonstrating that the quenching curves always represent a convolution of the domain purity and the degree of phase separation. Without additional information on the domain structure the results might be misleading. Nevertheless, for a comparison among samples with a nominally similar morphology these measurements can provide information that are otherwise not accessible. This can be observed in the CF-cast samples. Here, EF-TEM also shows the presence of large P(NDI2OD-T2) fibres (Fig. A.3 in App. A.1), which are embedded in an impure P3HT matrix. The comparison of the PQE profiles now shows that this matrix must contain a significantly larger amount of P(NDI2OD-T2) than in any other blend. For the as prepared CF-cast blends, the quenching of P3HT by P(NDI2OD-T2) is indeed as large as it is in the P3HT:PCBM blends. This suggest that in the CF-cast blends, P(NDI2OD-T2) can intermix closely and in a large amount into the donor domains. Furthermore, the effect of annealing can be clearly seen by a distinct decrease of the PQE, which suggest an improved domain purity. This is of particular importance, as this change has not been observed by any other of the morphology experiments, including R-SOXS, SAXS and EF-TEM.

Internal quantum efficiency and CTS splitting

In order to further elaborate the efficiency limiting process, the PQE values from the former section can be compared to the IQE. For all blends the IQE is below 20% (Fig. 4.19) over the entire spectral region, significantly lower than the PQE meaning that a process in the quantum efficiency cascade subsequent to exciton quenching must be the dominant loss

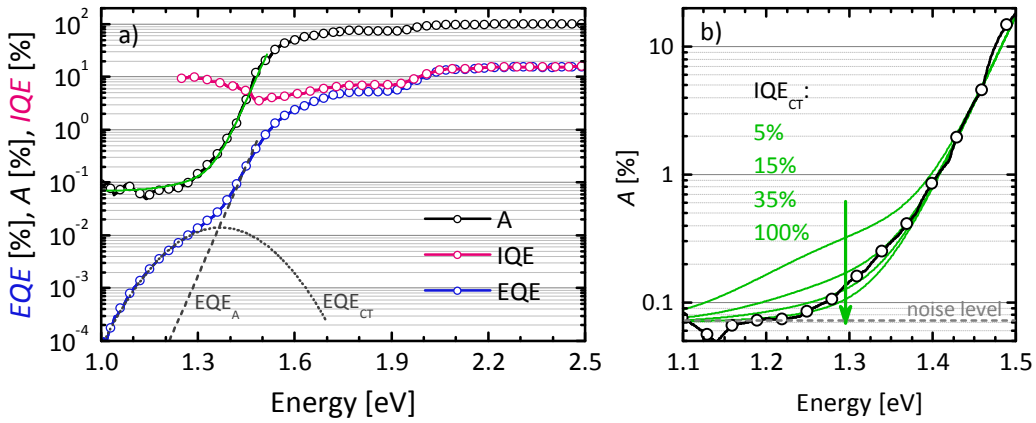

Figure 4.25: *a)* EQE (blue circles), IQE (pink circles) and active layer absorption (black circles) of the 50:50 Xy:CN-cast blend. The main contribution to the IQE in the range up to 1.5 eV, from 1.5 to 1.9 eV and above 1.9 eV are assigned to CTS, P(NDI2OD-T2) and P3HT, respectively. Also shown are a gaussian and an exponential fit to the CTS region (EQE_{CT}, gray dotted line) and the P(NDI2OD-T2) band gap region (EQE_A, gray dashed line), respectively, as well as the best fit to the absorption (green line) with IQE_{CT} of 35%. The absorption is fitted from a superposition of the two signals and a constant background noise level (C): $A = EQE(E)_A/IQE_A + EQE(E)_{CT}/IQE_{CT} + C$. *b)* Influence of the fit parameter IQE_{CT}, while the other parameters $IQE_A = 6\%$ and $C = 0.07$ were held constant.

mechanism for these devices as a whole. The next step in the cascade is the separation of interfacial charge transfer states that are created upon exciton quenching. These states are per definition still coupled to his ground state and can decay before producing free charge carriers. In order to gain insight into their role in determining the quantum efficiency of our samples we employed the techniques of photothermal deflection spectroscopy (PDS) to accurately determine the efficiency of charge separation over the entire spectrum, including directly created CTS.

Fig. 4.25.a displays the logarithmically plotted EQE, A and IQE spectra of the 50 vol.% CN-cast blend, measured from the visible absorption of P3HT, then P(NDI2OD-T2), down to the near infrared (NIR) absorption of the directly excited interfacial charge-transfer state at photon energies below 1.4 eV. In the EQE spectrum, the two characteristic regions of the P3HT and P(NDI2OD-T2), as they are shown in Fig. 4.19.a, can be easily identified. Below the band gap of P(NDI2OD-T2) a pronounced shoulder appears which originates from the excitation of the CTS.[67,68,71] With the measured absorbance, the IQE spectrum is calculated which shows similar features as they were seen in Fig. 4.19.b, comprising the maximum at photon energies where P3HT dominates the absorption, and a drop in the region where P(NDI2OD-T2) primarily absorbs. Importantly, the IQE then increases again to about 10% in the sub-band gap region of photon energies less than 1.4 eV where the very weak sample absorption is explained by direct excitation of the interfacial charge-transfer

states.[67] To estimate a more realistic value, we separated the EQE into the contribution originating from the CTS and from the P(NDI2OD-T2) and recalculated the absorption in the NIR region from the modeled EQE spectrum, using the IQE as variable parameters (see Fig. 4.25.b). The best fit is obtained when the IQE of the charge transfer states (IQE_{CT}) is equal to 35%, although it is not possible to define an upper boundary. This important result suggests that the CTS can split with significantly higher efficiency than the direct excitation of either the donor or acceptor polymer. This clarifies that the CTS can act as a precursor for the generation of free charges, and that it is likely that it defines the overall conversion efficiency of excitons. However, we like to point out that these measurements can not conclusively proof if also the excitons that split up into free charge carriers do this via the CTS.

Ultrafast spectroscopy

The previous section demonstrated once more that the free charge carrier yield is limited by the low IQE of both the excitons and the CTS. Consequently, there must be a significant loss channel related to the precursor of free charge carriers. In this section we will follow the change in photoinduced absorptions and bleaching as excitons move to the interface to create geminate charge carrier pairs, and how these then behave. The spectral signatures of the different excited-state species contributing to the TAS spectrum are shown in Fig. 4.26 for the pristine P3HT and P(NDI2OD-T2). The well separated spectra of both polymers, allows for a selective exciton generation in only one of both components in the blend as well as the investigation of the dynamics of the single processes. A detailed analysis was performed for the 50 vol.% CN-cast blend.

In Fig. 4.27 we display the temporal evolution of the TAS spectra together with the kinetics obtained in three different wavelength rigions. At the beginning of the experiment, P(NDI2OD-T2) excitons are selectively excited at an energy of 1.51 eV. The change of the transient transmission is than analyzed at an energy of about 2.25 eV (called “P3HT bleach region”). Here, only the positive ground state bleach (GSB) of P3HT and the negative photoinduced absorption (PIA) of P(NDI2OD-T2) excitons contribute to the signal. Thus, as the P(NDI2OD-T2) excitons move to the interfaces and form charge carrier pairs, the signal in this region should go from negative to positive. Indeed this is what we observe in Fig. 4.27.b in the time region marked *A*. In the first few picoseconds the signal in this region changes from negative to positive as the PIA of P(NDI2OD-T2) excitons that are quenched is replaced by the P3HT absorption bleach of the resultant holes. Fitting the rise of P3HT bleach yields the violet line and a lifetime for the P(NDI2OD-T2) in the blend of 0.96 ± 0.04 ps, about 40 times faster than the luminescence lifetime of pristine P(NDI2OD-T2).

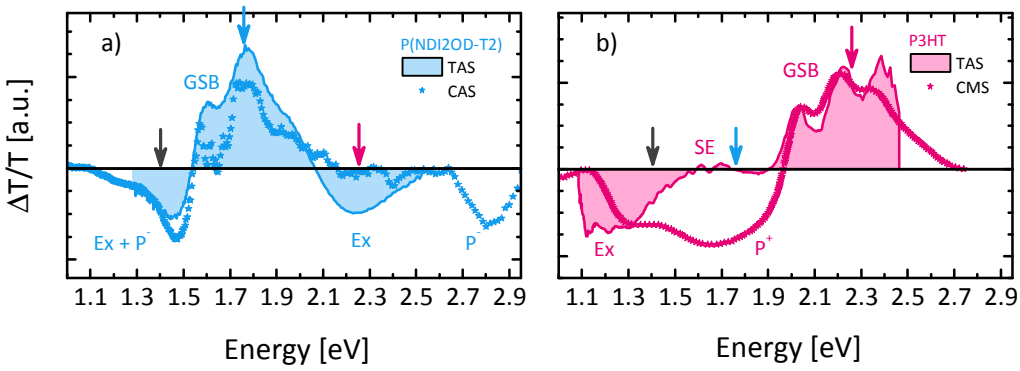

Figure 4.26: Transient absorption spectroscopy (TAS) and charge accumulation spectroscopy (CAS) of *a)* pristine P(NDI2OD-T2) and *b)* pristine P3HT. Excitons (Ex) and polarons (P) contribute a negative photo-induced absorption signal, while the ground-state bleach (GSB) and stimulated emission (SE) give a positive change in transmission. Kinetics at selected energies (marked by the colored arrows) are analyzed in Fig. 4.27.

Now following the kinetics of this region further ahead in time we see that the signal decreases in the time range marked *B*, which can clearly be explained by a loss of P3HT bleach due to fast charge carrier recombination. This ultrafast geminate recombination is than followed by an increase of the intensity in time region *C*. We attribute this increase of the intensity to the gradual recombination of long-lived P(NDI2OD-T2) excitons, that do not reach a heterojunction. More precisely, the decreasing (negative) PIA of P(NDI2OD-T2) and the constant (positive) GSB of holes on P3HT result in an total signal that increases with time. This is in agreement with the incomplete quenching observed for P(NDI2OD-T2) in the 50 vol.% CN-cast blend and was further proofed by the similar kinetics of the decay of long-lived P(NDI2OD-T2) states measured in the blend and in the pristine material. This suggests that there are two populations of P(NDI2OD-T2) excitons, one which promptly generates geminate pairs (probably CTS) which transfer with an inverse rate of around 1 ps (in time region *A*), and one that is much longer lived and accounts for the P(NDI2OD-T2) emission observed under steady-state illumination as well as for the increase in the P3HT bleach in time region *C*.

The data in Fig. 4.27.b also allow to estimate the percentage of initially formed charges that become long-lived charge carriers. For that, we analyzed the kinetics at an energy of 1.8 eV (P(NDI2OD-T2) bleach region), where the signal is composed of the positive P(NDI2OD-T2) GSB (either excitons or electrons) and the negative PIA of positive charges on P3HT. However, due to the simultaneous decay of several excited state species, a straightforward interpretation of this curve is not meaningful. The same is true for the analysis of the kinetics at an energy of 2.25 eV (P3HT bleach region), where the signal is composed of the positive GSB of polarons on P3HT and of the negative PIA of

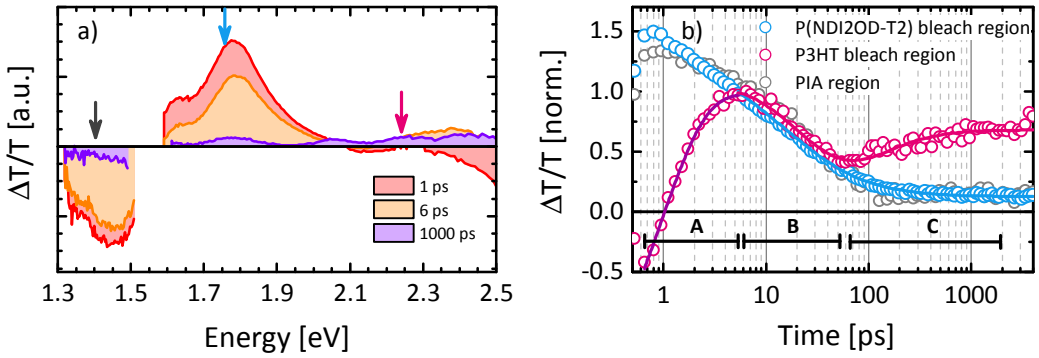

Figure 4.27: *a)* TAS spectra of the 50 vol.% CN-cast blend after selective excitation of P(NDI2OD-T2) at 1.51 eV. *b)* Evolution of the transient absorption signals at three wavelength regions (marked with an arrow in sub-figure a)The signals are normalized to their value when charge carrier generation is complete (end of rise in P3HT bleach in time region A). The kinetics are overlaid with the fit described in the text. (right) Comparison of the bleach of the blend components to the kinetics of pristine P(NDI2OD-T2) (inverted and offset) in time region C. The kinetics of the P3HT bleach in this region match with the decay of long-lived P(NDI2OD-T2) excited states causing an apparent signal increase in the bleach region (as their PIA which previously masked the bleach is removed) and a decrease in the region of the P(NDI2OD-T2) bleach.

long-lived P(NDI2OD-T2) excitons. However, based on the knowledge of the nature of the involved excited species that contribute to these signals, the kinetics can be fitted with a global model, which is able to describe the dynamics in both regions over the complete time-range. From this fit, the percentage of charges, that survive geminate recombination (during region B) can be estimated to 30%. In other words, of the geminate pairs that are formed during time region A, approx. 1/3 form long lived charges while 70% of these electron hole pairs decay geminately on the 100 ps time scale. This directly demonstrates that the majority of excitons that reach the heterojunction undergo a fast geminate recombination process and only a small fraction dissociates into free charge carriers. A ca. 30% efficiency of free charge formation from initial electron-hole pairs sets an upper limit for the IQE of the devices. As the IQE is below that value for direct excitation of P3HT or P(NDI2OD-T2), other decay processes must also be functional, one important being exciton trapping on well crystallized polymer domains.

Discussion

Based on the analysis of the structure and excited state dynamics, Fig. 4.28 sketches the interplay of morphology and charge generation in the best performing P3HT:P(NDI2OD-T2) blend processed from a 50:50 Xy:CN mixture. Fig. 4.28.a schematically shows the domain structure of this blend, reconstructed from the EF-TEM map and R-SoXS profile. It provides a detailed overview of the most important morphological and structural features, which dominate the charge generation process, as we will discuss in the following.

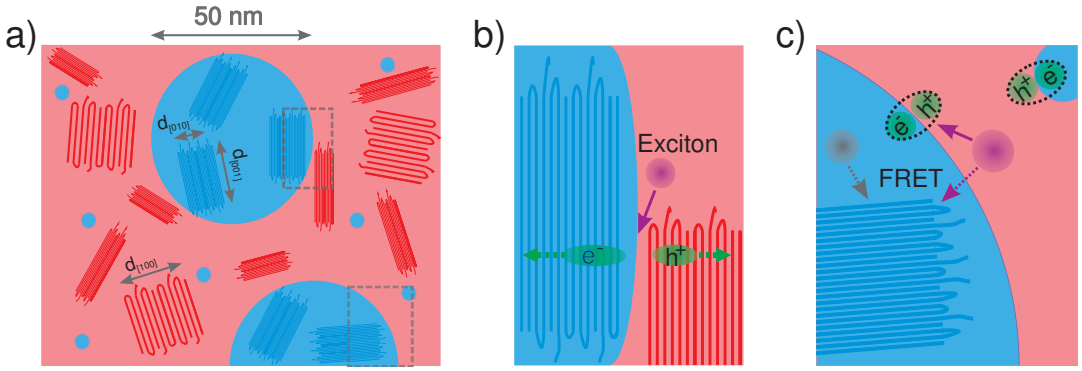

Figure 4.28: a) Schematic representation of the morphology of the 50:50 Xy:CN-cast blend. The image illustrates an cross section in-plane with the substrate (top view), showing P(NDI2OD-T2) domains (blue) and the P3HT matrix (red). Ordered regions with darker colors represent the polymer backbones in crystalline domains, where face-on crystals have a 5 times larger lattice plane spacing than edge-on crystals. Small P(NDI2OD-T2) enclosures, which have the size of a single aggregate,[105] account for the lower purity of the P3HT domains. b) Face-to-face donor/acceptor orientation at the heterojunction. This geometry is proposed to facilitate electron-hole dissociation. c) Effect of exciton self-trapping in isolated P(NDI2OD-T2) aggregates, mediated through Förster-resonant energy transfer (FRET) of excitons to aggregated or crystalline P(NDI2OD-2) regions. In addition, amorphous donor/acceptor interfaces are illustrated, were electron-hole pairs undergo fast geminate recombination.

In order to identify the factors dominating the free charge carrier yield in P3HT: P(NDI2OD-T2) blends, we tried to correlate the photocurrent of the solar cell devices from Fig. 4.18.a to the domain size, the domain purity and to the size and DoC of the polymer crystallites. However, the comparison of the dependence of the PL quenching (see Tab. 4.2), the TSI (see Fig. 4.21.b), the DoC and the coherence length (see Fig. A.2) to the photocurrent reveal that these parameters all show either a marginal change over the whole CN concentration or an abrupt change upon addition of only 5 vol.% CN followed by more or less constant value. The only parameter that mimics the continuous change of the photocurrent is the redistribution of the P(NDI2OD-T2) crystal, as it is evident from the pole figure in Fig. 4.23. Note that in a recent study, Fabiano and co-workers also observed a perpendicular orientation of the P3HT and P(NDI2OD-T2) crystallites in low performing devices prepared from xylene and dichlorobenzene, while the best performing blend cast from Xy:CN reveals a parallel edge-on orientation of the polymer crystals.[150] Thus, we investigated the orientation of the polymer crystallites relative to each other in more details.

We start our discussion from the orientation distributions in the Xy-cast blend. Here, the donor and acceptor crystals are oriented almost perpendicular to each other. Addition of the co-solvent CN re-orients the originally face-on P(NDI2OD-T2) distribution to a predominantly edge-on orientation. At the same time, when the P(NDI2OD-T2) crystals

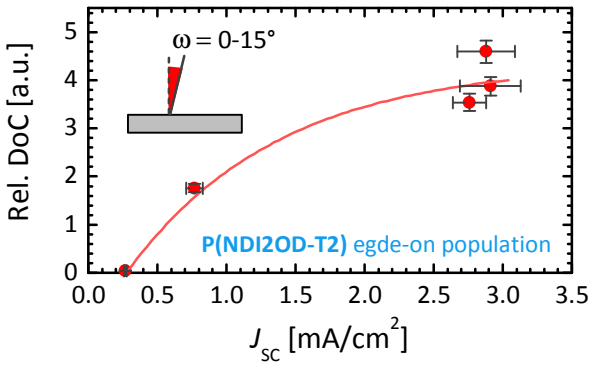

Figure 4.29: Correlation of the fraction of the P(NDI2OD-T2) edge-on crystal population with the J_{SC} of the solar cell devices from Fig. 4.18.a. DoC uncertainties derived from that of the illuminated sample volume, and J_{SC} uncertainties derived from device statistics.

start to adopt an orientation distribution that is similar to that of the P3HT polymer crystallites, the photocurrent also increases. Obviously, the highest photocurrents are observed for blends were P3HT and P(NDI2OD-T2) have comparable orientation distributions comprising a strong edge-on preference. Thus, we make the assumption that not absolute crystal orientation but rather the face-to-face relative orientation of P3HT and P(NDI2OD-T2) crystallites represents the configuration in which efficient dissociation of charge-transfer states is possible. To demonstrate this correlation more quantitatively, we first calculated the relative DoC of P(NDI2OD-T2) edge-on crystals, which we obtained by counting all crystals with a polar angle smaller than 15° (this is proportional to the area under the corrected pole figures from $\omega = 0$ to 15°). Fig. 4.29 displays the relative population of edge-on oriented P(NDI2OD-T2) crystals, plotted against the J_{SC} of the solar cells. The plot reveals the gradual increase of the photocurrent upon the generation of more and more edge-on oriented P(NDI2OD-T2) crystals.

A consequence of the proposed correlated face-to-face orientation is that the total area of favorable interfaces is the product of the edge-on DoC and the size of the crystallites of both the donor and the acceptor. This is particularly interesting for P3HT, were the strongly increasing DoC (Fig. A.2) seems to be in contradiction to the gradually changing photocurrent. However, the orientation distribution in Fig. 4.23 reveals that the increased DoC is mainly due to the generation of randomly oriented crystals while the fraction of edge-on oriented crystals (counted again from 0 to 15°) indeed decreases by 40% with increasing CN concentration. On the other hand, the lamella coherence doubles, which leads to an overall marginal increase of the edge-on P3HT crystal surface with increasing CN concentration. We also note the continuous decrease of the P(NDI2OD-T2) lamella DoC with increasing CN concentration. This discussion illustrates the complex interplay of several parameters that need to be considered and may explain why the trend in Fig. 4.29 is not linear. In addition, the important role of the polymer crystals might be surprising

in the view of the findings of our previous publication (presented in Sec. 4.3). There, we observed that the increase of the photocurrent goes along with an increasing exciton bandwidth of the P3HT aggregates, presumably due to more disordered or smaller P3HT aggregates (Fig. 4.16) caused by a reduced domain size and stronger intermixing of the components. An explanation for this observation might be the limited size of the aggregates along the π-stacking direction. Due to non-nearest neighbor interactions, the excitonic coupling saturates for an aggregate with about 50 stacked chains.[151] However, the P3HT coherence length in π-stacking direction in the 50 vol.% CN-cast blend is only about 5.5 nm, corresponding to 15 interacting chains. In the Xy-cast film, the scattering signals of both polymers overlap which impedes a direct comparison between both blends. Nevertheless, this demonstrates that the analysis of macroscopic optical data should be taken with care, as long as the knowledge of the microscopic domain structure is limited.

In order to understand the role of polymer crystals in the charge generation process it is instructive to reflect on some recent models aiming to describe photocurrent generation at organic donor/acceptor heterojunctions under consideration of the semi-crystalline nature of the materials. It has been noted that efficient carrier generation at distributed heterojunctions requires an unidirectional flow of carriers away from the heterojunction.[83,87,142] The driving force behind that is supposed to originate from an energy gradient of the potential energy pointing from the heterojunction into the bulk of the pure phases. Recent experimental and theoretical results imply that this gradient is introduced by the difference in ionization energy or electron affinity caused by the larger disorder in regions close to the heterojunction compared to better ordered or perfectly crystalline regions in the bulk (see Sec. 2.4).[68,83,87,89,152,153] The decrease of the band gap in the ordered relative to the disordered phases can be strongly enhanced by the formation of intermolecular excited states, so called aggregates, as it has been described for P3HT, which lowers the band gap by about 0.35 eV.[48] For pure P(NDI2OD-T2), we demonstrated the strong tendency to form such aggregate states, which have a, by 0.3 eV, lower band gap compared to intra-chain excitons on disordered P(NDI2OD-T2) segments.[105]

A consequence of such a microscopic energy landscape is that charges as well as excitons are repelled from the heterojunction, preventing the quenching of excitons (and subsequent formation of CTS) directly at the interface. Instead, exciton dissociation requires that charge carriers are transferred over several nanometers via tunneling, as it was recently proposed by *Troisi* and coworkers.[88] The distance over which this process is efficient critically depends on the coupling between neighboring hopping sites, which is orders of magnitude larger along the polymer backbone and pi-stacking direction than in the lamella-stacking direction.[88] Thus, the face-to-face donor/acceptor orientation found in the optimized solar cells is favorable with respect to the tunneling assisted exciton dissociation mechanisms. In this case, both polymer crystals stand edge-on which exposes the

polymer backbone towards the heterojunction. Fig. 4.28.b illustrates this situation where e.g. an electron tunneling out of a P3HT crystal can easily reach the P(NDI2OD-T2) backbone within a crystalline acceptor domain. This process will be largely suppressed if the P(NDI2OD-T2) crystals are oriented face-on, as the bulky aliphatic side chains, now oriented towards the heterojunction, will constitute an additional tunneling barrier. Alternatively, if the CTS is indeed the precursor for all free charge carriers it is expected that the formation of coplanar crystals will also improve the efficiency for the CTS dissociation, due to the larger delocalization within the crystals, according to the simulations of *Tamura and Burghardt.*[84–86]

The fact that not only the crystallinity but also the relative orientation must be optimized to enable optimal charge separation might display a special problem of conjugated polymers which usually carry long, insulating alkyl chains. In contrast, fullerenes are spherical symmetrical objects with no or relatively short side chains which have no preferential orientation with respect to the donor molecules. In addition, electrons can delocalize efficiently over neighbored fullerene molecules,[85,86] and may therefore perform better than any other class of acceptor materials.

At the end, we point out that the energy gradients between amorphous and ordered regions also affect the quantum efficiency in a negative way. Due to the large potential difference between amorphous and crystalline phases, excitons quickly migrate to the ordered, low energy states, as it is illustrated in Fig. 4.28c. We found that the spectral diffusion into these low energy states occurs on a timescale of about 10 ps in pristine P(NDI2OD-T2),[105] meaning that it competes with exciton quenching and the subsequent formation of charge–separated states. Once an exciton is generated on or transferred to a P(NDI2OD-T2) aggregate that is surrounded by amorphous content, it is restricted to exist deep within the ordered region. In effect, this has similar consequences to the phenomenon known as exciton self-trapping observed in molecular aggregates.[154] As a consequence, given that the domains are sufficiently large and pure, excitons on P(NDI2OD-T2) chains are isolated from the heterojunction, which explains the low quenching efficiency of acceptor PL observed in the P3HT:P(NDI2OD-T2) blends.

In summary, we propose a microscopic framework in which efficient and ultrafast charge carrier generation at organic heterojunctions can be realized. However, for very anisotropic systems, which conjugated polymers are in general, the correlated orientation of donor and acceptor crystals at the heterojunction is a challenging task, which requires a much larger control over the nanometer morphology, the degree of crystallinity, as well as of the crystal orientation. Nevertheless, the actual efficiency record for all-polymer solar cells of 4.1%, recently published by Mori and coworkers,[33] was achieved with P(NDI2OD-T2) as acceptor component, which demonstrates that a further improvements of the microscopic morphology and a more efficient free charge carrier generation can be realized.

5

Conclusions

In this thesis the charge transport and photovoltaic properties of two classes of electron transporting D-A copolymers were investigated. The complex interplay of molecular structure and charge transport was investigated in a series of chemically modified copolymers. Several transient photocurrents methods were applied to determine the charge carrier mobility. The effect of charge carrier trapping on the characteristics of the measurements is discussed in detail and first indications for the structural origin of the trap states can be drawn from the comparison of the different copolymers. After determination of the intrinsic bulk mobility of this copolymer, it has been applied to organic solar cells. Optimization of the photovoltaic parameters of the blends requires a solvent that prevents the pre-aggregation of the electron transporting polymer in solution. Similar results were obtained for a second NDI-containing acceptor polymer. The morphology and charge carrier dynamics of the optimized solar cells were further investigated and finally provide a detailed picture of the device limiting processes. The findings presented in this thesis finally allows to propose a microscopic model for the charge generation process in all-polymer solar cells.

In the first part of this thesis the focus is put on the investigation of the transport of electrons in the D-A copolymers PFTBTT and P(NDI2OD-T2). The ambipolar polymer alt-PF8TBTT exhibits rather unusual transient photocurrent characteristics. Therefore, I first demonstrated that the transient photocurrent in the photo-CELIV experiments is indeed dominated by the transport of electrons. The major emphasis is than placed on the description of the current transients and the understanding of the time-dependent mobility. By applying a one-dimensional Monte Carlo simulation I was able to rationalize that

trapping of electrons in an exponential DOS causes the strong divergence of the shape of the transients from the case of trap free charge transport. Very characteristic features are found for the photo-CELIV technique, which should allow an easy detection of charge carrier trapping in other materials. These features comprise a strong broadening of the photocurrent maximum, accompanied by a temporal shift, which reflects the underlying time-dependence of the mobility. Although observed in the literature before, a systematic modeling of a photo-CELIV transient that is subject to charge carrier trapping hasn't been demonstrated so far. As a last point, the comparison of different structurally modified copolymers suggest that the origin of the traps is related to the molecular structure of the copolymer itself. However, one can suppose that a direct observation of the electron traps in alt-PF8TBTT on the molecular scale is actually beyond the capability of experimental techniques. More promising, the application of quantum chemical simulations of realistic polymer structures may provide a deeper understanding of the interplay between molecular structure and shape of the DOS. Such simulations has recently revealed that several amorphous polymers exhibit very broad, intrinsic band tails that can cause trapping of charges as it is found for PFTBTT copolymers in this thesis.

Secondly, the bulk electron transport in P(NDI2OD-T2) is investigated. This copolymer evolved as one of the few standard materials in the field of organic electronics and is actually the best investigated electron transporting material. Our transient photocurrent measurements revealed that it comprises one of the highest electron mobilities ever reported for a conjugated polymer. However, we also find a counter-intuitive result regarding the charge injection into this polymer. The presence of a severe injection barrier for a wide range of electrode materials was not expected because of the very low ionization energy of this polymer. A possible explanation arises from recent experiments, that disclose the orientation of the copolymer at the top-surface of spin coated films. We propose that the long insulating alkyl chains of the P(NDI2OD-T2) are responsible for the strongly limited electron injection. The proof of the excellent bulk electron mobility directly served as motivation for the following studies of the photovoltaic properties of P(NDI2OD-T2).

The studies *in the second part of this thesis* focus on the optimization and understanding of all-polymer solar cells with NDI-containing D-A copolymers. Our studies started from a situation were several publications reported a rather low efficiency of the P3HT:P(NDI2OD-T2) blends. By using the high boiling point solvent CN, and through incorporation of a special preparation recipe, I could increase the power conversion efficiency significantly. CN was used as we had discovered that it is one of a few solvents were P(NDI2OD-T2) does not pre-aggregate in solution. The positive effect of such a solvent was demonstrated for a second acceptor. Initial morphology studies and the analysis of optical properties indicated a suppression of the phase separation in the optimized blends.

To identify the overall limitations and to disclose the microscopic factors that drive the charge generation process, a systematic study of the CN-processed solar cells was initiated. For all experiments shown *in the last part of my thesis*, the electron accepting P(NDI2OD-T2) was blended with the hole accepting P3HT. The correlation of the widely changing photocurrent with a number of morphological parameters suggest that the orientation of the donor and acceptor crystallites relative to each other has a major impact on the efficiency to dissociate charge transfer states into free charge carriers. For blends of conjugated polymers, this relationship has not been described so far. This finding provides an interesting possibility for a further optimization of D/A blends thought that a proper manipulation of the orientation of both components can be realized. On the other hand, the necessity of a correlated D/A orientation provides an explanation for the overall low free charge carrier yields that are generally observed in organic solar cells whenever fullerenes are replaced by any other electron accepting material. The major loss of excited states was experimentally determined by transient and steady state spectroscopic investigations. Ultrafast geminate recombination within 100 ps is found to annihilate about 70% of the initial electron-hole pairs. Furthermore, exciton self-trapping in rather pure and semi-crystalline P(NDI2OD-T2) domains account for an additional reduction of the internal quantum efficiency. This process was also not yet described by any other group.

In summary, the results of this thesis emphasis the great potential of D-A copolymers for various applications. The basis of these prospects are their excellent charge transport properties. In particular, P(NDI2OD-T2) owns tremendous relevance as it combines several rather unique properties into one material that one can expect a further efficiency improvement of the solar cells that are based on this copolymer. The recent improvement of the efficiency of all-polymer solar cells to 4.1%[33] and 6.4% for a research and commercial device, respectively, clearly reflect their excellent properties. However, in order to be fully competitive with fullerene acceptors, it might be possible to identify suitable donor polymers which don't need to form crystalline domains to facilitate free charge carrier generation. Possibly, engineering of the polymer structure to enhance the delocalization (through planarization and increasing the size of the conjugated systems in the backbone) of the charge carriers or to reduce the binding energy of the charge transfer state (by steric hindrance at the heterojunction)[39] will further increase the free charge carrier yield of all-polymer solar cells.

6

Publications

6.1 Publications presented within this thesis and declaration of contributions

Mobility relaxation and electron trapping in a donor-acceptor copolymer

M. Schubert, E. Preis, J. C. Blakesley, P. Pingel, U. Scherf, and D. Neher

Published in *Physical Review B* **87**, 024203 (2013), DOI 10.1103/PhysRevB.87.024203.

MS carried out device preparation, measurements, data analysis and edited the initial manuscript. PFTBTT copolymers were synthesized by EP. JCB wrote the MC simulation software. Simulations were performed by MS. OFET measurements by PP. DN and US supervised the project. DN and JCB co-edited the manuscript.

Bulk electron transport and charge injection in a high mobility n-type semiconducting polymer

Robert Steyrleuthner, Marcel Schubert, Frank Jaiser, James C. Blakesley, Zhihua Chen, Antonio Facchetti, and Dieter Neher

Published in *Advanced Materials* **25**, 2799 (2010), DOI 10.1002/adma.201000232.

RS conducted single-carrier device preparation and characterization, and edited the initial manuscript. MS and FJ conducted TOF measurements. ZC synthesized the polymer. MS, JB, AF, and DN co-edited the manuscript.

Influence of aggregation on the performance of all-polymer solar cells containing low-bandgap naphthalenediimide copolymers

M. Schubert, D. Dolfen, J. Frisch, S. Roland, R. Steyrleuthner, B. Stiller, Z. H. Chen, U. Scherf, N. Koch, A. Facchetti, and D. Neher

Published in *Advanced Energy Materials* **2**, 369 (2012), DOI 10.1002/aenm.201100601.

MS prepared, optimized, measured, and analyzed solar cell devices, measured and analyzed optical absorption spectra of all blend layers and of P(NDI-TCPDTT) in different solutions, calculated SNOM maps and prepared the manuscript. JF performed and analyzed UPS measurements, and wrote the corresponding section of the manuscript. RS measured solution spectra of P(NDI2OD-T2) and analysed the aggregation of the pure polymer in solution. DD and ZC synthesized P(NDI-TCPDTT) and P(NDI2OD-T2), respectively. SR assisted in the preparation and measurement of solar cell devices. BS acquired raw SNOM and AFM data. D.N., U.S., N.K., and A.F. supervised the project within their work groups. All authors contributed in discussing and editing the manuscript.

Correlated donor/acceptor crystal orientation and geminate recombination controls photocurrent generation in all-polymer solar cells

Marcel Schubert, Brian A. Collins, Hannah Mangold, Ian A. Howard, Koen Vandewal, Wolfram Schindler, Steffen Roland, Jan Behrends, Felix Kraffert, Robert Steyrleuthner, Zhihua Chen, Konstantinos Fostiropoulos, Robert Bittl, Alberto Salleo, Antonio Facchetti, Frédéric Laquai, Harald Ade, and Dieter Neher

Submitted to *Advanced Functional Materials* on 18$^{\text{th}}$ Dec. 2013 (current status: under review)

MS edited the initial manuscript and coordinated the different experiments. All samples were prepared by MS and SR except PDS samples, prepared by KV. Measurements and data analysis: OPV characterization by MS and SR, EF-TEM by WS; R-SOXS, GIWAXS, and STXM by BAC; TAS by HM and IAH; EPR by JB and FK, PDS by KV, PL quenching by MS. P(NDI2OD-T2) synthesis by ZC. KF, RB, AS, AF, FL, HA, and DN supervised and supported the work within their groups. BAC, IAH, KV, WS, JB, and DN co-edited the manuscript.

6.2 Further publications

• **The role of regioregularity, crystallinity and chain orientation on electron transport in a high mobility n-type copolymer**

R. Steyrleuthner, R. Di Pietro, B. A. Collins, F. Polzer, S. Himmelberger, M. Schubert, Z Chen, S. Zhang, A. Salleo, H. Ade, A. Facchetti, D. Neher

Submitted

• **Chain-growth polycondensation of perylene diimide-based copolymers: a new route to regio-regular perylene diimide-based acceptors for all-polymer solar cells and n-type transistors**

W. Liu, R. Tkachov, V. Senkovskyy, M. Schubert, Z. Wei, A. Facchetti, D. Neher, and A. Kiriy

Submitted

• **Efficient charge generation by relaxed charge-transfer states at organic interfaces**

K. Vandewal, S. Albrecht, E. T. Hoke, K. R. Graham, J. Widmer, J. D. Douglas, M. Schubert, W. R. Mateker, J. T. Bloking, G. F. Burkhard, A. Sellinger, J. M. J. Fréchet, A. Amassian, M. K. Riede, M. D. McGehee, D. Neher, and A. Salleo

Published in *Nature Materials* (2013), DOI 10.1038/nmat3807

• **Influence of sintering on the structural and electronic properties of TiO2 nano-porous layers prepared via a non-sol-gel approach**

S. Schattauer, B. Reinhold, S. Albrecht, C. Fahrenson, M. Schubert, S. Janietz, and D. Neher

Published in *Colloid and Polymer Science* **290**, 1843 (2012), DOI 10.1007/s00396-012-2708-9.

• **Aggregation in a high-mobility n-type low-bandgap copolymer with implications on semicrystalline morphology**

R. Steyrleuthner, M. Schubert, I. Howard, B. Klaumünzer, K. Schilling, Z. Chen, P. Saalfrank, F. Laquai, A. Facchetti, and D. Neher

Published in *Journal of the American Chemical Society* **134**, 18303 (2012), DOI 10.1021/ja306844f.

• **Full electronic structure across a polymer heterojunction solar cell**

J. Frisch, M. Schubert, E. Preis, J. P. Rabe, D. Neher, U. Scherf, and N. Koch

Published in *Journal of Materials Chemistry* **22**, 4418 (2012), DOI 10.1039/c1jm14968g.

• **Photogeneration and recombination in P3HT/PCBM solar cells probed by time-delayed collection field experiments**

J. Kniepert, M. Schubert, J. C. Blakesley, and D. Neher

Published in *The Journal of Physical Chemistry Letters* **2**, 700 (2011), DOI 10.1021/jz200155b.

• **Time-of-flight measurements and vertical transport in a high electron-mobility polymer**

J. C. Blakesley, M. Schubert, R. Steyrleuthner, Z. H. Chen, A. Facchetti, and D. Neher

Published by *Applied Physics Letters* **99**, 183310 (2011), DOI 10.1063/1.3657827.

• **The relationship between the electric field-induced dissociation of charge transfer excitons and the photocurrent in small molecular/polymeric solar cells**

S. Inal, M. Schubert, A. Sellinger, and D. Neher

Published in *The Journal of Physical Chemistry Letters* **1**, 982 (2010), DOI 10.1021/jz100121t.

• **Charge mobility determination by current extraction under linear increasing voltages: Case of nonequilibrium charges and field-dependent mobilities**

S. Bange, M. Schubert, and D. Neher

Published in *Physical Review B* **81**, 035209 (2010), DOI 10.1103/PhysRevB.81.035209.

6.3 Selected conference contributions

May 2012 · **Talk** · *Influence of aggregation on the performance of all-polymer solar cells containing low-bandgap naphthalenediimide copolymers*, EMRS spring meeting, Straßbourg (France)

March 2012 · **Talk** · *Influence of aggregation on the performance of all-polymer solar cells containing low-bandgap naphthalenediimide copolymers*, DPG spring meeting, Berlin (Germany)

May 2011 · **Talk** · *Talk, Charge transport and electron trapping in a donor/acceptor-type copolymer*, DPG spring meeting, Dresden (Germany)

Apri 2010 · **Talk** · *Comparing alternating and statistical copolymers: The influence of charge transport on the performance of polymer solar cells*, MRS spring meeting, San Francisco (USA)

March 2009 · **Talk** · *Effects of geminate and bimolecular recombination on the performance of polymeric-small molecular solar cells*, DPG spring meeting, Dresden (Germany)

6.4 Funding

I greatly acknowledge funding from the German Science Foundation (DFG) within the priority program “Elemental processes of organic photovoltaics” (SPP 1355).

Bibliography

[1] S. Holliday, J. E. Donaghey, I. McCulloch, *Chemistry of Materials* **2013**, *na*, URL http://dx.doi.org/10.1021/cm402421p.

[2] I. Kang, H.-J. Yun, D. S. Chung, S.-K. Kwon, Y.-H. Kim, *Journal of the American Chemical Society* **2013**, *135*, 14896, URL http://dx.doi.org/10.1021/ja405112s.

[3] H. Dong, X. Fu, J. Liu, Z. Wang, W. Hu, *Advanced Materials* **2013**, *25*, 6158, URL http://dx.doi.org/10.1002/adma.201302514.

[4] T. Lei, J.-H. Dou, Z.-J. Ma, C.-H. Yao, C.-J. Liu, J.-Y. Wang, J. Pei, *Journal of the American Chemical Society* **2012**, *134*, 20025, URL http://dx.doi.org/10.1021/ja310283f.

[5] J. Lee, A. R. Han, H. Yu, T. J. Shin, C. Yang, J. H. Oh, *Journal of the American Chemical Society* **2013**, *135*, 9540, URL http://dx.doi.org/10.1021/ja403949g.

[6] R. Kim, P. S. K. Amegadze, I. Kang, H.-J. Yun, Y.-Y. Noh, S.-K. Kwon, Y.-H. Kim, *Advanced Functional Materials* **2013**, *na*, n/a, URL http://dx.doi.org/10.1002/adfm.201301197.

[7] G. Brocks, A. Tol, *The Journal of Physical Chemistry* **1996**, *100*, 1838, URL http://dx.doi.org/10.1021/jp952276c.

[8] H. Yan, Z. H. Chen, Y. Zheng, C. Newman, J. R. Quinn, F. Dotz, M. Kastler, A. Facchetti, *Nature* **2009**, *457*, 679, URL http://dx.doi.org/10.1038/nature07727.

[9] J. Rivnay, M. F. Toney, Y. Zheng, I. V. Kauvar, Z. H. Chen, V. Wagner, A. Facchetti, A. Salleo, *Advanced Materials* **2010**, *22*, 4359, URL http://dx.doi.org/10.1002/adma.201001202.

[10] J. Rivnay, R. Steyrleuthner, L. H. Jimison, A. Casadei, Z. H. Chen, M. F. Toney, A. Facchetti, D. Neher, A. Salleo, *Macromolecules* **2011**, *44*, 5246, URL http://dx.doi.org/10.1021/ma200864s.

[11] J. Rivnay, R. Noriega, J. E. Northrup, R. J. Kline, M. F. Toney, A. Salleo, *Physical Review B* **2011**, *83*, 121306, URL http://dx.doi.org/10.1103/PhysRevB.83.121306.

[12] M. A. Green, K. Emery, Y. Hishikawa, W. Warta, E. D. Dunlop, *Progress in Photovoltaics: Research and Applications* **2013**, *21*, 1, URL http://dx.doi.org/10.1002/pip.2352.

[13] S. E. Shaheen, C. J. Brabec, N. S. Sariciftci, F. Padinger, T. Fromherz, J. C. Hummelen, *Applied Physics Letters* **2001**, *78*, 841, URL http://dx.doi.org/10.1063/1.1345834.

[14] F. Padinger, R. S. Rittberger, N. S. Sariciftci, *Advanced Functional Materials* **2003**, *13*, 85,

URL http://dx.doi.org/10.1002/adfm.200390011.

[15] G. Li, V. Shrotriya, J. S. Huang, Y. Yao, T. Moriarty, K. Emery, Y. Yang, *Nature Materials* **2005**, *4*, 864, URL http://dx.doi.org/10.1038/nmat1500.

[16] J. Peet, J. Y. Kim, N. E. Coates, W. L. Ma, D. Moses, A. J. Heeger, G. C. Bazan, *Nature Materials* **2007**, *6*, 497, URL http://dx.doi.org/10.1038/nmat1928.

[17] S. H. Park, A. Roy, S. Beaupre, S. Cho, N. Coates, J. S. Moon, D. Moses, M. Leclerc, K. Lee, A. J. Heeger, *Nature Photonics* **2009**, *3*, 297, URL http://dx.doi.org/10.1038/nphoton.2009.69.

[18] Y. Y. Liang, Z. Xu, J. B. Xia, S. T. Tsai, Y. Wu, G. Li, C. Ray, L. P. Yu, *Advanced Materials* **2010**, *22*, E135, URL http://dx.doi.org/10.1002/adma.200903528.

[19] Z. He, C. Zhong, X. Huang, W.-Y. Wong, H. Wu, L. Chen, S. Su, Y. Cao, *Advanced Materials* **2011**, *23*, 4636, URL http://dx.doi.org/10.1002/adma.201103006.

[20] Z. He, C. Zhong, S. Su, M. Xu, H. Wu, Y. Cao, *Nature Photonics* **2012**, *6*, 591, URL http://dx.doi.org/10.1038/nphoton.2012.190.

[21] J. You, L. Dou, K. Yoshimura, T. Kato, K. Ohya, T. Moriarty, K. Emery, C.-C. Chen, J. Gao, G. Li, Y. Yang, *Nat Commun* **2013**, *4*, 1446, URL http://dx.doi.org/10.1038/ncomms2411.

[22] M. Granstrom, K. Petritsch, A. C. Arias, A. Lux, M. R. Andersson, R. H. Friend, *Nature* **1998**, *395*, 257, URL http://dx.doi.org/10.1038/26183.

[23] T. Kietzke, H. H. Horhold, D. Neher, *Chemistry of Materials* **2005**, *17*, 6532, URL http://dx.doi.org/10.1021/cm050148n.

[24] M. M. Koetse, J. Sweelssen, K. T. Hoekerd, H. F. M. Schoo, S. C. Veenstra, J. M. Kroon, X. N. Yang, J. Loos, *Applied Physics Letters* **2006**, *88*, 083504, URL http://dx.doi.org/10.1063/1.2176863.

[25] C. R. McNeill, A. Abrusci, J. Zaumseil, R. Wilson, M. J. McKiernan, J. H. Burroughes, J. J. M. Halls, N. C. Greenham, R. H. Friend, *Applied Physics Letters* **2007**, *90*, 193506, URL http://dx.doi.org/10.1063/1.2738197.

[26] Z. A. Tan, E. J. Zhou, X. W. Zhan, X. Wang, Y. F. Li, S. Barlow, S. R. Marder, *Applied Physics Letters* **2008**, *93*, 073309, URL http://dx.doi.org/10.1063/1.2975160.

[27] X. M. He, F. Gao, G. L. Tu, D. Hasko, S. Huttner, U. Steiner, N. C. Greenham, R. H. Friend, W. T. S. Huck, *Nano Letters* **2010**, *10*, 1302, URL http://dx.doi.org/10.1021/nl904098m.

[28] E. J. Zhou, J. Z. Cong, Q. S. Wei, K. Tajima, C. H. Yang, K. Hashimoto, *Angewandte Chemie-International Edition* **2011**, *50*, 2799, URL http://dx.doi.org/10.1002/anie.201005408.

[29] D. Mori, H. Benten, H. Ohkita, S. Ito, K. Miyake, *Acs Applied Materials & Interfaces* **2012**, *4*, 3325, URL http://dx.doi.org/10.1021/am300623f.

[30] C. Guo, Y.-H. Lin, M. D. Witman, K. A. Smith, C. Wang, A. Hexemer, J. Strzalka, E. D. Gomez, R. Verduzco, *Nano Letters* **2013**, *13*, 2957, URL http://dx.doi.org/10.1021/nl401420s.

[31] Y. Zhou, Q. Yan, Y.-Q. Zheng, J.-Y. Wang, D. Zhao, J. Pei, *Journal of Materials Chemistry A* **2013**, *1*, 6609, URL http://dx.doi.org/10.1039/C3TA10864C.

[32] T. Earmme, Y.-J. Hwang, N. M. Murari, S. Subramaniyan, S. A. Jenekhe, *Journal of the American Chemical Society* **2013**, *135*, 14960–14963, URL http://dx.doi.org/10.1021/ja4085429.

[33] D. Mori, H. Benten, I. Okada, H. Ohkita, S. Ito, *Advanced Energy Materials* **2013**, *3*, n/a, URL http://dx.doi.org/10.1002/aenm.201301006.

[34] E. Zhou, J. Cong, K. Hashimoto, K. Tajima, *Advanced Materials* **2013**, *25*, n/a, URL http://dx.doi.org/10.1002/adma.201303170.

[35] Y. Kim, S. Cook, S. M. Tuladhar, S. A. Choulis, J. Nelson, J. R. Durrant, D. D. C. Bradley, M. Giles, I. McCulloch, C. S. Ha, M. Ree, *Nature Materials* **2006**, *5*, 197, URL http://dx.doi.org/10.1038/nmat1574.

[36] M. Schubert, D. Dolfen, J. Frisch, S. Roland, R. Steyrleuthner, B. Stiller, Z. H. Chen, U. Scherf, N. Koch, A. Facchetti, D. Neher, *Advanced Energy Materials* **2012**, *2*, 369, URL http://dx.doi.org/10.1002/aenm.201100601.

[37] S. Fabiano, Z. Chen, S. Vahedi, A. Facchetti, B. Pignataro, M. A. Loi, *Journal of Materials Chemistry* **2011**, *21*, 5891, URL http://dx.doi.org/10.1039/c0jm03405c.

[38] J. R. Moore, S. Albert-Seifried, A. Rao, S. Massip, B. Watts, D. J. Morgan, R. H. Friend, C. R. McNeill, H. Sirringhaus, *Advanced Energy Materials* **2011**, *1*, 230, URL http://dx.doi.org/10.1002/aenm.201000035.

[39] T. W. Holcombe, J. E. Norton, J. Rivnay, C. H. Woo, L. Goris, C. Piliego, G. Griffini, A. Sellinger, J.-L. Brédas, A. Salleo, J. M. J. Fréchet, *Journal of the American Chemical Society* **2011**, *133*, 12106, URL http://dx.doi.org/10.1021/ja203235z.

[40] Y. Kim, H. R. Yeom, J. Y. Kim, C. Yang, *Energy & Environmental Science* **2013**, *6*, 1909, URL http://dx.doi.org/10.1039/C3EE00110E.

[41] N. Zhou, H. Lin, S. J. Lou, X. Yu, P. Guo, E. F. Manley, S. Loser, P. Hartnett, H. Huang, M. R. Wasielewski, L. X. Chen, R. P. H. Chang, A. Facchetti, T. J. Marks, *Advanced Energy Materials* **2013**, *3*, n/a, URL http://dx.doi.org/10.1002/aenm.201300785.

[42] G. D. Scholes, G. Rumbles, *Nature Materials* **2006**, *5*, 683, URL http://dx.doi.org/10.1038/nmat1710.

[43] E. D. Glowacki, M. Irimia-Vladu, M. Kaltenbrunner, J. Gsiorowski, M. S. White, U. Monkowius, G. Romanazzi, G. P. Suranna, P. Mastrorilli, T. Sekitani, S. Bauer, T. Someya, L. Torsi, N. S. Sariciftci, *Advanced Materials* **2013**, *25*, 1563, URL http://dx.doi.org/10.1002/adma.201204039.

[44] N. E. Jackson, B. M. Savoie, K. L. Kohlstedt, M. Olvera de la Cruz, G. C. Schatz, L. X. Chen, M. A. Ratner, *Journal of the American Chemical Society* **2013**, *135*, 10475, URL http://dx.doi.org/10.1021/ja403667s.

[45] S. Sato, K. Tajima, K. Hashimoto, *Macromolecules* **2009**, *42*, 1785, URL http://dx.doi.org/10.1021/ma802661x.

[46] K. Tajima, Y. Suzuki, K. Hashimoto, *The Journal of Physical Chemistry C* **2008**, *112*, 8507, URL http://dx.doi.org/10.1021/jp802688s.

[47] S. Garreau, M. Leclerc, N. Errien, G. Louarn, *Macromolecules* **2003**, *36*, 692, URL http://dx.doi.org/10.1021/ma021358d.

[48] F. C. Spano, *Journal of Chemical Physics* **2005**, *122*, 234701, URL http://dx.doi.org/

10.1063/1.1914768.

[49] F. C. Spano, *Accounts of Chemical Research* **2010**, *43*, 429, URL http://dx.doi.org/10.1021/ar900233v.

[50] G. Li, R. Zhu, Y. Yang, *Nat Photon* **2012**, *6*, 153, URL http://dx.doi.org/10.1038/nphoton.2012.11.

[51] N. Tessler, Y. Preezant, N. Rappaport, Y. Roichman, *Advanced Materials* **2009**, *21*, 2741, URL http://dx.doi.org/10.1002/adma.200803541.

[52] H. Bassler, *Physica Status Solidi B-Basic Research* **1993**, *175*, 15, URL http://dx.doi.org/10.1002/pssb.2221750102.

[53] T. Tiedje, A. Rose, *Solid State Communications* **1981**, *37*, 49, URL http://dx.doi.org/10.1016/0038-1098(81)90886-3.

[54] A. Salleo, T. W. Chen, A. R. Völkel, Y. Wu, P. Liu, B. S. Ong, R. A. Street, *Physical Review B* **2004**, *70*, 115311, URL http://dx.doi.org/10.1103/PhysRevB.70.115311.

[55] W. L. Kalb, B. Batlogg, *Physical Review B* **2010**, *81*, 035327, URL http://dx.doi.org/10.1103/PhysRevB.81.035327.

[56] S. Himmelberger, J. Dacuña, J. Rivnay, L. H. Jimison, T. McCarthy-Ward, M. Heeney, I. McCulloch, M. F. Toney, A. Salleo, *Advanced Functional Materials* **2013**, *23*, 2091, URL http://dx.doi.org/10.1002/adfm.201202408.

[57] C. W. Tang, *Applied Physics Letters* **1986**, *48*, 183, URL http://link.aip.org/link/doi/10.1063/1.96937.

[58] J. M. Guo, H. Ohkita, H. Benten, S. Ito, *Journal of the American Chemical Society* **2010**, *132*, 6154, URL http://dx.doi.org/10.1021/ja100302p.

[59] F. Etzold, I. A. Howard, R. Mauer, M. Meister, T. D. Kim, K. S. Lee, N. S. Baek, F. Laquai, *Journal of the American Chemical Society* **2011**, *133*, 9469, URL http://dx.doi.org/10.1021/ja201837e.

[60] J. Kniepert, M. Schubert, J. C. Blakesley, D. Neher, *Journal of Physical Chemistry Letters* **2011**, *2*, 700, URL http://dx.doi.org/10.1021/jz200155b.

[61] K. Vandewal, S. Albrecht, E. T. Hoke, K. R. Graham, J. Widmer, J. D. Douglas, M. Schubert, W. R. Mateker, J. T. Bloking, G. F. Burkhard, A. Sellinger, J. M. J. Fréchet, A. Amassian, M. K. Riede, M. D. McGehee, D. Neher, A. Salleo, *Nature Materials* **2013**, *advance online publication*, URL http://dx.doi.org/10.1038/nmat3807.

[62] R. D. Pensack, J. B. Asbury, *Journal of the American Chemical Society* **2009**, *131*, 15986, URL http://dx.doi.org/10.1021/ja906293q.

[63] R. D. Pensack, C. Guo, K. Vakhshouri, E. D. Gomez, J. B. Asbury, *The Journal of Physical Chemistry C* **2012**, *116*, 4824, URL http://dx.doi.org/10.1021/jp2083133.

[64] J. Lee, K. Vandewal, S. R. Yost, M. E. Bahlke, L. Goris, M. A. Baldo, J. V. Manca, T. Van Voorhis, *Journal of the American Chemical Society* **2010**, *132*, 11878, URL http://dx.doi.org/10.1021/ja1045742.

[65] D. H. K. Murthy, M. Gao, M. J. W. Vermeulen, L. D. A. Siebbeles, T. J. Savenije, *The Journal of Physical Chemistry C* **2012**, *116*, 9214, URL http://dx.doi.org/10.1021/jp3007014.

[66] A. A. Bakulin, A. Rao, V. G. Pavelyev, P. H. M. van Loosdrecht, M. S. Pshenichnikov, D. Niedzialek, J. Cornil, D. Beljonne, R. H. Friend, *Science* **2012**, *335*, 1340, URL http:

//dx.doi.org/10.1126/science.1217745.

[67] L. Goris, K. Haenen, M. Nesladek, P. Wagner, D. Vanderzande, L. De Schepper, J. D'Haen, L. Lutsen, J. V. Manca, *Journal of Materials Science* **2005**, *40*, 1413, URL http://dx.doi.org/10.1007/s10853-005-0576-0.

[68] K. Vandewal, A. Gadisa, W. D. Oosterbaan, S. Bertho, F. Banishoeib, I. Van Severen, L. Lutsen, T. J. Cleij, D. Vanderzande, J. V. Manca, *Advanced Functional Materials* **2008**, *18*, 2064, URL http://dx.doi.org/10.1002/adfm.200800056.

[69] C. Yin, T. Kietzke, D. Neher, H. H. Horhold, *Applied Physics Letters* **2007**, *90*, 092117, URL http://dx.doi.org/10.1063/1.2710474.

[70] K. Tvingstedt, K. Vandewal, A. Gadisa, F. Zhang, J. Manca, O. InganaÌˆs, *Journal of the American Chemical Society* **2009**, *131*, 11819, URL http://dx.doi.org/10.1021/ja903100p.

[71] K. Vandewal, K. Tvingstedt, A. Gadisa, O. Inganas, J. V. Manca, *Nature Materials* **2009**, *8*, 904, URL http://dx.doi.org/10.1038/nmat2548.

[72] G. Grancini, M. Maiuri, D. Fazzi, A. Petrozza, H. J. Egelhaaf, D. Brida, G. Cerullo, G. Lanzani, *Nat Mater* **2013**, *12*, 29, URL http://dx.doi.org/10.1038/nmat3502, 10.1038/nmat3502.

[73] L. Onsager, *Physical Review* **1938**, *54*, 554.

[74] C. L. Braun, *Journal of Chemical Physics* **1984**, *80*, 4157, URL http://dx.doi.org/10.1063/1.447243.

[75] J. Noolandi, K. M. Hong, *Journal of Chemical Physics* **1979**, *70*, 3230, URL http://dx.doi.org/10.1063/1.437912.

[76] R. A. Marsh, C. Groves, N. C. Greenham, *Journal of Applied Physics* **2007**, *101*, 083509, URL http://dx.doi.org/10.1063/1.2718865.

[77] B. P. Lyons, N. Clarke, C. Groves, *Energy & Environmental Science* **2012**, *5*, 7657, URL http://dx.doi.org/10.1039/c2ee21327c.

[78] C. Groves, *Energy & Environmental Science* **2013**, *6*, 3202, URL http://dx.doi.org/10.1039/C3EE41621F.

[79] T. Offermans, S. C. J. Meskers, R. A. J. Janssen, *Chemical Physics* **2005**, *308*, 125, URL http://dx.doi.org/10.1016/j.chemphys.2004.08.015.

[80] H. van Eersel, R. A. J. Janssen, M. Kemerink, *Advanced Functional Materials* **2012**, *22*, 2700, URL http://dx.doi.org/10.1002/adfm.201200249.

[81] M. C. Heiber, A. Dhinojwala, *The Journal of Chemical Physics* **2012**, *137*, 014903, URL http://dx.doi.org/10.1063/1.4731698.

[82] C. Deibel, T. Strobel, V. Dyakonov, *Physical Review Letters* **2009**, *103*, 036402, URL http://dx.doi.org/10.1103/PhysRevLett.103.036402, pRL.

[83] F. C. Jamieson, E. B. Domingo, T. McCarthy-Ward, M. Heeney, N. Stingelin, J. R. Durrant, *Chemical Science* **2012**, *3*, 485, URL http://dx.doi.org/10.1039/C1SC00674F.

[84] H. Tamura, I. Burghardt, *The Journal of Physical Chemistry C* **2013**, *117*, 15020, URL http://dx.doi.org/10.1021/jp406224a.

[85] H. Tamura, M. Tsukada, *Physical Review B* **2012**, *85*, 054301, URL http://dx.doi.org/10.1103/PhysRevB.85.054301.

[86] H. Tamura, I. Burghardt, *Journal of the American Chemical Society* **2013**, *135*, 16364–16367, URL http://dx.doi.org/10.1021/ja4093874.

[87] D. P. McMahon, D. L. Cheung, A. Troisi, *The Journal of Physical Chemistry Letters* **2011**, *2*, 2737, URL http://dx.doi.org/10.1021/jz201325g.

[88] D. Caruso, A. Troisi, *Proceedings of the National Academy of Sciences of the United States of America* **2012**, *109*, 13498, URL http://dx.doi.org/10.1073/pnas.1206172109.

[89] G. D'Avino, S. Mothy, L. Muccioli, C. Zannoni, L. Wang, J. Cornil, D. Beljonne, F. Castet, *The Journal of Physical Chemistry C* **2013**, *117*, 12981, URL http://dx.doi.org/10.1021/jp402957g.

[90] D. Hertel, H. Bassler, *ChemPhysChem* **2008**, *9*, 666, URL http://dx.doi.org/10.1002/cphc.200700575.

[91] G. Juska, K. Arlauskas, M. Viliunas, J. Kocka, *Physical Review Letters* **2000**, *84*, 4946, URL http://dx.doi.org/10.1103/PhysRevLett.84.4946.

[92] G. Juska, N. Nekrasas, V. Valentinavicius, P. Meredith, A. Pivrikas, *Physical Review B* **2011**, *84*, 155202, URL http://dx.doi.org/10.1103/PhysRevB.84.155202.

[93] S. Bange, M. Schubert, D. Neher, *Physical Review B* **2010**, *81*, 035209, URL http://dx.doi.org/10.1103/PhysRevB.81.035209.

[94] R. Coehoorn, P. A. Bobbert, *physica status solidi (a)* **2012**, *209*, 2354, URL http://dx.doi.org/10.1002/pssa.201228387.

[95] W. F. Pasveer, J. Cottaar, C. Tanase, R. Coehoorn, P. A. Bobbert, P. W. M. Blom, D. M. de Leeuw, M. A. J. Michels, *Physical Review Letters* **2005**, *94*, 206601, URL http://dx.doi.org/10.1103/PhysRevLett.94.206601.

[96] S. Bange, *Transient Optical and Electrical Effects in Polymeric Semiconductors*, Dissertation, University of Potsdam, Potsdam, **2009**, URL http://opus.kobv.de/ubp/volltexte/2009/3631/.

[97] S. Albrecht, S. Janietz, W. Schindler, J. Frisch, J. Kurpiers, J. Kniepert, S. Inal, P. Pingel, K. Fostiropoulos, N. Koch, D. Neher, *Journal of the American Chemical Society* **2012**, *134*, 14932, URL http://dx.doi.org/10.1021/ja305039j.

[98] J. Y. Kim, S. H. Kim, H. H. Lee, K. Lee, W. L. Ma, X. Gong, A. J. Heeger, *Advanced Materials* **2006**, *18*, 572, URL http://dx.doi.org/10.1002/adma.200501825.

[99] Y. M. Sun, J. H. Seo, C. J. Takacs, J. Seifter, A. J. Heeger, *Advanced Materials* **2011**, *23*, 1679, URL http://dx.doi.org/10.1002/adma.201004301.

[100] J. Frisch, M. Schubert, E. Preis, J. P. Rabe, D. Neher, U. Scherf, N. Koch, *Journal of Materials Chemistry* **2012**, *22*, 4418, URL http://dx.doi.org/10.1039/c1jm14968g.

[101] M. Svensson, F. L. Zhang, S. C. Veenstra, W. J. H. Verhees, J. C. Hummelen, J. M. Kroon, O. Inganas, M. R. Andersson, *Advanced Materials* **2003**, *15*, 988, URL http://dx.doi.org/10.1002/adma.200304150.

[102] L. H. Slooff, S. C. Veenstra, J. M. Kroon, D. J. D. Moet, J. Sweelssen, M. M. Koetse, *Applied Physics Letters* **2007**, *90*, 143506, URL http://dx.doi.org/10.1063/1.2718488.

[103] M. H. Chen, J. Hou, Z. Hong, G. Yang, S. Sista, L. M. Chen, Y. Yang, *Advanced Materials* **2009**, *21*, 4238, URL http://dx.doi.org/10.1002/adma.200900510.

[104] J. Liu, H. Choi, J. Y. Kim, C. Bailey, M. Durstock, L. Dai, *Advanced Materials* **2011**, *24*,

538, URL http://dx.doi.org/10.1002/adma.201103623.

[105] R. Steyrleuthner, M. Schubert, I. Howard, B. Klaumünzer, K. Schilling, Z. Chen, P. Saalfrank, F. Laquai, A. Facchetti, D. Neher, *Journal of the American Chemical Society* **2012**, *134*, 18303, URL http://dx.doi.org/10.1021/ja306844f.

[106] K. G. Jespersen, W. J. D. Beenken, Y. Zaushitsyn, A. Yartsev, M. Andersson, T. Pullerits, V. Sundstrom, *Journal of Chemical Physics* **2004**, *121*, 12613, URL http://dx.doi.org/10.1063/1.1817873.

[107] R. Mauer, M. Kastler, F. Laquai, *Advanced Functional Materials* **2010**, *20*, 2085–2092, URL http://dx.doi.org/10.1002/adfm.201000320.

[108] R. Osterbacka, A. Pivrikas, G. Juska, K. Genevicius, K. Arlauskas, H. Stubb, *Current Applied Physics* **2004**, *4*, 534, URL http://dx.doi.org/10.1016/j.cap.2004.01.013.

[109] A. Pivrikas, P. Stadler, H. Neugebauer, N. S. Sariciftci, *Organic Electronics* **2008**, *9*, 775, URL http://dx.doi.org/10.1016/j.orgel.2008.05.021.

[110] A. Devizis, A. Serbenta, K. Meerholz, D. Hertel, V. Gulbinas, *Physical Review Letters* **2009**, *103*, 027404, URL http://dx.doi.org/10.1103/PhysRevLett.103.027404.

[111] A. Devizis, K. Meerholz, D. Hertel, V. Gulbinas, *Physical Review B* **2010**, *82*, 155204, URL http://dx.doi.org/10.1103/PhysRevB.82.155204.

[112] M. Kuik, G. Wetzelaer, J. G. Ladde, H. T. Nicolai, J. Wildeman, J. Sweelssen, P. W. M. Blom, *Advanced Functional Materials* **2011**, *21*, 4502, URL http://dx.doi.org/10.1002/adfm.201100374.

[113] H. T. Nicolai, M. Kuik, G. A. H. Wetzelaer, B. de Boer, C. Campbell, C. Risko, J. L. Brédas, P. W. M. Blom, *Nature Materials* **2012**, *11*, 882, URL http://dx.doi.org/10.1038/nmat3384.

[114] Z. M. Beiley, E. T. Hoke, R. Noriega, J. Dacuna, G. F. Burkhard, J. A. Bartelt, A. Salleo, M. F. Toney, M. D. McGehee, *Advanced Energy Materials* **2011**, *1*, 954, URL http://dx.doi.org/10.1002/aenm.201100204.

[115] T. M. Clarke, J. Peet, A. Nattestad, N. Drolet, G. Dennler, C. Lungenschmied, M. Leclerc, A. J. Mozer, *Organic Electronics* **2012**, *13*, 2639, URL http://dx.doi.org/10.1016/j.orgel.2012.07.037.

[116] A. Dieckmann, H. Bassler, P. M. Borsenberger, *Journal of Chemical Physics* **1993**, *99*, 8136, URL http://dx.doi.org/10.1063/1.465640.

[117] S. Kilina, N. Dandu, E. R. Batista, A. Saxena, R. L. Martin, D. L. Smith, S. Tretiak, *The Journal of Physical Chemistry Letters* **2013**, *4*, 1453, URL http://dx.doi.org/10.1021/jz4003197.

[118] A. J. Mozer, G. Dennler, N. S. Sariciftci, M. Westerling, A. Pivrikas, R. Osterbacka, G. Juska, *Physical Review B* **2005**, *72*, 035217, URL http://dx.doi.org/10.1103/PhysRevB.72.035217.

[119] M. Schubert, R. Steyrleuthner, S. Bange, A. Sellinger, D. Neher, *Physica Status Solidi a-Applications and Materials Science* **2009**, *206*, 2743, URL http://dx.doi.org/10.1002/pssa.200925312.

[120] L. L. Chua, J. Zaumseil, J. F. Chang, E. C. W. Ou, P. K. H. Ho, H. Sirringhaus, R. H. Friend, *Nature* **2005**, *434*, 194, URL http://dx.doi.org/10.1038/nature03376.

[121] C. Tanase, E. J. Meijer, P. W. M. Blom, D. M. de Leeuw, *Physical Review Letters* **2003**, *91*, 216601, URL http://dx.doi.org/10.1103/PhysRevLett.91.216601.

[122] P. H. Wobkenberg, D. D. C. Bradley, D. Kronholm, J. C. Hummelen, D. M. de Leeuw, M. Colle, T. D. Anthopoulos, *Synthetic Metals* **2008**, *158*, 468, URL http://dx.doi.org/10.1016/j.synthmet.2008.03.016.

[123] C.-Z. Li, C.-C. Chueh, H.-L. Yip, J. Zou, W.-C. Chen, A. K. Y. Jen, *Journal of Materials Chemistry* **2012**, *22*, 14976, URL http://dx.doi.org/10.1039/C2JM32693K.

[124] V. I. Arkhipov, E. V. Emelianova, Y. H. Tak, H. Bassler, *Journal of Applied Physics* **1998**, *84*, 848, URL http://dx.doi.org/10.1063/1.368146.

[125] J. C. Scott, G. G. Malliaras, *Chemical Physics Letters* **1999**, *299*, 115, URL http://dx.doi.org/10.1016/S0009-2614(98)01277-9.

[126] Z. Chen, Y. Zheng, H. Yan, A. Facchetti, *J Am Chem Soc* **2009**, *131*, 8, URL http://dx.doi.org/10.1021/ja805407g.

[127] A. J. Campbell, D. D. C. Bradley, H. Antoniadis, M. Inbasekaran, W. S. W. Wu, E. P. Woo, *Applied Physics Letters* **2000**, *76*, 1734, URL http://dx.doi.org/10.1063/1.126182.

[128] I. Lange, J. C. Blakesley, J. Frisch, A. Vollmer, N. Koch, D. Neher, *Physical Review Letters* **2011**, *106*, 216402, URL http://dx.doi.org/10.1103/PhysRevLett.106.216402.

[129] M. Caironi, M. Bird, D. Fazzi, Z. H. Chen, R. Di Pietro, C. Newman, A. Facchetti, H. Sirringhaus, *Advanced Functional Materials* **2011**, *21*, 3371, URL http://dx.doi.org/10.1002/adfm.201100592.

[130] T. Schuettfort, L. Thomsen, C. R. McNeill, *Journal of the American Chemical Society* **2013**, *135*, 1092, URL http://dx.doi.org/10.1021/ja310240q.

[131] S. Fabiano, H. Yoshida, Z. Chen, A. Facchetti, M. A. Loi, *Acs Applied Materials & Interfaces* **2013**, *5*, 4417, URL http://dx.doi.org/10.1021/am400786c.

[132] J. C. Blakesley, M. Schubert, R. Steyrleuthner, Z. H. Chen, A. Facchetti, D. Neher, *Applied Physics Letters* **2011**, *99*, 183310, URL http://dx.doi.org/10.1063/1.3657827.

[133] K. J. Ihn, J. Moulton, P. Smith, *Journal of Polymer Science Part B: Polymer Physics* **1993**, *31*, 735, URL http://dx.doi.org/10.1002/polb.1993.090310614.

[134] S. Berson, R. De Bettignies, S. Bailly, S. Guillerez, *Advanced Functional Materials* **2007**, *17*, 1377, URL http://dx.doi.org/10.1002/adfm.200600922.

[135] G. Dennler, M. C. Scharber, C. J. Brabec, *Advanced Materials* **2009**, *21*, 1323, URL http://dx.doi.org/10.1002/adma.200801283.

[136] J. Clark, J. F. Chang, F. C. Spano, R. H. Friend, C. Silva, *Applied Physics Letters* **2009**, *94*, 163306, URL http://dx.doi.org/10.1063/1.3110904.

[137] J. Rivnay, R. Noriega, R. J. Kline, A. Salleo, M. F. Toney, *Physical Review B* **2011**, *84*, 045203, URL http://dx.doi.org/10.1103/PhysRevB.84.045203, pRB.

[138] T. Schuettfort, S. Huettner, S. Lilliu, J. E. Macdonald, L. Thomsen, C. R. McNeill, *Macromolecules* **2011**, *44*, 1530, URL http://dx.doi.org/10.1021/ma102451b.

[139] S. T. Turner, P. Pingel, R. Steyrleuthner, E. J. W. Crossland, S. Ludwigs, D. Neher, *Advanced Functional Materials* **2011**, *21*, 4640, URL http://dx.doi.org/10.1002/adfm.201101583.

[140] S. S. van Bavel, E. Sourty, G. de With, J. Loos, *Nano Letters* **2009**, *9*, 507, URL http://dx.doi.org/10.1021/nl8014022.

[141] J. M. Hodgkiss, A. R. Campbell, R. A. Marsh, A. Rao, S. Albert-Seifried, R. H. Friend, *Physical Review Letters* **2010**, *104*, 177701, URL http://dx.doi.org/10.1103/PhysRevLett.104.177701.

[142] S. Westenhoff, I. A. Howard, J. M. Hodgkiss, K. R. Kirov, H. A. Bronstein, C. K. Williams, N. C. Greenham, R. H. Friend, *Journal of the American Chemical Society* **2008**, *130*, 13653, URL http://dx.doi.org/10.1021/ja803054g.

[143] A. Troisi, *Faraday Discussions* **2013**, *163*, 377, URL http://dx.doi.org/10.1039/C3FD20142B.

[144] B. A. Collins, J. E. Cochran, H. Yan, E. Gann, C. Hub, R. Fink, C. Wang, T. Schuettfort, C. R. McNeill, M. L. Chabinyc, H. Ade, *Nat Mater* **2012**, *11*, 536, URL http://dx.doi.org/10.1038/nmat3310.

[145] H. P. Yan, B. A. Collins, E. Gann, C. Wang, H. Ade, C. R. McNeill, *ACS Nano* **2012**, *6*, 677, URL http://dx.doi.org/10.1021/nn204150f.

[146] J. L. Baker, L. H. Jimison, S. Mannsfeld, S. Volkman, S. Yin, V. Subramanian, A. Salleo, A. P. Alivisatos, M. F. Toney, *Langmuir* **2010**, *26*, 9146, URL http://dx.doi.org/10.1021/la904840q.

[147] M. R. Hammond, R. J. Kline, A. A. Herzing, L. J. Richter, D. S. Germack, H.-W. Ro, C. L. Soles, D. A. Fischer, T. Xu, L. Yu, M. F. Toney, D. M. DeLongchamp, *ACS Nano* **2012**, *5*, 8248, URL http://dx.doi.org/10.1021/nn202951e.

[148] J. Rivnay, S. C. B. Mannsfeld, C. E. Miller, A. Salleo, M. F. Toney, *Chemical Reviews* **2012**, *112*, 5488, URL http://dx.doi.org/10.1021/cr3001109.

[149] O. V. Mikhnenko, H. Azimi, M. Scharber, M. Morana, P. W. M. Blom, M. A. Loi, *Energy & Environmental Science* **2012**, *5*, 6960, URL http://dx.doi.org/10.1039/c2ee03466b.

[150] S. Fabiano, S. Himmelberger, M. Drees, Z. Chen, R. M. Altamimi, A. Salleo, M. A. Loi, A. Facchetti, *Advanced Energy Materials* **2013**, *3*, URL http://dx.doi.org/10.1002/aenm.201301409.

[151] J. Gierschner, Y.-S. Huang, B. Van Averbeke, J. Cornil, R. H. Friend, D. Beljonne, *The Journal of Chemical Physics* **2009**, *130*, 044105, URL http://dx.doi.org/10.1063/1.3065267.

[152] T. J. Savenije, J. E. Kroeze, X. N. Yang, J. Loos, *Thin Solid Films* **2006**, *511*, 2, URL http://dx.doi.org/10.1016/j.tsf.2005.12.123.

[153] F. Piersimoni, S. Chambon, K. Vandewal, R. Mens, T. Boonen, A. Gadisa, M. Izquierdo, S. Filippone, B. Ruttens, J. D'Haen, N. Martin, L. Lutsen, D. Vanderzande, P. Adriaensens, J. V. Manca, *Journal of Physical Chemistry C* **2011**, *115*, 10873, URL http://dx.doi.org/10.1021/jp110982m.

[154] R. F. Fink, J. Seibt, V. Engel, M. Renz, M. Kaupp, S. Lochbrunner, H. M. Zhao, J. Pfister, F. Wurthner, B. Engels, *Journal of the American Chemical Society* **2008**, *130*, 12858, URL http://dx.doi.org/10.1021/ja804331b.

[155] H. W. Ro, B. Akgun, B. T. O'Connor, M. Hammond, R. J. Kline, C. R. Snyder, S. K. Satija, A. L. Ayzner, M. F. Toney, C. L. Soles, D. M. DeLongchamp, *Macromolecules* **2012**, *45*, 6587–6599, URL http://dx.doi.org/10.1021/ma3008527.

Appendix

A.1 Additional results

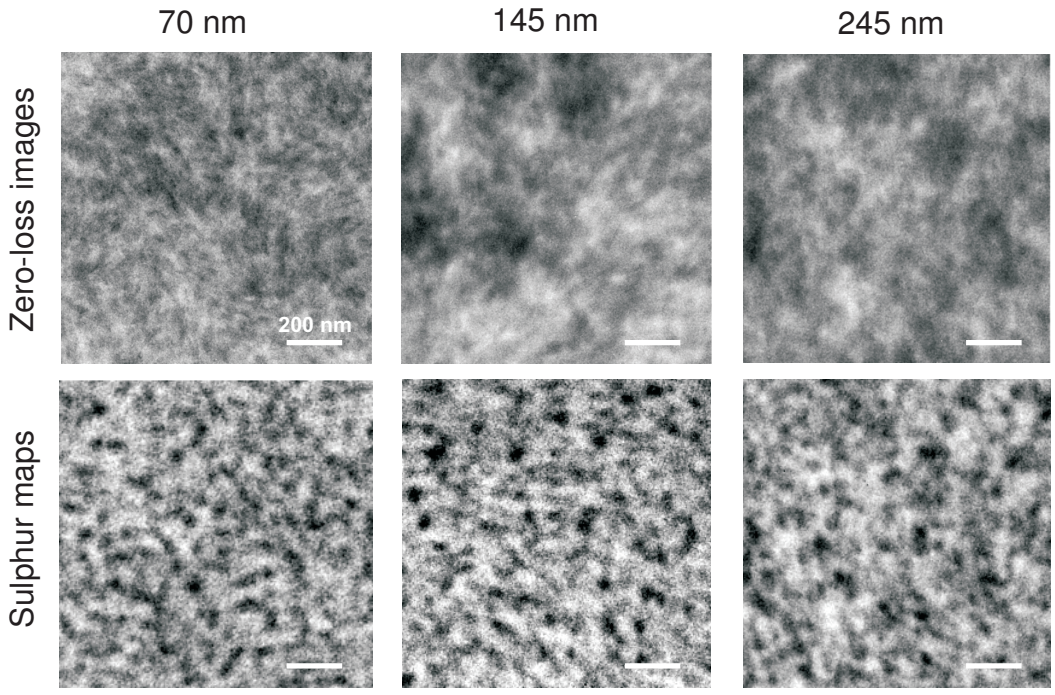

Figure A.1: Energy-filtered TEM zero-loss images (top) and sulphur maps (bottom) of 50:50 Xy:CN-cast P3HT:P(NDI2OD-T2) films with an active layer thickness of about 70 nm (left), 145 nm (middle) and 245 nm (right).

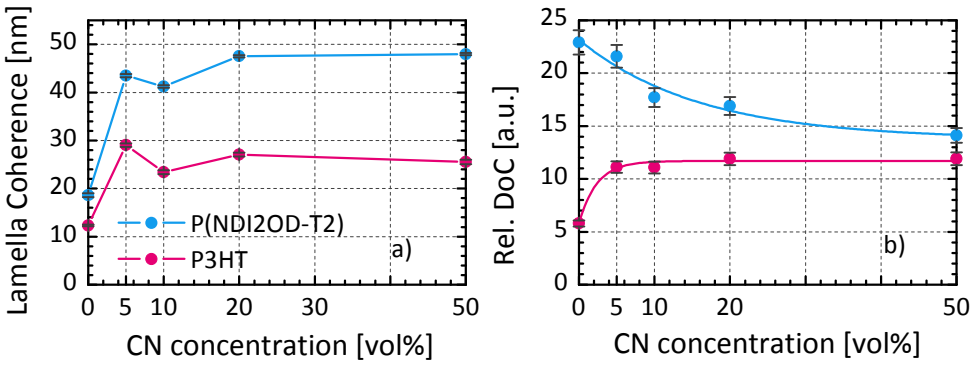

Figure A.2: *a)* Lamella coherence and *b)* DoC, calculated from the data in Fig. 4.22. The change in P3HT and P(NDI2OD-T2) lamella coherence for the various CN concentrations is comparable for both polymers. From the relatively large values of 12 nm for P3HT and 18 nm for P(NDI2OD-T2), the coherence length jumps to about 30 nm and 45 nm for P3HT and P(NDI2OD-T2), respectively, when adding 5% of CN. More CN then causes only a marginal change of the crystal coherence. Note that these values are larger than what has been commonly reported for thermally annealed blends of polymers with soluble fullerenes and even larger than those reported for pure P3HT and P(NDI2OD-T2), which means that the high temperature drying procedure we use for the preparation of our active layers enables the growing of relatively large polymer crystals.[9,145,155] The abrupt change of the crystal coherence for CN-cast blends can be also seen in the evolution of the DoC of P3HT, which also doubles compared to the Xy-cast blend but is constant above 5% CN in the solution. Interestingly, the DoC of P(NDI2OD-T2) doesn't show this jump but instead decreases continuously by 30% from 0 to 50% CN. Since the bulk of the photocurrent enhancement occurs at CN concentrations above 5% CN, these changes in DoC and lamellar coherence cannot explain the changes in device performance.

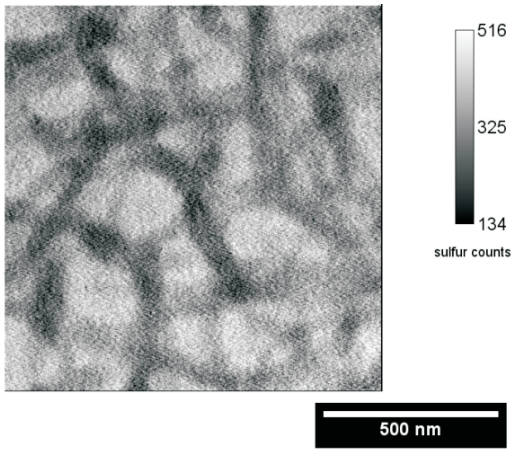

Figure A.3: EF-TEM sulphur map of an annealed CF-cast P3HT:P(NDI2OD-T2) film (thickness approximately 70 nm).

A.2 Original publications and manuscripts

Mobility relaxation and electron trapping in a donor/acceptor copolymer

Marcel Schubert,[1] Eduard Preis,[2] James C. Blakesley,[1] Patrick Pingel,[1] Ullrich Scherf,[2] and Dieter Neher[1]
[1]*University of Potsdam, Institute of Physics and Astronomy, Karl-Liebknecht-Str. 24-25, 14476 Potsdam, Germany*
[2]*Bergische University Wuppertal, Macromolecular Chemistry, 42119 Wuppertal, Germany*
(Received 6 September 2012; published 17 January 2013)

To address the nature of charge transport and the origin of severe (intrinsic) trapping in electron-transporting polymers, transient and steady-state charge transport measurements have been conducted on the prototype donor/acceptor copolymer poly[2,7-(9,9-dialkyl-fluorene)-alt-5,5-(4′,7′-di-2-thienyl-2′,1′,3′-benzothiadiazole)] (PFTBTT). A charge-generation layer technique is used to selectively address transport of the desired charge carrier type, to perform time-of-flight measurements on samples with <200 nm thickness, and to combine the time-of-flight and the photocharge extraction by linearly increasing voltage (photo-CELIV) techniques to investigate charge carrier dynamics over a wide time range. Significant trapping of free electrons is observed in the bulk of dioctyl-substituted PFTBTT (alt-PF8TBTT), introducing a strong relaxation of the charge carrier mobility with time. We used Monte-Carlo simulation to simulate the measured transient data and found that all measurements can be modeled with a single parameter set, with the charge transport behavior determined by multiple trapping and detrapping of electrons in an exponential trap distribution. The influence of the concomitant mobility relaxation on the transient photocurrent characteristics in photo-CELIV experiments is discussed and shown to explain subtle features that were seen in former publications but were not yet assigned to electron trapping. Comparable studies on PFTBTT copolymers with chemical modifications of the side chains and backbone suggest that the observed electron trapping is not caused by a distinct chemical species but rather is related to interchain interactions.

DOI: 10.1103/PhysRevB.87.024203 PACS number(s): 73.50.Dn, 73.61.Ph, 72.20.Fr, 72.40.+w

I. INTRODUCTION

The effectiveness of conjugated polymers in applications, not only in organic photovoltaic cells, light-emitting diodes (LEDs), and organic field-effect transistors (OFETs) but also in more complex, integrated smart systems, depends on their ability to transport charge. Thus, from the first days of organic electronics, the investigation and description of charge transport phenomena provided the basis of a deeper understanding and further optimization of conjugated materials. In that sense, the charge carrier mobility is mostly used to describe the charge transport capability of an organic semiconductor. Unfortunately, the mobility represents one of the most complex parameters, as it is influenced by temperature, electric field, and charge carrier density. These dependencies are further related to the shape and width of the density of states (DOS) distribution. Numerous investigations and models have attempted to describe and understand the influence of these parameters on the charge carrier mobility. Two popular semiempirical models are the Gaussian disorder model (GDM) and the multiple trapping (MT) and release model. The GDM describes charge transport by hopping of localized charges between transport sites that are Gaussian distributed in energy and space.[1] In contrast to this, the MT model treats charge carriers as free until they become trapped in an (exponential) density of trap states (DOTS).[2] Displacement of these charges requires that they be thermally excited back to the transport manifold. Both the GDM and the MT model have been extensively used to analyze steady-state current voltage characteristics of uni- and bipolar polymer-based devices,[3,4] to understand the dependence of the mobility on carrier and dopant concentration,[4–7] to quantify the energy alignment at the polymer–metal contacts,[8,9] and to model charge carrier mobilities measured by transient photocurrent techniques as a function of field and temperature.[10–13] One unique property of MT with an exponential trap distribution is that the energetic distribution of carriers generated, e.g., by pulsed illumination in a transient photocurrent experiment never adopts a stationary state but rather decays continuously in energy. Tiedje and Rose pointed out that under these particular conditions, the time dependence of mobility follows a simple power law: $\mu(t) = \mu_0 \cdot (t/t_0)^{\alpha-1}$, with $\alpha < 1$ describing the energetic width of the exponential trap distribution relative to thermal energy.[2] Interestingly, few reports demonstrate explicitly the power-law decay of the mobility over a considerable range in mobility and time. Devizis *et al.* investigated the mobility relaxation of a polyspirobifluorene derivative in the pico- to nanosecond time regime. A very high mobility was found for free charges directly after photogeneration, followed by a power-law decay over five orders in time.[14] Surprisingly, in contradiction to the GDM and the MT model, this relaxation was found to be independent of temperature,[15] which underlines the importance of further experimental investigations of these phenomena. Besides the relaxation process on ultrashort timescales, relaxation processes on the micro- to millisecond regime were mostly reported for blends consisting of an electron-donating and electron-accepting compound.[11,16,17] Here, the intermixing on molecular dimensions seems to introduce a variety of additional electronic states that significantly influences charge transport and recombination, which are both highly relevant for device operation. However, neither a proper explanation on the origin of the mobility relaxation nor a description of the current transients under such conditions has existed until now; both of these primarily motivate this article.

Here, we report temporal relaxation of the electron mobility covering the microsecond range in the well-known polymer poly[2,7-(9,9-dialkyl-fluorene)-alt-5,5-(4′,7′-di-2-thienyl-2′,1′,3′-benzothiadiazole)] (PFTBTT), also called PFDTBT or APFO-3.[18] It was one of the first donor/acceptor-type copolymers designed especially for use in bulk heterojunction organic solar cells. The relatively small optical band gap of 1.88 eV and the low-lying highest occupied molecular orbital render this polymer one of the most promising materials for organic photovoltaics. When used as a polymeric donor, in combination with soluble fullerene derivatives, power conversion efficiencies (PCEs) of $\leqslant$5% have been achieved, with the exact value depending in part on the position of side-chain attachment to the PFTBTT backbone.[19–21] In combination with PCBM, Veldman *et al.* predicted that PCEs as high as 9% should be achievable.[22] Recently, a 2% all-polymer solar cell was presented by Mori *et al.* that incorporated PFTBTT as the electron-accepting material.[23] This value represents one of the best efficiencies for all-polymer solar cells. He *et al.* also reported excellent all-polymer solar cells with a more soluble derivative of PFTBTT, poly((9,9-dioctylfluorene)-2,7-diyl-alt-[4,7-bis(3-hexylthien-5-yl)-2,1,3-benzothiadiazole]-2′,2″-diyl) (F8TBT), with PCEs of 1.9%.[24] This demonstrates that PFTBTT-based copolymers can work as both the electron-donating and the electron-accepting components, meaning that these copolymers are capable of transporting electrons and holes with adequate mobilities. To the best of our knowledge, it is the only material for which the ambipolar nature of charge transport has been successfully transferred to efficient solar cells. Such polymers may gain increasing interest, since they offer the opportunity to produce ternary blends with cascade photocurrent generation.[25] This motivated studies of the charge transport properties in blend layers. Most of these studies addressed the hole mobility of the polymer in blends with soluble fullerenes.[26–28]

However, there are several reports of electron trapping in blends of F8TBT with the hole-transporting polymer poly(3-hexylthiophene) (P3HT), despite the rather good performance of these blend devices. Hwang *et al.*, numerically modeled the transient photocurrent response of a F8TBT:P3HT blend by assuming a MT mechanism for the electron transport.[29] It was found that the free electron mobility of $\mu_e = 1 \times 10^{-3}$ cm^{2}V^{-1}s^{-1} is reduced by more than two orders of magnitude on timescales relevant for charge extraction in solar cell devices under working conditions. The trap-dominated transport in pristine F8TBT was further confirmed by the observation of highly dispersive photocurrent transients.[28] A comparison to blends with a fullerene derivative as the electron-accepting compound implied that the solar cell performance of F8TBT:P3HT blends is limited by the proposed trapping process.[30]

In the following, we present a detailed analysis of the charge transport in PFTBTT-based copolymers. We first show the ambipolar nature of charge transport in the alternating copolymer poly[2,7-(9,9-dioctylfluorene)-alt-5,5-(4′,7′-di-2-thienyl-2′,1′,3′-benzothiadiazole)] (alt-PF8TBTT). After that, transient electron transport is addressed with the photocharge extraction by linearly increasing voltage (photo-CELIV) technique. To investigate electron transport and trapping, a thin charge-generation layer (CGL) is introduced that enables time-of-flight (TOF) and time-delayed time-of-flight (td-TOF) measurements on sub-200-nm-thick films. Monte-Carlo (MC) simulations based on the MT formalism are performed to rationalize the experimental current transients. Finally, side chain- and backbone-modified PFTBTT copolymers are investigated to elucidate the origin of the electron trapping in alt-PF8TBTT.

II. DEVICE PREPARATION AND EXPERIMENTAL TECHNIQUES

A. Polymer synthesis

The monomers 2,7-dibromo-9,9-dialkyl fluorene[31–33] and dibromo/distannylated TBTT[32,34–36] have been synthesized according to literature procedures. Two batches of alt-PF8TBTT with a molecular weight M_n of 5000 g/mol and polydispersity indices (PDIs) of 2.5 and 2.0 were synthesized in a Stille-type cross-coupling reaction using distannylated TBTT and 2,7-dibromo-9,9-dialkylfluorenes with $Pd(PPh)_2Cl_2$.[34,35] No differences in the charge transport properties were observed between the batches. Films were prepared by dissolving PFTBTT in chloroform and spin coating the solution at a speed of 1500 rpm. The standardized preparation conditions include thermal annealing of the films for 10 min at 140 °C. The alternating copolymer poly[2,7-(9,9-dioctyldodecylfluorene)-alt-5,5-(4′,7′-di-2-thienyl-2′,1′,3′-benzothiadiazole)] (alt-PF8/12TBTT) with elongated alkyl chains was synthesized in a similar way as alt-PF8TBTT; it had a M_n of 8000 g/mol, while the PDI was 2.1.

Poly[2,7-(9,9-dioctylfluorene)-co-5,5-(4′,7′-di-2-thienyl-2′,1′,3′-benzothiadiazole)] (part-PF8TBTT) is a "partially" alternating PFTBTT copolymer prepared in a Stille-type cross-coupling reaction of the three monomers distannylated TBTT, dibromo TBTT, and 2,7-dibromo-9,9-dioctylfluorene. The feed ratio of these three monomers was 50:10:40, respectively. The resulting copolymer possesses a molecular weight of 4500 g/mol and a PDI of 1.5. The chemical structures of the described copolymers are summarized in Fig. 1.

B. Device preparation

OFETs were built on highly doped silicon substrates on which a silicon oxide (SiO_2) layer of ~300 nm served as the gate dielectric. The SiO_2 surface was further treated with hexamethyldisilazane to remove electron traps that naturally exist on top of bare SiO_2.[37] The width and length of the channel and the areal capacitance of the device are 14.85 cm, 100 μm, and 11.9 nF/cm^2, respectively. Gold source and drain electrodes were thermally evaporated at a pressure of ~10^{-6} mbar.

Devices for photo-CELIV, TOF, and td-TOF measurements were built on prestructured indium tin oxide-coated glass substrates on which a 50-nm-thick layer of PEDOT:PSS (Clevios P VP AI 4083) was spin coated in air and dried at 180 °C for 10 min inside of a nitrogen-filled glove box. In case P3HT was used as CGL, it was spin coated on top of PEDOT:PSS and thermally annealed at 180 °C for 10 min.

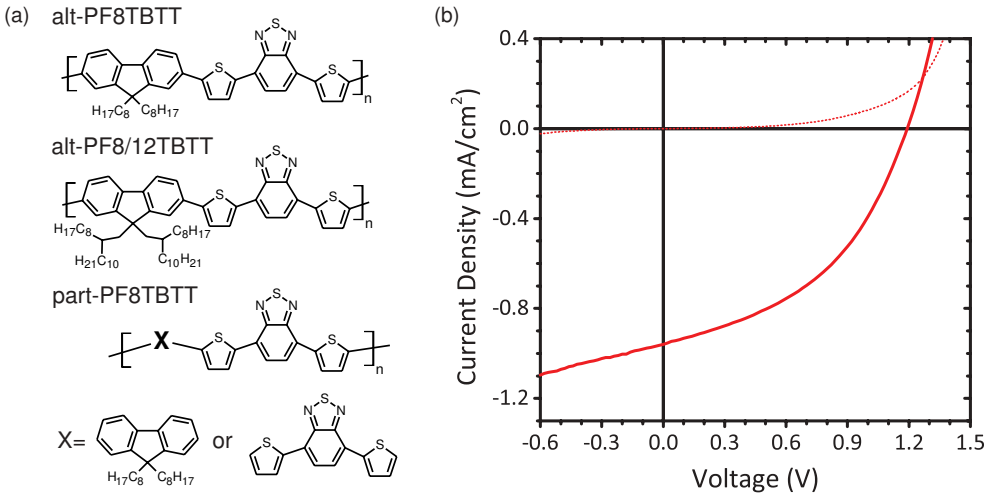

FIG. 1. (Color online) (a) Chemical structures of the PFTBTT copolymers. (b) Solar cell device characteristic of 40-nm alt-PF8TBTT on top of a P3HT CGL under AM 1.5G illumination at 100 mW/cm^2 (straight red line) and in the dark (dotted red line).

Washing this layer three times with chlorobenzene resulted in the formation of a 3-nm P3HT interlayer (as proven by optical absorption measurements).[38,39] The PFTBTT copolymers were spin coated from a chloroform solution, and the devices were completed by evaporation of 20-nm samarium covered by 100-nm aluminum. The active area of the final devices is 1 mm^2. To protect the samples against oxidization in air, a thin glass substrate fixed with a two-component epoxy resin was used for encapsulation.

C. Transient photocurrent experiments

Optical excitation for TOF and pulsed extraction techniques came from an optical parametric oscillator fed by the third harmonic of a neodymium-doped yttrium aluminum garnet laser working at 500 Hz (Ekspla, NT series). The excitation wavelength was 600 nm, and the pulse width was 6 ns. Samples were mounted in a homemade sample holder or in a closed-cycle He cryostat. Currents were amplified by a Femto DLH current amplifier and recorded by a Yakagawa 500-MHz storage Oscilloscope. For all transient measurement techniques, the intensity of the laser was adjusted to keep the photogenerated charge $<10\%$ of the capacitive charge to ensure that neither the internal field redistributes due to the photogenerated charge nor the transients were influenced by bimolecular recombination.[40] The corresponding charge carrier densities were $<5 \times 10^{21}$ m^{-3} in all cases. This ensured that all experiments were performed in the low charge carrier density regime, where the bulk mobility is not affected by the charge carrier density.[5,7] For td-TOF measurements, our sample design allowed a voltage pulse rise time of <20 ns. In all transient measurements, the internal electric field was corrected by the built-in voltage. A value of 1.2 eV was found, determined as the voltage at which no photocurrent flows immediately after excitation.

D. MC simulation

In general, the simulation of current transients with hopping models needs to consider all possible jumps between all states within the DOS. However, in the low-energy tail of the DOS, the distance between sites of approximately the same energy is large. Thus, for charges in tail states to move, thermal excitation to sites close to the center of the DOS, with larger electronic coupling, is necessary.

Charge transport occurs predominately in a small energy range around a "transport energy." The MT model simplifies this situation by defining a "mobility edge," which is equivalent to the transport energy, and divides the DOS into free states and trap states. Carriers occupying states above the mobility edge are assumed to be free and have a fixed, constant mobility μ_0, while carriers occupying states below the mobility edge (DOTS) are trapped and have zero mobility. We assumed an exponential DOTS, which was motivated by the observed power-law decay of the photocurrent in the TOF experiments (described later). The simplicity of the MT model allows fast MC simulations[41] of current transients in seconds on a desktop computer, as opposed to the cluster-scale computation resources required for performing MC simulations with more complex hopping models.

Our MC simulation considers the motion of individual, noninteracting charge carriers. At the beginning of the simulation, each carrier is treated as free at a displacement $x = 0$. The time until the first trapping event is randomly sampled from an exponential distribution with mean time t_{trap}. During this interval, the carrier moves at a velocity $F\mu_0$, where F is the electric field, and generates a corresponding displacement current $eF\mu_0/d$ in the external circuit, where d is the film thickness and e is the elementary charge. At the end of this interval, the carrier becomes trapped. The energy of the trap site E is sampled at random from the exponential DOTS with mean trap energy of E_0. The carrier then remains immobile, generating no displacement current, until it becomes detrapped. The dwell time the carrier remains in the trapped state is randomly sampled from an exponential distribution with mean time $t_{\text{trap}} \exp(E/k_{\text{B}}T)/N_{\text{eff}}$, determined by detailed balance, where $k_{\text{B}}T$ is the thermal energy and $N_{\text{eff}} = N_{\text{trap}}/N_{\text{free}}$ is the effective concentration of trap states, the ratio between the densities of trap and those of free states.

The trapping and detrapping process is repeated until the charge carrier reaches the counter electrode $x = d$. Current transients were constructed by averaging 10^5 carriers to give noise-free curves.

An effective mobility μ_{eff} of a charge carrier at any time is given by the free carrier mobility multiplied by the fraction of carriers in a free state. When simulating transient photocurrents with a long delay between excitation and extraction, it was necessary to include a field-dependent detrapping rate to accurately fit the measured transients. This was implemented by increasing the detrapping rate by a factor of $\exp(aF/k_{\text{B}}T)$ (up to $aF = E$). The fitting parameter a loosely represents the typical hopping distance from a trap state to a nearby free carrier state in the downfield direction.[42]

III. RESULTS AND DISCUSSION

A. Electron transport in alternating PF8TBTT

Two contradicting views of the charge transport properties of PFTBTT-based OFETs can be found in literature. While work by Muller *et al.*[26] and Andersson *et al.*[43] did not reveal electron transport in pristine PFTBTT OFETs, McNeill *et al.* nicely demonstrated ambipolar behavior of F8TBT in a light-emitting OFET.[44] We performed OFET measurements in bottom gate–top electrode geometry with a silanized SiO_2 gate insulator (displayed in Fig. S1 of the supplementary material),[71] which clearly showed ambipolar charge transport in alt-PF8TBTT and reveal mobilities for holes and electrons of $\mu_{\text{h}} = 2 \times 10^{-3}$ $\text{cm}^2\text{V}^{-1}\text{s}^{-1}$ and $\mu_{\text{e}} = 4 \times 10^{-4}$ $\text{cm}^2\text{V}^{-1}\text{s}^{-1}$, respectively, that are comparable to those reported in Ref. 44. Therefore, we conclude here that alt-PF8TBTT can be regarded as an ambipolar material with overall good electron transport, consistent with the observation of the excellent acceptor properties of alt-PF8/12TBTT in organic solar cells, where sufficiently high electron mobility is a prerequisite.[23]

In order to address bulk transport properties of alt-PF8TBTT, we applied different transient photocurrent techniques. A common technique for determining charge carrier mobilities is the photo-CELIV technique.[45] Here, photogenerated charges are continuously accelerated by a linear increasing voltage. Given a homogeneous charge carrier density, extraction of charge carriers at one side of the device sets in simultaneously, leading to a characteristic maximum in the current signal from which the electron mobility can be calculated. In addition, the delay time between the pulsed excitation and the beginning of the extraction pulse t_{del} can be varied, which allows the investigation of charge recombination or charge relaxation phenomena. The advantage of CELIV is that it can be applied to thin organic layers of some 100 nm. Thus, charge transport can be studied on spatial and temporal dimensions that are relevant for active devices like solar cells or LEDs.

Photo-CELIV transients of a 205-nm-thick film of alt-PF8TBTT are displayed in Fig. 2(a). Transients are shown for several delay times, spanning three orders of magnitude in time from 150 ns to 100 μs. A distinct extraction peak is seen in the photo-CELIV transients for a short delay, while with increasing t_{del}, the maximum current decreases and the time t_{max}, which is the time between the beginning of the extraction pulse and the time at the photocurrent maximum, increases. In addition, all transients exhibit a rather pronounced tail, whose height is only slightly affected by the delay time. For delay times above 20 μs, the transients have no distinct maximum and instead consist of a slowly increasing current. Such characteristic features were also observed by others,[11,16,17,46,47]

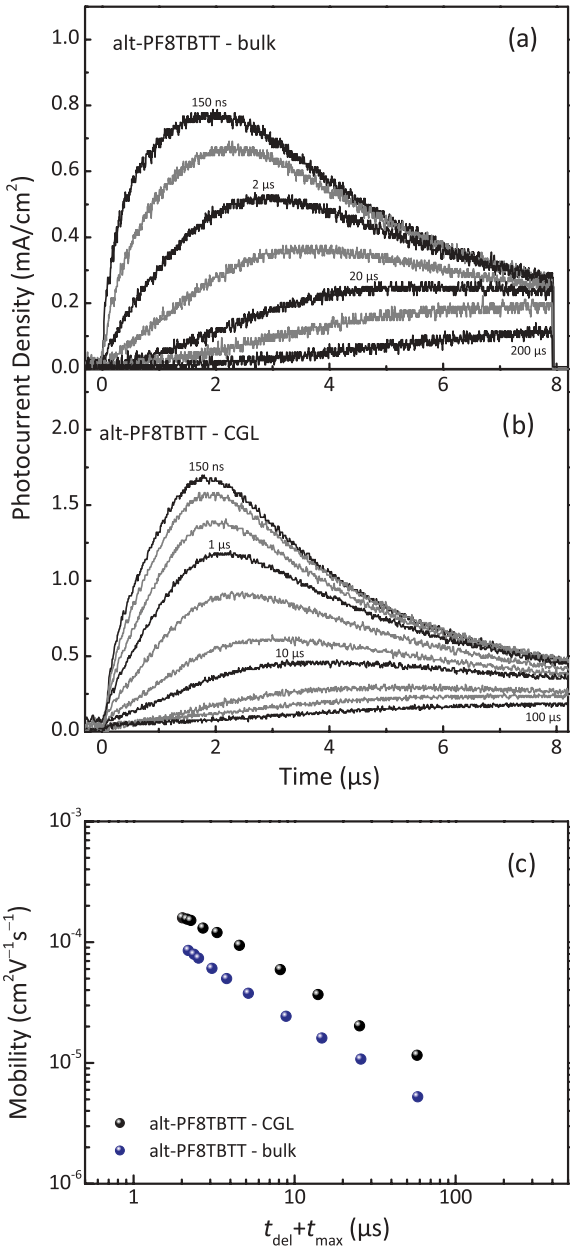

FIG. 2. (Color online) Room-temperature photo-CELIV transients at various delay times for (a) a 205-nm-thick single layer of alt-PF8TBTT and (b) a 170-nm alt-PF8TBTT layer with an additional 3-nm P3HT CGL. The capacitive loading current j_{cap} was subtracted to visualize photocurrents only. Transients are shifted to $t = 0$, which denotes the beginning of the extraction ramp that had slopes of 0.86 V/μs (bulk) and 1.09 V/μs (CGL). To avoid charge extraction during the delay time, a forward bias of 1.2 V was applied during photoexcitation and delay. (c) CELIV mobilities μ_{CELIV} deduced from experiments on bulk and CGL devices, plotted over $t_{\text{del}} + t_{\text{max}}$ (for calculation, see text).

but their origin has not been discussed so far. In the low carrier density regime, the corresponding mobility μ_{CELIV} is obtained via $\mu_{\mathrm{CELIV}} = 2d^2[3t_{\mathrm{max}}^2 A']^{-1}$, where A' is the voltage rise speed.[48] The calculated mobility as a function of delay time is displayed in Fig. 2(c). This plot shows a continuous decrease of μ_{CELIV} with increasing delay time. This decay, as well as the unusual shape of the current transients, suggests that the mobility must be a function of time throughout the entire temporal range considered here. In this context, the initial rise of the CELIV transients is highly nonlinear for short delay times, in contrast to the predicted linear rise for a time- and field-independent mobility.[48] Note that, the nature of the mobile (faster) charge carrier type, either electron or hole, can in general distinguished in a CELIV experiment, and both carrier types can significantly contribute to the current.[49] Indeed, our OFET measurements suggest that in alt-PF8TBTT, both types of charge carriers are mobile, which therefore represents a fundamental problem whenever photogenerated carriers are generated over the entire layer thickness. Thus, the understanding of the current transient and a definitive identification of the electron transport in alt-PF8TBTT is, at this point, not possible and requires a more sophisticated measurement technique.

An elegant approach to avoid the difficulties of the standard CELIV measurement in distinguishing charge carrier types is to insert a CGL.[50] Here, a thin photoactive layer is inserted into the device structure to create a planar heterojunction (PHJ) between the CGL and the transport layer, the latter being the material under study. After excitation, excitons predominantly dissociate at the PHJ, generating free charge carriers. The polarity of the generated carriers inside the transport layer depends only on the relative position of the energy levels between generation and transport layer. As a further benefit of the CGL technique, the optical field profile within the device may not be known for the exact analysis of the transients, since free charge generation is almost exclusively at the PHJ.[50] Here, we apply this technique to measure carrier mobilities in thin polymer layers $<$200 nm using photo-CELIV and TOF, where for the latter technique, several-micrometer-thick layers are normally required.

To study electron transport in PFTBTT copolymers, we introduced a P3HT CGL between the PEDOT:PSS anode and the PFTBTT transport layer. In this combination, the CGL acts as a donor while PFTBTT represents the electron-accepting and electron-transporting phase.[23,44,51] A typical current–voltage characteristic of a solar cell device comprising a 3-nm P3HT CGL and a 40-nm- thin alt-PF8TBTT layer is displayed in Fig. 1(b). This cell gives a reasonable PCE of 0.5% under 100 mW/cm^2 air mass 1.5 global (AM 1.5G) illumination with a short circuit current density of $\sim$1 mA/cm^2. In addition, the external quantum efficiency at the excitation wavelength of 600 nm of this device is $\sim$100 times higher than of a device without CGL. This demonstrates that the photocurrent originates from free carriers generated at the PHJ.

Photo-CELIV current transients of devices comprising a P3HT CGL recorded over the range of delay times, as for the bulk device, are displayed in Fig. 2(b). The general characteristics of the photocurrent are comparable for the CGL and the bulk device, including the strong shift of t_{max} with increasing t_{del}, the pronounced tail at the end of the extraction pulse, and the slowly increasing current at high delay times. This result strongly implies that electrons also determine the transient current in the bulk photo-CELIV experiment. The corresponding electron mobility values were extracted from the maximum of the photo-CELIV transient t_{max} in the CGL device. Assuming that charges are generated only at the interface to the thin CGL and accelerated by a linear increasing field $E(t) = A't/d$ with a slope of A', the mobility is simply derived from $s(t) = \int v(\tau)d\tau = \mu \int E(\tau)d\tau$. Assuming that $s(t_{\mathrm{max}}) = d$ yields

$$\mu_{\mathrm{CELIV,CGL}} = \frac{2d^2}{t_{\mathrm{max}}^2 A'}. \tag{1}$$

This formula is correct in that the CGL is much thinner than the layer thickness d and that the photogenerated charge is much smaller than the capacitive charge stored at the electrodes $Q_{\mathrm{photo}} \ll Q_{\mathrm{cap}}$ (see also Fig. S2 of the supplementary material).[71] The latter condition rules out that space charges distort or screen the external applied field. Equation (1) differs by a factor of 1/3 from the case of an initially homogeneously distributed charge density. Mobilities obtained by Eq. (1) are displayed in Fig. 2(c). Again, the mobility drops continuously over a time span of two orders of magnitude, following a power-law decay with an exponent of $\sim 0.81 \pm 0.01$. To summarize, the photo-CELIV transients in bulk and CGL devices both reflect the electron transport characteristics of alt-PF8TBTT and reveal a pronounced mobility relaxation over two orders in time.

One drawback of photo-CELIV is that extraction is with a nonconstant, linearly rising electric field. Therefore, care must be taken when interpreting CELIV transients, where the photocurrent maximum appears at different times and consequently at different electric fields. To circumvent this problem, we performed experiments using the td-TOF method. Here, a rectangular voltage pulse is applied to the sample after an adjustable delay time. Thus, this technique merges advantages of photo-CELIV and TOF. To the best of our knowledge, this is the first time that transport dynamics have been investigated using the td-TOF technique. A detailed description of the setup and working principle can be found in a recent publication by Kniepert *et al.*[52]

Experimental td-TOF transients are displayed in Fig. 3, together with the standard TOF transient for a P3HT CGL device with a 170-nm-thick alt-PF8TBTT layer. The top electrode was positively charged to probe the transport of electrons. No transients were detected when the polarity is changed, which proves that electrons are efficiently generated at the CGL and transported through the alt-PFTBTT layer. In td-TOF, a constant voltage of 1.2 V was applied during the delay time as in the CELIV experiment to avoid carrier extraction. Then, the voltage is switched to -0.5 V (top electrode positively charged within 20 ns) to create an extraction field. The same voltage of -0.5 V was applied in the regular TOF experiment.

The regular TOF current transient displayed in Fig. 3 is strongly dispersive, and its initial decay follows a strict power-law dependence of $j(t) \propto t^{\alpha-1}$. As pointed out in Sec. I, such time dependence is characteristic for charge transport that is dominated by MT and detrapping in an exponential DOS distribution $g(E) = N_t k_B^{-1} T_0^{-1} \exp[-(E_L - E)/(E_0)]$ of

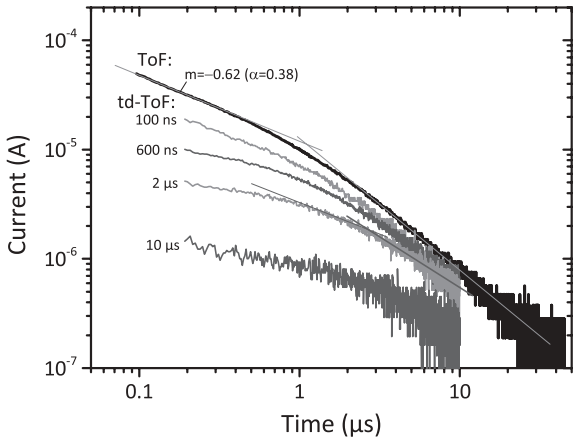

FIG. 3. TOF (black) and td-TOF (light and dark gray) current transients at a temperature of 295 K and an extraction field of 1×10^7 V/m. td-TOF transients are shown for several delay times to display the increase in the transit time. The thickness of the alt-PF8TBTT active layer was 170 nm. Straight lines are a visual guide for the two linear regions.

trapping states, where N_t is the total DOTS, $E_0 = k_B T_0$ is the characteristic energy, E_L is the energy of the lowest unoccupied molecular orbital, k_B is Boltzmann's constant, and T_0 is the characteristic temperature.[13] The slope parameter α is then given by $\alpha = T/T_0$. For the data shown in Fig. 3, the double-logarithmic slope $m = \alpha - 1 = -(1 - k_B T/E_0)$ is equal to -0.62, which yields E_0 67 meV for alt-PF8TBTT, corresponding to a characteristic temperature of 775 K. In this model, the current at a given time is directly proportional to the effective mobility in the organic semiconductor. In other words, the power-law decay of the current reflects the time dependence of the mobility. Above 1 μs, the TOF transient's slope changes, indicative of the arrival of the fastest electrons at the counter electrode. At an internal field of 1×10^7 V/m, the transit time of the electrons is $\sim$1 μs. From this, the electron mobility was calculated to be 1.7×10^{-4} cm^2/Vs, close to the mobility obtained by photo-CELIV measurements at very short delay times [Fig. 2(c)]. This value for the electron mobility is even higher than reported bulk hole mobilities in pure PFTBTT,[27] showing that in the bulk, electrons might be the faster type of charge carriers. The small thickness of 3 nm and the high hole mobility in regioregular P3HT of $\sim 1 \times 10^{-4}$ cm^2/Vs[53] sets the transit time of holes in the CGL to $\sim$1 ns, orders of magnitude faster than the observed transit time, again confirming that we are able to probe exclusively the electron transport through the alt-PF8TBTT layer.

For short delay times, td-TOF and TOF show comparable current transients with similar transit times. With increasing delay time, the initial slope of the td-TOF transient decreases and reaches a nearly constant value at a delay time of 10 μs. Also, the change in slope is seen at later times, suggesting a larger transit time. This is exemplarily shown in Fig. 3 for the td-TOF transient after a 2-μs delay. The calculated mobility is 7×10^{-5} cm^2/Vs, which is comparable to the value obtained by photo-CELIV at the same delay. Thus, our td-TOF measurements unambiguously reveal a pronounced time dependence of the mobility.

B. Simulation of current transients

The qualitative agreement between the results from td-TOF (constant field) and those from photo-CELIV (linearly increasing field) measurements as described previously suggests that time-dependent electron mobility in an exponential DOTS rather than its explicit field dependence governs the CELIV transients at different delay times. To confirm this, a numerical MC simulation based on a MT model was used to simulate the measured current transients. The algorithm of the simulation is described is Sec. II D, and best fits are displayed in Fig. 4. The parameters used for these simulations are summarized in Table I and were determined as follows. First, the initial current decay m of the TOF transient in Fig. 3 is used to fix the trap energy E_0 to 67 meV. In a next step, the free carrier mobility μ_0, the trap time t_{trap}, and the effective trap density N_{eff} were chosen to accurately reproduce photo-CELIV transients at very short delay times. Then t_{trap} and N_{eff} were fixed. Finally, the parameter a describing the field-assisted detrapping is

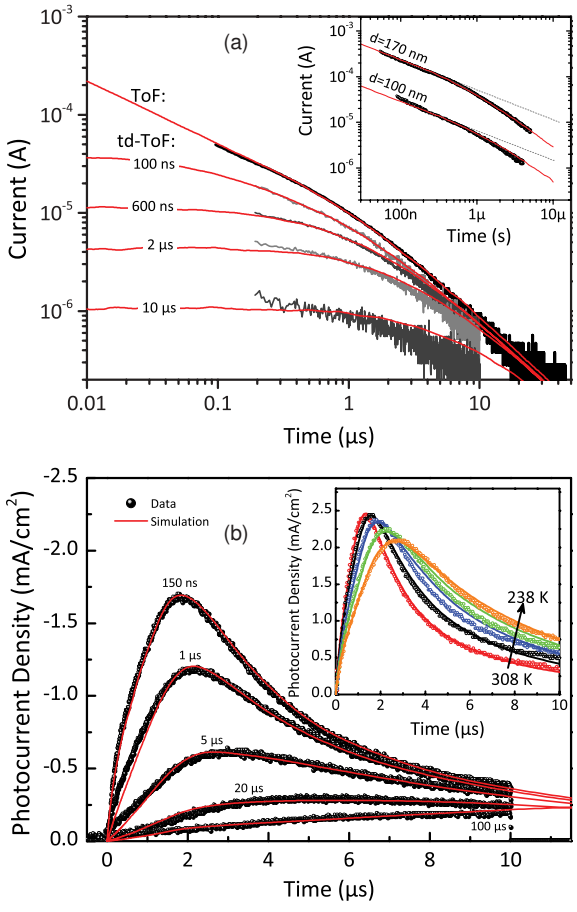

FIG. 4. (Color online) Comparison of MC simulation results with measured transients obtained by (a) TOF and td-TOF and (b) photo-CELIV. The data are taken from Figs. 2 and 3. Delay times are indicated at each transient. Inset (a): Room-temperature TOF transients of CGL devices with a 170- and a 100-nm-thick alt-PF8TBTT layer at a field of 1×10^7 and 5×10^6 V/m, respectively. The dotted lines represent the extension of the initial current decay with a slope of $m = -0.62$. Inset (b): Photo-CELIV transients after a 150-ns delay at 308, 287, 269, 256, and 238 K.

TABLE I. Fit parameters used for the simulation in Fig. 4.

Parameter	Description	Value
t_{trap}	Trap time	0.5 ns
E_0	Trap energy	67 meV
N_{eff}	DOTS/density of free states	0.05
μ_0	Free carrier mobility	$2.3{\cdot}10^{-3}$ $cm^2V^{-1}s^{-1}$ (TOF) $2.8{\cdot}10^{-3}$ $cm^2V^{-1}s^{-1}$ (CELIV)
a	Field activation length	1.1 nm
d	Active layer thickness	170 nm
F	Extraction field (TOF, td-TOF)	1×10^7 V/m
A'	Voltage ramp (photo-CELIV)	1.09 V/μs

introduced into the simulation by fitting the long delay time transients, while μ_0 was allowed to slightly vary until all photo-CELIV transients were accurately described with the same set of parameters. The mobility is treated as field independent, in good agreement with our measurements (see Fig. S3 of the supplementary material).[71] Every feature of the experimental photo-CELIV transients for different delay times and temperatures is reproduced by the simulation, including the pronounced shift of the current maximum with increasing delay, which resembles the power-law mobility decay shown in Fig. 2(c). The simulation also reproduced TOF and td-TOF data with the same set of parameters. Here, the current of a second device with an active layer thickness of only 100 nm is shown for comparison. This demonstrates that the MT model with an exponential trap distribution provides an excellent description of the data for all experimental techniques, temperatures, and delay times considered here. Regarding the physical meaning of the simulation parameters, the three parameters μ_0, t_{trap}, and N_{eff} do not define a unique set of parameters, meaning that a change of one of these parameters can be compensated by the other to give the same transient. Rather, it is the experimentally found trap energy E_0 that critically determines the width and tail of the photo-CELIV transients. Thus, E_0 determines not only the slope of the photocurrent decay in TOF measurements but also the primary shape of the photo-CELIV transients, which unequivocally connects the different experimental techniques investigated here by this single parameter.

The good agreement between the measured and the simulated data allows us to explore general aspects of the influence of charge carrier trapping on transient photocurrent experiments. A dominant feature of the td-TOF transients is the reduced initial slope of the current with increasing delay time, which is quite well reproduced by the simulation. The reason for this is that for a power-law decay, the rate at which mobility changes with time becomes smaller for increasing delay. Therefore, the mobility in a sample measured after prolonged delay is nearly constant on the timescale of carrier extraction, and so is the initial photocurrent in a log–log presentation. The same phenomenon should affect photo-CELIV measurements, where we observe a rather linear increase of the initial photocurrent with extraction time after long delay, indicative of a constant mobility.

Surprisingly, although the shape of the photo-CELIV transients is reproduced with great accuracy by the simulation, mobilities extracted from the photo-CELIV (and td-TOF) transients for different delays are about one order of magnitude larger than the effective mobility μ_{eff} of the charge carriers at time $t_{del} + t_{max}$. In accordance to the MT model, μ_{eff} is defined as the product of the fraction of free charge carriers times the free carrier mobility $\mu_{eff} = \mu_0 \cdot \phi$ and is obtained directly from the simulation by calculating the fraction of the mobile (free) charge concentration to the overall charge concentration, $\phi = N_{free}/(N_{free} + N_{trap})$ (black solid line in Fig. 5). Furthermore, the mobility decay in the simulation (and in the initial TOF transients) perfectly matches a power-law decay with an exponent of $m = -0.62$, while the mobility decay derived from the maximum of the photo-CELIV transients with increasing delay time is much faster (slope of $m = -0.81$, Fig. 5). We might propose that the overall larger mobility derived from the photo-CELIV experiment is due Eq. (1) assuming a constant mean carrier mobility. However, for a power-law decay, the carrier mobility might be substantially higher at the beginning of the voltage ramp than at t_{max}. To address this issue, we derived an expression for t_{max} in considering the mobility relaxation due by a MT process. For this, the time-dependent effective mobility has been parameterized by

$$\mu(t + t_{del}) = \mu_0 \cdot ((t + t_{del})/t_{trap})^{\alpha-1}. \quad (2)$$

Using the parameters from Table I, Eq. (2) perfectly resembles the effective mobility obtained from the MC simulation. The average path length s of a carrier drifting in a time-dependent electric field $E(t)$ with a time-dependent mean mobility is $s(t) = \int_0^t \mu(t' + t_{del}) \cdot E(t')dt'$. Here, extraction commences

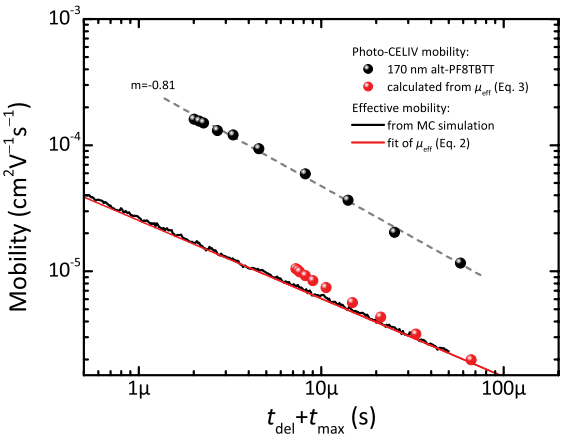

FIG. 5. (Color online) Comparison of the measured and simulated mobility relaxation. Black spheres display mobilities from measured photo-CELIV transients. The effective mobility obtained from the MC simulation is shown as a black solid line, while the solid red line displays the best fit of the time-dependent mobility to a power-law relaxation according to Eq. (2). Red spheres are the correspondent apparent photo-CELIV mobilities $\mu_{CELIV,app}$, which are obtained by applying Eq. (1) to the transit time according to Eq. (3). The dashed gray line visualizes the power-law decay of the measured mobility, where the exponent was found to be $m = -0.81$. For clarity, the simulation was performed without assuming field-activated detrapping, which is shown in Fig. 6.

at $t = 0$. This equation also contains the delay time to take into account the mobility relaxation during the delay. Assuming again, that $t = t_{tr} \cong t_{\max}$ and $s(t_{tr}) = d$ gives the following equation for $t_{\max}$:

$$\frac{d^2 \cdot t_{\text{trap}}^{\alpha-1} \cdot N_{\text{eff}}^{\alpha}}{A' \cdot \mu_0} \frac{\alpha}{1-\alpha} = (t_{\max} + t_{\text{del}})^{\alpha} t_{\max} - \frac{1}{1+\alpha} \times [(t_{\max} + t_{\text{del}})^{1+\alpha} - (t_{\text{del}})^{1+\alpha}], \quad (3)$$

which can be solved numerically for delay time. Knowing $t_{\max}$, an apparent photo-CELIV mobility $\mu_{\text{CELIV,app}}$ can be calculated from Eq. (1). This is the mobility that would be extracted by the classical photo-CELIV analysis from a photocurrent transient that is subject to mobility relaxation. Values of $\mu_{\text{CELIV,app}}$ for different delay times calculated with the simulation parameters in Table I are shown by red spheres in Fig. 5. As expected, the apparent mobility resembles the underlying time-dependent effective mobility for larger delay times, but it is slightly larger than the effective mobility, where the delay time is smaller than the transit time. This is because $\mu_{\text{CELIV,app}}$ obtained from $t_{\max}$ displays a field-averaged value over the whole extraction time. Only for delay times smaller than the transit time does a significant relaxation of the mobility take place during extraction, while for delay times higher than the transit time, the mobility is rather constant at the timescale of extraction. Even for the shortest delay time considered here (150 ns), the apparent photo-CELIV mobility is only slightly larger than the effective mobility. Therefore, we can rule out that the large difference between the mobility values extracted from our experimental photo-CELIV transients using Eq. (1) and μ_{eff} is solely caused by the power-law decrease of the mean carrier mobility.

However, the calculation according to Eqs. (1)–(3) assumes that all charge carriers have the same (mean) mobility, the same relaxation rate, and with that, the same transit time. This is far from reality for a system, where random trapping and detrapping create a wide distribution of transit times. In Fig. 6, we replotted the photo-CELIV and simulated transients from Fig. 4 on a logarithmic timescale, together with the simulated time-dependent fraction of charges that have not yet reached the extracting electrode. Clearly, the current maximum in the photo-CELIV transient at short delays appears at the moment the first charge carriers (and not the majority of carriers) leave the device. For example, at a delay of 1 μs, only 3% of the initially photoinduced charge have left the device at $t_{\max}$, and most remaining carriers are trapped ($\phi = 0.007$). In other words, the position of the current maximum after a short delay is determined by the fastest charge carriers, which have undergone only a few trapping events. Consequently, photo-CELIV and TOF strongly overestimate the effective charge carrier mobility in presence of MT.

The situation is quite different for longer delay times. Here, field-induced detrapping becomes a relevant process. The introduction of a field activation process is found to be essentially important to reproduce the current tail at the end of the extraction pulse (see also simulation results without field-induced detrapping in Fig. S4 of the supplementary material).[71] Analyzing the effective mobility in Fig. 6 shows that from a certain time on, the effective mobility starts to increase. We attribute this to the steadily increasing extraction

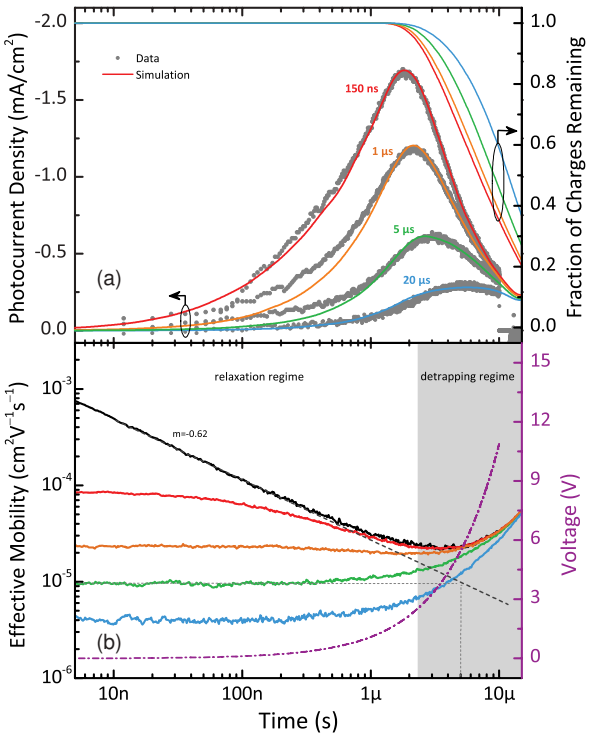

FIG. 6. (Color online) (a) Photo-CELIV (gray circles) and simulated transients (solid lines) (both left axis) together with the fraction of charges that remain in the device at time t (right axis). The abscissa is on a logarithmic scale, and $t = 0$ denotes the beginning of the extraction pulse. Colors refer to the different delay times of 0 ns (black), 150 ns (red), 1 μs (orange), 5 μs (green), and 20 μs (blue). (b) Effective mobility obtained from MC simulations for different delay times (left axis). For the effective mobility with a 0-ns delay, the fit to the linear regime in the log–log representation (dashed gray line) is also shown. It reflects the power-law mobility decay without field-activated detrapping, occurring during the delay (see also Fig. 5). This is exemplarily shown for the green curve. Here, the mobility at the beginning of the transient (starting after a 5-μs delay) is the same as for the dashed gray line at $t = 5$ μs. The time interval at which the field-activated detrapping starts to significantly increase the effective mobility is denoted as the detrapping regime. The prior time interval, where mobilities are influenced by the internal relaxation only, is denoted as the relaxation regime. The applied voltage (violet dashed–dotted line), increasing with a slope of 1.09 V/μs, is given at the right axis.

field, also displayed in Fig. 6, which increases the fraction of free charge carriers due to field-assisted detrapping. The increased mobility toward the end of the extraction pulse shifts the current maximum to later times, thus increasing $t_{\max}$. The concomitant decrease in mobility finally explains the faster power-law decay of the photo-CELIV mobility ($m = -0.81$) compared to the decay of the effective mobility ($m = -0.62$). In view of these results, TOF rather than photo-CELIV should be preferred for evaluation of characteristic trapping parameters from the current or mobility decay.

As alternatives to transient measurements, steady-state techniques are also capable of determining E_0. Figure S5 of the supplementary material[71] shows that space charge-limited

currents of alt-PF8TBTT electron-only devices[54] can be well described with a model developed by Mark and Helfrich,[55] with an exponential trap state distribution that is comparable to the one deduced from the simulation of the current transients. This further demonstrates that the processes that determine charge transport in the presence of electronic trap states are independent of the origin of the charge carriers, either injected or photogenerated, and can be consistently described within the framework of MT and release.

C. Origin of the electron traps

After having demonstrated the pronounced influence of trapping on the electron transport in alt-PF8TBTT, finding the origin of these trap states is of great interest. Because chemical impurities, e.g., residual catalyst or imperfect endcapping of polymer chains, can likely influence the charge transport of alt-PF8TBTT, we carefully revisited the synthetic procedures. For this purpose, two independent polymer batches were synthesized, from which one was further purified.[56] In addition, a third batch was provided by a collaborating laboratory. However, all three batches showed the same transport characteristics, as described in the previous section. We therefore rule out chemical impurities. This raises the question of whether trap formation is related to the specific molecular structure of the copolymer. Therefore, two different polymers with either the same polymer backbone but different side chains or the same side chain but a modified polymer backbone were synthesized. The former of these two polymers, alt-PF8/12TBTT, is a alternating PFTBTT with branched octyldodecyl side chains, while the latter, stat-PF8TBTT, contains octyl side chains and shows a partial statistical variation along the backbone (for details, see Sec. II A and Fig. 1). Here, the regular alternation of the donor and acceptor unit, as it is for alt-PF8TBTT, is disturbed by replacing a few fluorene units by TBTT segments. In Fig. 7, the photo-CELIV transients of alt-PF8/12TBTT and part-PF8TBTT CGL devices are shown for varying delay times. In contrast to the results obtained for the alt-PF8TBTT (Fig. 2), the current maximum of the two modified PFTBTT copolymers do not shift with increasing delay time. Furthermore, a distinct maximum can be observed also for high delay times of 100 μs. This means that the mobility is constant in time (at least within the observable time range from 150 ns to 100 μs). This reveals an important structure–property relationship for this type of copolymer. Emphasizing that for all polymers investigated here the synthesis, as well as the device preparation and measurement, is carried out under the same conditions, we infer that the severe mobility relaxation in alt-PF8TBTT is related to its specific molecular structure. The comparison of alt-PF8TBTT and alt-PF8/12TBTT shows that the mobility relaxation on the microsecond timescale disappears when long and branched rather than linear side chains are attached to the PFTBTT backbone. Interestingly, despite its longer side chains, alt-PF8/12TBTT exhibits significantly higher photo-CELIV mobilities than does alt-PF8TBTT. However, mobility relaxation on the timescale measured here is also suppressed when the strict alternation of the donor and acceptor unit is slightly disturbed, as seen for part-PF8TBTT. This clear correlation between the backbone structure and the specific transient transport properties rules out that the mobility relaxation observed for alt-PF8TBTT is caused to extrinsic impurities.

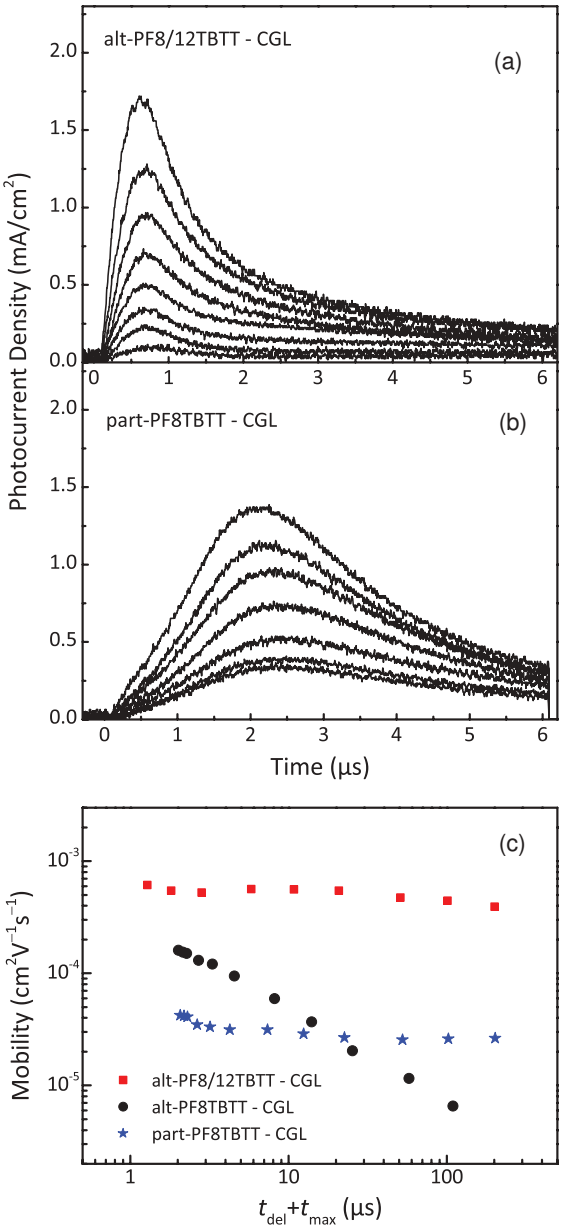

FIG. 7. (Color online) Room-temperature photo-CELIV transients at various delay times for (a) a 200-nm-thick layer of alt-PF8/12TBTT and (b) a 170-nm layer of part-PF8TBTT. In both devices, a 3-nm P3HT CGL was used. The capacitive loading current was subtracted to visualize photocurrents only. To avoid charge extraction during the delay time, a forward bias of 1.2 V was applied. (c) Mobility calculated via Eq. (1) plotted over $t_{del} + t_{max}$, together with the mobility of the alt-PF8TBTT CGL device displayed in Fig. 2.

IV. DISCUSSION

In this paper, we examine the charge transport in the donor/acceptor copolymer alt-PF8TBTT, which has been widely applied in organic solar cells. A pronounced relaxation

of the electron mobility is unambiguously proven by three transient photocurrent techniques and is the most important feature of the experiments described here. It continues over a period of at least 100 μs and is likely caused by an energetic thermalization process that follows photogeneration of free charge carriers inside the organic semiconductor.

Thermalization of photogenerated charge carriers and time-dependent mobilities has been rarely observed for conjugated polymers.[11,14–17,46,57] Österbacka *et al.* assigned the time-dependent mobility observed in regiorandom P3HT to originate from thermalization of hot, photogenerated carriers within the Gaussian DOS.[46] According to Pautmeier *et al.*, the relaxation to the thermodynamic equilibrium proceeds via a decrease in carrier mobility; however, in the case of a Gaussian DOS, it is also accompanied by a later transition to constant equilibrium mobility.[58] This so-called transition from the dispersive to nondispersive regime is predicted to shift to shorter times with increasing temperature or smaller energetic disorder, but this effect has, to best of our knowledge, not yet been observed for conjugated polymers. Recently, we showed that recombination of photogenerated charges at high carrier densities can alter photo-CELIV current transients and lead to an apparent time dependence of the CELIV mobility.[40] As the shapes of our photo-CELIV transients are independent of intensity, recombination phenomena during extraction are expected to be insignificant (see Figs. S6 and S7 of the supplementary material[71]).[59]

A model that is able to describe the continuous mobility relaxation as observed here is MT formalism, which was theoretically described by Orenstein and Kastner for an exponential DOTS.[13,60] Beside the ongoing mobility decrease, direct evidence for MT comes from the power-law decay of the TOF transients on timescales less than the transit time. To further support this, MC simulations of MT in one dimension were performed. These simulations reproduce the power-law decay of the effective mobility. Furthermore, experimental transients of several techniques and for various parameters (delay time and temperature) can be described with a single set of parameters. Thus, we are able to explain the anomalous shape of photo-CELIV transients entirely by MT, acting on the transport of a single charge carrier type only.

Our results also allow us to speculate about the origin of electron traps in the alt-PF8TBTT copolymer. Chemical defects that act as electronic trap states, i.e., hydrated oxygen complexes, were recently proposed by Nicolai *et al.* to rationalize widely observed trap-limited electron currents in many semiconducting polymers, including alt-PF10TBTT.[61] Furthermore, Kuik *et al.* demonstrated that the prominent keto defect in poly(9,9-dioctylfluorene) (PF8),[62,63] created through oxidation of a fluorene monomer, also acts as efficient electron trap.[64] However, these authors already observe a trap-dominated electron current for defect-free PF8. In contrast, the results of the previous section show that rather small changes of the molecular structure of either the side chains or the backbone of the PFTBTT copolymer investigated here causes the disappearance of the mobility relaxation, making it unlikely that the electron traps are originating from doping, chemical defects, or impurities. Thus, we suppose that in our case, the electron traps causing the mobility relaxation in alt-PF8TBTT must be related to the microscopic morphology or the molecular design of the copolymer itself. It was recently noted that solar cells of the high-performance donor material poly[N-9′-hepta-decanyl-2,7-carbazole-alt-5,5-(4′,7′-di-2-thienyl-2′,1′,3′-benzothiadiazole)] (PCDTBT) may suffer from significant intrinsic trapping of free charge carriers, introduced by morphological changes of the PCDTBT phase.[65,66] Here, we note the great chemical similarity of PCDTBT and alt-PF8TBTT, only differing by two atoms (the nitrogen or carbon atom at the bridge position of the carbazole or fluorene monomer, respectively, and an additional carbon atom that mediates the dioctyl substitution with the bridging nitrogen atom in PCDTBT). Through measurement of the paracrystalline disorder and in combination with density functional theory-based molecular simulations, a connection between the microscopic morphology and the development of exponentially distributed trap states was also recently proposed by Rivnay *et al.*[67]

An alternative explanation for the particular trapping properties of alt-PF8TBTT arises from work by Dieckmann *et al.* These authors showed that the electrostatic interactions of transport sites and randomly oriented dipoles can cause a significant broadening of the DOS.[68] Such permanent dipoles might be created via intermolecular coulombic interactions between the electron-attracting TBTT (acceptor) unit and the electron-withdrawing fluorene (donor) group of neighboring chains, driven by π–π stacking. A particularly favorable situation would occur if neighboring chains in a stack were shifted by half a repeat unit, a pattern that may be introduced due to the sp^3 hybridization of the side chain-containing bridging atom, which forces the side chains to stick out of the plane of the polymer backbone.[21] The regular donor/acceptor stacking and the proximity of neighboring chains might be altered by attaching longer side chains (as in alt-PF8/12TBTT) or by disturbing the regular alternation of donor and acceptor units along the backbone (as in part-PF8TBTT). In this context, other dioctyl-substituted fluorene copolymers show pronounced electron trapping. Namely, electron trapping is demonstrated for pure poly(9,9′-dioctylfluorene-co-benzothiadiazole),[47,54] F8TBT,[29,30] and finally, in this study, for alt-PF8TBTT. In contrast copolymers that perform best in devices carry longer or branched substituents.[19–21,23,69,70]

V. CONCLUSIONS

We performed various transient photocurrent experiments on a model donor/acceptor copolymer. Our measurements reveal time-dependent electron mobility. The origin of the strong mobility relaxation was identified by a multiple trapping model–based MC simulation and is explained by the significant trapping of electrons. It is further demonstrated that the electron trapping has a severe influence on the shape of the current transients. Chemical modifications of the polymers structure revealed the origin of the electron trapping to be related to the molecular structure, specific morphology, or both of the copolymer. Our results show that small changes of the molecular design of donor/acceptor copolymers can introduce electronic trap states with severe impact on their charge transport properties.

ACKNOWLEDGMENTS

The authors thank Sylvia Janietz (Frauenhofer Institute for Applied Polymer Research, Potsdam) for providing a batch of alt-PF8TBTT, and Heinz Bässler and Anna Köhler for directing our attention to the influence of dipolar interactions on charge transport. We also acknowledge laboratory assistance by Steffen Roland. M.S. and E.P. acknowledge funding by the German Research Foundation within Priority Program No. SPP 1355.

[1]H. Bässler, Phys. Status Solidi B **175**, 15 (1993).
[2]T. Tiedje and A. Rose, Solid State Comm. **37**, 49 (1981).
[3]P. W. M. Blom and M. Vissenberg, Mater. Sci. Eng. R Rep. **27**, 53 (2000).
[4]C. Tanase, E. J. Meijer, P. W. M. Blom, and D. M. de Leeuw, Phys. Rev. Lett. **91**, 216601 (2003).
[5]W. F. Pasveer, J. Cottaar, C. Tanase, R. Coehoorn, P. A. Bobbert, P. W. M. Blom, D. M. de Leeuw, and M. A. J. Michels, Phys. Rev. Lett. **94**, 206601 (2005).
[6]V. I. Arkhipov, P. Heremans, E. V. Emelianova, and H. Bässler, Phys. Rev. B **71**, 045214 (2005).
[7]R. Coehoorn, W. F. Pasveer, P. A. Bobbert, and M. A. J. Michels, Phys. Rev. B **72**, 155206 (2005).
[8]I. Lange, J. C. Blakesley, J. Frisch, A. Vollmer, N. Koch, and D. Neher, Phys. Rev. Lett. **106**, 216402 (2011).
[9]J. Hwang, E. G. Kim, J. Liu, J. L. Bredas, A. Duggal, and A. Kahn, J. Phys. Chem. C **111**, 1378 (2007).
[10]P. M. Borsenberger, L. Pautmeier, and H. Bässler, J. Chem. Phys. **94**, 5447 (1991).
[11]A. J. Mozer, G. Dennler, N. S. Sariciftci, M. Westerling, A. Pivrikas, R. Österbacka, and G. Juška, Phys. Rev. B **72**, 035217 (2005).
[12]R. U. A. Khan, D. Poplavskyy, T. Kreouzis, and D. D. C. Bradley, Phys. Rev. B **75**, 035215 (2007).
[13]J. Orenstein and M. Kastner, Phys. Rev. Lett. **46**, 1421 (1981).
[14]A. Devizis, A. Serbenta, K. Meerholz, D. Hertel, and V. Gulbinas, Phys. Rev. Lett. **103**, 027404 (2009).
[15]A. Devizis, K. Meerholz, D. Hertel, and V. Gulbinas, Phys. Rev. B **82**, 155204 (2010).
[16]A. Pivrikas, P. Stadler, H. Neugebauer, and N. S. Sariciftci, Org. Electron. **9**, 775 (2008).
[17]M. Schubert, R. Steyrleuthner, S. Bange, A. Sellinger, and D. Neher, Phys. Status Solidi A **206**, 2743 (2009).
[18]M. Svensson, F. L. Zhang, S. C. Veenstra, W. J. H. Verhees, J. C. Hummelen, J. M. Kroon, O. Inganäs, and M. R. Andersson, Adv. Mater. **15**, 988 (2003).
[19]L. H. Slooff, S. C. Veenstra, J. M. Kroon, D. J. D. Moet, J. Sweelssen, and M. M. Koetse, Appl. Phys. Lett. **90**, 143506 (2007).
[20]M. H. Chen, J. Hou, Z. Hong, G. Yang, S. Sista, L. M. Chen, and Y. Yang, Adv. Mater. **21**, 4238 (2009).
[21]J. Liu, H. Choi, J. Y. Kim, C. Bailey, M. Durstock, and L. Dai, Adv. Mater. **24**, 538 (2011).
[22]D. Veldman, S. C. J. Meskers, and R. A. J. Janssen, Adv. Funct. Mater. **19**, 1939 (2009).
[23]D. Mori, H. Benten, J. Kosaka, H. Ohkita, S. Ito, and K. Miyake, ACS Appl. Mater. Interfac. **3**, 2924 (2011).
[24]X. M. He, F. Gao, G. L. Tu, D. Hasko, S. Huttner, U. Steiner, N. C. Greenham, R. H. Friend, and W. T. S. Huck, Nano Lett. **10**, 1302 (2010).
[25]M. Koppe, H. J. Egelhaaf, G. Dennler, M. C. Scharber, C. J. Brabec, P. Schilinsky, and C. N. Hoth, Adv. Funct. Mater. **20**, 338 (2010).
[26]C. Muller, E. G. Wang, L. M. Andersson, K. Tvingstedt, Y. Zhou, M. R. Andersson, and O. Inganäs, Adv. Funct. Mater. **20**, 2124 (2010).
[27]D. J. D. Moet, M. Lenes, J. D. Kotlarski, S. C. Veenstra, J. Sweelssen, M. M. Koetse, B. de Boer, and P. W. M. Blom, Org. Electron. **10**, 1275 (2009).
[28]C. R. McNeill and N. C. Greenham, Appl. Phys. Lett. **93**, 203310 (2008).
[29]I. Hwang, C. R. McNeill, and N. C. Greenham, J. Appl. Phys. **106**, 094506 (2009).
[30]Z. Li, F. Gao, N. C. Greenham, and C. R. McNeill, Adv. Funct. Mater. **21**, 1419 (2011).
[31]J. A. Letizia, M. R. Salata, C. M. Tribout, A. Facchetti, M. A. Ratner, and T. J. Marks, J. Am. Chem. Soc. **130**, 9679 (2008).
[32]R. C. Mulherin, S. Jung, S. Huettner, K. Johnson, P. Kohn, M. Sommer, S. Allard, U. Scherf, and N. C. Greenham, Nano Lett. **11**, 4846 (2011).
[33]H.-G. Nothofer, Flüssigkristalline Polyfluorene, Dissertation, University of Potsdam, Potsdam, http://opus.kobv.de/ubp/volltexte/2005/24/ (2001).
[34]V. P. Baillargeon and J. K. Stille, J. Am. Chem. Soc. **108**, 452 (1986).
[35]J. H. Li, Y. Liang, D. P. Wang, W. J. Liu, Y. X. Xie, and D. L. Yin, J. Org. Chem. **70**, 2832 (2005).
[36]S. Ellinger, U. Ziener, U. Thewalt, K. Landfester, and M. Moller, Chem. Mat. **19**, 1070 (2007).
[37]L. L. Chua, J. Zaumseil, J. F. Chang, E. C. W. Ou, P. K. H. Ho, H. Sirringhaus, and R. H. Friend, Nature **434**, 194 (2005).
[38]C. Yin, B. Pieper, B. Stiller, T. Kietzke, and D. Neher, Appl. Phys. Lett. **90**, 133502 (2007).
[39]D. M. Huang, S. A. Mauger, S. Friedrich, S. J. George, D. Dumitriu-LaGrange, S. Yoon, and A. J. Moule, Adv. Funct. Mater. **21**, 1657 (2011).
[40]S. Bange, M. Schubert, and D. Neher, Phys. Rev. B **81**, 035209 (2010).
[41]N. Metropolis and S. Ulam, J. Am. Stat. Assoc. **44**, 335 (1949).
[42]A. Miller and E. Abrahams, Phys. Rev. **120**, 745 (1960).
[43]L. M. Andersson, F. L. Zhang, and O. Inganäs, Appl. Phys. Lett. **91**, 071108 (2007).
[44]C. R. McNeill, A. Abrusci, J. Zaumseil, R. Wilson, M. J. McKiernan, J. H. Burroughes, J. J. M. Halls, N. C. Greenham, and R. H. Friend, Appl. Phys. Lett. **90**, 193506 (2007).
[45]G. Juška, K. Arlauskas, M. Viliunas, K. Genevicius, R. Österbacka, and H. Stubb, Phys. Rev. B **62**, R16235 (2000).
[46]R. Österbacka, A. Pivrikas, G. Juška, K. Genevicius, K. Arlauskas, and H. Stubb, Curr. Appl. Phys. **4**, 534 (2004).
[47]G. C. Faria, R. M. Faria, E. R. deAzevedo, and H. von Seggern, J. Phys. Chem. C **115**, 25479 (2011).
[48]G. Juška, K. Arlauskas, M. Viliunas, and J. Kocka, Phys. Rev. Lett. **84**, 4946 (2000).

[49]C. Deibel, A. Wagenpfahl, and V. Dyakonov, Phys. Rev. B **80**, 075203 (2009).
[50]D. Hertel and H. Bässler, ChemPhysChem **9**, 666 (2008).
[51]J. Frisch, M. Schubert, E. Preis, J. P. Rabe, D. Neher, U. Scherf, and N. Koch, J. Mater. Chem. **22**, 4418 (2012).
[52]J. Kniepert, M. Schubert, J. C. Blakesley, and D. Neher, J. Phys. Chem. Lett. **2**, 700 (2011).
[53]A. Kumar, M. A. Baklar, K. Scott, T. Kreouzis, and N. Stingelin-Stutzmann, Adv. Mater. **21**, 4447 (2009).
[54]R. Steyrleuthner, S. Bange, and D. Neher, J. Appl. Phys. **105**, 064509 (2009).
[55]P. Mark and W. Helfrich, J. Appl. Phys. **33**, 205 (1962).
[56]Z. Zhu, D. Waller, R. Gaudiana, M. Morana, D. Muhlbacher, M. Scharber, and C. Brabec, Macromolecules **40**, 1981 (2007).
[57]W. C. Germs, J. J. M. van der Holst, S. L. M. van Mensfoort, P. A. Bobbert, and R. Coehoorn, Phys. Rev. B **84**, 165210 (2011).
[58]L. Pautmeier, R. Richert, and H. Bässler, Philos. Mag. Lett. **59**, 325 (1989).
[59]G. Juška, N. Nekrasas, V. Valentinavicius, P. Meredith, and A. Pivrikas, Phys. Rev. B **84**, 155202 (2011).
[60]J. Orenstein and M. A. Kastner, Solid State Comm. **40**, 85 (1981).
[61]H. T. Nicolai, M. Kuik, G. A. H. Wetzelaer, B. de Boer, C. Campbell, C. Risko, J. L. Brédas, and P. W. M. Blom, Nat. Mater. **11**, 882 (2012).
[62]U. Scherf and E. J. W. List, Adv. Mater. **14**, 477 (2002).
[63]E. Zojer, A. Pogantsch, E. Hennebicq, D. Beljonne, J. L. Bredas, P. S. de Freitas, U. Scherf, and E. J. W. List, J. Chem. Phys. **117**, 6794 (2002).
[64]M. Kuik, G. Wetzelaer, J. G. Ladde, H. T. Nicolai, J. Wildeman, J. Sweelssen, and P. W. M. Blom, Adv. Funct. Mater. **21**, 4502 (2011).
[65]Z. M. Beiley, E. T. Hoke, R. Noriega, J. Dacuna, G. F. Burkhard, J. A. Bartelt, A. Salleo, M. F. Toney, and M. D. McGehee, Adv. Energy Mater. **1**, 954 (2011).
[66]T. M. Clarke, J. Peet, A. Nattestad, N. Drolet, G. Dennler, C. Lungenschmied, M. Leclerc, and A. J. Mozer, Org. Electron. **13**, 2639 (2012).
[67]J. Rivnay, R. Noriega, J. E. Northrup, R. J. Kline, M. F. Toney, and A. Salleo, Phys. Rev. B **83**, 121306 (2011).
[68]A. Dieckmann, H. Bässler, and P. M. Borsenberger, J. Chem. Phys. **99**, 8136 (1993).
[69]D. Veldman, O. Ipek, S. C. J. Meskers, J. Sweelssen, M. M. Koetse, S. C. Veenstra, J. M. Kroon, S. S. van Bavel, J. Loos, and R. A. J. Janssen, J. Am. Chem. Soc. **130**, 7721 (2008).
[70]J. Gilot, M. M. Wienk, and R. A. J. Janssen, Adv. Mater. **22**, E67 (2010).
[71]See Supplemental Material at http://link.aps.org/supplemental/10.1103/PhysRevB.87.024203 for additional experimental data.

Supplemental Material

Mobility relaxation and electron trapping in a donor/acceptor-type copolymer

Marcel Schubert[1], Eduard Preis[2], James C. Blakesley[1], Patrick Pingel[1], Ullrich Scherf[2], Dieter Neher[1]

1. University of Potsdam, Institute of Physics and Astronomy, Karl-Liebknecht-Str. 24-25, 14467 Potsdam, Germany
2. Bergische University Wuppertal, Macromolecular Chemistry, 42119 Wuppertal, Germany

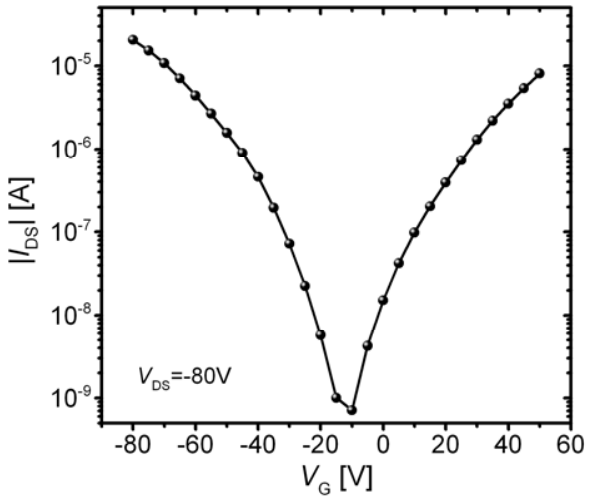

S1. Transfer characteristic of a alt-PF8TBTT bottom gate field effect transistor at a source-drain voltage of -80 V. Thermally grown and HMDS treated SiO_2 on top of a Si substrate served as the gate dielectric, while 100 nm gold was used for the source and drain electrode. It has been shown that n-type transport in bottom-gate OFET structures can be realized for a wide variety of conjugated polymers if the surface of the widely used SiO_2 gate dielectric, which contains a high number of intrinsic electron traps, is treated in a proper way.[37] As the measurements of Inganäs and co-workers were carried out on bare SiO_2,[26, 43] electron transport along the semiconductor/insulator interface might have been disturbed by these traps. We note that the electron mobility may be even higher with optimized gate dielectrics.

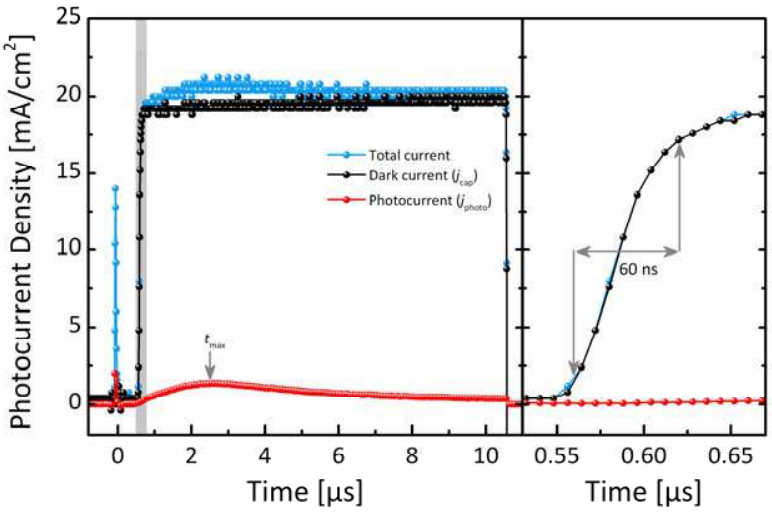

S2. (left) Typical Photo-CELIV transients in the dark (black) and 550 ns after illumination (blue) with a 6 ns laser pulse. The difference between total and dark current is denoted as photocurrent (red). The arrival of the laser pulse at t=0 is visible but no current is flowing during the delay time which demonstrates the accurate setting of the built in voltage. The rectangular shape of the capacitive loading current also demonstrates that injection of charge carriers is negligible even at very high extraction voltages. (right) Zoom into the beginning of the voltage pulse (gray area in the left figure). Time to go from 10% to 90% of the capacitive current is approximately 60 ns, while fastest observed t_{max} is about 1.8 µs. The low resolution of the dark and total current originates from data processing. The oscilloscope digitizes the signals with 8 bit vertical resolution for the full display scale. Further internal calculations such as averaging and subtraction of traces are performed with 12 bit resolution. In order to improve data quality, first the dark current gets measured several times and averaged internally. After that the light current (total current) is measured and the photocurrent is calculated by subtracting the averaged dark current from the light transients. The photocurrent is then displayed at screen filling vertical resolution before transfer (at 8 bit resolution). Effectively, the photocurrent gets digitized at a much higher

resolution, thus it shows markedly less conversion artefacts compared to the raw light and dark transients.

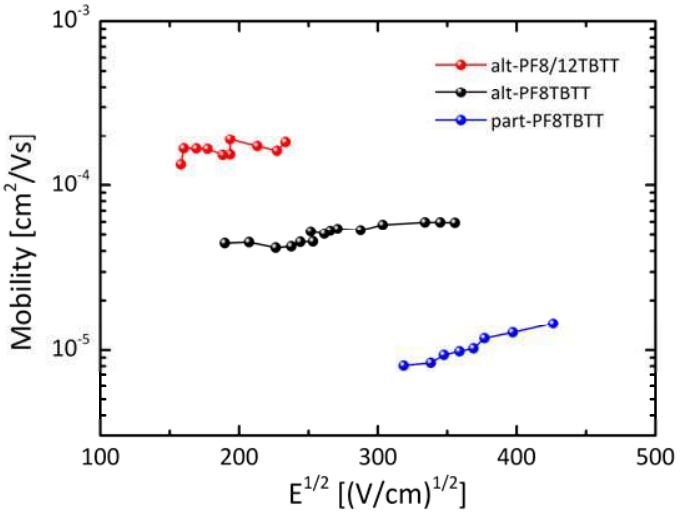

S3. Field-dependence of the electron mobility for the three copolymers investigated here, determined with Photo-CELIV. The devices were the same as described in the main text and measurements were performed with a short delay time of 0.5 µs. A weak field-dependence is observed only for part-PF8TBTT.

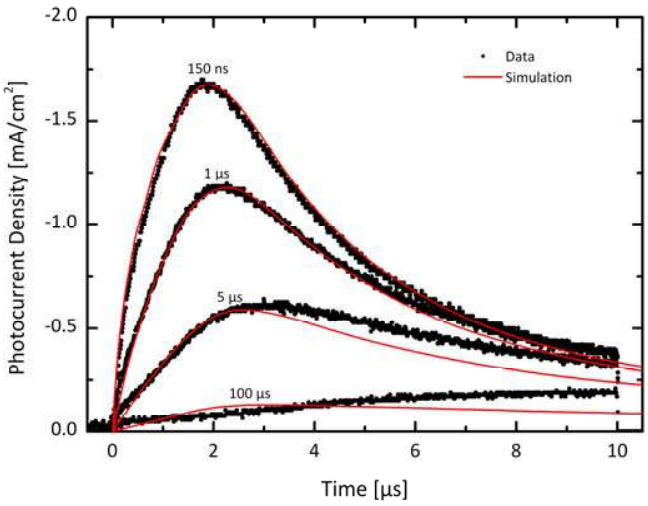

S4. Experimental Photo-CELIV transients of the 170 nm thick alt-PF8TBTT device as displayed in Fig. 2, Fig. 4 and Fig.6 of the main text. Here, the simulation was performed without field-dependent detrapping, while all trapping parameters were identical to those used in the simulation presented in Fig. 4 of the main text. Only the free carrier mobility was slightly varied ($2.5 \cdot 10^{-3}$ $cm^2 V^{-1} s^{-1}$). It is obvious that detrapping of charge carriers is of crucial importance to describe the transients after a long delay time and at the end of the extraction pulse, and that this detrapping must be field-assisted.

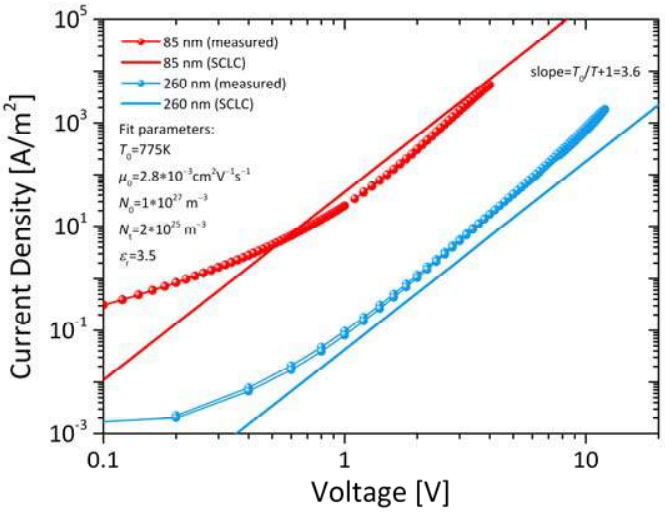

S5. Electron-only currents as function of applied voltage (red and blue spheres). The structure of the single carrier devices was ITO/PEDOT/Al/alt-PF8TBTT/Sm/Al. Injection was from the samarium (Sm) top-electrode, while the aluminium (Al) bottom-contact served as hole-blocking contact. Solid lines correspond to solutions of Eq. 1 with the parameters indicated in the graph. Space charge limited conductance in the presence of an exponential trap state distribution has been treated by Mark and Hellfrich and was experimentally observed for a variety of conjugated polymers. Within this model, the current is given by:[55]

$$J = eN_0\mu_0\left(\frac{l}{l+1}\frac{\varepsilon_0\varepsilon_r}{eN_t}\right)^l\left(\frac{2l+1}{l+1}\right)^{l+1}\frac{V^{l+1}}{d^{2l+1}} \qquad (l = T_0/T), \qquad (1)$$

where V is the applied voltage, ε_0 the permittivity of free space and ε_r the dielectric constant. The other parameters have the same meaning as described above. Despite small deviations between the model and the measured current, the current-voltage characteristics can be well described by Eq. 1, when similar parameters as for the simulation of the current transients were used. Especially, the slope of the current versus voltage, which only depends on the trap temperature (slope = $T_0/T+1$), is rather well reproduced by the value T_0 = 775K (corresponding to E_0 = 67 meV) derived from the transient experiments.

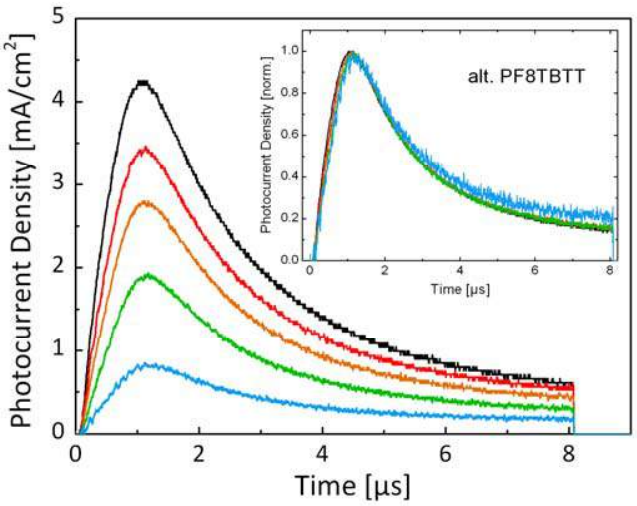

S6. Room temperature photo-CELIV transients at various excitation intensities measured for an alt-PF8TBTT CGL device. The capacitive loading current j_{cap} was subtracted to visualize photocurrents only. The inset shows normalized transients to demonstrate the intensity-independent shape of the photocurrents.

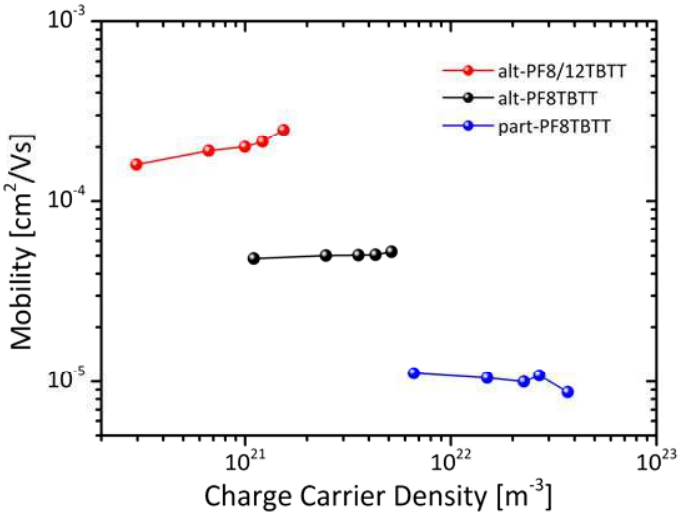

S7. Charge carrier density-dependence of the electron mobility for the three copolymers investigated here, extracted from intensity modulated Photo-CELIV experiments. Again, measurements were performed with a very short delay of 0.5 µs.

References

[37] L. L. Chua, J. Zaumseil, J. F. Chang, E. C. W. Ou, P. K. H. Ho, H. Sirringhaus, and R. H. Friend, Nature **434**, 194 (2005).

[26] C. Muller, E. G. Wang, L. M. Andersson, K. Tvingstedt, Y. Zhou, M. R. Andersson, and O. Inganas, Adv. Funct. Mater. **20**, 2124 (2010).

[43] L. M. Andersson, F. L. Zhang, and O. Inganas, Appl. Phys. Lett. **91**, 071108 (2007).

[55] P. Mark and W. Helfrich, J. Appl. Phys. **33**, 205 (1962).

ADVANCED MATERIALS
www.advmat.de

Bulk Electron Transport and Charge Injection in a High Mobility n-Type Semiconducting Polymer

By *Robert Steyrleuthner, Marcel Schubert, Frank Jaiser, James C. Blakesley, Zhihua Chen, Antonio Facchetti,* and *Dieter Neher**

Understanding charge injection mechanisms and charge transport in organic semiconductors is of fundamental importance for the further advancement of electronic and optoelectronic devices. The charge-carrier mobility (μ) is one of the key performance parameters of organic-semiconductor-based functional devices such as light-emitting diodes (OLEDs), field-effect transistors (OFETs) or solar cells (OSCs). Organic semiconductor charge-carrier mobility is often several orders of magnitude lower than in their inorganic counterparts and frequently is a limiting factor affecting the rate of charge injection from the device contacts, charge recombination, and photogeneration.[1–3] Several studies have addressed how the semiconductor molecule/polymer chemical structure influence charge transport properties. However, several questions remain addressing how charges flow from the electrical contact to the semiconducting material, particularly in electron-transporting polymers.

It is well-known that the electronic structure of π-conjugated polymers can be tuned by the introduction of substituents with different electronegativity.[4] The majority of conjugated polymers are hole-transporting (p-type), meaning that they can accept and transport holes efficiently, whereas the development of efficient electron-transporting (n-type) polymers has been far more challenging. Holes are often the dominant charge carriers in several functional devices,[5–6] although no fundamental reason for the superiority of hole versus electron transport in the bulk of organic semiconductors is known.[7] Reduced electron currents in organic semiconductors are usually attributed to the presence of trap states distributed energetically below the lowest occupied molecular orbital (LUMO).[6,8–9] De Leeuw et al. pointed out that conducting polymers with an electron affinity lower than ~3 eV have a strong tendency to be oxidized by oxygen and water.[10] Such oxidative processes are known to create electron-accepting units.[11–14] Additionally, the formation of electron-accepting defects during synthesis, device fabrication, and measurement, even in controlled atmosphere, might be one of the major reasons for the common observation of trap-limited electron transport. Consequently, polymeric structures with increased electron affinity should dramatically reduce the trap density in order to enable efficient electron transport.[15]

In 2005 Chua et al. demonstrated comparable electron and hole field-effect mobilities under inert atmosphere for conjugated polymers thought to be exclusively p-type in OFET devices.[16] Several π-conjugated polymers have been specifically designed to be n-type, however, in OFETs the electron mobilities (μ_{FET}) are in the range of 0.001-0.1 cm^2/Vs, typically in vacuum conditions.[17–20] Recently, a novel electron-transporting polymer based on a naphthalene diimide core (Polyera ActivInk N2200) exhibited μ_{FET} values of up to 0.85 cm^2/Vs in ambient conditions.[21] In addition to the high μ_{FET}, the location of the LUMO at ~4 eV and an optical bandgap of 1.45 eV[21] make N2200 a promising candidate for other electronic devices.[22]

In OFETs, charge transport occurs exclusively parallel to the semiconductor layer within a narrow sheet at the interface with the gate insulator. In addition, when the devices are operating, the OFET charge-carrier density in the active layer is typically very high in comparison to those of OLEDs and OSCs. The charge-carrier density difference between these types of devices is often used to explain the discrepancy between the mobility determined from charge-only space-charge limited current (SCLC) measurements and the field-effect mobility,[23] the latter known to be orders of magnitude higher. The effect of carrier density on mobility can be quantitatively understood in the framework of the Gaussian disorder model (GDM). In particular, localized states in the tail of the density of states, which might function as carrier traps at low carrier densities, will be permanently occupied at high carrier densities. Consequently, charge-carrier mobilities measured in OFETs might be rather insignificant when considering bulk carrier transport at low carrier densities, e.g. in OLED and OSC devices. Time-of-flight (TOF) and electron-only current measurements are mostly used to study electron transport perpendicular to the layer plane at low carrier concentrations, thus relevant to bulk processes. Unfortunately, electron-only devices often suffer from negative differential resistance effects which hinder the consistent analysis of the current/voltage characteristics. We have recently discussed the experimental difficulties related to the NDR effect and explained the origins of this effect.[8] In addition, a reliable method for the fabrication of electron-only devices was presented. Using this approach we showed the field- and temperature dependence of the space-charge limited electron current (J_{SCL}) in two well known n-type polymers to be determined by an exponential distribution of electron trap states.

In this paper we report the first measurements on the bulk electron transport in N2200. Time-of-flight experiments yielded a room temperature mobility of ca. 5×10^{-3} cm^2/Vs, which is

[*] R. Steyrleuthner, M. Schubert, Dr. F. Jaiser, Dr. J. C. Blakesley, Prof. D. Neher
Institut für Physik und Astronomie, Universität Potsdam
Karl-Liebknecht-Straße 24-25, 14476 Potsdam (Germany)
Email: neher@uni-potsdam.de
Z. Chen, Prof. A. Facchetti
Polyera Corporation, 8045 Lamon Avenue, Illinois 60077 (USA)

DOI: 10.1002/adma.201000232

the largest value yet reported for the electron mobility of a conjugated polymer. Clearly, this result highlights the potential usage of this new polymer for applications that rely on efficient bulk electron transport. To our surprise, the current through electron-only devices with different cathode materials was injection-limited throughout a wide range of thicknesses, despite the low LUMO level of 4.0 eV. This raises severe concerns regarding the general applicability of metal contacts for efficient electron injection into polymers with high electron mobility.

Electron-only devices based on N2200 were fabricated for a wide range of semiconductor layer thicknesses (d = 80-1300 nm) following the approach published in Ref [8]. Current-voltage (J-V) characteristics of devices comprising a flat aluminum (Al) bottom electrode on poly(3,4-ethylenedioxythiophene):poly (styrenesolfonate) (PEDOT:PSS) and a barium (Ba) top contact are shown in **Figure 1b**. Due to the low lying LUMO of N2200 and the disregardance of any interface effects, such as Fermi-level-pinning,[24–25] one expects ohmic electron injection, as anticipated for most low workfunction metals.

The current-voltage characteristics in Figure 1b show that N2200-based devices exhibit far higher currents when compared with electron-only currents in layers of PPV-derivates and polyfluorene copolymers of comparable thickness.[6,8] Furthermore, hysteresis effects observed earlier for different polymers at low voltages are not observed (not shown here). In the N2200-based devices the current increases superlinearly with the voltage, except for the smallest layer thickness at low bias. Such nonlinear dependencies are characteristic for injection- or space-charge-limited currents. In fact, the currents at high electric fields follow roughly a quadratic dependence on the bias, as predicted for trap-free SCL transport. Recently, trap-free SCL electron transport was claimed in a study on a related polymer.[26]

A distinguishing feature between SCL and injection-limited currents is the scaling of the current with the thickness of the

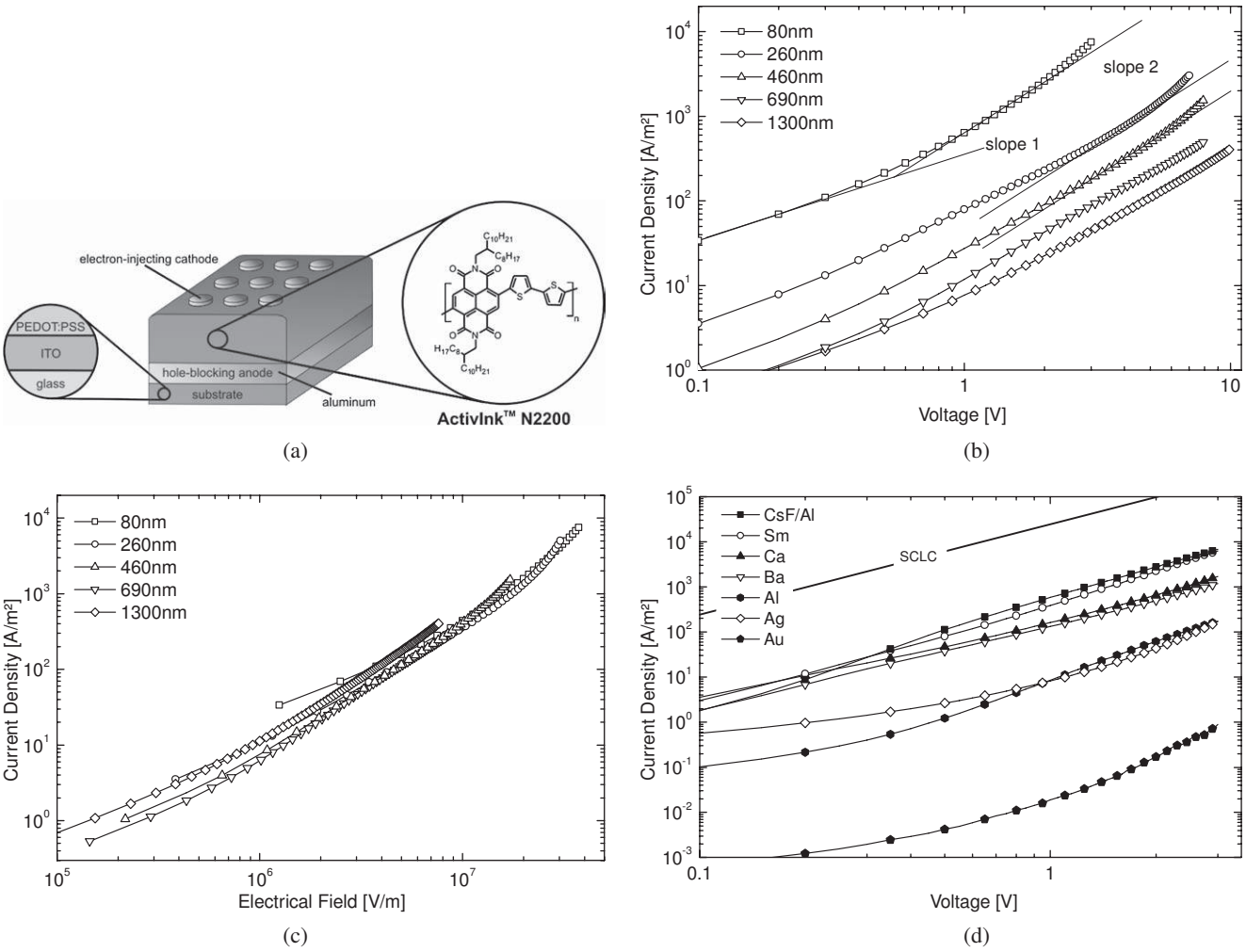

Figure 1. a) Schematic illustration of an electron-only device used to investigate the charge transport of the conjugated n-type polymer N2200 used in this work. PEDOT:PSS is used as a smoothing layer for the hole-blocking bottom aluminum anode to avoid negative differential resistance effects.[8] b) J-V characteristics of N2200 electron-only devices with a barium cathode for several N2200 layer thicknesses. c) J-E characteristics of N2200 electron-only devices with barium cathode for several layer thicknesses. d) J-V characteristics of N2200 electron-only devices (d = 85 nm) with different electron-injecting top electrodes. The straight line shows the expected current according to the Mott-Gurney law using the average TOF-mobility ($\mu_{TOF} = 5 \times 10^{-3}$ cm^2/Vs, vide infra).

active polymer layer.[27] SCL-theories predict that the current-density (J) at a given electric field (E) decreases with increasing layer thickness (d) according to a simple power law:

$$J(E) \propto d^{-l}, \tag{1}$$

where $l = 1$ in the trap-free space charge transport regime[28] and $l > 1$ in the case of trapping.[29] For most n-type polymers, high values of l, ranging typically between 3 and 5, have been reported.[8] In contrast, common models describing charge injection into organic layers predict the injection rates to depend explicitly on E but not on d[1,30–31]:

$$J(E) \neq f(d). \tag{2}$$

Surprisingly, the J-V characteristics measured for N2200 electron-only devices with very different polymer layer thicknesses (see Figure 1b) fall onto a single curve when plotted as a function of E (**Figure 1c**). Evidentially, the current is limited by either electron injection from the Ba cathode into the organic layer or by the extraction at the bottom electrode for all layer thicknesses.

To understand whether charge injection or extraction imposes the major limitation to the electron-only current, we varied the cathode material of the injecting electrode for a wide range of workfunctions. The investigated top electrodes are cesium fluoride (CsF), samarium (Sm), barium, calcium (Ca), all capped with aluminum, pure aluminum, silver (Ag) and gold (Au), in order of increasing workfunction. **Figure 1d** shows the electron-only current increases by several orders of magnitude when the workfunction is decreased from ~ 5.0 eV (for Au) to ~ 2.7 eV (for Sm). Moreover, J increases considerably when going from Ba (or Ca) to Sm (or CsF/Al). This result demonstrates the current-voltage characteristics shown in Figure 1b and 1c for Ba top electrodes are severely injection limited. In the Supporting Information the dependence of the injection current on the nominal workfunction of the evaporated cathodes is shown, which clearly does not follow the Schottky-type thermionic emission model. This behavior was observed previously for injection into disordered systems[32] and is an indication for strong Fermi-level-pinning at localized surface states.[24–25]

In order to address the bulk transport properties, time-of-flight (TOF) experiments were performed for devices with a structure of: ITO/PEDOT/PFB/N2200/Ba/Al/encapsulation. Experimental details can be found in Ref [33]. In our work, light was incident through the transparent ITO/PEDOT:PSS bottom contact, which was negatively biased. In order to reduce the leakage current, a ca. 2 nm thick PFB-interlayer with HOMO and LUMO energies of 2 eV and 4.9 eV, respectively, was formed on top of PEDOT:PSS.[34] **Figure 2** shows typical TOF electron transient measurements for a 5200 nm thick N2200 layer. In general, it can be seen that the electron transport appears dispersive with weak field dependence. The TOF mobility (μ_{TOF}) can be expressed by the equation

$$\mu_{TOF} = \frac{d^2}{t_{1/2}V} \tag{3}$$

where $t_{1/2}$ is the time at which the current has decreased to the half of the value at the inflection point. It has been shown that

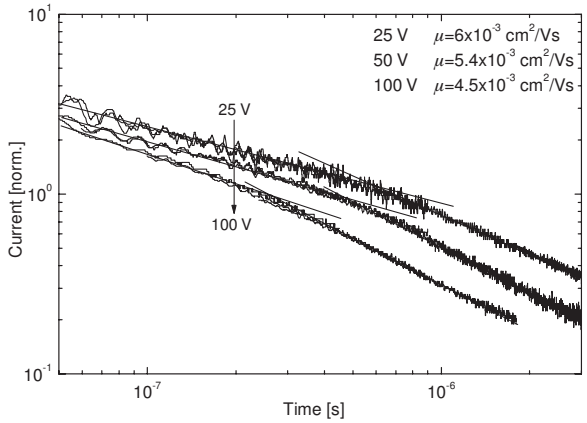

Figure 2. Time-of-flight transients of N2200 with 5200 nm layer thickness at various electric fields (normalized to the current at the inflection point).

the use of $t_{1/2}$ yields mobilities which are well comparable to values determined from dark-injection and steady-state current measurements.[35] Within the accuracy of our experiment μ_{TOF} is ~ 5×10^{-3} cm^2/Vs and nearly independent of the electric field. To the best of our knowledge this is the highest room temperature electron mobility yet reported for a conjugated polymer in TOF experiments.[33,36–37]

The space-charge limited electron current according to the Mott–Gurney equation is given by

$$J_{SCL} = \frac{9}{8}\varepsilon_0\varepsilon_r\mu\frac{V^2}{d^3} \tag{4}$$

in the case of trap-free space-charge limited transport. By using the experimentally determined TOF-mobility the calculated electron current is also shown in Figure 1d. It can be seen the predicted transport-limited current is almost two orders of magnitude larger than measured for the best injecting, low workfunction electrodes, Sm or CsF/Al, and exceeds the currents achieved with Ba or Ca by almost three orders of magnitude. This suggests the presence of severe injection barriers for all cathode materials.

The data measured at different temperatures for electron-only devices with Ba cathode are shown in **Figure 3**. This analysis affords an activation energy of ~ 0.25 eV, which is independent of the bias. Unfortunately, accurate conclusions regarding barrier heights are difficult to draw from these experiments as the temperature-dependence of the injection current is largely determined by the energetic disorder in this material, which is unknown for the present polymer.[31–32]

Finally, in an attempt to realize conditions for space-charge-limited electron-only current for N2200, devices with a very thick N2200 layer were fabricated by drop-casting. In this way, the injection barrier is still present but the device behavior is mainly limited by the bulk-transport characteristics rather than electron injection.[38] **Figure 4** shows the electron-only characteristics of devices with a Sm top contact for three different N2200 thicknesses, ranging from 85 nm to 48000 nm. The J-E characteristics of the 85 nm and 1800 nm thick devices are essentially identical, demonstrating the contact-limited

ADVANCED MATERIALS
www.advmat.de

Materials Views
www.MaterialsViews.com

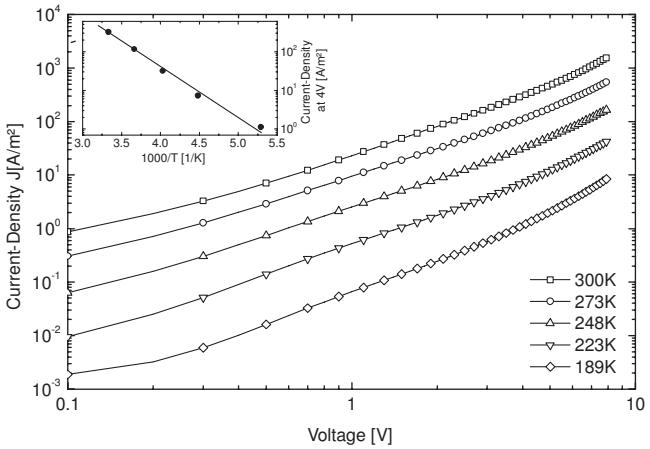

Figure 3. Temperature dependent *J-E* characteristics of N2200 electron-only devices with barium cathode and 460 nm semiconductor layer thickness. The inset shows the Arrhenius scaling of the current at 4 V.

currents under these conditions. In contrast, the current for a given field is significantly reduced when increasing the layer thickness to 48 μm, pointing to a transition from the injection-limited to the transport-limited regime. For this device, the shape of the *J-E* characteristics can be satisfactorily described by space-charge-limited transport with an electron mobility of 3.5×10^{-3} cm^2/Vs. This value is comparable to the TOF mobility, corroborating intrinsic transport for the thickest device.[39]

In conclusion, for the first time bulk electron transport for the high filed-effect mobility Polyera ActivInk N2200 semiconductor has been studied. The results from both time-of-flight and electron-only current measurements suggest a bulk mobility of ~5×10^{-3} cm^2/Vs, which is to our knowledge the highest value reported for TOF electron-transport in conjugated polymers. Importantly, the electron-only device currents

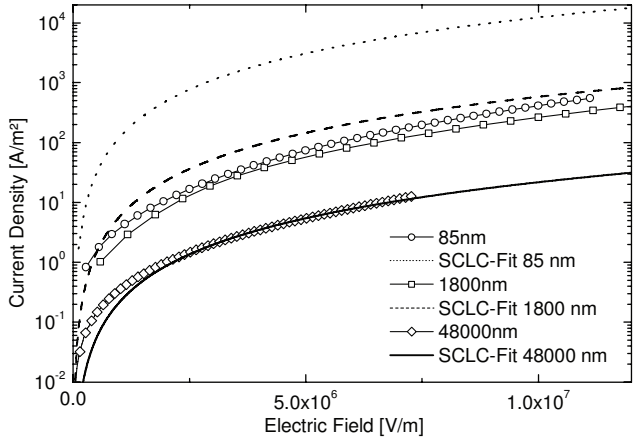

Figure 4. *J-V* characteristics of electron-only devices with various N2200 layer thicknesses and Sm cathode. The straight line is a fit to the 48000 nm device using equation (4) with a mobility of $\mu = 3.5 \times 10^{-3}$ cm^2/Vs while the dotted and dashed line predict the expected SCL currents for the thinner devices for the same mobility.

are injection limited for a wide range of electrode workfunctions and semiconductor layer thicknesses, despite the rather high electron-affinity of this polymer. Contact-limited currents were observed even when low workfunction metals such as Sm, Ca, Ba or CsF/Al are employed, which are known to form ohmic contacts with other n-type polymers.[6,8] However, the previously investigated polymers typically exhibit rather low bulk-transport limited currents owing e.g. to severe electron trapping in an exponential density of states distribution. Thus, we believe that evaporation of reactive metals onto layers of conjugated polymers may commonly cause injection barriers (through the formation of oxides and chemical defects[40–41]), but that these barriers are masked by the low bulk currents in the majority of n-type polymers that have been investigated to date.

Experimental

ActivInk™ N2200 is available from Polyera Corporation, USA. PEDOT:PSS was obtained from H.C. Starck GmbH, Germany under the trade name Clevios P VP AI4083. Indium tin oxide (ITO)-covered glass was obtained from Präzisions Glas & Optik GmbH, Germany, and cleaned by ultrasonication in acetone, detergent solution, de-ionized water, and isopropanol. These substrates have a 25 nm thick SiO_2 protection layer between the soda-lime glass and the conducting ITO of 100 nm thickness and 15 Ω sheet resistance. N2200 layers were deposited by spin coating from polymer chlorobenzene (purity = 99.9% from Sigma-Aldrich) solution inside the glovebox. Layer thicknesses were varied by changing the polymer concentration and spin-coating speed and measured using a Dektak 3ST profilometer in air. The two thick devices (1800 nm and 48000 nm) shown in Figure 4 were prepared by drop-casting, while the thinnest device (85 nm) was conventionally spin-coated.

Metal contacts were fabricated by thermal evaporation at a base pressure $<2 \times 10^{-6}$ mbar. All metals used for thermal evaporation of the bottom and top electrodes had a purity of 99.99%. The evaporator vacuum chamber is directly connected to a nitrogen-filled glovebox system, allowing the loading of evaporation crucibles under an inert atmosphere.

Current-voltage characteristics were measured inside the glovebox by a computer-controlled Keithley 2400 source/measure unit. Oxygen and water contaminations of the glovebox atmosphere were < 2 ppm and samples were transferred without contact to air. Temperature dependent measurements were carried out by placing the samples on a Linkam LTS350 cooling stage retrofitted for use inside the glovebox.

For TOF measurements, free charge carriers were generated by illuminating the polymer with 355 nm wavelength laser pulses of 20 ns pulse length through the glass substrate and ITO/PEDOT:PSS/PFB layer while applying varying bias voltages. The devices were capped with 20 nm barium and 100 nm Al. In that arrangement injection from both electrodes is suppressed, while extraction of both charge carriers is still possible. Furthermore, TOF devices were encapsulated with an epoxy resin to be measured outside of the glovebox.

Acknowledgements

The authors wish to thank Madlen Klötzer and Steffen Roland for laboratory assistance. This work was financially supported by the German Federal Ministry of Science and Education (BMBF FKZ 03X3525D) and the German Research Foundation (DFG SPP 1355). Polyera Corporation thanks the FlexTech Alliance (Mr. Michael Ciesinski and Dr. Robert Tulis) for support.

Supporting Information

Supporting Information is available online from Wiley InterScience or from the author.

Received: January 20, 2010
Revised: March 11, 2010
Published online:

[1] J. C. Scott, G. G. Malliaras, *Chemical Phys. Lett.* **1999**, *299*, 115.
[2] P. Langevin, *Ann. Chim. Phys.* **1903**, *28*, 433.
[3] C. L. Braun, *J. Chem. Phys.* **1984**, *80*, 4157.
[4] J. Roncali, *Macromol. Rapid Commun.* **2007**, *28*, 1761.
[5] P. W. M. Blom, M. J. M. deJong, J. J. M. Vleggaar, *Appl. Phys. Lett.* **1996**, *68*, 3308.
[6] M. M. Mandoc, B. de Boer, P. W. M. Blom, *Phys. Rev. B* **2006**, *73*, 155205.
[7] J. Cornil, J. L. Bredas, J. Zaumseil, H. Sirringhaus, *Adv. Mater.* **2007**, *19*, 1791.
[8] R. Steyrleuthner, S. Bange, D. Neher, *J. Appl. Phys.* **2009**, *105*, 8.
[9] C. R. McNeill, N. C. Greenham, *Appl. Phys. Lett.* **2008**, *93*, 3.
[10] D. M. deLeeuw, M. M. J. Simenon, A. R. Brown, R. E. F. Einerhand, *Synth. Met.* **1997**, *87*, 53.
[11] H. Antoniadis, L. J. Rothberg, F. Papadimitrakopoulos, M. Yan, M. E. Galvin, M. A. Abkowitz, *Phys. Rev. B* **1994**, *50*, 14911.
[12] E. J. W. List, R. Güntner, P. S. d. Freitas, U. Scherf, *Adv. Mater.* **2002**, *14*, 374.
[13] V. R. Nikitenko, J. M. Lupton, *J. Appl. Phys.* **2003**, *93*, 5973.
[14] X. H. Yang, F. Jaiser, D. Neher, P. V. Lawson, J. L. Brédas, E. Zojer, R. Güntner, P. Scanduicci de Freitas, M. Forster, U. Scherf, *Adv. Funct. Mater.* **2004**, *14*, 1097.
[15] C. R. Newman, C. D. Frisbie, D. A. da Silva, J. L. Bredas, P. C. Ewbank, K. R. Mann, *Chem. Mat.* **2004**, *16*, 4436.
[16] L.-L. Chua, J. Zaumseil, J.-F. Chang, E. C. W. Ou, P. K. H. Ho, H. Sirringhaus, R. H. Friend, *Nature* **2005**, *434*, 194.
[17] A. Babel, S. A. Jenekhe, *J. Am. Chem. Soc.* **2003**, *125*, 13656.
[18] S. Huttner, M. Sommer, M. Thelakkat, *Appl. Phys. Lett.* **2008**, *92*, 3.
[19] J. A. Letizia, M. R. Salata, C. M. Tribout, A. Facchetti, M. A. Ratner, T. J. Marks, *J. Amer. Chem. Soc.* **2008**, *130*, 9679.
[20] X. W. Zhan, Z. A. Tan, B. Domercq, Z. S. An, X. Zhang, S. Barlow, Y. F. Li, D. B. Zhu, B. Kippelen, S. R. Marder, *J. Amer. Chem. Soc.* **2007**, *129*, 7246.
[21] H. Yan, Z. H. Chen, Y. Zheng, C. Newman, J. R. Quinn, F. Dotz, M. Kastler, A. Facchetti, *Nature* **2009**, *457*, 679.
[22] K. Szendrei, D. Jarzab, Z. Chen, A. Facchetti, M. A. Loi, *J. Mater. Chem.*, **2010**, *20*, 1317.
[23] C. Tanase, E. J. Meijer, P. W. M. Blom, D. M. de Leeuw, *Phys. Rev. Lett.* **2003**, *91*, 216601.
[24] S. Braun, W. R. Salaneck, M. Fahlman, *Adv. Mater.* **2009**, *21*, 1450.
[25] N. Koch, *ChemPhysChem* **2007**, *8*, 1438.
[26] J. A. Mikroyannidis, M. M. Stylianakis, G. D. Sharma, P. Bahraju, M. S. Roy, *J. Phys. Chem. C* **2009**, *113*, 7904.
[27] W. Brütting, S. Berleb, A. G. Muckl, *Synth. Met.* **2001**, *122*, 99.
[28] M. A. Lampert, *Rep. Prog. Phys.* **1964**, *27*, 329.
[29] P. Mark, W. Helfrich, *J. Appl. Phys.* **1962**, *33*, 205.
[30] J. G. Simmons, *Phys. Rev. Lett.* **1965**, *15*, 967.
[31] V. I. Arkhipov, E. V. Emelianova, Y. H. Tak, H. Bässler, *J. Appl. Phys.* **1998**, *84*, 848.
[32] T. van Woudenbergh, P. W. M. Blom, M. Vissenberg, J. N. Huiberts, *Appl. Phys. Lett.* **2001**, *79*, 1697.
[33] S. Bange, A. Kuksov, D. Neher, A. Vollmer, N. Koch, A. Ludemann, S. Heun, *J. Appl. Phys.* **2008**, *104*, 7.
[34] C. Yin, B. Pieper, B. Stiller, T. Kietzke, D. Neher, *Appl. Phys. Lett.* **2007**, *90*, 133502.
[35] A. J. Campbell, D. D. C. Bradley, H. Antoniadis, M. Inbasekaran, W. S. W. Wu, E. P. Woo, *Appl. Phys. Lett.* **2000**, *76*, 1734.
[36] A. J. Campbell, D. D. C. Bradley, H. Antoniadis, *Appl. Phys. Lett.* **2001**, *79*, 2133.
[37] K. Yang, Y. Wang, A. Jain, L. Samulson, J. Kumar, *J. Macromol. Sci. Part A-Pure Appl. Chem.* **2007**, *44*, 1261
[38] Y. L. Shen, A. R. Hosseini, M. H. Wong, G. G. Malliaras, *ChemPhysChem* **2004**, *5*, 16.
[39] D. Poplavskyy, W. C. Su, F. So, *J. Appl. Phys.* **2005**, *98*, 11.
[40] A. Crispin, A. Jonsson, M. Fahlman, W. R. Salaneck, *J. Chem. Phys.* **2001**, *115*, 5252.
[41] S. Schols, L. Van Willigenburg, R. Mueller, D. Bode, M. Debucquoy, S. De Jonge, J. Genoe, P. Heremans, S. Lu, A. Facchetti, *Appl. Phys. Lett.* **2008**, *93*, 263303.

Supporting Information

DOI: 10.1002/ adma.201000232

Bulk Electron Transport and Charge Injection in a High Mobility n-Type Semiconducting Polymer

By *Robert Steyrleuthner*[1], *Marcel Schubert*[1], *Frank Jaiser*[1], *James C. Blakesley*[1], *Zhihua Chen*[2], *Antonio Facchetti*[2] and *Dieter Neher*[1] *

[1]Institut für Physik und Astronomie, Universität Potsdam, Karl-Liebknecht-Straße 24-25, 14476 Potsdam, Germany
[2]Polyera Corporation, 8045 Lamon Avenue, Illinois 60077, USA

Dependence of Injection Current on Cathode Material

The Graph shows the injection current measured at 3V for devices of ca. 85 nm thickness In general, the current density decreases with increasing work function, but the dependence of the current on Φ_M is far less pronounced then predicted by Schottky-type thermionic emission. This observation is consistent with the current being limited by the rate of electron injection through a barrier into a density of states distribution[1]. Remarkably, a dependence of the injection current on work function is observed even for metals with Φ_M considerably smaller than the reported electron affinity of PAI-N-2200 of ca. 4.0 eV (shaded area in Figure S1). For these metals, the electron-injection barrier should be zero. The results are indicative for strong Fermi-level-pinning at localized surface states[2, 3].

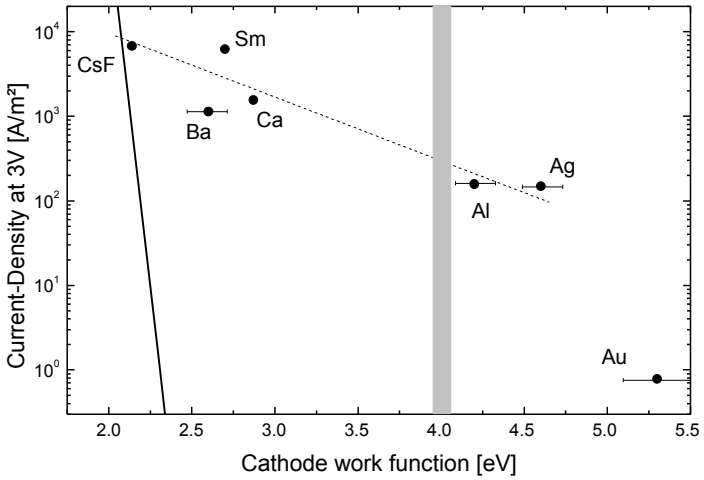

Figure S1: Electron-only current at 3 V though PAI-N-2200 of ca. 85 nm thickness, plotted as function of the nominal work function of the electron-injecting cathode according. The horizontal error bar sketches the typical range of values for a given metal. The solid line was calculated according to

$$j = j_0 \times \exp\left\{-\frac{\Delta_e}{k_B T}\right\},$$

with T set to room temperature and $\Delta_e = \Phi_M - E_{LUMO}$ being the nominal electron-injection barrier between a metal with work function Φ_M and the polymer with LUMO energy E_{LUMO}. The shaded area indicates the approximate LUMO energy of PAI-N-2200. The dashed line is a guide to the eye.

[1] T. van Woudenbergh, P. W. M. Blom, M. Vissenberg, and J. N. Huiberts, Applied Physics Letters **79,** 1697-1699 (2001).

[2] S. Braun, W. R. Salaneck, and M. Fahlman, Advanced Materials **21,** 1450-1472 (2009).

[3] N. Koch, Chemphyschem **8,** 1438-1455 (2007).

Influence of Aggregation on the Performance of All-Polymer Solar Cells Containing Low-Bandgap Naphthalenediimide Copolymers

Marcel Schubert, Daniel Dolfen, Johannes Frisch, Steffen Roland, Robert Steyrleuthner, Burkhard Stiller, Zhihua Chen, Ullrich Scherf, Norbert Koch, Antonio Facchetti, and *Dieter Neher**

The authors present efficient all-polymer solar cells comprising two different low-bandgap naphthalenediimide (NDI)-based copolymers as acceptors and regioregular P3HT as the donor. It is shown that these naphthalene copolymers have a strong tendency to preaggregate in specific organic solvents, and that preaggregation can be completely suppressed when using suitable solvents with large and highly polarizable aromatic cores. Organic solar cells prepared from such nonaggregated polymer solutions show dramatically increased power conversion efficiencies of up to 1.4%, which is mainly due to a large increase of the short circuit current. In addition, optimized solar cells show remarkable high fill factors of up to 70%. The analysis of the blend absorbance spectra reveals a surprising anticorrelation between the degree of polymer aggregation in the solid P3HT:NDI copolymer blends and their photovoltaic performance. Scanning near-field optical microscopy (SNOM) and atomic force microscopy (AFM) measurements reveal important information on the blend morphology. It is shown that films with high degree of aggregation and low photocurrents exhibit large-scale phase-separation into rather pure donor and acceptor domains. It is proposed that, by suppressing the aggregation of NDI copolymers at the early stage of film formation, the intermixing of the donor and acceptor component is improved, thereby allowing efficient harvesting of photogenerated excitons at the donor–acceptor heterojunction.

1. Introduction

Organic photovoltaic (OPV) cells have become a major topic in the field of organic semiconductors. Bulk-heterojunction (BHJ) solar cells are commonly fabricated by combining an electron-donating and an electron-accepting compound. The understanding of the physical processes determining the conversion of light into electricity and the development of spectroscopic techniques to explore the nanometer morphology of these multicomponent systems are a prime example of interdisciplinary science. Within the fast-growing field of organic photovoltaics, solution-processed solar cells are currently the most promising devices because they may allow low-cost and large-area production essential to compete with fossil energy sources. During the last years, several soluble photovoltaic organic systems comprising conjugated small molecules, conjugated polymers, and/or inorganic nanoparticles have been studied. Solar cells based on the soluble, electron-accepting small molecular fullerene derivative PCBM ([6,6]-phenyl C_{61}-butyric acid methyl ester) are currently heading the efficiency table, with reported power conversion efficiencies (PCEs) exceeding 7%.[1,2] The need for high chemical purity of the fullerenes,[3] their low absorption at long wavelength but also the metastable morphology of fullerene-doped photoactive layers[4] still motivates the ongoing search of alternative electron-accepting and electron-transporting materials.[5,6] One important alternative to PCBM-based OPVs are all-polymer solar cells, where π-conjugated polymers are used as both the

M. Schubert, S. Roland, R. Steyrleuthner, B. Stiller, Prof. D. Neher
Institute of Physics and Astronomy
University of Potsdam
Karl-Liebknecht-Str. 24-25, 14476, Potsdam, Germany
E-mail: neher@uni-potsdam.de

D. Dolfen, Prof. U. Scherf
Macromolecular Chemistry
University of Wuppertal
42119 Wuppertal, Germany

J. Frisch, Prof. N. Koch
Institute of Physics
Humboldt University Berlin
Newtonstr. 15, 12489 Berlin, Germany

Dr. Z. Chen, Prof. A. Facchetti
Polyera Corporation
8045 Lamon Avenue, Illinois 60077, USA

DOI: 10.1002/aenm.201100601

donor and acceptor component.[7] So far, the major drawback of all-polymer solar cells is their relatively low efficiency of ≈2%,[8–12] which is mainly the result of low photocurrents and fill factors, seldom exceeding 5 mA cm^{-2} and 50%, respectively. It has been proposed that a pronounced field-dependence of free carrier generation in competition to geminate recombination may be the major cause for the poor performance of these cells.[13–14] So far, the low charge carrier mobility of the acceptor polymer, a strong intermixing of donor and acceptor components and severe electron trapping were identified as possible origins of the inefficient and field-dependent charge carrier formation.[13,15,16] Materials that bear the greatest potential to overcome the above-described limitations are so called donor–acceptor-type copolymers.[7,17] Recently, a new class of copolymers based on rylenes has been developed, which in most cases comprise a naphthalene (NDI) or perylene diimide (PDI) unit. These polymers exhibit nearly ideal properties for constituting the acceptor phase in organic solar cells, such as excellent ambient and thermal stability, and high electron affinities and electron mobilities.[18–20] A particularly well-suited polymer may be poly([*N*,*N*′-bis(2-octyldodecyl)-naphthalene-1,4,5,8-bis(dicarboximide)-2,6-diyl]-*alt*-5,5′-(2,2′-bithiophene)) P(NDI2OD-T2).[19] The measurement of the electron mobility in top-gate organic field-effect transistor (OFET) structures yielded a record mobility of 0.85 cm^2 V^{-1} s^{-1}, whereas the analysis of the space charge limited current in electron-only devices and time-of-flight measurements yielded remarkable values for the bulk mobility of more than 10^{-3} cm^2 V^{-1} s^{-1}.[21,22] Structural investigations regarding the origin of the exceptional high electron mobility in P(NDI2OD-T2) revealed a significant degree of crystallinity in pristine films,[23] which directly affects its bulk charge transport properties.[24] Recent investigations on PCBM-based organic solar cells pointed out that the formation of crystalline nano-sized domains in the donor[25,26] and the acceptor phase[27] is highly important for good device performance. For this reason, the high degree of crystallinity in P(NDI2OD-T2) films should be beneficial for the use of P(NDI2OD-T2) as acceptor material in all-polymer solar cells. First investigations on ambipolar, BHJ OFETs suggested that the high mobility of P(NDI2OD-T2) is indeed preserved upon blending with regioregular P3HT.[28] Surprisingly, BHJ solar cells comprising blends of P(NDI2OD-T2) with P3HT (in a 1:1 ratio) prepared from different solvents showed disappointing PCEs of about 0.2%.[29] By performing steady state and transient optical spectroscopy in combination with scanning X-ray transmission microscopy (SXTM) studies, Moore et al.[29] came to the conclusion that the studied P3HT:P(NDI2OD-T2) systems exhibit a hierarchical blend morphology with a mesoscale phase separation into impure donor-rich and acceptor-rich domains. It was further proposed that the high degree of intermixing within these domains causes the localization of charges on individual chains, which facilitates geminate recombination and prevents the effective extraction of free charges to the electrodes.[29] A higher PCE of 0.6% was achieved by increasing the weight fraction of P(NDI2OD-T2) in the blend and by using xylene as the solvent.[30] P3HT is known to self-assemble in the form of ribbon-like crystals in dilute solutions of poor solvents such as cyclohexanone or p-xylene,[31,32] and the better performance of the xylene-coated blend was attributed to the formation of an interpenetrating network of well-crystallized P3HT nanofibers, embedded into the P(NDI2OD-T2) phase.[30]

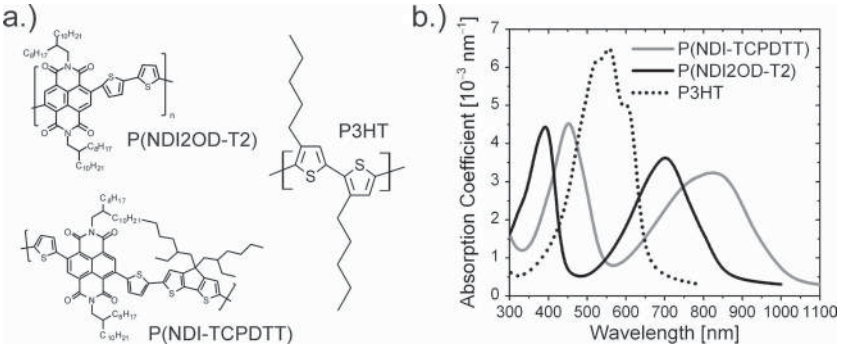

Figure 1. a) Chemical structure of the two electron-transporting copolymers P(NDI2OD-T2) and P(NDI-TCPDTT), and of the hole transporting polymer regioregular P3HT. b) Optical absorption spectra of spin-coated films of the three polymers.

In this study, two naphthalenediimide-based copolymers, P(NDI2OD-T2) and a related polymer with lower bandgap, poly[*N*,*N*′-bis(2-octyldodecyl)-2,6-bis(thieno-2-*yl*)naphthalene-1,4,5,8-tetracarboxylicdiimide-5′,5″-*diyl*-*alt*-4,4-bis(2-ethylhexyl)-4*H*-cyclopenta (1,2-b:5,4-b′]dithiophene-2,6-*diyl*)] P(NDI-TCPDTT) were investigated as the acceptor component in all-polymer solar cells with regioregular P3HT as the donor. The chemical structures of P(NDI2OD-T2) and P(NDI-TCPDTT) are shown in **Figure 1**. The backbone of both copolymers comprises the same NDI core and two thiophene units. P(NDI-TCPDTT) has one additional cyclopentadithieno (CPDT) group as the third building block. Our investigations show that the solar cell performance of BHJ devices is strongly enhanced when preventing the polymers to form large and well-ordered crystallites in the blend layer. By combining optical spectroscopy and morphological investigations, we come to the conclusion that a more optimized nanomorphology is introduced by suppressing the aggregation of the NDI copolymers at the early stage of film formation. The better intermixing of the donor and acceptor domains is proposed to be the origin of the strongly improved device performance. Optimized devices have exceptional high fill factors of over 70% and power conversion efficiency reaching 1.4%.

2. Results and Discussion

2.1. Optical Properties and Electronic Structure

An important aspect in the process of optimizing organic solar cells is the spectral match of solar spectrum and absorption of the organic semiconductor. This is commonly reached by decreasing the optical bandgap of the donor and/or acceptor component. Here, an optimum bandgap of about 1.4 eV was

Adv. Energy Mater. **2012**,
DOI: 10.1002/aenm.201100601

Table 1. Summarized optical and electronic properties of both NDI copolymers.

Polymer	$\lambda_{max,Film}$ [nm][a] (E_{gap} [eV][c])	$\lambda_{max,CN}$ [nm][b] (E_{gap} [eV][c])	VB onset [eV][d]	CB onset [eV][e]
P(NDI2OD-T2)	392/701 (1.45)	372/626 (1.75)	−5.8	−4.35
P(NDI-TCPDTT)	452/830 (1.25)	450/723 (1.43)	−5.35	−4.15

[a]Wavelength of high and low energy peak absorption in the solid state; [b]Wavelength of high and low energy peak absorption in chloronaphthalene solution; [c]Optical bandgap determined from the onset of the absorption; [d]Valence band (VB) onset measured by UPS, the vacuum level is set to zero; [e]Conduction band (CB) onset estimated by adding the optical bandgap to the valance band onset. Note that this approach neglects the exciton binding energy, which is not known for these polymers.

estimated to ideally match the trade-off between generating maximum photocurrent while still providing a sufficient electrochemical potential difference.[33] From the solid state absorption of both copolymers displayed in Figure 1, the optical bandgap of P(NDI2OD-T2) and P(NDI-TCPDTT) is calculated to 1.45 eV and 1.25 eV (see **Table 1**), respectively, which perfectly fits to the proposed optimum bandgap. Furthermore, the broad absorption minimum in the spectra of both copolymers is compensated for by the P3HT absorption. Thus, a nearly complete coverage of the solar spectrum from the visible to the near infrared (NIR) is possible in the blend.

To assess the energy level alignment at the donor–acceptor (DA) heterojunction, bilayer model structures were analyzed with ultraviolet photoelectron spectroscopy (UPS). These samples consist of indium tin oxide (ITO) coated glass substrates covered with a commercially available poly(ethylene-dioxythiophene):poly(styrenesulfonate) (PEDOT:PSS) layer serving as the anode, a ≈5 nm thick P3HT interlayer (P3HT-IL) and a ≈20 nm thick layer of either P(NDI2OD-T2) or P(NDI-TCPDTT). The P3HT-IL was obtained by annealing a thin P3HT layer on top of PEDOT:PSS above the glass transition temperature of P3HT. After repeated washing, an insolubilized interlayer remains,[34] which allows the acceptor polymer layer to be coated on top without strong intermixing of the two materials.[35] The work function of the PEDOT:PSS layer was 4.75 eV (see **Figure 2**a). The deposition of a P3HT interlayer decreased the sample work function by 0.65 eV because the P3HT occupied levels are pinned at the anode Fermi-level via formation of a dipolar layer at the interface.[36] From the valence region spectra (Figure 2b) we infer the position of the P3HT valence band (VB) onset is 0.40 eV from the Fermi-Energy (EF), corresponding to the hole injection barrier (HIB) at the anode-donor interface. Adding the sample work function to the HIB yields a P3HT ionization energy of 4.50 eV. The position of the conduction band (CB) onset was obtained by assuming a transport gap for P3HT of 2.5 eV.[37] Upon deposition of either P(NDI2OD-T2) or P(NDI-TCPDTT) onto the P3HT-IL, the work function increased by 0.35 eV. This observation is consistent with pinning of the acceptor empty energy levels (which tails into the gap from the CB onset[38]) due to the low work function of the P3HT-IL. The valence spectra for P(NDI2OD-T2) and P(NDI-TCPDTT) on the P3HT-IL display a valence band onset of the acceptors at 1.35 eV and 0.9 eV below the Fermi-level, respectively. Consequently, the VB offset between the donor P3HT and the acceptor P(NDI2OD-T2) [P(NDI-TCPDTT)] is 0.95 eV (0.5 eV) and the acceptor polymer ionization energies are −5.8 eV (−5.35 eV). The value for P(NDI2OD-T2) agrees rather well with earlier reported values for this polymer.[38]

The energy level alignment at the P(NDI2OD-T2) and P(NDI-TCPDTT)/P3HT-IL/PEDOT:PSS interfaces is schematically summarized in Figure 2c and d. The estimated electron affinity values (expressed as conduction band onset energy with respect to the vacuum level) is summarized in Table 1. The photovoltaic

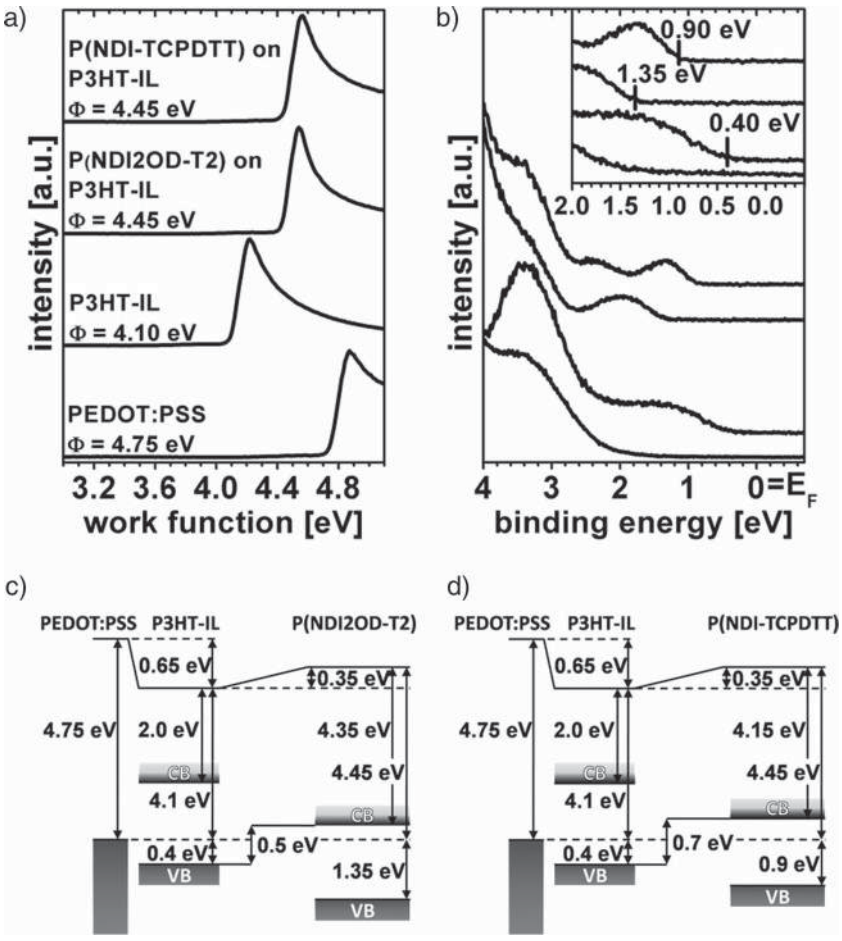

Figure 2. Ultraviolet photoelectron spectra of PEDOT:PSS/ITO substrates with an insolubilized P3HT interlayer and with either P(NDI2OD-T2) or P(NDI-TCPDTT) spin-coated on top of the P3HT-interlayer: a) secondary electron cutoff (SECO) and b) valence region spectra. Also shown is the energy level alignment diagram at c) the P3HT-IL/P(NDI2OD-T2) and d) at the P3HT-IL/P(NDI-TCPDTT) heterojunctions.

gap (energy difference between the VB onset of the donor and the CB onset of the acceptor polymer) is estimated to be 0.5 eV for P3HT/P(NDI2OD-T2) and 0.7 eV for P3HT/P(NDI-TCPDTT). These values set an upper limit to the open-circuit voltage (V_{OC}) in heterojunction devices.[39,40]

2.2. Photovoltaic Properties of Bilayer Devices

Bilayer solar cell devices comprising a ≈5 nm thick P3HT interlayer and a ≈60 nm thick acceptor layer were built to investigate the charge carrier photogeneration across a rather well-defined DA heterojunction. Cells with PC[70]BM were studied for reference. The current–voltage characteristics shown in **Figure 3** display only small short-circuit currents (J_{SC}) for both acceptor polymers. The PCE of the bilayer cell with P(NDI2OD-T2) is only 0.2%, which compares well with values measured on laminated or solution-processed bilayer structures.[9,29] Cells with P(NDI-TCPDTT) have a slightly higher open-circuit voltage but an even smaller J_{SC}. The higher V_{OC} for the P3HT/P(NDI-TCPDTT) cells is in agreement with the energy level scheme of Figure 2.

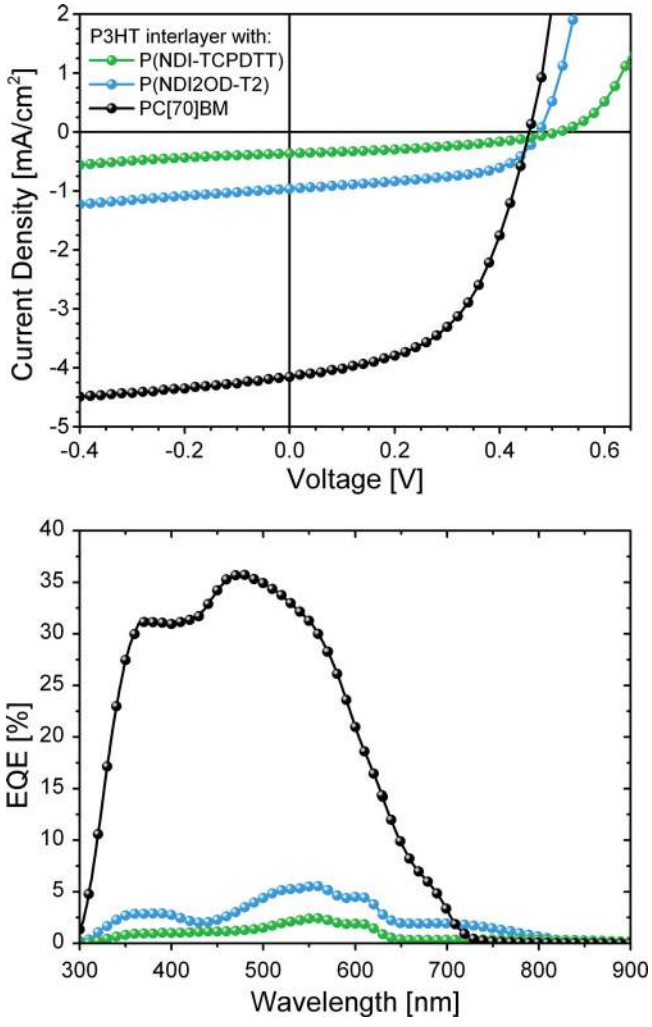

Figure 3. *J–V* characteristics (top) and EQE spectra (bottom) of bilayer solar cells. The structure of the solar cells was ITO/PEDOT:PSS/P3HT interlayer (5 nm)/acceptor/Sm/Al. The thickness of the acceptor layer was 55 nm, 60 nm or 55 nm for PC[70]BM, P(NDI2OD-T2) and P(NDI-TCPDTT), respectively. Please note that the *J–V* characteristic of the PC[70]BM cell is measured at 80 mW cm^{-2}, whereas the others are recorded at 100 mW cm^{-2}.

Compared to the all-polymer devices, bilayer cells with a spin-coated PC[70]BM acceptor layer exhibited markedly higher photocurrent, which can be related to a sustainably higher external quantum efficiency (EQE). Note that the EQE spectrum of the P3HT/PC[70]BM cell perfectly resembles the absorption spectra of PC[70]BM with a very small contribution by the thin donor layer (see Figure S2, Supporting Information). In contrast, the contribution of P(NDI2OD-T2) or P(NDI-TCPDTT) to the EQE spectra in Figure 3 is marginal and even smaller than the contribution of the only 5 nm thick P3HT interlayer. Therefore, an exciton generated on either P(NDI2OD-T2) or P(NDI-TCPDTT) has a much smaller probability to generate a free charge carrier at the heterojunction than an exciton created on the fullerene acceptor. This hints to a smaller exciton diffusion length in the polymeric acceptor layer and/or a smaller efficiency for free carrier generation via interfacial electron transfer at the heterojunction between P3HT and the polymeric acceptors. It has been proposed that the spatial rearrangement of cofacially stacked perylene bisimides (PDIs) in the excited state may lead to strong localization of excitations (exciplex formation) and that this process drastically reduces the exciton diffusion length in pure PDI layers.[41] Recently, Rivnay et al.[23] reported X-ray diffraction data of solid P(NDI2OD-T2) suggesting that the polymer forms crystallites with cofacial stacking of the conjugated units. Motivated by these observations, we studied in detail the aggregation of both NDI-containing polymers, with particular focus on the interrelation between aggregate formation and photovoltaic properties.

2.3. Preaggregation of the Pure Copolymers in Solution

Perylene- and naphthalenediimide molecules are extensively used as dye materials providing a unique variability in structure and a widely tuneable color. The origin of their great versatility relies on the strong tendency to aggregate and the related formation of intermolecular excitations, which is a result of strong noncovalent interactions between the large conjugated cores of these molecules.[42] A well-established approach to investigate the aggregation of small molecules or polymer chains is to study their absorption in different solvents.[43] **Figure 4** displays the absorption spectra of P(NDI2OD-T2) and P(NDI-TCPDTT) in various organic solvents including chloroform, toluene, chlorobenzene, as well as chloronaphthalene (CN), the latter used rarely for solar cell preparation. For both polymers, similar changes of the optical absorption spectra, especially in the red and near-infrared part of the spectra, are visible. The solutions from CN show a completely unstructured spectrum with two absorption maxima at 372 nm and 626 nm for P(NDI2OD-T2) and at 450 nm and 723 nm for P(NDI-TCPDTT). We assign the high and low energy peak to the π–π^* and the charge-transfer (CT) excitation, respectively. This assignment is in full agreement with the interpretation of the absorption of typical

Adv. Energy Mater. 2012,
DOI: 10.1002/aenm.201100601

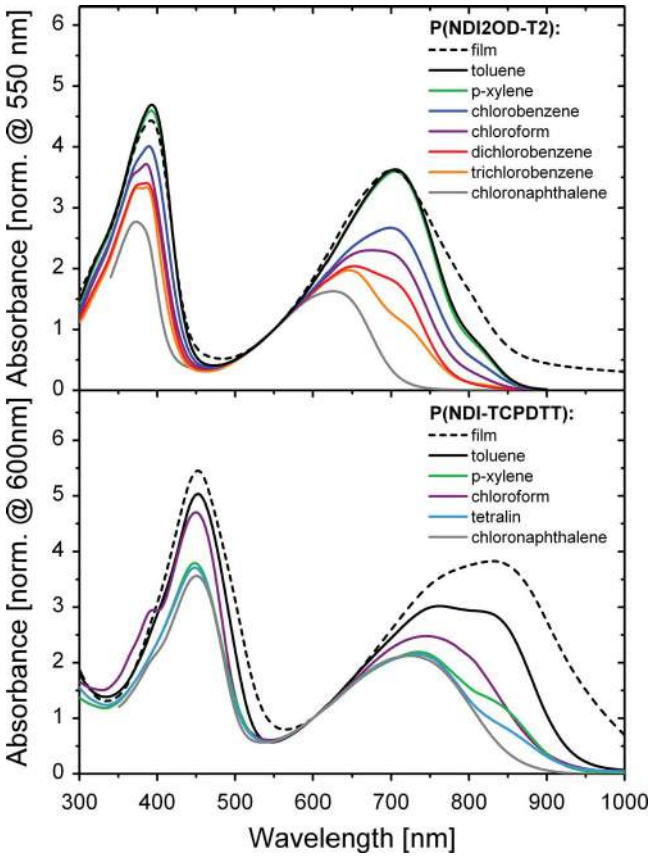

Figure 4. Optical absorption spectra of P(NDI2OD-T2) (top) and P(NDI-TCPDTT) (bottom) in various organic solvents (colored solid lines) and of a film spin-coated from toluene (black dashed line). All spectra are normalized to the absorption of the amorphous polymer content to visualize the evolution of the aggregate species.

donor–acceptor-type copolymers.[44] Among the other solvents, the most structured and red-shifted spectrum is measured in toluene. When compared to CN, the onset of absorption of P(NDI2OD-T2) dissolved in toluene shifts from 710 nm to 860 nm, corresponding to 0.3 eV in energy. This is due to the appearance of a new absorption band centered at 710 nm with a pronounced shoulder at 800 nm. For comparison, Figure 4 also contains a spectrum of a spin-coated P(NDI2OD-T2) film, which resembles typical features of the toluene spectrum, except the more pronounced shoulder at 800 nm. Several recent publications investigated the microstructure of P(NDI2OD-T2) in the solid state. Structure analysis of thin P(NDI2OD-T2) layers by Rivnay et al.[23] and Schuettfort et al.[45] revealed crystallites that are 10–30 nm in width and about 4 nm thick. Though the exact orientation and degree of crystallinity is currently under debate[24,45] these studies showed evidence that spin-coated films of P(NDI2OD-T2) contain a significant amount of crystalline domains.

The close correspondence of film and toluene solution spectra allows us to conclude that a high proportion of the P(NDI2OD-T2) polymer chains is preaggregated in toluene solution. On the other hand, chain aggregation in CN is apparently rather weak or even absent, whereas a weakly aggregated state prevail in the other solvents. The detailed analysis of this aggregation process, including the study of the size and amount of the aggregates in different solvents will be published separately. Analogous features as described above for P(NDI2OD-T2) are found for P(NDI-TCPDTT). In direct comparison, the aggregation of P(NDI-TCPDTT) in solution is less pronounced than for the P(NDI2OD-T2). Aggregation is mainly the result of the strong interactions between the NDI units and the insertion of CPDT into the backbone may considerably distort the formation of aggregates in solution because of a higher degree of conformational disorder along the polymer chain. Evidently, solvent molecules with large and highly polarizable naphthalene units (such as CN and tetralin) tend to suppress the aggregation of these NDI-based copolymers in solution. These large aromatic solvent molecules may interact mainly with the backbone of the polymer, thus screening the strong noncovalent forces between adjacent NDI units. We also like to point out that the optical absorption spectra of pristine polymer films spin-coated from different solvents are almost identical (see Figure S1, Supporting Information), meaning that both copolymers show a pronounced tendency to aggregate during film formation, independent of the degree of preaggregation in solution.

2.4. Bulk-Heterojunction Solar Cells

BHJ solar cells were fabricated with either P(NDI2OD-T2) or P(NDI-TCPDTT) as the acceptor material, and regioregular P3HT as the donor. P3HT:P(NDI2OD-T2) BHJ solar cells with the active layer being deposited from chlorobenzene, p-xylene, dichlorobenzene, or chloroform solutions revealed similar results as already reported by other groups, with very small PCEs of ≈0.2% (not shown).[9,29,30] As demonstrated in the previous section, these commonly used solvents cause the P(NDI2OD-T2) copolymer chains to preaggregate already in solution. To investigate the influence of the degree of preaggregation on the device performance, we systematically tuned the degree of preaggregation by going from a strongly collapsed, hence aggregated conformation of P(NDI2OD-T2) chains (as in pure p-xylene) to a more and more coiled or aggregate free conformation (as in pure CN). **Figure 5** displays the evolution of the *J–V* characteristics of solar cells prepared from a p-xylene:CN solvent mixture with increasing CN content (see also **Table 2**). The pure p-xylene-derived device shows a high fill factor (FF) (as reported earlier), but the power conversion efficiency (PCE) is only 0.24%, and limited by the very small short-circuit current of only 0.8 mA cm^{-2}. The addition of CN results in a marked improvement of all photovoltaic parameters. The best performing cell is found for a 1:1 mixture of p-xylene and CN, giving a PCE of 1.4%. This is the highest efficiency reported so far for PDI- or NDI-based acceptor polymers in combination with regioregular P3HT and it is among the best values for all-polymer solar cells. Increasing the CN content has the largest effect on J_{SC} but small improvements are also seen in the fill factor (61% –65%) and the open-circuit voltage (0.47 –0.56 V). The increase in the photocurrent parallels systematic changes of the EQE spectra (shown in Figure 5), with the highest EQE (23%) measured for the 1:1 p-xylene:CN solvent mixture. Here, the preaggregation of the P(NDI2OD-T2) is completely suppressed

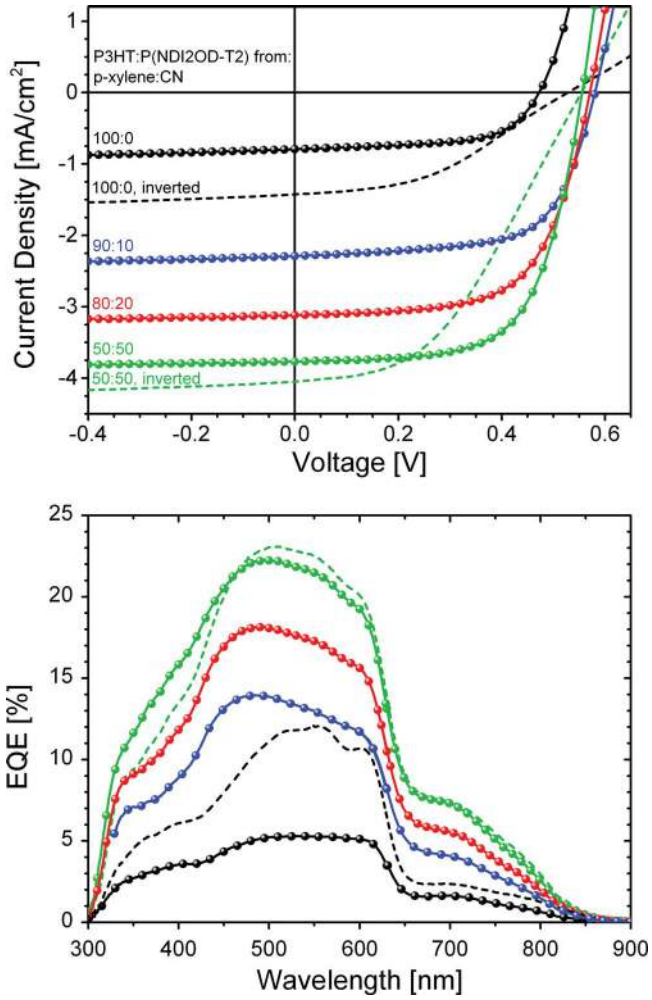

Figure 5. *J–V* characteristics under simulated AM 1.5 illumination (top) and EQE spectra (bottom) of P3HT:P(NDI2OD-T2) (1:0.75) BHJ solar cells spin-coated from solvent mixtures of p-xylene and CN. The mixing ratios of p-xylene:CN are 100:0 (black), 90:10 (blue), 80:20 (red), and 50:50 (green); and the active layer thickness is 200 nm, 300 nm, 310 nm, and 275 nm, respectively. All films were dried for 1 min at 200°C. Inverted solar cells, prepared following the same recipe, are also displayed (dotted lines) for cells with 0% (black) and 50% (green) CN. Dark currents are negligible small ($J_{dark}/J_{photo} \approx 10^{-4}$ at –1 V) and therefore not shown.

(see Figure S3, Supporting Information). Higher CN fractions do not significantly improve the solar cell performance further. Also, BHJ layers are rather difficult to fabricate from solvent mixtures with high CN content, due to a facile dewetting of the solution from the anode. Interestingly we found that the temperature of drying directly after spin-coating had a strong influence on solar cell performance, while an additional thermal annealing step performed thereafter neither improved nor degraded the P3HT:P(NDI2OD-T2) BHJ solar cell properties (see Figure S4, Supporting Information). This implies that the drying process introduces a (meta-)stable blend morphology which cannot be further altered by thermal annealing. The comparison of the EQE spectra with the absorption spectra in Figure 1 shows that the P3HT phase contributes strongest to the photocurrent, with the vibronic structure of P3HT still

Table 2. Photovoltaic parameters of the P3HT:P(NDI2OD-T2) (1:0.75) BHJ solar cells presented in Figure 5.

p-Xylene:CN	Structure	J_{SC} [mA cm^{-2}]	FF [%]	V_{OC}	η [%]
100:0	Standard	0.79	61	0.47	0.2
100:0	Inverted	1.43	41	0.53	0.3
90:10	Standard	2.29	65	0.58	0.9
80:20	Standard	3.12	63	0.57	1.2
50:50	Standard	3.77	65	0.56	1.4
50:50	Inverted	4.05	43	0.55	1.0

visible in the EQE spectrum. To understand if the improvement in the device performance is dominated by changes of the vertical composition profile, inverted solar cells with the device structure ITO/TiO_x/blend/MoO_3/Ag were fabricated (for details, see the Experimental Section). These inverted cells exhibit an overall larger short circuit current, whereas the smaller fill factors of the inverted devices is mostly related to different injection and extraction barriers in comparison to the standard devices.[46] Most important, the increase of the J_{SC} for higher CN content was reproduced for the inverted solar cell (see Figure 5). We, therefore, conclude that the preparation of blend layers from a solution with a smaller degree of preaggregation improves the solar cell performance mainly by a more efficient photogeneration of free charge carriers in the bulk of the film.

For the P3HT:P(NDI-TCPDTT) blend, we, again observe an improvement in the device performance when adding CN to p-xylene (see **Table 3**), but the effect is weaker than for P(NDI2OD-T2)-based blends. We attribute this to the overall lower tendency of P(NDI-TCPDTT) to preaggregate in solution. Interestingly, we found rather different device characteristics when comparing blends spin-coated from chloroform, p-xylene, or tetralin (which is 1,2,3,4-tetrahydronaphthalene), despite similar contributions from aggregate absorption in the solution spectra of P(NDI-TCPDTT) in these three solvents. *J–V* characteristics and corresponding EQE spectra are displayed in **Figure 6** (characteristics measured at an irradiance of about 1.3 mW cm^{-2} are shown in Figure S5, Supporting Information). While the cells from chloroform and p-xylene have similar J_{SC} of ≈1.5 mA cm^{-2} and fill factors of 46% and 60%, respectively, cells coated from tetralin show an improvement of all solar cell parameters. The PCE of the tetralin device is 1.1%. Most notably, the fill factor in this cell reaches 70%, the highest fill factor ever observed for all-polymer solar cells. This very high fill factor implies that free carrier generation does not involve an

Table 3. Photovoltaic parameters of the P3HT:P(NDI-TCPDTT) (1:1.5) solar cells presented in Figure 6.

Solvent	J_{SC} [mA cm^{-2}]	FF [%]	V_{OC}	η [%]
chloroform	1.41	46	0.59	0.4
p-xylene	1.48	60	0.62	0.6
p-xylene:CN (1:1)	2.04	71	0.59	0.9
tetralin	2.43	70	0.63	1.1

Adv. Energy Mater. **2012**,
DOI: 10.1002/aenm.201100601

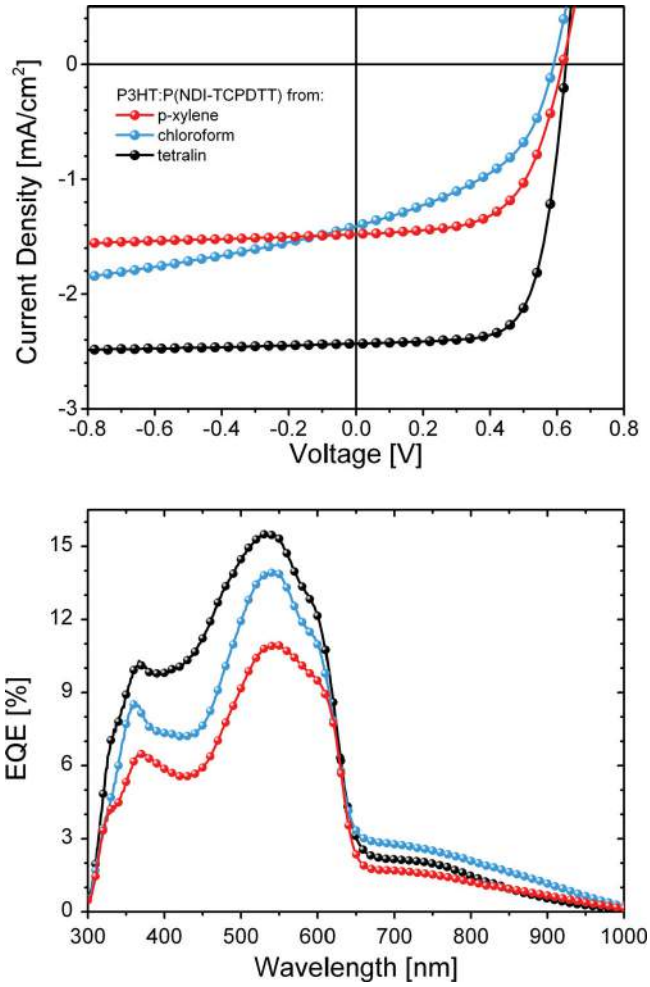

Figure 6. *J–V* characteristics under simulated AM 1.5 illumination (top) and EQE spectra (bottom) of P3HT:P(NDI-TCPDTT) (1:1.5) bulk-heterojunction solar cells spin-coated from chloroform (blue), p-xylene (red) and tetralin (black), where the film thickness is 310 nm, 340 nm and 410 nm, respectively. Dark currents are negligible small ($J_{dark}/J_{photo} \approx 10^{-4}$ at −1 V) and therefore not shown.

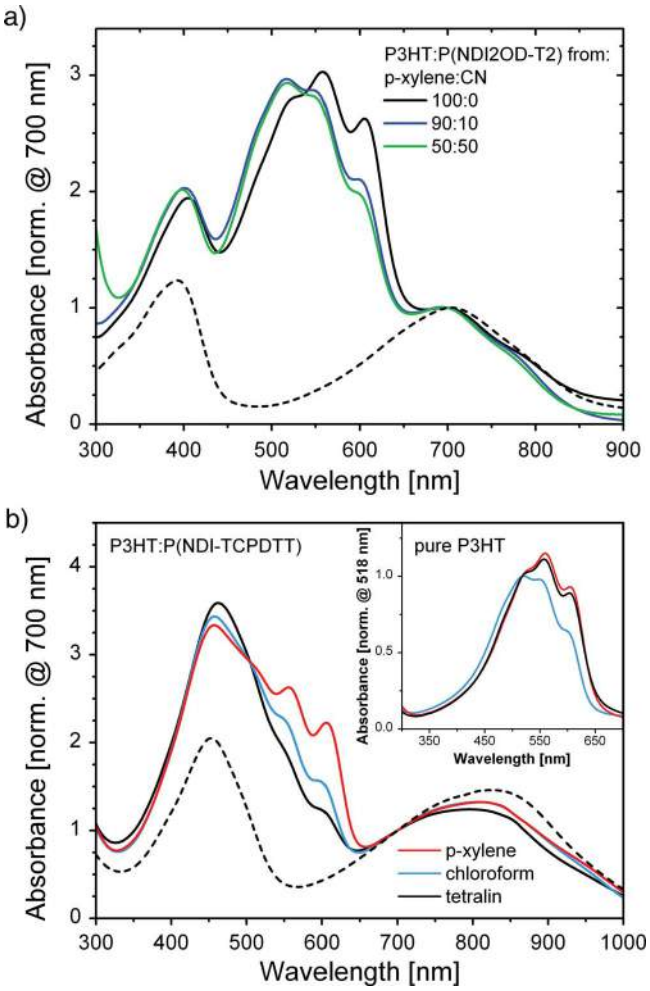

Figure 7. a) Absorption spectra of the solar cells displayed in Figure 5 (solid lines), measured between the active areas of the solar cells, where no top electrode is evaporated. Dashed black line represents the spectrum of a P(NDI2OD-T2) film spin-coated from pure p-xylene. b) Absorption spectra of the blend films (solid lines) of P3HT:P(NDI-TCPDTT) solar cells displayed in Figure 6 and spin-coated from p-xylene (red), chloroform (blue) and tetralin (black). A spectrum of a pure P(NDI-TCPDTT) (dashed black line) film spin-coated from p-xylene is shown for comparison. The inset shows the absorption spectra of pure P3HT films spin-coated from the same solvents and treated exactly the same way as the blend films.

appreciable field-dependence. Also note that this fill factor has been measured for an active layer thickness of 410 nm, meaning that carrier extraction must be efficient in the tetralin-coated blend. Contrary to this, the performance of the chloroform-coated cell under 1 sun illumination is largely affected by space-charge effects in combination with bimolecular recombination, and CF-coated cell outperforms the device prepared from tetralin at low illumination intensities (Figure S5, Supporting Information).

2.5. Chain Aggregation in Blend Layers

The results presented in the previous section demonstrate that suppression of preaggregation in solution leads to significantly higher short-circuit currents, but that this process might not fully account for the strong differences between the solar cells efficiencies. Therefore, a more detailed investigation of the optical and morphological properties of the blend layers solar cells was performed. **Figure 7**a displays the absorption of the BHJ solar cells from Figure 5. The complementary absorbance of P3HT and P(NDI2OD-T2) allows the direct probing of the evolution of the crystallinity in both polymers. Compared to the pristine P(NDI2OD-T2) layer, the absorption spectrum of the P(NDI2OD-T2) in the blend shows only small differences, notably a slightly reduced shoulder of the aggregate band between 700 and 850 nm for the blend spin-coated from the 1:1 mixture of p-xylene:CN. Hence, neither the addition of CN nor the presence of the P3HT is able to largely distort aggregation of the P(NDI2OD-T2) chains in the blend during film formation. On the other hand, the spectral contributions attributed to the P3HT phase change largely with increasing CN content. Blend films spin-coated from pure p-xylene show a strongly aggregated P3HT spectrum with pronounced 0–0 and

0–1 vibronic progressions at 610 nm and 560 nm. Addition of CN clearly suppresses the 0–0 transition while the 0–2 peak at 510 nm becomes more pronounced. According to the recently published model by Spano and co-workers,[47,48] the relative strength of the 0–0 vibronic transition is a direct measure of the intermolecular coupling strength, which is further related to the conjugation length and intrachain order of the interacting chains in P3HT aggregates. We, therefore, conclude that the addition of CN does not primarily prevent the formation of polymer aggregates but leads to more ill-defined domains. Presumably, the presence of long nonaggregated P(NDI2OD-T2) chains in the drying solution prevents large-scale phase separation into pure domains of the donor and the acceptor components.

A similar correlation between optical and photovoltaic properties is also seen for P(NDI-TCPDTT):P3HT blends. Figure 7b plots the absorption spectra of the solar cells from Figure 6. As before, only small changes in the P(NDI-TCPDTT) band above 650 nm are visible for all solvents, whereas the crystalline P3HT features are highly sensitive to the solvents. The best performing cell, spin-coated from tetralin shows the weakest 0–0 transition from aggregated P3HT. Note that the absorption spectra of pristine P3HT films prepared from tetralin are nearly identical to those of films deposited from p-xylene (see inset of Figure 7b), both exhibiting high P3HT crystallinity. The suppression of the 0–0 transition is accompanied by an overall decrease of the higher vibronic transitions, meaning that the overall P3HT crystallinity decreases when going from p-xylene to chloroform or tetralin. Evidently, the final degree of crystallization and the quality of the crystals in the P3HT:P(NDI-TCPDTT) blend is not purely determined by the extend of preaggregation of the acceptor chains in solution. We like to point out that strong aggregation and gel formation was reported for P3HT dissolved in xylene.[49] However, because of the relatively small molecular weight (<50.000 g mol^{-1}) of our P3HT in combination with the high temperature of the blend solution for spin-coating we can rule out any preaggregation of the P3HT. This is confirmed by the light orange color of the P3HT in pure p-xylene and p-xylene:CN mixture, as it is typical for nonaggregated P3HT chains (see also Figure S3, Supporting Information).

Thus, our data demonstrate a strong anticorrelation between the presence of large and well-ordered P3HT aggregates in the blend layer and the device efficiency for both acceptor polymers. This is in clear contrast to the well-established properties of P3HT:PCBM blends, where the formation of needle-like P3HT nanofibers with high intra- and interchain order was proven to be a major prerequisite for high short-circuit currents.[25,26,50]

2.6. Morphology

Scanning near-field optical microscopy (SNOM) measurements were performed to investigate the nanomorphology of blend films prepared from different solvents. Here, monochromatic illumination through an optical fibre with an aperture of about 100 nm is used to visualize either P3HT or the acceptor copolymers. This is possible due to the complementary absorbance of P3HT and the copolymers (see Figure 1). Given that a temporal constant light intensity is used, a variation in the transmitted light intensity can be either due to a variation of the film thickness or in the chemical composition of the blend. All SNOM images were taken directly on the solar cell samples (at areas not covered by the cathode). For the SNOM images presented below, the averaged optical density (OD) at the particular wavelength differed by less than 10% of the macroscopic optical density, ensuring that a characteristic part of the film is probed.

SNOM and AFM images of the P3HT:P(NDI2OD-T2) solar cells from Figure 5 spun from pure p-xylene and from a 1:1 p-xylene:CN mixture are presented in **Figure 8**. At 500 nm,

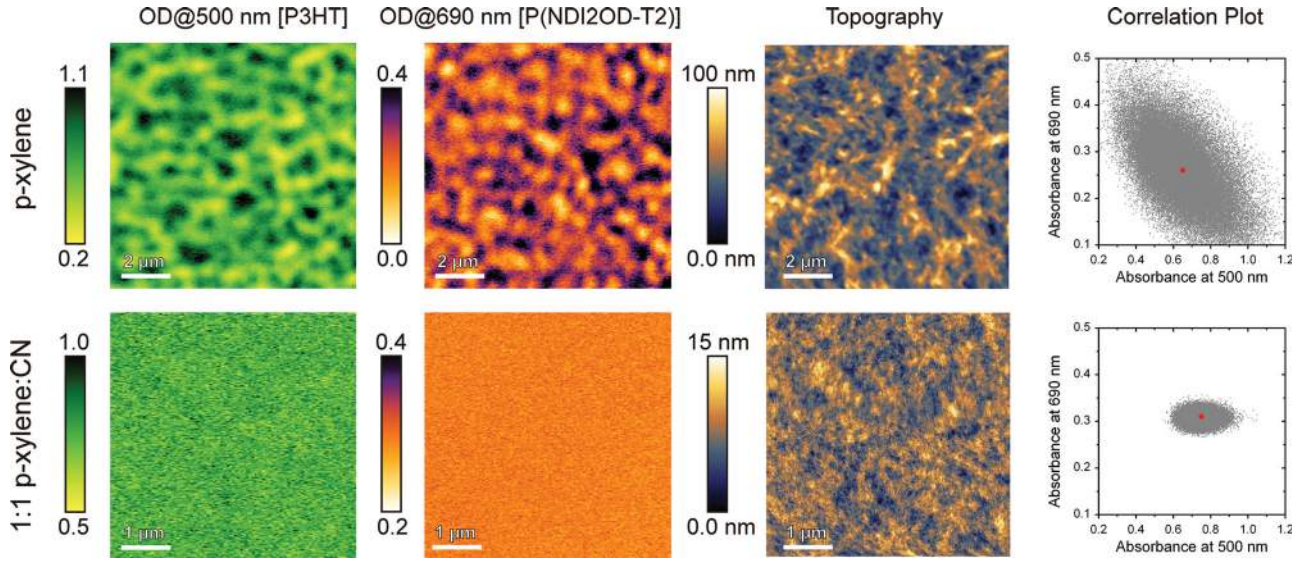

Figure 8. SNOM images of the blends of the solar cells from Figure 5 fabricated from p-xylene (top) and 1:1 p-xylene:CN (bottom), taken at 500 and 690 nm. The scale bar is expressed in optical density OD, defined via $OD = -Log_{10}(I/I_0)$, where I_0 is the incident and I the transmitted photon flux. AFM height images are obtained by independent measurements with a Si-cantilever. Thus, the SNOM and height images were taken at different positions, but we chose images which show similar features as the AFM traces measured parallel to the SNOM signal. Please note the different scale bars of the images for the different blends. Red dots in the correlation plots represent average OD values at the respective wavelength obtained by averaging over the whole SNOM image.

Adv. Energy Mater. 2012,
DOI: 10.1002/aenm.201100601

which is in the absorption minimum of P(NDI2OD-T2), the P3HT fraction of the blend is probed, whereas at 690 nm only P(NDI2OD-T2) absorbs (see Figure 1). For both wavelengths, the films cast from pure p-xylene exhibits a high contrast in the optical density and the AFM height image reveals variations in the film thickness of up to 100 nm. To ensure that the SNOM contrast is not the results of the thickness variation, we performed a simple correlation analysis, where for every coordinate the optical density at 690 nm is plotted against the optical density at 500 nm. The correlation plot for the two SNOM images (also shown in Figure 8) reveal a clear anticorrelation, meaning that regions with high OD at 500 nm have low OD at 690 nm and vice versa. We conclude that P(NDI2OD-T2) and P3HT strongly phase separate at a length scale of about 1 µm. Furthermore, AFM height images (not shown) recorded in parallel to each SNOM image revealed that hills in the AFM signal correspond to minimum OD values at 500 nm and maximum OD values at 690 nm. Therefore, the morphology of the p-xylene cast blend can be described by a network of elevated P(NDI2OD-T2)-rich domains, while P3HT-rich domains fill up the valleys in loosely connected islands, comparable to what was published earlier for the same blend and solvent.[29] The strong transmission contrast of the SNOM images and the similarity of AFM and SNOM features suggest that the domains extend through the whole film thickness with little vertical gradient. Addition of CN to the p-xylene solution has a strong effect on the nanoscale morphology of the resulting films. First, images of films spun from a 1:1 p-xylene:CN mixture are much more homogeneous and lack a pronounced domain structure in the SNOM images. Also, we see no evidence for a pronounced anticorrelation between the absorption at 500 and 690 nm. Both observations indicate a homogeneously intermixed blend morphology. However, the minimum and maximum OD values for both wavelengths deviate by 15% and 25% from the mean OD at 690 nm and 500 nm, respectively, whereas the film thickness varies only by about 5% (see height profile). Therefore we propose that phase separation in this blend is still present while the size of the domains is too small (below ≈100 nm) to be resolved by our SNOM setup. Nevertheless, the strong increase in photocurrent observed for this blend can be directly related to an improved intermixing of P3HT and P(NDI2OD-T2).

Figure 9 shows SNOM images of the P3HT:P(NDI-TCPDTT) solar cells presented in Figure 6. Here, all films are relatively smooth, with a variation of the thickness smaller than 10% of the overall thickness. Thus, SNOM measurements provide direct information about the spatial composition of the P3HT:P(NDI-TCPDTT) blends. As for the P(NDI2OD-T2)-based blend, the film spun from p-xylene shows a high absorption contrast, especially under 690 nm illumination, where the P(NDI-TCPDTT) contribution is visible. Here, the minimum and maximum OD differs by a factor of 4 between domains that are rich and poor in the acceptor polymer. The biggest domain features are several micrometers in size. For the P3HT phase, probed at 550 nm, a smaller contrast and minimum OD values of 0.7 are found. A more detailed analysis of the SNOM image shows that the sample consists of two types of domains, one P3HT-rich domain [where the OD of P(NDI-TCPDTT) is close to zero] and one intermixed phase [where minimum P3HT OD coincides with maximum P(NDI-TCPDTT) OD]. Note that these blend layers had a thickness of about 340 nm, and an even stronger phase separation at the mesoscale may be masked by overlaying domains that reduce the contrast in these images. Phase separation is also seen in the SNOM images of the cells spun from tetralin, but the overall optical density variation at 550 nm and 690 nm is more moderate than in the p-xylene coated layers. Also, the characteristic size of both P3HT- and P(NDI-TCPDTT)-rich domains are smaller (≈500 nm) and more regular in shape and size. We do not observe a strong anticorrelation between images taken at 550 and 690 nm. Thus, the morphology of the tetralin-coated layers might best be described by sub-micrometer-sized domains which consist of both P3HT and P(NDI-TCPDTT). This implies that the acceptor copolymer is incorporated in P3HT-rich domains, where it considerably distorts the crystallization of P3HT, consistent with the strong reduction of P3HT crystallinity in the blend seen in Figure 7. In contrast to all other blends, films made of chloroform do not show any notable contrast or domain features, neither in the P3HT nor in the P(NDI-TCPDTT) related image. Because the variation of the OD is less than 10% of the mean value, we propose that the donor and acceptor chains intermix homogeneously, at least on a length scale of about 100 nm.

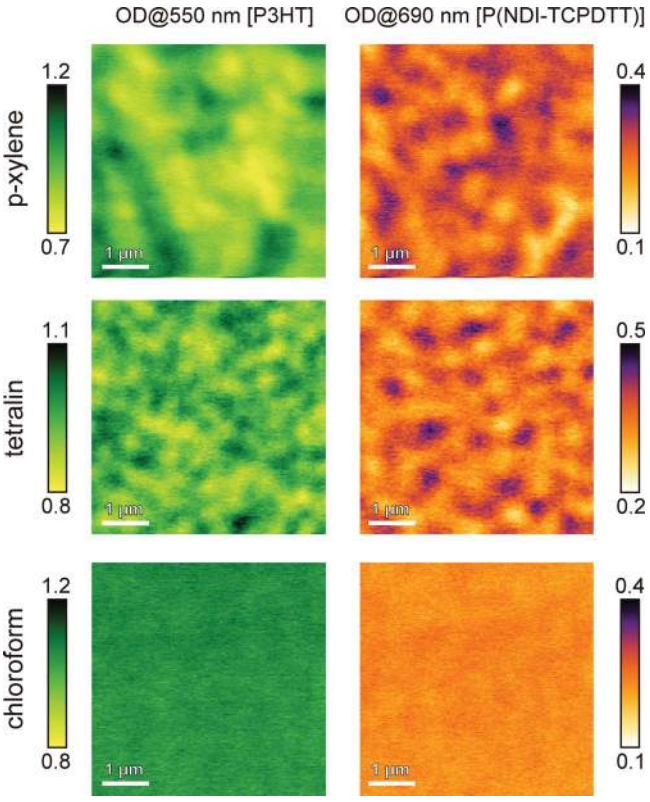

Figure 9. SNOM images of the solar cells from Figure 5, taken at 550 and 690 nm, where mainly P3HT or P(NDI-TCPDTT) absorb, respectively. The scale bar is expressed in optical density OD. Images at different wavelengths are slightly shifted (some hundreds of nm) and not taken at exactly the same place.

3. Summary and Conclusion

Our UPS data suggest that the energy levels at the P3HT:NDI acceptor heterojunctions should enable efficient exciton dissociation for the devices based on both copolymers. Furthermore, we found that simple vacuum level alignment is not sufficient to describe the level alignment of NDI-based copolymers in contact to P3HT, where a shift of the vacuum level of 0.35 eV is observed after deposition of the acceptor polymer onto the P3HT interlayer. The estimated open-circuit voltage agree rather well with the measured V_{OC} under AM 1.5 illumination conditions for both bilayer and blend devices. This underlines the importance of determining the acceptor energy levels in direct contact to the donor material. The close correspondence is rather intriguing, as the measured V_{OC} is usually significantly smaller than the photovoltaic gap.[51] Recently, a very small energetic disorder of P(NDI2OD-T2) was observed by Kelvin Probe and OFET measurements.[38,52] Thus, energetic losses attributed to the relaxation of free charge carriers inside the density of state could be minimized in NDI-copolymer-based solar cells, which might explain the high attainable open-circuit voltage.

Based on the energetic structure of the two investigated heterojunctions and the excellent charge transport properties of the donor P3HT and the acceptor P(NDI2OD-T2), good photovoltaic performance is expected. Indeed, we demonstrate solar cells with a peak PCE of 1.4%, which is 100% greater than that of previous studies. Analysis of the absorption spectra of the corresponding BHJ solar cells reveals an important anticorrelation between the solar cell performance and P3HT crystallinity.

For P3HT blended with P(NDI2OD-T2), the highest efficiency is observed for layers coated from a 1:1 p-xylene:CN solvent mixture, where the preaggregation of the acceptor chains is completely suppressed. The analysis of the optical spectra demonstrates that addition of CN to p-xylene does not suppress the crystallization of the donor and acceptor chains in the final solid layer, but that it prevents the formation of large and well-ordered donor crystallites. Noticeably, the EQE spectrum is clearly dominated by aggregates of both polymer components. The comparison of the normalized EQE and absorption spectra in Figure S6 (Supporting Information) shows that the EQE follows well the blend absorption spectrum, though with a smaller contribution by P(NDI2OD-T2) aggregates. We propose that addition of CN to the p-xylene solvent leads to an interpenetrating network of nanometer-sized crystalline polymer domains, where excitons formed on either the donor or the acceptor domain have a large probability to reach the heterojunction. Note that all low-efficiency P3HT:P(NDI2OD-T2) blends reported in the literature displayed a very aggregated P3HT spectrum in the blend, probably a result of the strong phase separation of both components.[29,30] Our conclusions are consistent with a recently published study of oligothiophene-functionalized NDI molecules, where a comparable efficiency of 1.5% was achieved for blends where no strong phase separation could be observed.[53] We also like to note that the high active layer thickness of the optimized solar cells implies a rather low internal quantum efficiency (see Figure S8, Supporting Information). Hence, the short-circuit current increases with increasing film thicknesses as long as efficient extraction of free carriers is provided. Future optimization should, therefore, mainly focus on improving the internal quantum efficiency.

The situation is more complex for blends of P3HT and P(NDI-TCPDTT). Here, adding CN to p-xylene (or changing to tetralin or chloroform) reduces not only the intrachain order within the crystals (as seen by the strong reduction of the 0–0 absorption in the P3HT absorption in Figure S7, Supporting Information), but also the overall degree of P3HT crystallinity. The blend coated from tetralin that exhibits the largest suppression of the 0–0 transition and the strongest reduction in P3HT crystallinity shows the highest fill factor and J_{SC}. The very high fill factor of the tetralin-coated blend indicates that the mobility in the P3HT phase is still sufficiently high to avoid the buildup of space-charges and with this strong bimolecular recombination of free charges.[16] Kamm et al.[54] recently investigated OPV devices with several molecular PDI derivatives blended with regioregular P3HT. Their solar cells, which are among the best for PDI:P3HT-based blends, showed a strongly suppressed P3HT aggregation. Interestingly the analysis of the EQE of our P3HT:P(NDI-TCPDTT) blend cells reveals that amorphous P(NDI-TCPDTT) chains (absorbance centered at 750 nm) rather than crystalline acceptor domains (centered at 850 nm) contribute mostly to the photocurrent. We conclude that excitons formed on crystalline P(NDI-TCPDTT) have a very low probability to generate free carriers, probably due to a short exciton diffusion length, a conclusion that is supported by the very low efficiency of bilayer devices with a pure P(NDI-TCPDTT) layer in Figure 3.

Local absorption measurements with the SNOM, which are sensitive to layer composition on the hundred nanometer length scale, yield further insights into the blend morphology. SNOM images of P3HT:P(NDI2OD-T2) solar cells prepared from p-xylene solution reveal a strong phase separation on the micrometer scale while the granular structure of the SNOM images of layers coated from the p-xylene:CN blend implies a phase separated morphology on the 100 nm length scale. Here, the suppressed preaggregation of the P(NDI2OD-T2) might help to impede strong phase separation of the donor and acceptor polymer. For P3HT:P(NDI-TCPDTT) blends, going from p-xylene to tetralin to chloroform led to a continuous reduction in domain size. A homogeneous morphology is found for the solar cell prepared from chloroform, which yielded the highest short-circuit current at low intensity. However, this high degree of intermixing led to a reduced efficiency to extract free carriers from the layer, as seen by the poorer device performance at high illumination intensity. Clearly, the best compromise is realized for tetralin. We propose that intermixing of the NDI-based copolymers with P3HT generally leads to higher efficiencies, provided that the nanomorphology allows for efficient charge transport to impede recombination of free charges.

To summarize, we were able to fabricate efficient solar cells from regioregular P3HT and two NDI-based low-bandgap copolymers. For the first time, PCE > 1% is achieved for rylene-based polymer acceptors using regioregular P3HT instead of more complex thiophene copolymers.[8,20] Important correlations between the macroscopic absorption and solar cell performance are found, which are further supported by morphological analyses. The high fill factors and the strong improvement of the PCE upon changing device preparation conditions imply that a further optimization of NDI-based solar cells is possible.

Adv. Energy Mater. 2012,
DOI: 10.1002/aenm.201100601

4. Experimental Section

Materials: P(NDI2OD-T2) was synthesized by Polyera Corporation according to a modified procedure to accurately control the polymer molecular weight.[19] Thus, NDI2OD-Br2 (1.10 eq) and 5,5′-bis(trimethylstannyl)-2,2′-bithiophene (1.00 eq) were employed. The molecular weight of P(NDI2OD-T2), as determined by Polymer Laboratories PL-GPC 220 using trichlorobenzene as eluent at 170 °C, is M_n/M_w = 26.200/85.200 g mol^{-1}. P(NDI-TCPDTT) was prepared by the group of Prof. Scherf in a Stille-type coupling as previously described.[55] The molecular weight was M_n/M_w = 36.600/59.300 g mol^{-1}. Highly regioregular P3HT was purchased from Rieke Metals (Sepiolid P200 from BASF, regioregularity >98%, M_n/M_w = 17.500/32.700 g mol^{-1}), PEDOT:PSS (Clevios P VP AI 4083) from Heraeus. All solvents where purchased from Sigma Aldrich, except chloronaphthalene (85% 1-chloronaphthalene with 15% 2-chloronaphthalene) from Alfa Aesar.

Photoemission Spectroscopy: Ultraviolet photoelectron spectroscopy (UPS) measurements were conducted at the Humboldt-Universität using He I radiation ($h\nu$ = 21.22 eV) of a helium discharge lamp. Photo-excited electrons were detected with a Specs Phoibos 100 hemispherical energy analyzer. The error of energy values reported in the text is estimated to be 0.05 eV for UPS. The secondary electron cut-off (SECO) spectra were obtained with the samples biased at −10 V to clear the analyzer work function. Clevios P VP AI 4083 was spin-coated (25 rps) on UV/O_3 treated (30 min) indium-tin oxide glass substrates (sheet resistance 15–30 Ω) from aqueous dispersion and dried at 200 °C for 5 min in ambient conditions. Film deposition of the active material was done in a N_2-filed glovebox (O_2 and H_2O < 1 ppm). P3HT was spin-coated from chloroform solution (6 mg mL^{-1}, 25 rps) and in-situ annealed at 180 °C for 30 min. Films were subsequently washed with chloroform remaining an insolubilized P3HT-interlayer (P3HT-IL) (≈5 nm). Figure S9 (Supporting Information) shows the X-ray photoelectron spectroscopy (XPS) spectrum of a pure PEDOT:PSS layer in comparison to the spectrum of a P3HT-IL on top of PEDOT:PSS. No residual features of the underlying PEDOT:PSS can be detected. Hence, we propose that P3HT forms a closed and rather homogeneous interlayer. P(NDI2OD-T2) and P(NDI-TCPDTT) were spin-coated from chloroform solution (2 mg mL^{-1}, 50 rps) on top of the P3HT-IL.

Solar Cell Preparation and Characterization: BHJ solar cells were prepared in the structure ITO/PEDOT:PSS(35 nm)/blend/Sm(20 nm)/Al(100 nm). Prepatterned ITO substrates were cleaned and O_2 plasma-edged prior to deposition of the PEDOT:PSS anode layer. PEDOT:PSS was used as received and spin-coated in air at 3000 rpm. The substrates were then transferred to a nitrogen filled glovebox and dried 10 min at 180 °C. After the samples had cooled down to room temperature, the active layers were prepared by spin-coating inside the glovebox. Active layer preparation from blends that contain a high CN fraction turned out to be quite challenging due to the high boiling point of CN of about 260 °C, which causes the film to be still wet after spin-coating, resulting in a fast dewetting and the formation of droplets. Therefore, we developed a preparation routine which allows the preparation of very homogeneous films. The essence of this routine is to spin-coat from hot solutions (>80 °C) for a short time, immediately followed by transferring the polymer-covered substrates onto a 200 °C hot plate. Films then dry within 5–10 s, which is fast enough to prevent the formation of solvent droplets due to the bad wetting of the CN-containing solutions. All devices were dried for 1 min at 200 °C. No further annealing was applied during the preparation. This recipe was applied to all solar cells, independent of the solvent used to prepare the blend solutions. The weight ratio of all P3HT:P(NDI2OD-T2) solar cells was kept constant at 1:0.75 which we found is the optimal ratio for cells with a high CN content, although a weight ratio of 1:2 gives slightly better results for pure p-xylene solutions (similar to what was reported earlier[30]). For solar cells from P3HT:P(NDI-TCPDTT) a optimized weight ratio of 1:1.5 is found. Devices were completed by evaporation of 20 nm samarium top electrode, covered by 100 nm aluminium via evaporation through a shadow mask. We used a solution-based sol-gel process to prepare TiO_x cathode layers for inverted solar cells.[56] Films were spin-coated in air from methanol at 5000 rpm and afterwards heated for 10 min at 140 °C inside a nitrogen-filled glovebox. All solar cell characterization steps and sample transfers were made under nitrogen atmosphere. No encapsulation is used. The active layer thickness was determined on the solar cell devices using a Dektak profilometer, where the thickness of the PEDOT:PSS layer (35 nm) is already subtracted. The active area of the solar cells was 16 mm^2.

Solar cells where characterized under simulated sunlight of a Newport Oriel Sol2A solar simulator. The mismatch factor was determined to 0.96 by using a calibrated, KG5 filtered reference silicon solar cell and the intensity was set to 100 mW cm^{-2} if not stated otherwise The irradiance of the solar simulator was monitored before each IV-curve by a calibrated KG5 filtered solar cell which is directly integrated into the home build, temperature controlled sample holder, with the temperature set to 20 °C. For the EQE measurements, frequency modulated monochromatic light of a 150 W halogen lamp, feed into a cornerstone monochromator was used. The current was recorded over a 50 Ohm resistor at the input of a Stanford Research Instruments lock-in amplifier. The setup is calibrated before each measurement by a calibrated Si photodiode from Newport. To avoid second-order diffraction effects, the spectra were separately measured from 300–630 nm and from 630–1100 nm, were for the later measurement a 630 nm edge filter (which absorbs wavelengths below 630 nm) was placed in front of the monochromator. Measured short circuit currents agreed within 5% with the integrated EQE spectra, assuming a reference AM1.5G standard solar spectral distribution defined by the ASTM standard G173-03.

Optical Absorption Measurements: All absorption measurements were performed on a Cary 5000 absorption spectrometer and taken in two beam transmission mode, where one beam contains the sample, whereas in the other a reference sample is placed to subtract the background absorption. Pure copolymer absorption spectra are taken for 1 g L^{-1} concentrated solutions. Absorption spectra of blend films are taken near the centre of the solar cells where no top electrode is evaporated. As reference, a solar cell substrate covered only with PEDOT-PSS was used.

SNOM and AFM Measurements: Scanning near field optical microscopy (SNOM) measurements were performed using a MultiView 2000 from Nanonics Imaging Ltd., Israel. All images were taken in transmission mode. The sample surface was illuminated through a bent fiber optic probe with an aperture of 100 nm, vibrating at a resonant frequency of ≈65 kHz. The transmitted light was collected by a 50x long work distance objective and detected by an avalanche photodiode (APD). Light from a computer controlled, monochromatic light source (SC 450-AOTF, Fianium Ltd, UK) was coupled into the fiber optic probe. This enables optical excitation in the spectral range from 450 to 700 nm, with a spectral band width of about 5 nm. A thin scratch in the film was scanned to calibrate the setup and to obtain the incident photon flux I_0. In parallel to SNOM transmission measurements, the topography was collected simultaneously with the same tip.

In addition, the film topography was investigated with an atomic force microscopy (AFM) setup (Solver SPM, NT-MDT, Russia) in tapping mode with silicon cantilevers from µ-mash Russia (NSG10, 10 nm tip radius).

SNOM images (256 pixels × 256 pixels) are analyzed and displayed with a self-written Mathematica script, while Gwyddion was used to visualize AFM height data.

Supporting Information

Supporting Information is available from the Wiley Online Library or from the author.

Acknowledgements

We thank Steve Albrecht for synthesis of the TiO_x precursor solution for the preparation of the bottom contact of the inverted solar cells. Marcel

Schubert, Daniel Dolfen, and Johannes Frisch acknowledge funding by the German Science Foundation (DFG) within the priority program "Elementary Processes of Organic Photovoltaics" (SPP 1355) and Robert Steyrleuthner by the German Federal Ministry of Science and Education (BMBF) within SOHyb (FKZ 03 × 3525D).

Received: October 10, 2011
Revised: November 3, 2011
Published online:

[1] Y. Y. Liang, Z. Xu, J. B. Xia, S. T. Tsai, Y. Wu, G. Li, C. Ray, L. P. Yu, *Adv. Mater.* **2010**, *22*, E135.
[2] H. J. Son, W. Wang, T. Xu, Y. Y. Liang, Y. E. Wu, G. Li, L. P. Yu, *J. Am. Chem. Soc.* **2011**, *133*, 1885.
[3] S. R. Cowan, W. L. Leong, N. Banerji, G. Dennler, A. J. Heeger, *Adv. Funct. Mater.* **2011**, *21*, 3083.
[4] C. He, D. S. Germack, R. J. Kline, D. M. Delongchamp, D. A. Fischer, C. R. Snyder, M. F. Toney, J. G. Kushmerick, L. J. Richter, *Sol. Energy Mater. Sol. Cells* **2011**, *95*, 1375.
[5] P. Sonar, J. P. F. Lim, K. L. Chan, *Energy Environ. Sci.* **2011**, *4*, 1558.
[6] X. G. Zhao, X. W. Zhan, *Chem. Soc. Rev.* **2011**, *40*, 3728.
[7] A. Facchetti, *Chem. Mater.* **2011**, *23*, 733.
[8] E. J. Zhou, J. Z. Cong, Q. S. Wei, K. Tajima, C. H. Yang, K. Hashimoto, *Angew. Chem.-Int. Ed.* **2011**, *50*, 2799.
[9] T. W. Holcombe, J. E. Norton, J. Rivnay, C. H. Woo, L. Goris, C. Piliego, G. Griffini, A. Sellinger, J.-L. Brédas, A. Salleo, J. M. J. Fréchet, *J. Am. Chem. Soc.* **2011**, *133*, 12106.
[10] D. Mori, H. Benten, J. Kosaka, H. Ohkita, S. Ito, K. Miyake, *ACS Appl. Mater. Interfaces* **2011**, *3*, 2924.
[11] X. M. He, F. Gao, G. L. Tu, D. Hasko, S. Huttner, U. Steiner, N. C. Greenham, R. H. Friend, W. T. S. Huck, *Nano Lett.* **2010**, *10*, 1302.
[12] T. Kietzke, H. H. Horhold, D. Neher, *Chem. Mater.* **2005**, *17*, 6532.
[13] C. Yin, M. Schubert, S. Bange, B. Stiller, M. Castellani, D. Neher, M. Kumke, H. H. Horhold, *J. Phys. Chem. C* **2008**, *112*, 14607.
[14] R. A. Marsh, C. Groves, N. C. Greenham, *J. Appl. Phys.* **2007**, *101*, 083509.
[15] Z. Li, F. Gao, N. C. Greenham, C. R. McNeill, *Adv. Funct. Mater.* **2011**, *21*, 1419.
[16] M. Schubert, C. Yin, M. Castellani, S. Bange, T. L. Tam, A. Sellinger, H. H. Horhold, T. Kietzke, D. Neher, *J. Chem. Phys.* **2009**, *130*, 094703.
[17] D. Gendron, M. Leclerc, *Energy Environ. Sci.* **2011**, *4*, 1225.
[18] X. W. Zhan, A. Facchetti, S. Barlow, T. J. Marks, M. A. Ratner, M. R. Wasielewski, S. R. Marder, *Adv. Mater.* **2011**, *23*, 268.
[19] H. Yan, Z. H. Chen, Y. Zheng, C. Newman, J. R. Quinn, F. Dotz, M. Kastler, A. Facchetti, *Nature* **2009**, *457*, 679.
[20] X. W. Zhan, Z. A. Tan, B. Domercq, Z. S. An, X. Zhang, S. Barlow, Y. F. Li, D. B. Zhu, B. Kippelen, S. R. Marder, *J. Am. Chem. Soc.* **2007**, *129*, 7246.
[21] J. C Blakesley, M. Schubert, R. Steyrleuthner, Z. Chen, A. Facchetti, D. Neher, *Appl. Phys. Lett.* **2011**, *99*, 183310.
[22] R. Steyrleuthner, M. Schubert, F. Jaiser, J. C. Blakesley, Z. Chen, A. Facchetti, D. Neher, *Adv. Mater.* **2010**, *22*, 2799.
[23] J. Rivnay, M. F. Toney, Y. Zheng, I. V. Kauvar, Z. H. Chen, V. Wagner, A. Facchetti, A. Salleo, *Adv. Mater.* **2010**, *22*, 4359.
[24] J. Rivnay, R. Steyrleuthner, L. H. Jimison, A. Casadei, Z. H. Chen, M. F. Toney, A. Facchetti, D. Neher, A. Salleo, *Macromolecules* **2011**, *44*, 5246.
[25] S. S. van Bavel, E. Sourty, G. de With, J. Loos, *Nano Lett.* **2009**, *9*, 507.
[26] S. S. van Bavel, M. Barenklau, G. de With, H. Hoppe, J. Loos, *Adv. Funct. Mater.* **2010**, *20*, 1458.
[27] J. Jo, S. S. Kim, S. I. Na, B. K. Yu, D. Y. Kim, *Adv. Funct. Mater.* **2009**, *19*, 866.
[28] K. Szendrei, D. Jarzab, Z. H. Chen, A. Facchetti, M. A. Loi, *J. Mater. Chem.* **2010**, *20*, 1317.
[29] J. R. Moore, S. Albert-Seifried, A. Rao, S. Massip, B. Watts, D. J. Morgan, R. H. Friend, C. R. McNeill, H. Sirringhaus, *Adv. Energy Mater.* **2011**, *1*, 230.
[30] S. Fabiano, Z. Chen, S. Vahedi, A. Facchetti, B. Pignataro, M. A. Loi, *J. Mater. Chem.* **2011**, *21*, 5891.
[31] K. J. Ihn, J. Moulton, P. Smith, *J. Polym. Sci., Part B: Polym. Phys.* **1993**, *31*, 735.
[32] S. Berson, R. De Bettignies, S. Bailly, S. Guillerez, *Adv. Funct. Mater.* **2007**, *17*, 1377.
[33] G. Dennler, M. C. Scharber, C. J. Brabec, *Adv. Mater.* **2009**, *21*, 1323.
[34] D. M. Huang, S. A. Mauger, S. Friedrich, S. J. George, D. Dumitriu-LaGrange, S. Yoon, A. J. Moule, *Adv. Funct. Mater.* **2011**, *21*, 1657.
[35] C. Yin, B. Pieper, B. Stiller, T. Kietzke, D. Neher, *Appl. Phys. Lett.* **2007**, *90*, 133502.
[36] J. Frisch, A. Vollmer, J. P. Rabe, N. Koch, *Org. Electron.* **2011**, *12*, 916.
[37] Z. L. Guan, J. B. Kim, H. Wang, C. Jaye, D. A. Fischer, Y. L. Loo, A. Kahn, *Org. Electron.* **2010**, *11*, 1779.
[38] I. Lange, J. C. Blakesley, J. Frisch, A. Vollmer, N. Koch, D. Neher, *Phys. Rev. Lett.* **2011**, *106*, 216402.
[39] B. P. Rand, D. P. Burk, S. R. Forrest, *Phys. Rev. B* **2007**, *75*, 115327.
[40] J. C. Blakesley, D. Neher, *Phys. Rev. B* **2011**, *84*, 075210.
[41] R. F. Fink, J. Seibt, V. Engel, M. Renz, M. Kaupp, S. Lochbrunner, H. M. Zhao, J. Pfister, F. Wurthner, B. Engels, *J. Am. Chem. Soc.* **2008**, *130*, 12858.
[42] F. Wurthner, *Chem. Commun.* **2004**, 1564.
[43] J. Clark, J. F. Chang, F. C. Spano, R. H. Friend, C. Silva, *Appl. Phys. Lett.* **2009**, *94*, 163306.
[44] K. G. Jespersen, W. J. D. Beenken, Y. Zaushitsyn, A. Yartsev, M. Andersson, T. Pullerits, V. Sundstrom, *J. Chem. Phys.* **2004**, *121*, 12613.
[45] T. Schuettfort, S. Huettner, S. Lilliu, J. E. Macdonald, L. Thomsen, C. R. McNeill, *Macromolecules* **2011**, *44*, 1530.
[46] C. Uhrich, D. Wynands, S. Olthof, M. K. Riede, K. Leo, S. Sonntag, B. Maennig, M. Pfeiffer, *J. Appl. Phys.* **2008**, *104*, 043107.
[47] F. C. Spano, *J. Chem. Phys.* **2005**, *122*, 234701.
[48] J. Clark, C. Silva, R. H. Friend, F. C. Spano, *Phys. Rev. Lett.* **2007**, *98*, 206406.
[49] M. Koppe, C. J. Brabec, S. Heiml, A. Schausberger, W. Duffy, M. Heeney, I. McCulloch, *Macromolecules* **2009**, *42*, 4661.
[50] S. T. Turner, P. Pingel, R. Steyrleuthner, E. J. W. Crossland, S. Ludwigs, D. Neher, *Adv. Funct. Mater.* **2011**, *21*, 4640.
[51] D. Veldman, S. C. J. Meskers, R. A. J. Janssen, *Adv. Funct. Mater.* **2009**, *19*, 1939.
[52] M. Caironi, M. Bird, D. Fazzi, Z. H. Chen, R. Di Pietro, C. Newman, A. Facchetti, H. Sirringhaus, *Adv. Funct. Mater.* **2011**, *21*, 3371.
[53] E. Ahmed, G. Q. Ren, F. S. Kim, E. C. Hollenbeck, S. A. Jenekhe, *Chem. Mater.* **2011**, *23*, 4563.
[54] V. Kamm, G. Battagliarin, I. A. Howard, W. Pisula, A. Mavrinskiy, C. Li, K. Mullen, F. Laquai, *Adv. Energy Mater.* **2011**, *1*, 297.
[55] C. J. Kudla, D. Dolfen, K. J. Schottler, J. M. Koenen, D. Breusov, S. Allard, U. Scherf, *Macromolecules* **2010**, *43*, 7864.
[56] J. Y. Kim, S. H. Kim, H. H. Lee, K. Lee, W. L. Ma, X. Gong, A. J. Heeger, *Adv. Mater.* **2006**, *18*, 572.

Adv. Energy Mater. **2012**,
DOI: 10.1002/aenm.201100601

ADVANCED ENERGY MATERIALS

Supporting Information

for *Adv. Energy Mater.*, DOI: 10.1002/aenm. 201100601

Influence of Aggregation on the Performance of All-Polymer Solar Cells Containing Low-Bandgap Naphthalenediimide Copolymers

*Marcel Schubert , Daniel Dolfen , Johannes Frisch , Steffen Roland , Robert Steyrleuthner , Burkhard Stiller , Zhihua Chen , Ullrich Scherf , Norbert Koch , Antonio Facchetti , and Dieter Neher **

Submitted to ADVANCED ENERGY MATERIALS

Supporting Information

for *Adv. Energy Mater.*, DOI: aenm.201100601

Influence of aggregation on the performance of all-polymer solar cells containing low-bandgap naphthalenediimide-copolymers.

*Marcel Schubert, Daniel Dolfen, Johannes Frisch, Steffen Roland, Robert Steyrleuthner, Burkhard Stiller, Zhihua Chen, Ullrich Scherf, Norbert Koch, Antonio Facchetti and Dieter Neher**

Marcel Schubert, Steffen Roland, Robert Steyrleuthner, Burkhard Stiller, Prof. Dr. Dieter Neher
University of Potsdam, Institute of Physics and Astronomy,
Karl-Liebknecht-Str. 24-25, 14476, Potsdam (Germany)
E-mail: neher@uni-potsdam.de

Daniel Dolfen, Prof. Dr. Ullrich Scherf
University of Wuppertal, Macromolecular Chemistry, 42119 Wuppertal (Germany)

Johannes Frisch, Prof. Dr. Norbert Koch
Humboldt University Berlin, Institute of Physics, Newtonstr. 15, 12489 Berlin (Germany)

Zhihua Chen, Prof. Dr. Antonio Facchetti
Polyera Corporation, 8045 Lamon Avenue, Illinois 60077 (USA)

Keywords: Aggregation; Morphology; Naphthalenediimide; Organic Semiconductors; Organic Photovoltaics; P(NDI2OD-T2)

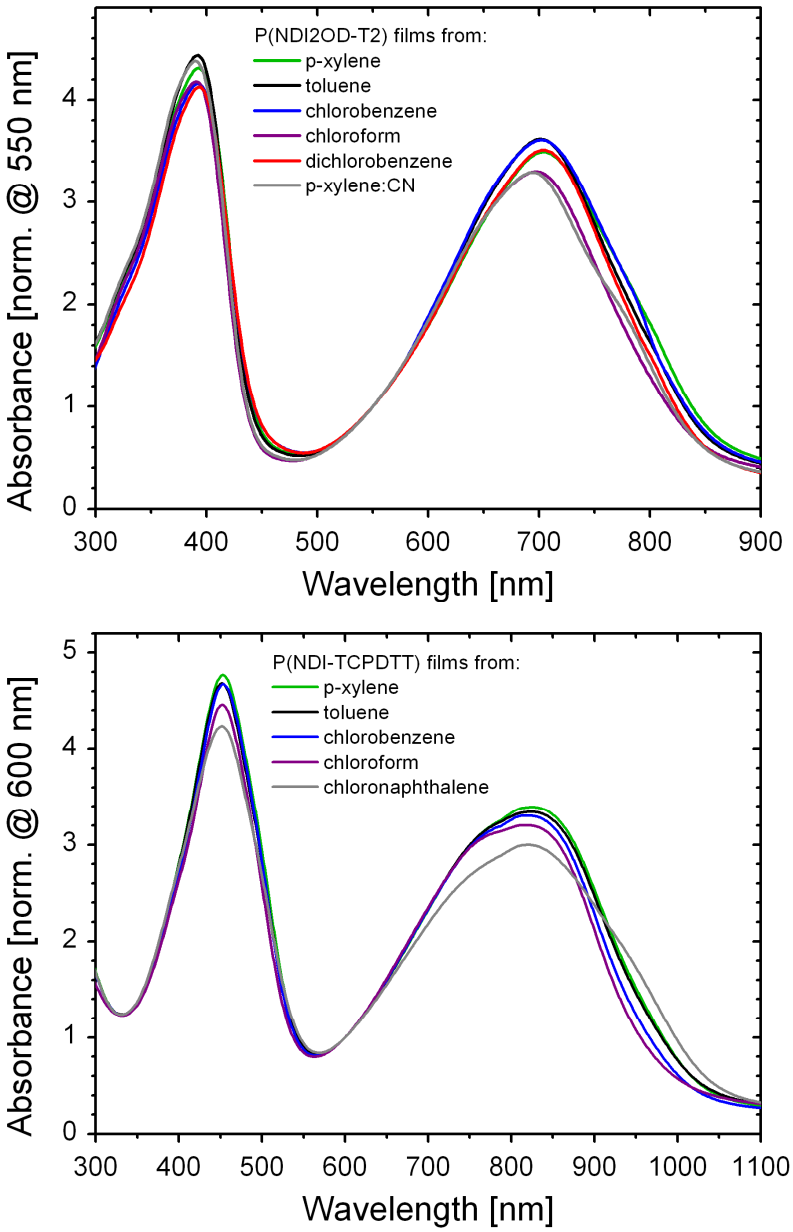

Figure S1. Absorption spectra of pristine P(NDI2OD-T2) (top) and P(NDI-TCPDTT) (botton) films prepared from various organic solvents. The film thickness was 60–100 nm and 40–60 nm, for P(NDI2OD-T2) and P(NDI-TCPDTT), respectively.

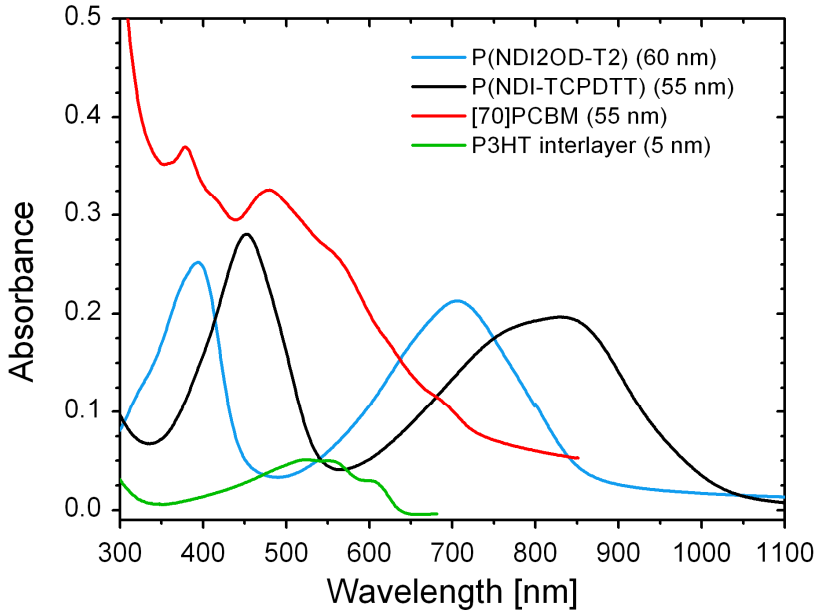

Figure S2. Film absorption spectra of PC[70]BM (red), P(NDI2OD-T2) (blue) and P(NDI-TCPDTT) (black). All films were spin-coated on glass substrates and prepared in parallel to bilayer solar cells (see Figure 2) following the same recipe. The absorption of the P3HT interlayer, prepared on top of PEDOT:PSS, is also shown. The thickness of all layers is displayed in the graph.

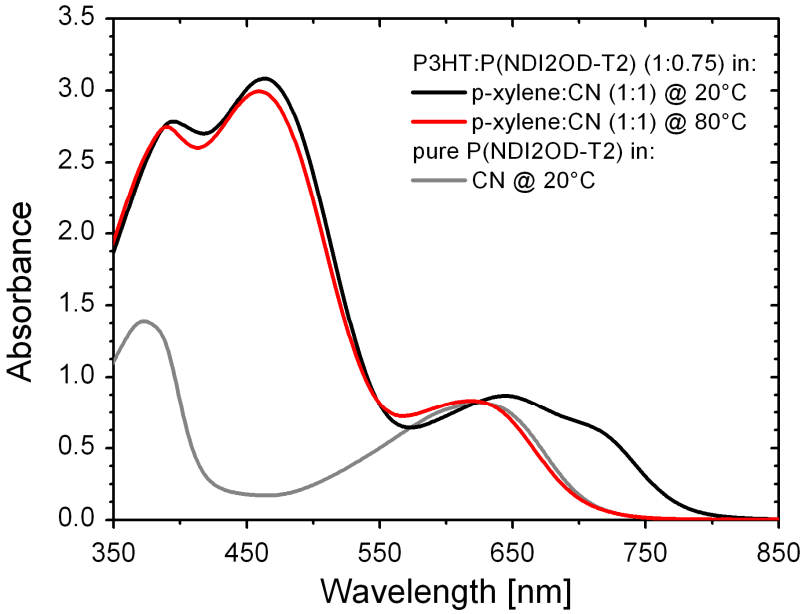

Figure S3. Absorption spectra of a mixture of P3HT with P(NDI2OD-T2) in 1:1 p-xylene:CN at 20°C (black) and at 80°C (red). For comparison, the absorption of pure P(NDI2OD-T2) in CN (gray) is also shown. The absorption maximum at about 460 nm, typical for non-aggregated P3HT and the absence of the vibronic P3HT features confirm that no aggregation or gel formation of the P3HT takes place in the mixed solvent.

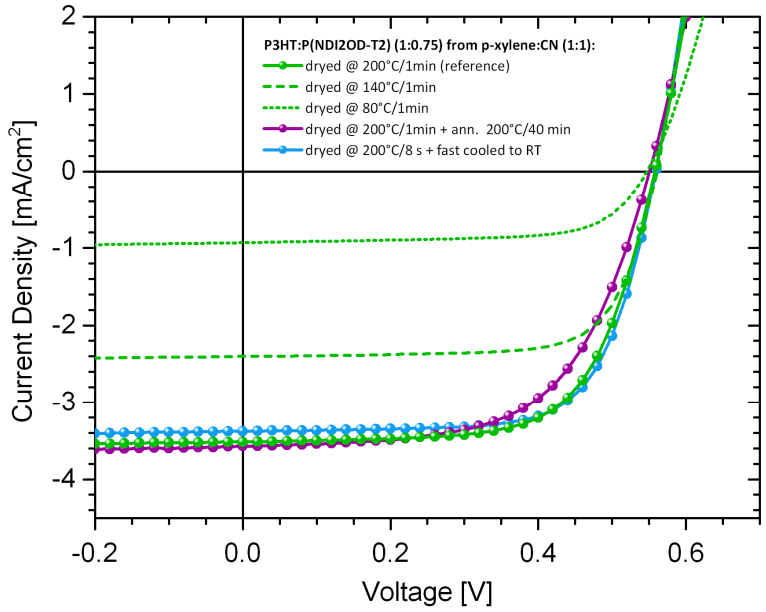

Figure S4. Influence of the drying and annealing procedure on the *J-V* characteristics of P3HT:P(NDI2OD-T2) (1:0.75) BHJ solar cells, all spin-coated from the same 1:1 solvent mixture of p-xylene:CN. The solar cell denoted as reference (green spheres) was dried at 200°C and gives best solar cell performance. Here, the film, which is still wet after spin-coating, dries within 8 s and then stays at the hot plate for 1 min. It is found that the temperature at which the film dries strongly influence device performance (dashed and dotted green line). On the other hand, fast cooling of the solar cell immediately after drying of the film (by putting it on a metal plate, blue spheres) or an additional thermal annealing step (violet spheres) only slightly affect the *J-V* characteristics.

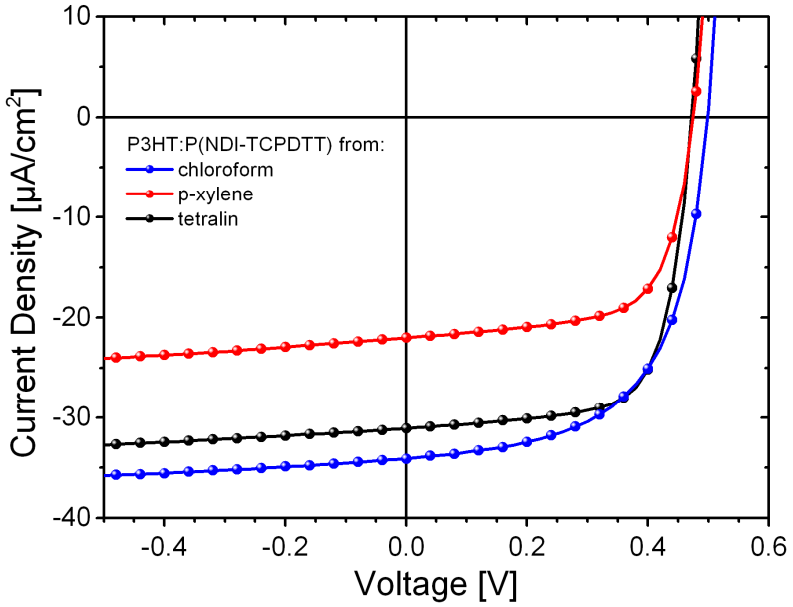

Figure S5. *J-V* characteristics of P3HT:P(NDI-TCPDTT) BHJ solar cells of the same devices as displayed in Figure 6 but at a lower illumination intensity of about 1.3 mW/cm^2

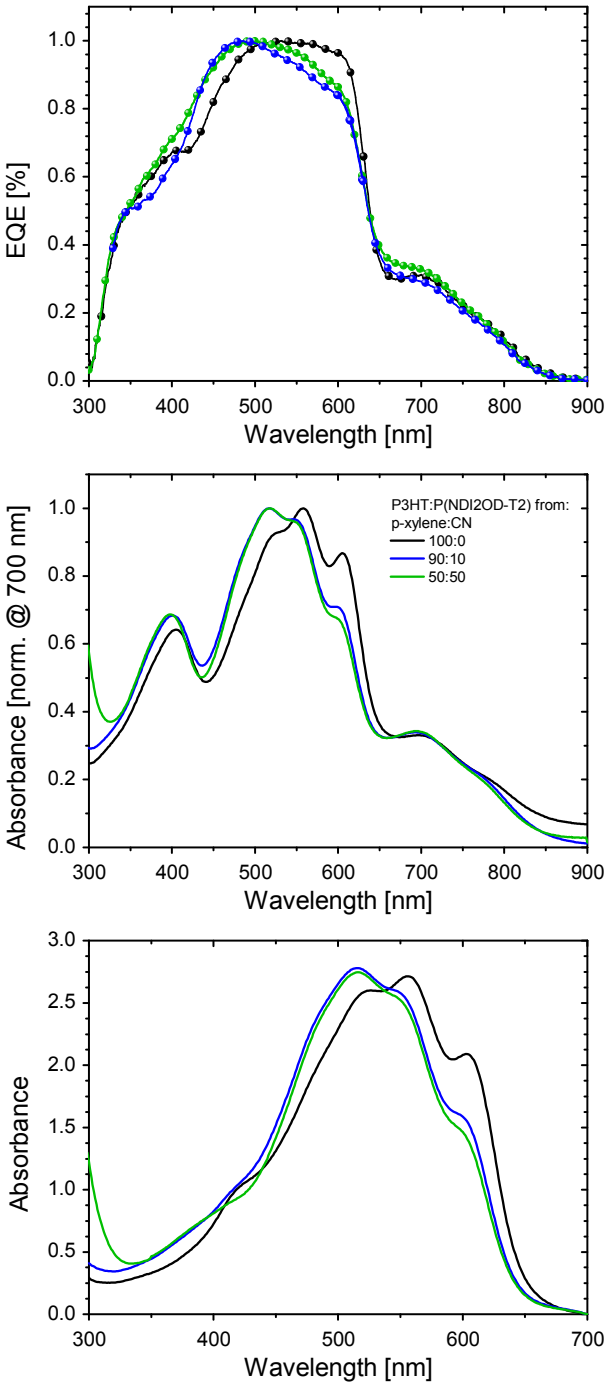

Figure S6. Normalized EQE and absorption spectra of P3HT: P(NDI2OD-T2) layers coated from p-xylene:CN solvent mixtures. Also shown is the contribution of the P3HT phase to the absorption as obtained by subtracting the absorption of a pristine P(NDI2OD-T2) layer coated from p-xylene from the total absorption in Figure 7a.

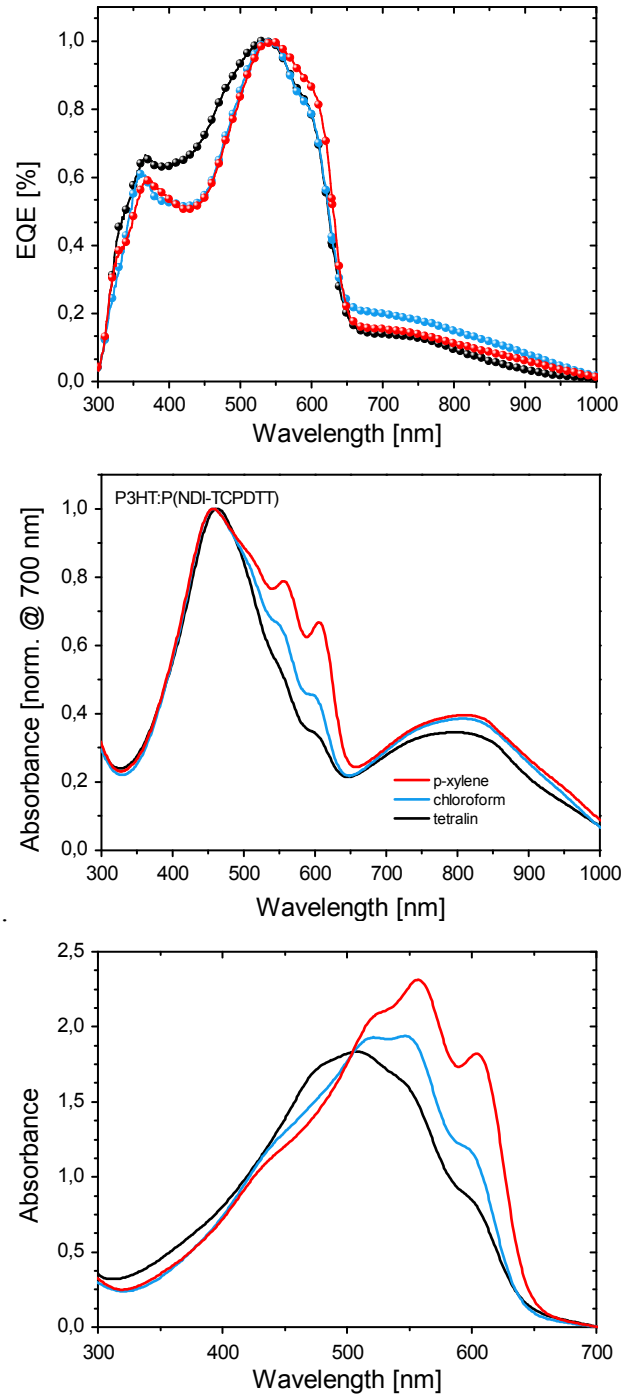

Figure S7. Normalized EQE and absorption spectra of P3HT:P(NDI-TCPDTT) layers coated from different solvents. Also shown is the contribution of the P3HT phase to the absorption as obtained by subtracting the absorption of a pristine P(NDI-TCPDTT) layer coated from p-xylene from the total absorption in Figure 7b.

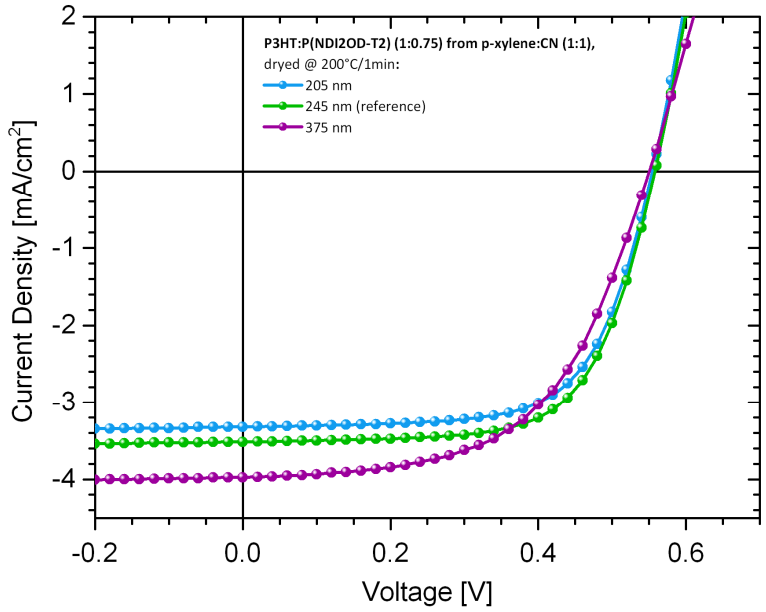

Figure S8. *J-V* characteristics of P3HT:P(NDI2OD-T2) (1:0.75) BHJ solar cells, all spin-coated from the same 1:1 solvent mixture of p-xylene:CN at 3000 rpm (blue), 2000 rpm (green) and 1200 rpm (violet). The corresponding active layer thicknesses are given in the graph. The green curve is denoted as reference since it was prepared following the recipe that gives best solar cells. Devices with smaller thickness than that of the reference cells show decreasing short circuit currents but similar fill factors, while thicker cells show even higher currents but decreasing fill factors, possibly due to the onset of space-charge and/or recombination effects.

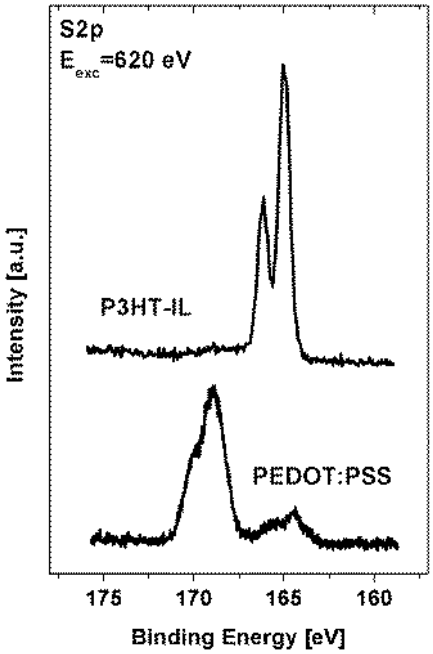

Figure S9. XPS spectra from pure PEDOT:PSS and from P3HT-IL on top of PEDOT:PSS. The illuminated area is about 2 mm^2 and the mean free path of the electrons is estimated to ~5 nm.

Advanced Functional Materials

Correlated Donor/Acceptor Crystal Orientation and Charge-Transfer State Recombination Controls Photocurrent Generation in All-Polymer Solar Cells

--Manuscript Draft--

Manuscript Number:	adfm.201304216
Full Title:	Correlated Donor/Acceptor Crystal Orientation and Charge-Transfer State Recombination Controls Photocurrent Generation in All-Polymer Solar Cells
Article Type:	Full Paper
Keywords:	photocurrent generation; charge-transfer state recombination; polymer crystals; alternative acceptors; organic solar cells
Corresponding Author:	Dieter Neher, Prof. University of Potsdam Potsdam, GERMANY
Additional Information:	
Question	**Response**
Please submit a plain text version of your cover letter here. **If you are submitting a revision of your manuscript, please do not overwrite your original cover letter. There is an opportunity for you to provide your responses to the reviewers later; please do not add them here.**	Dear Sir or Madam, Enclosed is the manuscript “Correlated Donor/Acceptor Crystal Orientation and Charge-Transfer State Recombination Controls Photocurrent Generation in All-Polymer Solar Cells” by Marcel Schubert et al., which we like to submit for publication as a Full Paper in Advanced Functional Materials. Statement on manuscript’s significance: New polymers with high electron mobilities have spurred research in organic solar cells using polymer rather than fullerene acceptors due to their potential of increased diversity, stability and scalability. However, all-polymer solar cells have struggled to keep up with the steadily increasing power conversion efficiency of polymer:fullerene cells. The lack of knowledge about the dominant recombination process as well as the missing concluding picture on the role of the semi-crystalline microstructure of conjugated polymers in the free charge carrier generation process impede a systematic optimization of all-polymer solar cells. In this manuscript, we combined advanced structural and photo-physical characterization on a series of poly(3-hexylthiphene) and P(NDI2OD-T2) blend devices to examine the role of the microscopic morphology in the free charge carrier generation process. For this, all relevant process, starting from the dissociation of excitons, the charge transfer states recombination and finally the free charge carrier generation were investigated. Our studies further reveal the effect of chloronapthalene co-solvent in reducing domain size, altering domain purity and reorienting the acceptor polymer crystals to be coincident with those of the donor. From this we conclude that efficient separation of charge transfer states at polymer/polymer interfaces may necessitate correlated donor/acceptor crystal orientation, which represents an extra hurtle compared with the isotropic fullerene acceptor in realizing efficient devices. This has not yet described in literature before and provides an explanation for the limited performance of polymeric acceptors. Furthermore, our findings contribute significantly to the more fundamental question of how the semi-crystalline morphology of organic semi-conductors affects their photovoltaic performance. Sincerely, Dieter Neher
Corresponding Author Secondary Information:	
Corresponding Author's Institution:	University of Potsdam

Corresponding Author's Secondary Institution:	
First Author:	Marcel Schubert
First Author Secondary Information:	
Order of Authors:	Marcel Schubert
	Brian A. Collins, Dr.
	Hannah Mangold
	Ian A Howard, Dr.
	Wolfram Schindler, Dr.
	Koen Vandewal, Dr.
	Steffen Roland
	Jan Behrends, Dr.
	Felix Kraffert
	Robert Steyrleuthner
	Zhihua Chen, Dr.
	Konstantinos Fostiropoulos, Dr.
	Robert Bittl, Prof. Dr.
	Alberto Salleo, Prof. Dr.
	Antonio Facchetti, Prof. Dr.
	Frederic Laquai, Dr.
	Harald W. Ade, Prof. Dr.
	Dieter Neher, Prof.
Order of Authors Secondary Information:	
Abstract:	New polymers with high electron mobilities have spurred research in organic solar cells using polymer rather than fullerene acceptors due to their potential of increased diversity, stability and scalability. However, all-polymer solar cells have struggled to keep up with the steadily increasing power conversion efficiency of polymer:fullerene cells. The lack of knowledge about the dominant recombination process as well as the missing concluding picture on the role of the semi-crystalline microstructure of conjugated polymers in the free charge carrier generation process impede a systematic optimization of all-polymer solar cells. We examine these issues by combining structural and photo-physical characterization on a series of poly(3-hexylthiphene) and P(NDI2OD-T2) blend devices. Our experiments reveal that geminate recombination is the major loss channel for photo-excited charge carriers. Direct detection of the charge-transfer state supports this conclusion. Advanced X-ray and electron-based studies reveal the effect of chloronapthalene co-solvent in reducing domain size, altering domain purity and reorienting the acceptor polymer crystals to be coincident with those of the donor. This reorientation correlates well with increased photocurrent from devices. Thus, efficient separation of charge transfer states at polymer/polymer interfaces may necessitate correlated donor/acceptor crystal orientation, which represents an extra hurtle compared with the isotropic fullerene acceptors.

Submitted to ADVANCED FUNCTIONAL MATERIALS

DOI: 10.1002/adfm.((please add manuscript number))
Article type: Full Paper

Correlated Donor/Acceptor Crystal Orientation and Charge-Transfer State Recombination Controls Photocurrent Generation in All-Polymer Solar Cells

*Marcel Schubert, Brian A. Collins, Hannah Mangold, Ian A. Howard, Wolfram Schindler, Koen Vandewal, Steffen Roland, Jan Behrends, Felix Kraffert, Robert Steyrleuthner, Zhihua Chen, Konstantinos Fostiropoulos, Robert Bittl, Alberto Salleo, Antonio Facchetti, Frédéric Laquai, Harald W. Ade, and Dieter Neher**

Marcel Schubert, Steffen Roland, Robert Steyrleuthner, and Prof. Dr. Dieter Neher
University of Potsdam, Institute of Physic and Astronomy, 14476 Potsdam, Germany
neher@uni-potsdam.de

Dr. Brian A. Collins, and Prof. Dr. Harald W. Ade
North Carolina State University, Department of Physics, Raleigh, NC 27695, USA

Dr. Brian A. Collins
National Institute of Standards and Technology (NIST), Gaithersburg, USA

Hannah Mangold, Dr. Ian A. Howard, and Dr. Frédéric Laquai
Max-Planck-Institute for Polymer Research (MPI-P), 55128 Mainz, Germany

Dr. Koen Vandewal, and Prof. Dr. Alberto Salleo
Stanford University, Department of Materials Science, Stanford, CA 94305-4034, USA

Dr. Wolfram Schindler and Dr. Konstantinos Fostiropoulos
Helmholtz-Zentrum Berlin (HZB), Institute for Heterogeneous Materials Systems, 14109 Berlin, Germany

Dr. Jan Behrends, Felix Kraffert, Robert Steyrleuthner, and Prof. Dr. Robert Bittl
Free University Berlin, Department of Physics, 14195 Berlin, Germany

Dr. Zhihua Chen and Prof. Dr. Antonio Facchetti
Polyera Corporation, Illinois 60077, USA

Keywords: photocurrent generation, charge-transfer state recombination, polymer crystals, alternative acceptors, organic solar cells

Abstract

New polymers with high electron mobilities have spurred research in organic solar cells using polymer rather than fullerene acceptors due to their potential of increased diversity, stability and scalability. However, all-polymer solar cells have struggled to keep up with the steadily increasing power conversion efficiency of polymer:fullerene cells. The lack of knowledge about the dominant recombination process as well as the missing concluding picture on the role of the semi-crystalline microstructure of conjugated polymers in the free charge carrier generation process impede a systematic optimization of all-polymer solar cells. We examine these issues by combining structural and photo-physical characterization on a series of poly(3-hexylthiphene) and P(NDI2OD-T2) blend devices. Our experiments reveal that geminate recombination is the major loss channel for photo-excited charge carriers. Direct detection of the charge-transfer state supports this conclusion. Advanced X-ray and electron-based studies reveal the effect of chloronapthalene co-solvent in reducing domain size, altering domain purity and reorienting the acceptor polymer crystals to be coincident with those of the donor. This reorientation correlates well with increased photocurrent from devices. Thus, efficient separation of charge transfer states at polymer/polymer interfaces may necessitate correlated donor/acceptor crystal orientation, which represents an extra hurtle compared with the isotropic fullerene acceptors.

1. Introduction

Conjugated polymers represent the most versatile material class in the field of organic photovoltaics. Their great chemical variability allows the modification of their optical, mechanical, energetic and charge transporting properties. Polymers with large electron affinities are being designed in an attempt to rival fullerene as the electron accepting moiety in organic solar cells (OSCs). Over the last decade, fullerenes have been used in almost all efficiency-breaking, solution-processed OSCs,[1-3] while devices incorporating polymeric acceptors lag significantly behind their fullerene counterparts, with modest power conversion efficiencies (PCE) between 3 and 4% at best.[4-8] A low external quantum efficiency (EQE) is primarily responsible for the poor performance of such all-polymer devices. To the best of our knowledge, the highest reported EQE of an all-polymer solar cell does not exceed 50%.[8]

In general, the primary excitation formed by photon absorption in an organic solar cell is a strongly bound, Frenkel-type singlet exciton. Charge transfer at a donor/acceptor heterojunction is so far the most efficient process to overcome the Coulombic interactions of this excited electron-hole pair, and produce spatially separated charges. However, charge transfer does not necessarily lead to free, uncorrelated electrons and holes. Rather, Coulombically bound interfacial electronic states can be formed that strongly influence the energy conversion efficiency of the OSC. The term charge-transfer state (CTS) is commonly used to describe such weakly-interacting interfacial excited-state species. Often a CTS has weak optical features discernable in the luminescence or absorbance spectra of D/A mixtures which assists in photophysical characterization of their properties and influence on device physics. For example this spectral information was used to disclose a direct correlation of CTS energy and open circuit voltage (V_{OC}).[9] In blends of conjugated polymers, previous work has assigned geminate recombination via CTS as a dominant pathway for the decay of the photo-induced excitations.[10-13] Thus, the low EQE, generally observed in all-polymer solar cells, suggest that geminate recombination is a common process in polymer-polymer blends.

It has been recently suggested that the efficiency to split CTS into free carriers is controlled by the extent of charge delocalization on the donor or acceptor.[14-18] However, the specific structural or electronic properties that assist exciton dissociation remain unclear. For many years, the high electron mobility was an almost exclusive feature of fullerenes in OSCs,[19, 20] especially when compared to common acceptor polymers, [6, 11, 21] and a possible key to their superior performance.[17, 22] In the last years several conjugated polymers with excellent electron mobility have been discovered.[23-28] The prototype is the donor/acceptor copolymer

P(NDI2OD-T2) which reaches mobilities of 0.85 $cm^2V^{-1}s^{-1}$ and 5×10^{-2} $cm^2V^{-1}s^{-1}$, in organic field-effect transistors (OFET) and single carrier diodes, respectively.[23, 29, 30] In addition, the large electron affinity of about -4 eV, the low optical bandgap of 1.45 eV and the manifold of available data on charge transport[23, 29-31], microscopic structure[31-33] and optoelectronic properties[34] render P(NDI2OD-T2) a good candidate as model electron-accepting material. Surprisingly, despite the excellent properties of the neat P(NDI2OD-T2) polymer, the first results of photoactive blends of P(NDI2OD-T2) in combination with P3HT as donor were surprisingly poor, with PCEs ranging between 0.2 and 0.6%.[35, 36] By incorporating chloronaphthalene (CN) as co-solvent and applying a high temperature drying process during film formation, we could increase the efficiency to 1.4%.[37] Despite the higher efficiency and excellent light harvesting properties, the solar cells were still limited by the modest EQE of about 20%.

It is the aim of this paper to address the reasons for the low photocurrent generation yields of blends of the donor P3HT and the acceptor P(NDI2OD-T2). Special emphasis is paid to the processes controlling free charge carrier generation to guide future improvements of all-polymer solar cells. Through variation of processing parameters, the magnitude of photocurrent produced by the solar cells was systematically explored and correlated to changes of the orientation of polymer crystallites by advanced structural and photo-physical characterization. Our analysis suggests that face-to-face staking of the D/A polymer crystals is necessary to generated free charges, while misoriented chains inescapably cause geminate recombination of the CTS. Furthermore, we observe that exciton self-trapping in the crystalline acceptor phase represents an additional major loss channel. Our results imply that an optimized relative orientation of the D/A crystallites is required to achieve high quantum efficiencies in all-polymer solar cells.

2. Results and Discussion

2.1 Solar cell performance

Firstly, the impact of film preparation conditions on the solar cell performance will be presented. We have previously shown that the mixture of solvents from which the active layer is cast has a large influence on the device performance. Specifically, we found that the amount of chloronaphthalene (CN) in the solution mixture with xylene (Xy) was a critical parameter in the solar cell optimization process.[37] **Figure 1**.a shows solar cell characteristics for different mixing ratios of Xy and CN. Both J_{SC} and *PCE* are found to increases with

increasing CN content by about one order of magnitude and reach a maximum of 3 mA/cm^2 and 1.1%, respectively, at 50 vol.% CN. In a recent study we could demonstrate that the high boiling point of the solvent CN suppresses the pre-aggregation of P(NDI2OD-T2) in solution.[34, 37] On the other hand, we see only slight changes in solar cell performance when the co-solvent Xy is replaced by other solvents (Supporting Material). Thus, the increase in photocurrent is mainly due to the addition of CN, while the co-solvent is only needed to prevent dewetting[37] of the film during the drying step at 200°C. After drying, the performance is not affected by further thermal annealing. Even a 1h solvent annealing step at elevated temperatures leaves the performance of the best blends unchanged (Supporting Material), which demonstrates the excellent thermal stability of the optimized P3HT:P(NDI2OD-T2) blends. A remarkable feature of the devices presented in **Figure 1**.a is the consistently high fill factor, ranging from 62% to 65% despite a 300 nm film thickness. This indicates that the bias voltage dependence of the photocurrent is small, which has important implications for our understanding of the device physics. Namely, it indicates that the electric field and voltage dependence of free charge carrier generation and recombination are almost negligible up to the voltage which produces the maximum output power. We will investigate this in more details in a forthcoming study. In the further experimentation and analysis, we will elucidate on the limitations of the short-circuit currents, where the external (*EQE*) and internal quantum efficiency (*IQE*) measurements will give a first insight.

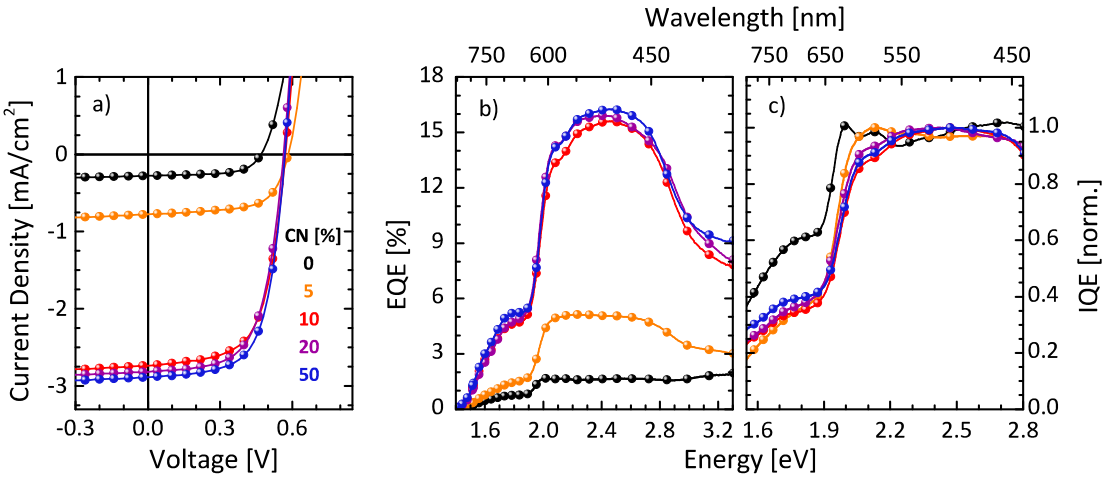

Figure 1 a) Current density-voltage characteristics of P3HT:P(NDI2OD-T2) solar cells prepared from Xy:CN solvent mixtures, measured under AM 1.5 G conditions. The CN concentration is indicated in the graph. The active layer thickness and donor:acceptor composition was held constant at 300 nm and 1:0.75, respectively. b) EQE and c) normalized IQE spectra of the same devices.

The EQE spectra are given in **Figure 1**.b. The maximum EQE varies between the cells proportional to their photocurrent and reaches 16% in the best performing cell. All spectra

have a similar shape and composition. The maximum EQE is measured between 2.8 and 2.0 eV, i.e. the range where P3HT constitutes the maximum absorption. In the range of maximum P(NDI2OD-T2) absorbance and the absence of P3HT absorption, from 1.9 eV to 1.6 eV, the EQE drops significantly to about one third of the maximum value. However, in order to compare the photon-to-electron conversion yields more meaningfully, we calculate the internal quantum efficiency (IQE), which is the EQE corrected by the fraction of photons absorbed in the active layer. In absolute values, the maximum EQE and IQE are almost identical and differ by less than one percent in the range displayed in **Figure 1**.c. This is a consequence of the large film thickness. Here, we make a first conclusion that the low IQE of the P3HT:P(NDI2OD-T2) solar cells is responsible for the low photocurrent and represents the device limiting processes. To compare the spectral shape of the IQE, **Figure 1**.c shows the normalized spectra of all devices. The IQE in the P(NDI2OD-T2) phase is only between 40% (in the CN-cast devices) and 60% (in the Xy-cast device) of the value measured in the P3HT domains. Thus, beside the overall small maximum IQE values, an additional process further lowers the charge carrier generation efficiency of excitons absorbed by P(NDI2OD-T2) as compared to excitations absorbed by P3HT.

Table 1 Averaged solar cell parameters (numbers in parentheses denote the uncertainty in the last digit), photoluminescence quenching efficiency (PQE) and active layer thickness *d* (numbers in square brackets denote the root-mean square roughness measured by atomic force microscopy) of the different P3HT:P(NDI2OD-T2) blend films.

Xy:CN	Drying	J_{SC} [mA/cm^2]	*FF* [%]	V_{OC}	η [%]	*PQE* (%) (P3HT/ P(NDI2OD-T2))	*d* [RMS] [nm]
100:0	as cast	0.27 (1)	62 (1)	0.47 (1)	0.08 (1)	91.9 / 44.7	300 [15]
95:5	dry@200°C	0.77 (6)	64 (1)	0.58 (1)	0.29 (2)	91.5 / -	300 [27]
90:10	"	2.8 (1)	63 (1)	0.57 (1)	0.99 (3)	94.9 / -	295 [6]
80:20	"	2.9 (2)	62 (1)	0.56 (1)	1.00 (6)	95.6 / -	300 [6]
50:50	"	2.9 (2)	65 (1)	0.57 (1)	1.07 (8)	96.2 / 54.8	300 [4]

2.2 Blend domain structure

To elucidate the influence of CN on the all-polymer blend film morphology, we combined resonant soft X-ray scattering (R-SoXS) and energy-filtered transmission electron microscopy (EF-TEM) measurements. Compared to conventional TEM, where the contrast relies mainly on the difference in mass density, EF-TEM shows enhanced chemical contrast. We analyzed the electron energy loss spectrum at the sulphur ionization edge (165 eV), where the interaction of the transmitted electrons with the sulphur containing thiophene units reduces their kinetic energy. Due to the three times larger sulphur density of P3HT compared to P(NDI2OD-T2), energy filtering provides sufficient chemical contrast between both polymers. Consequently, bright areas correspond to P3HT-rich domains, while dark areas are P(NDI2OD-T2)-rich domains. The EF-TEM sulphur map of the Xy-cast blend film is given in **Figure 2**.a. It displays a strongly phase separated morphology comprised of irregular shaped P3HT domains with a typical diameter of 1 µm, and a network of P(NDI2OD-T2) fibrils, which have a width of 0.5-1 µm. Additional scanning transmission X-ray microscopy (STXM) measurements reveal that the darkest regions in EF-TEM sulphur maps are regions of pure P(NDI2OD-T2) which probably represent crossing points of several fiber bundles (see Figure S4). From the EF-TEM, STXM and additional scanning Kelvin probe microscopy (SPKM, see Figure S5) data it is also apparent that the P(NDI2OD-T2) fiber bundles are embedded within a matrix of P3HT. Furthermore, the P3HT domains that do not overlap with P(NDI2OD-T2) fibres, visible as the brightest domains in the EF-TEM elemental maps, show an average P3HT concentration between 80 and 90 wt% (see line scans of STXM composition maps in Figure S4), indicating that these domains are rather impure and contain a significant fraction of P(NDI2OD-T2). The domain structure of the Xy-cast film is consistent with previous studies that used either STXM or near-field scanning optical microscopy (NSOM).[35, 37] However, the resolution of the NSOM and STXM was too small to disclose the morphology of the Xy:CN-cast films. A sufficient resolution is provided by EF-TEM and **Figure 2**.b reveals that the addition of CN strongly affects the structure of the P(NDI2OD-T2) domains. Compared to the micrometer large fibrillar network in the Xy-cast blend, P(NDI2OD-T2) arranges in circular domains in the 50:50 Xy:CN-cast film. Embedded in a P3HT matrix, these domains have a typical diameter between 30 and 50 nm, rather independent on the active layer thickness (see EF-TEM thickness series in Figure S6).

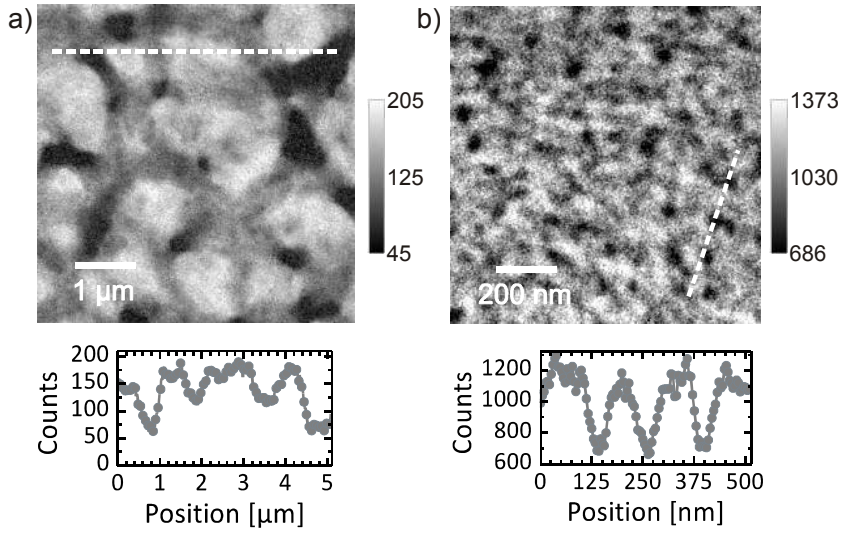

Figure 2 EF-TEM sulphur maps of ***a)*** Xy-cast and ***b)*** 50:50 Xy:CN-cast P3HT:P(NDI2OD-T2) blends. The signal is expressed in sulphur counts, where bright and dark areas correspond to P3HT- and P(NDI2OD-T2)-rich domains, respectively. The thickness of the film in *a)* and *b)* is 170 nm and 145 nm, respectively. Dashed lines indicate line scans shown below the images.

To investigate more quantitatively and with a higher resolution the morphology transition within the whole series of varying CN concentrations, R-SoXS experiments were performed. **Figure 3**.a shows profiles acquired at an energy of 285.3 eV, where the maximum chemical contrast between both polymers is observed.[38, 39] Profiles acquired at 270 eV are also shown. These correspond to the non-resonant conditions in conventional small angle- X-ray scattering (SAXS) and are more sensitive to mass density fluctuations. For the Xy-cast film the R-SoXS profile shows the highest intensity at q=0.0045 nm^{-1} and a shoulder at q=0.014 nm^{-1}. The corresponding characteristic lengths $l_c=2\pi/q$ of 1.4 and 0.44 µm can be retraced in the TEM images as the domain spacings and the mesh width of the P(NDI2OD-T2) network, respectively. However, both features exhibit rather broad distributions. In stark contrast to the Xy-cast film, the R-SoXS profile of the 50 vol.% CN-cast sample consists of a broad feature at q≈0.08–0.09 nm^{-1} (l_C=70 nm) and a shoulder at q≈0.2 nm^{-1} (l_c=35 nm), which we attribute to particle-like scattering from the circularly shaped domains seen in the EF-TEM images. Furthermore, an additional shoulder is identified in the pattern at lower values of q where log normal peak fits to the profile yields a position of q=0.056 nm^{-1} (l_C=112 nm), reflecting the typical spacing of the P(NDI2OD-T2) domains seen in EF-TEM. The two high-q features, caused by scattering from the smaller circularly shaped P(NDI2OD-T2) domains, are common in all films with any amount of CN, linking the formation of these domains to the presence of the CN. In contrast, the position of the low-q feature, interpreted as dominant domain spacing, changes with CN-concentration. Starting with l_C=1.4 µm at 0 vol.%, the

feature moves to l_C=690 nm with 5 vol.%, and l_C=123 nm with 10 vol.%. At higher CN concentration, the change in position stops, with the dominant domain spacing for 20 vol.% and 50 vol.% equal to each other at l_C=112 nm. Thus from the scattering profiles, it is likely that the mesoscale structural changes in the film largely saturate between 10 and 20 vol.% CN. STXM and SKPM on the film cast from 5 vol.% CN (see Figure S3 and S4) resolves a structure with large P(NDI2OD-T2) domains reminiscent of the fibers seen in the film cast from pure Xy. Thus, the 5 vol.% CN-cast film represents a transition morphology with coexisting remnant P(NDI2OD-T2) fibres and the emerging population of smaller circularly shaped domains.

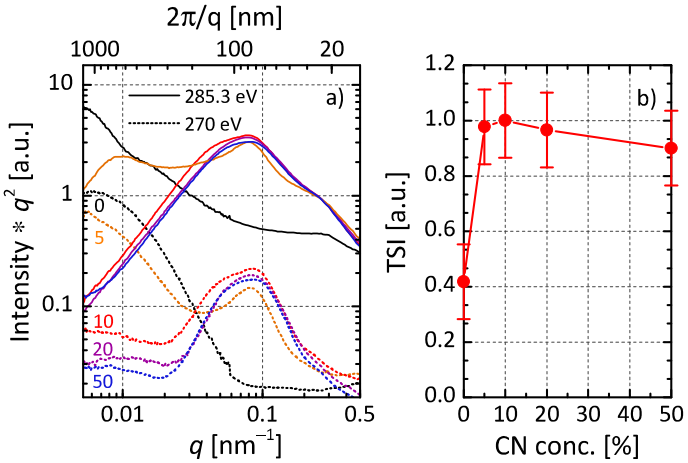

Figure 3 ***a)*** R-SoXS and SAXS profiles of blend layers with 300 nm thickness, measured at the C_{1s}-π* transition energy (285.3 eV, solid lines) and at non-resonant energy (270 eV, dashed lines). The CN concentration of the Xy:CN casting solution is indicated in the graph. ***b)*** Calculated total scattering intensity (TSI) from integrating the R-SoXS profiles shown in a) with uncertainties calculated from that of the film thickness and power law extensions to higher q.

In **Figure 3**.b. the total scattering intensity (TSI) has been calculated for each profile after extension to higher q with power-law fits, allowing for convergence of the integrals. As a function of CN-concentration, the TSI increases strongly upon addition of 5 vol.% CN and then remains the same for higher CN concentrations. This indicates that the CN-induced domains have a higher purity than those cast from pure xylene. Since the STXM analysis in Xy-cast films showed pure fibers of P(NDI2OD-T2) but impure P3HT domains, the comparison with the CN concentration dependence of the TSI suggests that mainly the purity of the P3HT domains increases upon addition of CN. Consequently, the smaller P(NDI2OD-T2) domains in the CN-cast blends are similarly pure. This conclusion is supported by the large contrast in the EF-TEM maps, which can be seen more clearly in the line scans in **Figure 2**.

2.3 Polymer crystallinity

It has been presumed that the generation of free charge carriers is dictated by the microscopic structure of the donor and acceptor at the heterojunction. P3HT and P(NDI2OD-T2) are semi-crystalline materials,[32, 40] which comprise well ordered aggregated or crystalline, as well as disordered amorphous fractions. While ordered regions are associated with better charge transport and larger exciton and charge delocalization, it is generally unknown which role they play in the exciton dissociation process.

Grazing-incidence wide-angle X-ray scattering (GIWAXS) measurements have been used to study the microstructure of the crystalline domains. The different molecular structure of both polymers gives rise to a relatively large number of well separated scattering peaks, which allows the extraction of the molecular packing structure, the size and orientation of the P3HT and P(NDI2OD-T2) crystallites. **Figure 4** displays 2D plots as well as sector averaged GIWAXS profiles of the Xy- and Xy:CN-cast blends. According to the usual convention, the crystal directions were labeled as lamella stacking [*h*00], π–π stacking [0*k*0] and backbone repeat [00*l*], while the letter P and N of the peak labels stands for P3HT and P(NDI2OD-T2), respectively. From the peak positions the real space repeat distances are obtained, which are in agreement with published values,[32] while the coherence of P3HT and P(NDI2OD-T2) crystallites is obtained from a Scherer analysis of the first order peak width. Furthermore, we use the intense [100] lamella stacking peak to probe the orientation of the crystals relative to the substrate.

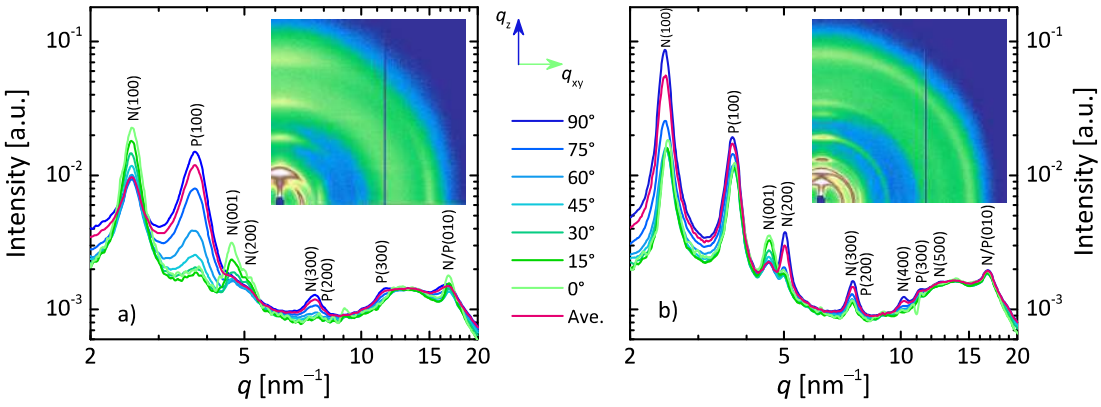

Figure 4 Sector averaged GIWAXS scattering intensity of the Xy- (left) and the 50 vol.% CN-cast (right) blend. The center angles of the 15° sectors are denoted between the graphs and range from in-plane scattering at 0° (q_{xy}, light green line) to out-of-plane scattering at 90° (q_z, dark blue line). The 2D detector images are shown as insets. Peaks belonging to P3HT and P(NDI2OD-T2) are labeled with P and N, respectively.

We start with a quantitative description of the orientation distribution of the polymer crystals. From the two-dimensional GIWAXS data, pole figures were constructed following previously published procedures. A pole figure displays the distribution of crystals as a function of the polar angle ω, defined as the angle between the substrate's surface normal and the [100] lamella stacking direction.[41, 42] **Figure 5** shows the lamella stacking orientation distribution of P3HT and P(NDI2OD-T2). In the Xy-cast blend, P3HT crystals adopt a preferential edge-on orientation where the majority of crystals are oriented within a polar angle of ±25° degrees, while P(NDI2OD-T2) crystals are oriented diametrical opposed, adopting a face-on orientation with the P(NDI2OD-T2) backbone lying parallel to the substrate. The use of CN introduces two distinct changes to these distributions. The first is the reorientation of the P(NDI2OD-T2) crystals from face- to edge-on. This transition is clearly visible in the blend processed from 5 vol.% CN. Here, a large face-on population of P(NDI2OD-T2) with a maximum at about ω=75° coexists with an edge-on population. The change of the orientation distribution saturates at about 20 vol.% CN, leaving a dominant edge-on population and a population with a random distribution, which is reflected by the nearly constant intensity from ω=30–90°. The close coincidence of the structural changes with increasing CN concentration seen in the R-SoXS (see **Figure 3**) and GIWAXS experiments reveals a close conjunction of mesoscale domain structure and crystal orientation. Since P(NDI2OD-T2) forms a fiber network in the Xy- cast film that is still present in the 5 vol.% CN-cast blend but disappear for 10 vol.% and larger CN concentrations, we propose that the fibers contain P(NDI2OD-T2) crystals with face-on orientation. On the other hand P(NDI2OD-T2) crystals are oriented edge-on in the circular domains which dominate the structure in the optimized blends. The CN-induced orientation change is also observed in pristine P(NDI2OD-T2) films,[43] which demonstrates that it is a solvent-controlled process that is also functional in the blend.

The second change appears to the P3HT crystal population. Here, higher CN concentrations introduce a significant fraction of randomly oriented crystals, while the edge-on preference is conserved. We note that the relative population of randomly oriented crystals is actually larger than it is implied by **Figure 5**, which can be seen after performing a geometrical correction of the raw pole figures (see Figure S11). After summing over all possible crystal angles, the corrected pole figures represent the total population distribution as a function of ω. Integration of this curve directly yields the relative degree of crystallinity (DoC). However, the same conclusion can be drawn from these corrected pole figures, that in the optimized

blends, P3HT and P(NDI2OD-T2) crystals adopt the same preferential edge-on orientation distribution, while they are almost perpendicularly oriented in the Xy-cast blend.

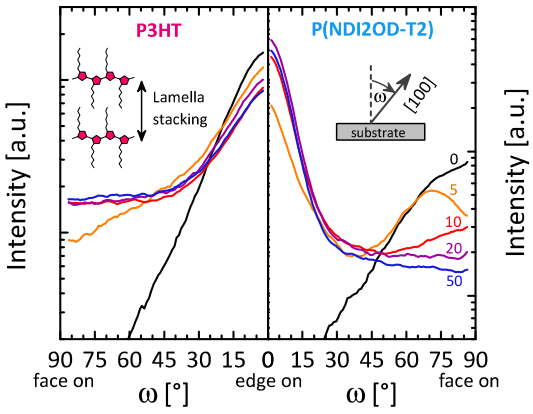

Figure 5 Pole figures of the [100] lamellar stacking of P3HT (left) and P(NDI2OD-T2) (right) crystals in the blend films. The CN concentration is indicated in the right figure. The definition of the polar angle ω, as well as the investigated molecular stacking direction are given as inset.

Beside orientation, the crystal coherence and the DoC are influenced by the formulation of the casting solution. **Figure 6** displays the change in P3HT and P(NDI2OD-T2) lamella coherence length for the various CN concentrations, which is comparable for both polymers. From the relatively large values of 12 nm for P3HT and 18 nm for P(NDI2OD-T2), the coherence length jumps to about 30 nm and 45 nm for P3HT and P(NDI2OD-T2), respectively, when adding 5 vol.% of CN. More CN does not seem to affect the crystal coherence dimension. Note that these values are larger than what has been commonly reported for thermally annealed blends of polymers with soluble fullerenes and even larger than those reported for pure P3HT and P(NDI2OD-T2), which means that the high temperature drying procedure we use for the preparation of our active layers enables the growing of relatively large polymer crystals.[32, 39, 43, 44] The abrupt change of the crystal coherence for CN-cast blends can be also seen in the evolution of the DoC of P3HT, which also doubles compared to the Xy-cast blend but is constant above 5 vol.% CN in the solution. Interestingly, the DoC of P(NDI2OD-T2) doesn't show this jump but instead decreases continuously by 30% from 0 to 50 vol.% CN. Since the bulk of the photocurrent enhancement occurs at CN concentrations above 5 vol.% CN, these changes in DoC and lamellar coherence cannot explain the changes in device performance.

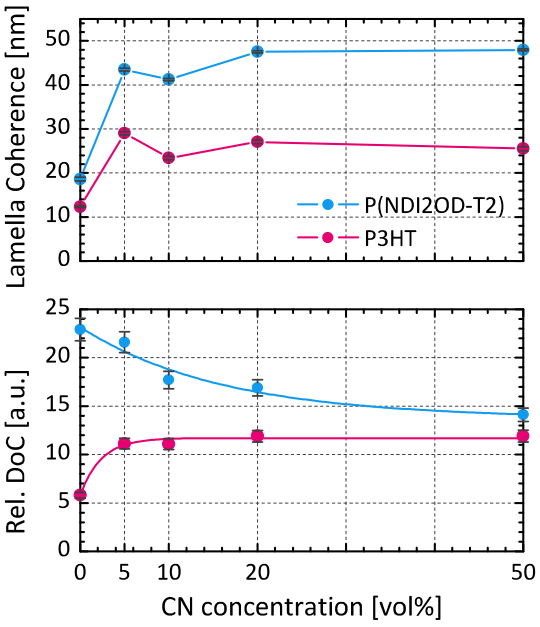

Figure 6 Lamella coherence (top) and relative DoC (bottom) of the different blends. Lines are guides to the eye. Uncertainties in the coherence are from the unweighted peak fits. Uncertainties in the relative DoC are derived from that of the illuminated sample volume.

2.4 Exciton quenching

From the investigation of the blend morphology, we next analyze the dynamics and yields of the excited states in the P3HT:P(NDI2OD-T2) blends. The quenching of excitons at the heterojunction initiates the cascade of elementary processes leading to the generation of the photocurrent. The quenching (by charge-transfer) of excitons created after photon absorption in competition with their recombination to the ground state is simply probed by measuring the decrease of the photoluminescence (PL) of the donor (acceptor) in presence of an acceptor (donor).[45] For P3HT, the singlet exciton quenching is almost complete and ranges from 92% to 96% (see Table 1). The high P3HT quenching for the micrometer large domains of the Xy-coated film is consistent with the observed low domain purity in the STXM experiment, while we assign the slightly increased quenching in the Xy:CN-processed films to the strongly reduced domain size. Determining the P(NDI2OD-T2) PL quenching efficiency (PQE) is much more challenging due to the very low PL quantum efficiency of pure P(NDI2OD-T2), which we find is only about 0.14%. In the 50 vol.% CN-cast blend only 55% of the excitons can be quenched, while in the Xy-cast film the PQE is even lower and reaches 45%. The incomplete quenching of the acceptor excitons therefore represents a direct and significant

loss channel. Furthermore, we can safely state that the decreased IQE for photons absorbed in the acceptor is mainly caused by the incomplete quenching of the primary-excited excitons in P(NDI2OD-T2).

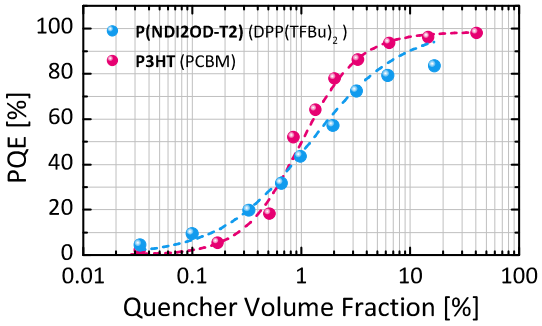

Figure 7 PQE of P3HT and P(NDI2OD-T2) as function of the PCBM and $DPP(TFBu)_2$ quencher volume fraction. Dotted lines are a guide to the eye. For P(NDI2OD-T2), the PQE saturates at about 85% for a $DPP(TBFu)_2$ concentration larger than 5 vol.% due to crystallisation of the quencher molecule.

We consider two possible explanations for the low PQE of P(NDI2OD-T2) compared to P3HT: a morphology in which the P(NDI2OD-T2) domains are purer than the P3HT domains, or a significantly reduced exciton mobility in P(NDI2OD-T2). With regard to the second hypothesis, Mikhnenko and co-workers recently designed an experiment to determine the exciton diffusion length from PQE measurements using a series of concentrations of well dispersed quenchers.[46] We adopted this technique to compare the exciton diffusion length in the donor and acceptor. In these experiments, a reduced exciton diffusion length would shift the whole curve to larger quencher concentrations. However, by using small conjugated molecules (PCBM for P3HT and $DPP(TBFu)_2$[47] for P(NDI2OD-T2)) which we suppose can intermix closely with the polymers (at least in dilute amounts), **Figure 7** shows that the centre of the quenching curves are at the same quencher concentration, suggesting that both polymers have a comparable diffusion length. Thus, the difference in quenching efficiency in the solar cell blends does not stem from a shorter exciton diffusion length in the acceptor but likely originates from a dissimilar composition of the donor and acceptor domains.

We observed in the last section that the P3HT-rich domains are larger than the P(NDI2OD-T2) domains in both the Xy- and 50:50 Xy:CN-cast films but the PL quenching of P3HT is about twice that of P(NDI2OD-T2). Furthermore, we demonstrated that both polymers have a comparable exciton diffusion length, which implies that a significant fraction of P(NDI2OD-T2) is dissolved in the P3HT-rich phases. On the other hand the poor quenching of P(NDI2OD-T2) even in the small domains of the 50:50 Xy:CN-cast blend, leads us to conclude that they are relatively pure and that the miscibility of P3HT in the P(NDI2OD-T2)

phase is rather low. This could be a consequence of a strong driving force for aggregation of P(NDI2OD-T2) during the transition from solution to the solid state,[34, 37] tending to exclude P3HT from the domains. Thus, the reduced IQE of the acceptor polymer is a result of the high domain purity and the incomplete quenching of excitons in the P(NDI2OD-T2) domains.

2.5 Charge transfer states and ultrafast geminate recombination

The former section showed that the IQE is significantly lower than the photoluminescence quenching over the entire spectral region meaning that a process in the quantum efficiency cascade subsequent to exciton quenching must be the dominant loss mechanism for these devices as a whole. The next step in the cascade is the separation of the interfacial state that is created after exciton quenching. The resulting CTS is per definition still coupled to its ground state and can decay before producing free charge carriers.[48] Geminate recombination through CTS is therefore a quantum efficiency loss channel. In order to gain insights into the role of the charge-transfer states in determining the quantum efficiency of our samples we combined the techniques of photothermal deflection spectroscopy (PDS) and transient absorption spectroscopy. We determine the efficiency of charge separation in directly created charge-transfer states, along with the population flows on the early timescales initiated by photons absorbed in both the donor and in the acceptor. Putting this information together with that from the preceding section, we obtain a holistic overview of the photophysical processes that limit the quantum efficiency in these blends.

2.5.1 Charge-transfer state splitting efficiency determined by IQE measurements

Figure 8 displays the logarithmically plotted *EQE*, *A* and *IQE* spectra of a 50 vol.% CN-cast blend, measured from the visible absorption of P3HT, then P(NDI2OD-T2), down to the near infrared (NIR) absorption of the directly excited interfacial charge-transfer state at photon energies below 1.4 eV. In the *EQE* spectrum, the two characteristic regions of P3HT and P(NDI2OD-T2), as they are shown in **Figure 1**, can be easily identified. Below the bandgap of P(NDI2OD-T2) a pronounced shoulder appears which originates from the electronic ground state excitation of the CTS.[9, 49-51] With the absorbance measured by PDS, the *IQE* spectrum is calculated. It shows similar features as the *EQE* spectrum, comprising a maximum of around 15% at photon energies greater than 2 eV where P3HT dominates the absorption, and drops, as discussed above, to 3–7% in the region 1.5 and 1.9 eV where P(NDI2OD-T2) is primarily responsible for the photon absorption. Importantly, the IQE then increases again to about 10% in the sub-bandgap region of photon energies less than 1.4 eV

where the very weak sample absorption is explained by direct excitation of the interfacial charge-transfer states.[52] The weak CTS absorption could be detected down to energies of about 1.2 eV, before it disappears behind the background signal of the PDS setup. Therefore, the background affects the IQE values in the CTS region and the calculated 10% represents only the lower boundary to the efficiency.

To estimate a more accurate value, we separated the EQE into the contribution originating from the CTS and from the P(NDI2OD-T2) and recalculated the absorbance A_{NIR} in the NIR region from the modelled *EQE* spectrum, using the *IQE* as a variable fit parameter (for details see Supporting Information). The best fit is obtained when the IQE of the charge transfer states (IQE_{CT}) is equal to 35% (see green line in **Figure 8**), although it is not possible to define an upper boundary. This important result suggests that the CTS can split with significantly higher efficiency than the direct excitation of either the donor or acceptor polymer. This clarifies that the CTS represents the precursor for the generation of free charges, and that the CTS dissociation efficiency defines the overall conversion efficiency, as it has been demonstrated very recently for several D/A combinations.[53] However, whereas the IQE of a directly-excited CTS in previous studies was equal to the internal quantum efficiency based on absorption by the donor or acceptor,[52, 53] we find a larger value for the P3HT:P(NDI2OD-T2) blend investigated here.

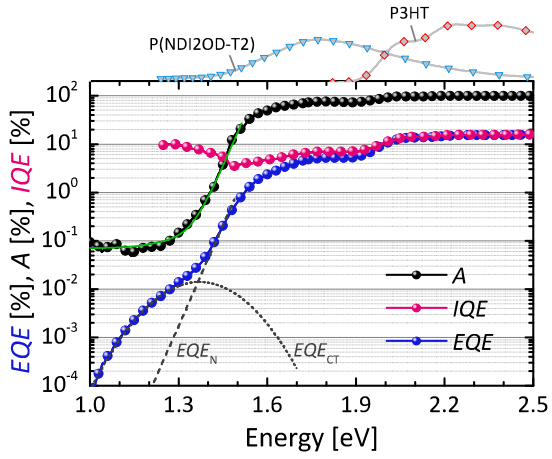

Figure 8 EQE (blue spheres), IQE (pink spheres) and active layer absorption (black spheres) of the 50:50 Xy:CN-cast blend. On top of the figure, the absorbance spectra of pure P3HT (red diamonds) and P(NDI2OD-T2) (blue triangles) are given. The main contribution to the IQE in the range up to 1.5 eV, from 1.5 to 1.9 eV and above 1.9 eV are assigned to CTS, P(NDI2OD-T2) and P3HT, respectively. Also shown are fits to the CTS region (EQE_{CT}, gray dotted line) and the P(NDI2OD-T2) band gap region (EQE_N, gray dashed line), as well as the best fit to the absorption (green line), assuming an IQE_{CT} of 35%.

2.5.2 Transient absorption measurements

In the previous section we have estimated that on top of the limited exciton quenching (~95% on P3HT but only 50% on P(NDI2OD-T2) – see Table 1) there is also a significant loss channel related to the CTS precursor of free charge carriers. In this section we will follow the change in photo-induced absorptions and bleaching as excitons move to the interface to create charge-transfer states, which subsequently create charge carriers or decay to the ground-state.

We will first assign the spectral signatures of the different excited-state species contributing to the TAS spectrum. **Figure 9**.a shows the transient absorption of the pristine P(NDI2OD-T2) film after a delay of about 1 ps, where the primary excitations are singlet excitons (Ex).[34] A negative change in transmission is observed in the NIR and visible spectral region, spanning the range from 1.25 to 1.55 eV and 2.1 to 2.5 eV, respectively, which we attribute to the photo-induced absorption (PIA) of P(NDI2OD-T2) singlet excitons. The positive change in transmission on the other hand, which dominates the spectrum from 1.55 to 2.1 eV, is assigned to the ground state bleach (GSB) of neutral P(NDI2OD-T2) chromophores, which has a characteristic double peak structure (with maxima at approximately 1.6 and 1.8 eV) which stems from the population of aggregate states. In our previous study of pristine P(NDI2OD-T2) we also described long-lived excitations (with ns lifetime) which showed only a ground state bleach but no photo-induced absorption.[34] Using transient electron paramagnetic resonance spectroscopy (EPR) we are able to identify this states as P(NDI2OD-T2) triplet states that are formed in pristine films (Figure S10). The PIA signal of negative polarons (P^-), is obtained from charge accumulation spectroscopy (CAS) spectra, also shown in **Figure 9**.a.[54] Two distinct PIA bands can be identified, ranging from 1.1 to 1.55 eV and 2.5 to 3.0 eV. We note that the latter is well separated from the PIA of the excitons.

TAS and CAS spectra are also used to clarify the spectral range of possible TAS features of pristine P3HT, which are displayed in **Figure 9**.b. Negative transmission changes in the CAS spectra are assigned to the PIA of positive charges (P^+), which have a very broad and featureless spectrum ranging from 1.2 to 1.9 eV. Previous TAS measurements showed that also the singlet excitons contribute a negative signal that overlaps with the P+ signal.[55] However, the Ex signal reaches a maximum at about 1.1 eV, as it is also apparent from **Figure 9**.b.[55, 56] According to the absorption spectra of aggregated, regio-regular P3HT, the positive GSB is observed for energies of 1.9 eV and higher.[35, 55] In addition, the positive contribution of stimulated emission (SE), which overlaps with the P^+ and Ex PIA signals, is observed in the range of 1.35 to 1.9 eV.[35, 55]

Figure 9.c shows the evolution of the TAS spectra for the 50 vol.% CN-cast blend within the first nanosecond, recorded upon selective excitation of P(NDI2OD-T2) at 1.51 eV. A first inspection reveals that the kinetics of the acceptor GSB in the blend evolves more rapidly than in the pristine layer, and that the bleach signal after 1 ns is rather faint. This demonstrates that the efficiency for forming long-lived species (charges or triplet excitons) is low, as we will discuss in the following section.

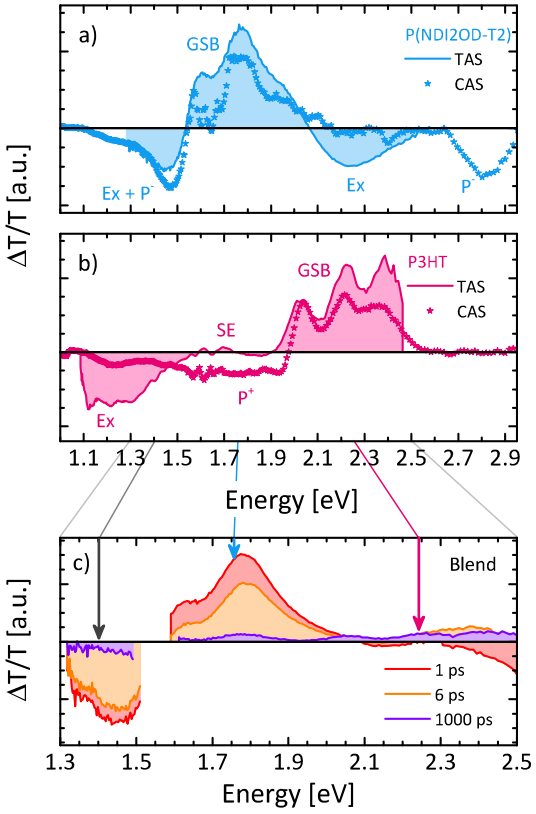

Figure 9 Transient absorption spectroscopy (TAS) and charge accumulation spectroscopy (CAS) of **a)** pristine P(NDI2OD-T2) and **b)** pristine P3HT. Excitons (Ex) and polarons (P) contribute a negative photo-induced absorption signal, while the ground-state bleach (GSB) and stimulated emission (SE) give a positive change in transmission. **c)** TAS spectra of the 50 vol.% CN-cast blend after selective excitation of P(NDI2OD-T2) at 1.51 eV. For further analysis, the dynamics within narrow energy intervals (indicated by the arrows) are shown in **Figure 10**.

2.5.2 Charge-transfer state formation and recombination

In **Figure 10** we display the transient absorption kinetics observed for the 50 vol.% CN-cast blend. At the beginning of the experiment, P(NDI2OD-T2) excitons were selectively excited at an energy of 1.51 eV. The change of the transient transmission is then analyzed at the energy of 2.25 eV (called "P3HT bleach region"). Here, only the positive ground state bleach (GSB) of P3HT and the negative photo-induced absorption (PIA) of P(NDI2OD-T2) excitons

contribute to the signal. Thus, as the P(NDI2OD-T2) excitons move to the interfaces and form charge carrier pairs, the signal in this region should go from negative to positive. Indeed this is what we observe in **Figure 10**.a in the time region marked A. In the first few picoseconds the signal in this region changes from negative to positive as the PIA of P(NDI2OD-T2) excitons that are quenched is replaced by the P3HT absorption bleach of the resultant holes. Fitting the rise of P3HT bleach yields the violet line and a lifetime for the P(NDI2OD-T2) in the blend of 0.96±0.04 ps, about 40 times faster than the luminescence lifetime of pristine P(NDI2OD-T2).[34]

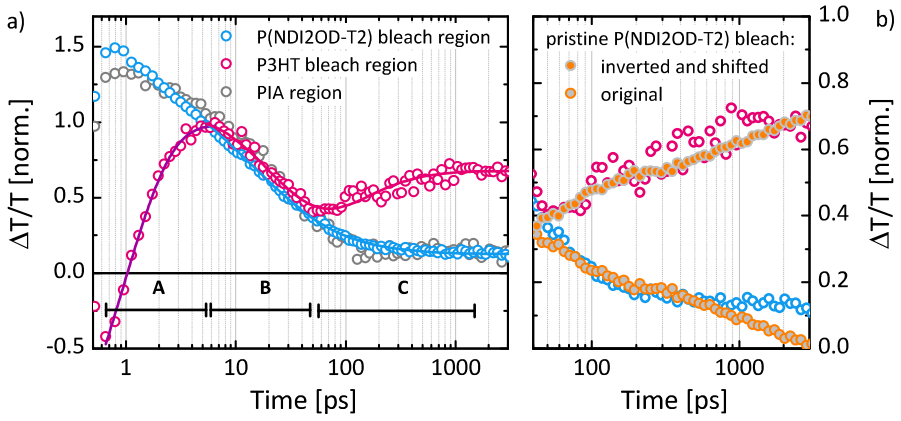

Figure 10 *(left)* Evolution of transient absorption spectra at 2.25 eV (P3HT bleach region), 1.75 eV (P(NDI2OD-T2) bleach region) and 1.4 eV (PIA region) in the 50 vol.% CN-cast blend after selective excitation of P(NDI2OD-T2) at 1.51 eV. The signals are normalized to their value when charge carrier generation is complete (end of rise in P3HT bleach in time region A). The kinetics are overlaid with the fit described in the text. (right) Comparison of the bleach of the blend components to the kinetics of pristine P(NDI2OD-T2) (inverted and offset) in time region C.

Now following the kinetics of this region further ahead in time we see that the signal decreases in the time range marked B, which can clearly be explained by a loss of P3HT bleach due to fast charge carrier recombination. This ultrafast geminate recombination is followed by an increase of the intensity in time region C. We attribute this increase of the intensity to the gradual recombination of long-lived P(NDI2OD-T2) excitons, that do not reach the heterojunction. More precisely, the decreasing (negative) PIA of P(NDI2OD-T2) excitons and the constant (positive) GSB of P3HT holes result in a total signal that increases with time. To support this assumption, we show in **Figure 10**.b the kinetics of the decay of long-lived P(NDI2OD-T2) excitations measured in the pristine polymer. If we invert and shift these kinetics, we can see that they reproduce well the kinetics in region C. This suggests that there are two populations of P(NDI2OD-T2) excitons, one which promptly generates free charge carriers which transfer with an inverse rate of around 1 ps (in time region A), and one that is much longer lived and accounts for the P(NDI2OD-T2) emission observed under

steady-state illumination as well as for the increase in the P3HT bleach in time region C. We note that the observation of long-lived P(NDI2OD-T2) excitons is in agreement with the low PQE of P(NDI2OD-T2), that was presented above.

The data in **Figure 10**.a also allow to estimate a lower bound for the percent of long-lived free charge carriers. For that, we can look at the kinetics at the energy of 1.8 eV (P(NDI2OD-T2) bleach region), where the signal is composed of the positive P(NDI2OD-T2) GSB (either excitons or electrons) and the negative PIA of positive charges on P3HT. Normalizing these signals to the value when charge carrier generation is complete (at 5 ps), and assuming that charges are the only species that causes the subsequent decay of the signals in the P3HT and P(NDI2OD-T2) bleach regions, then the value at long time would reflect the signal that is related to long-lived, free charge carriers. By looking at the data, this would give an estimate of ~15%. Now we know that some of the signal decay in these regions is actually due to decay of the long-lived P(NDI2OD-T2) excited-states, we conclude that at least 15% of charge carriers are long-lived.

In order to get a better estimate of the fraction of free charge carrier and to demonstrate the validity of our assumptions, the kinetics were fit with a global model. Here we take into account charge carriers that can either be short or long-lived, and long-lived P(NDI2OD-T2) excitations. Using stretched exponentials to parameterize the recombination of short-lived charge carriers and the long-lived P(NDI2OD-T2) excitations we can write $\Delta T/T_i = A_i\left(p_{1a}e^{-(t/\tau_1)^{b_1}} + p_{1b}\right) + B_i e^{-(t/\tau_2)^{b_2}}$; where A and B are constants relating to the splitting of the population into two species (charges and excitons) and the absorption cross sections of the charge carriers in each wavelength range. The remaining parameters are shared between the wavelength regions. Here, p_{1a} represents the fraction of the charge carriers that are short-lived and recombine with a rate described by τ_1 and b_1, p_{1b} represents the fraction of charge carriers that are long-lived (e.g. potentially useful in the solar cell), while τ_2 and b_2 represent the decay of the P(NDI2OD-T2) excited-states. The results of this global fit are shown as the pink and blue lines in **Figure 10**.a, and the parameters for both fits are given in Table 2. We find that p_{1b} is approximately 0.3, so only roughly 30% of the charge carriers formed are long-lived, while 70% of the charge carriers recombine geminately on the 100 picosecond timescale, far too fast to produce photocurrent. We note that the kinetics in the P(NDI2OD-T2) bleach region perfectly resembles the kinetics in the PIA region at 1.4 eV, where all excited states contribute to the signal, implying that our model is able to describe all relevant processes quantitatively.

Combining these results with the steady state quenching observations we can approximate the upper bound of the IQE in the P(NDI2OD-T2) phase as 0.50 (due to incomplete quenching) × 0.30 (due to fast CTS recombination), which yields an estimate of 0.15. This is still roughly a factor of 2 larger than the observed IQE for P(NDI2OD-T2) excitation, indicating perhaps that not all the long-lived charge carriers can be extracted. Nonetheless, we see that the combination of incomplete quenching and fast CTS recombination explain the majority of the quantum efficiency loss after excitation of P(NDI2OD-T2).

Table 2 Parameters extracted from fitting the data in **Figure 10**.a.

	p_{1a}	p_{1b}	τ_1 [ps]	b_1	τ_2 [ps]	b_2	A	B
P3HT bleach region	0.7±0.1	0.3±0.1	17±2	0.8±0.1	8±4	0.4±0.1	2.2±0.4	-3.3±0.7
P(NDI2OD-T2) bleach region							0.41±0.1	1.3±0.3

Transient absorption spectra were also measured upon excitation of P3HT. The results are displayed in Figure S8 and reveal that excitons on the P3HT are quenched within about 10 ps. Unfortunately, the shifting of the different excited states species between ordered and disordered regions complicate the analyses of the dynamics of these spectra. Furthermore, a possible energy transfer from P3HT to P(NDI2OD-T2) may also influence the kinetics, although we have no indications that this transfer is very efficient. However, one can again use the signal at 1.4 eV as a probe for the decay of CTS. Figure S9 shows that after quenching of the excitons, again an ultrafast recombination of the CTS destroys the majority of excited states within less than 200 ps and that the signal decreases to a value of about 15% of the original intensity. Thus, the carrier dynamics are broadly similar upon P3HT or P(NDI2OD-T2) excitation, which finally reveals that the fast CTS recombination is the dominant loss mechanism of the IQE. In conclusion, we can clearly say that losses on the order of 70% in the CTS (as suggested by the steady state spectroscopy) are reasonable, and that we can directly observe the sub-nanosecond CTS-based recombination that leads to these losses.

3. Discussion and Conclusion

Based on the above studies of structure and excited state dynamics, **Figure 11** sketches the interplay of morphology and charge generation in the best performing P3HT:P(NDI2OD-T2) blend processed from a 50:50 Xy:CN mixture. In **Figure 11**.a a schematic overview of the domain structure, reconstructed from the TEM image and R-SoXS profile, is shown. It

provides a detailed overview of the most important morphological and structural features, which dominate the charge generation process, as we will discuss in the following.

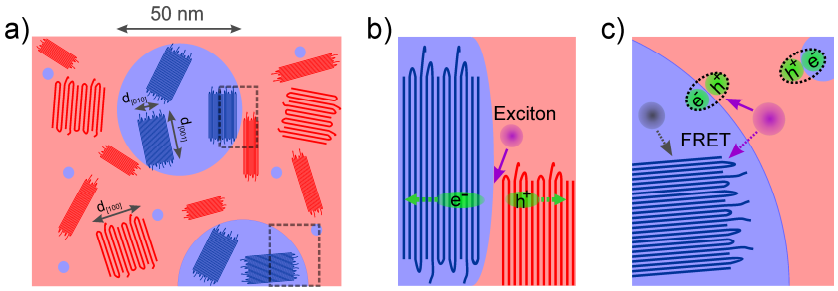

Figure 11 a) Schematic representation of the morphology of the 50:50 Xy:CN-cast blend. The image illustrates an cross section in-plane with the substrate (top view), showing P(NDI2OD-T2) domains (blue) and the P3HT matrix (red). Ordered regions with darker colors represent the polymer backbones in crystalline domains, where face-on crystals have a 5 times larger lattice plane spacing than edge-on crystals. Small P(NDI2OD-T2) enclosures, which have the size of a single aggregate,[34] account for the lower purity of the P3HT domains. b) Face-to-face donor/acceptor orientation at the heterojunction. This geometry is proposed to facilitate free charge carrier generation. c) Effect of exciton self-trapping in P(NDI2OD-T2) aggregates. Excitons from disordered acceptor or donor regions can transfer to aggregated or crystalline P(NDI2OD-2) regions by Förster-resonant energy transfer (FRET). In addition, amorphous donor/acceptor interfaces are illustrated, were CTS undergo fast geminate recombination.

In order to identify the factors dominating the free charge carrier yield in P3HT:P(NDI2OD-T2) blends, we tried to correlate the photocurrent of the solar cell devices from **Figure 1**.a to the domain size, the domain purity and to the size and DoC of the polymer crystallites. However, the comparison of the dependence of the PL quenching (see **Tab. 1**), the TSI (see **Figure 3**.b), the DoC (see **Figure 6**.a) and the coherence length (see **Figure 6**.b) to the photocurrent reveal that these parameters all show either a marginal change over the whole CN concentration or an abrupt change upon addition of only 5 vol.% CN followed by more or less constant value. The only parameter that mimics the continuous change of the photocurrent is the redistribution of the P(NDI2OD-T2) crystal, as it is evident from the pole figure in **Figure 5**. Note that in a recent study, Fabiano and co-workers also observed a perpendicular orientation of the P3HT and P(NDI2OD-T2) crystallites in low performing devices prepared from xylene and dichlorobenzene, while the best performing cells cast from Xy:CN reveal a parallel edge-on orientation of the polymer crystals.[57] In addition, a higher dissociation rate was also reported at a planar heterojunction for zinc phthalocyanine donor molecules that are oriented face-on with respect to the acceptor domain compared to the edge-on configuration.[58] Thus, we investigated the orientation of the polymer crystallites relative to each other in more details.

We start our discussion from the orientation distributions in the Xy-cast blend. Here, the donor and acceptor crystals are oriented almost perpendicular to each other. Addition of the co-solvent CN re-orients the originally face-on P(NDI2OD-T2) distribution to a predominantly edge-on orientation. At the same time, when the P(NDI2OD-T2) crystals start to adopt an orientation distribution that is similar to that of the P3HT polymer crystallites, the photocurrent also increases. Obviously, the highest photocurrents are observed for blends were P3HT and P(NDI2OD-T2) have comparable orientation distributions comprising a strong edge-on preference. Thus, we make the assumption that not absolute crystal orientation but rather the face-to-face relative orientation of P3HT and P(NDI2OD-T2) crystallites represents the configuration in which efficient dissociation of charge-transfer states is possible. To demonstrate this correlation more quantitatively, we first calculated the relative DoC of P(NDI2OD-T2) edge-on crystals, which we obtained by counting all crystals with a polar angle smaller than 15° (this is proportional to the area under the corrected pole figures from ω=0 to 15°). **Figure 12** displays the relative population of edge-on oriented P(NDI2OD-T2) crystals, plotted against the J_{SC} of the solar cells. The plot reveals the gradual increase of the photocurrent upon the generation of more and more edge-on oriented P(NDI2OD-T2) crystals.

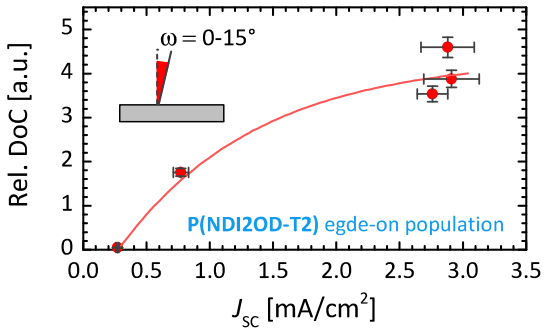

Figure 12 Correlation of the fraction of the P(NDI2OD-T2) edge-on crystal population with the short circuit current of the solar cell devices. DoC uncertainties derived from that of the illuminated sample volume, and J_{SC} uncertainties derived from device statistics.

A consequence of the proposed correlated face-to-face orientation is that the total area of favourable interfaces is the product of the edge-on DoC and the size of the crystallites of both the donor and the acceptor. This is particularly interesting for P3HT, were the strongly increasing DoC (**Figure 6**) seems to be in contradiction to the gradually changing photocurrent. However, the orientation distribution in **Figure 5** reveals that the increased DoC is mainly due to the generation of randomly oriented crystals while the fraction of edge–on oriented crystals (counted again from 0 to 15°) indeed decreases by 40% with increasing CN concentration. On the other hand, the lamella coherence doubles, which leads to an overall

marginal increase of the edge-on P3HT crystal surface with increasing CN concentration. We also note the continuous decrease of the P(NDI2OD-T2) lamella DoC with increasing CN concentration. This discussion illustrates the complex interplay of several parameters that need to be considered and may explain why the trend in **Figure 12** is not linear.

In order to understand the role of polymer crystals in the charge generation process it is instructive to reflect on some recent models aiming to describe photocurrent generation at organic donor/acceptor heterojunctions under consideration of the semi-crystalline nature of the materials. It has been noted that efficient carrier generation at distributed heterojunctions requires an unidirectional flow of carriers away from the heterojunction.[13, 59, 60] The driving force behind that is supposed to originate from an energy gradient of the potential energy pointing from the heterojunction into the bulk of the pure phases. Recent experimental and theoretical results imply that this gradient is introduced by the difference in ionization energy or electron affinity caused by the larger disorder in regions close to the heterojunction compared to better ordered or perfectly crystalline regions in the bulk.[9, 59-63] The decrease of the band gap in the ordered relative to the disordered phases can be strongly enhanced by the formation of intermolecular excited states, so called aggregates, as it has been described for P3HT, which lowers the band gap by about 0.35 eV.[64, 65] For pure P(NDI2OD-T2), we demonstrated the strong tendency to form such aggregate states, which have a, by 0.3 eV, lower band gap compared to intra-chain excitons on disordered P(NDI2OD-T2) segments.[34]

A consequence of such a microscopic energy landscape is that charges as well as excitons are repelled from the heterojunction, which suppresses the recombination of free charges but also prevents the charge transfer of excitons *directly* at the interface. Instead, exciton dissociation requires that charge carriers are transferred over several nanometers.[59, 66] This can be mediated by tunnelling through the potential well, which results in a separated electron-hole pair with reduced binding energy. Very recently, Troisi calculated the distance over which the rate for exciton dissociation exceeds the recombination rate. This distance critically depends on the coupling between neighbouring hopping sites, which is orders of magnitude larger along the polymer backbone and pi-stacking direction than in the lamella-stacking direction.[66] Thus, the face-to-face donor/acceptor orientation found in the optimized solar cells is favourable with respect to the tunnelling assisted exciton dissociation mechanisms described by Troisi and co-workers. In this conformation, both polymer crystals stand edge-on which exposes the polymer backbone towards the heterojunction. **Figure 11**.b illustrates this situation where charges in the interfacial CTS can easily access a crystal. Other P(NDI2OD-T2) crystal orientations (e.g. face-on) hinders the charge to enter the crystal, due

to screening by the alky side-chains. Without favourably oriented crystals and at heterojunction in amorphous donor or acceptor regions, the CTS cannot dissociate and will undergo an ultrafast geminate recombine within less than 100 ps.

The fact that not only the crystallinity but also the relative orientation must be optimized to enable optimal charge separation might display a special problem of conjugated polymers which usually carry long, insulating alky chains. In contrast, fullerenes are spherical symmetrical objects with no or relatively short side chains which have no preferential orientation with respect to the donor molecules. In addition, electrons can delocalize efficiently over neighboured fullerene molecules,[18, 67] and may therefore perform better than any other class of acceptor materials.

At the end, we point out that the energy gradients between amorphous and ordered regions also affect the quantum efficiency in a negative way. Due to the large potential difference between amorphous and crystalline phases, excitons quickly migrate to the ordered, low energy states, as it is illustrated in **Figure 11**.c. We found that the spectral diffusion into these low energy states occurs on a timescale of about 10 ps in pristine P(NDI2OD-T2),[34] meaning that it competes with exciton quenching and the subsequent formation of charge–separated states. Once an exciton is generated on or transferred to a P(NDI2OD-T2) aggregate that is surrounded by amorphous content, it is restricted to exist deep within the ordered region. In effect, this has similar consequences to the phenomenon known as exciton self-trapping observed in molecular aggregates.[68] As a consequence, given that the domains are sufficiently large and pure, excitons on P(NDI2OD-T2) chains are isolated from the heterojunction, which explains the low quenching efficiency of acceptor PL observed in the P3HT:P(NDI2OD-T2) blends. Recently, Mori and co-worker demonstrated an efficiency record for all-polymer solar cells of 4.1%, by combining the P(NDI2OD-T2) acceptor with a new donor copolymer.[69] Interestingly, the PL quenching of the P(NDI2OD-T2) is less than 80%, significantly smaller than the PQE in the donor which reaches nearly 100%. Thus, relatively pure acceptor domains may improve the charge carrier separation but then may also suffer from imperfect exciton quenching. Nevertheless, these results demonstrate the great potential of P(NDI2OD-T2) as acceptor for organic solar cells.

In summary, we propose a microscopic framework in which efficient and ultrafast charge carrier generation at organic heterojunctions can be realized. However, for very anisotropic systems, which conjugated polymers are in general, the correlated orientation of donor and acceptor crystals at the heterojunction is a challenging task, which requires a much larger

control over the nanometer morphology, the degree of crystallinity, as well as of the crystal orientation.

Experimental

Materials

P(NDI2OD-T2) has been synthesized following a recently described procedure.[23, 37] P3HT (BASF Sepiolid P200, purchased from Rieke Metals) was used as received. The molecular weights of P(NDI2OD-T2) and P3HT are M_n/M_w = 26.200/85.200 gmol^{-1} and M_n/M_w = 12.800/22.500 gmol^{-1}, respectively. Compared to our previous publication,[37] the actual P3HT batch has a significantly lower molecular weight (12.800 gmol^{-1} compared to 17.500 gmol^{-1}), which might explain the lower photocurrents in the present study. We note that for all measurements presented here, we used the same batch of P3HT and P(NDI2OD-T2) (except for the PDS measurements), to eliminate any batch- or molecular weight-related influences on the results. Solvents were purchased from Sigma Aldrich (CF, Xy, CB, DCB) or Alfa Aesar (85% 1-chloronaphthalene with 15% 2-chloronaphthalene).

Solar cell preparation and characterisation

Pre-structured, indium tin oxide (ITO) coated glass substrates were used for solar cell preparation. PEDOT:PSS (AI4083, 30 nm) and Samarium(20 nm)/Aluminium(100 nm) were used as hole and electron collecting contacts. The final structure of the cells was Glass/ITO/PEDOT:PSS/Active layer/Sm/Al and the active area of the cells 16 mm^2. Device preparation, transport and measurements were performed under inert atmosphere. Films that were prepared from a CN-containing solution were spin-coated for 5 s and subsequently transferred to a hot plate where they finally dried. The active layer thickness was determined with a Dektak profilometer.

Solar cells where characterized under simulated sunlight of a Newport Oriel Sol2A solar simulator. Calibration of the setup was done with a KG5 filtered reference silicon solar cell (calibrated by Fraunhofer ISE) and the intensity was set to 100 mW cm^{-2}. The irradiance of the solar simulator was monitored before each measurement by a calibrated KG5 filtered solar cell which is directly integrated into the home build, temperature controlled sample holder, with the temperature set to 20 °C.

For EQE measurements, light from a 100 W quartz halogen lamp (Philips 7724) was time-modulated by a mechanical chopper (90−140 Hz) and fed into a Cornerstone 260 1/4m monochromator (model 74100). The monochromatic output was focused onto a fibre to transfer the light into the glovebox. The modulated photocurrent from the solar cell was detected over the input resistor of a lock-in amplifier (Princeton Research Instruments). To

increase the sensitivity of the setup, an input resistance of 1 kΩ was used. No white light background illumination was applied. For IQE calculations, the absorption *A* was estimated from the measured optical density of the films. Hereby, the light was transfered twice the active layer thickness, which is a reasonable approximation for the thick films used for our devices.

PL quenching

Films for PL quenching measurements are prepared on uncovered glass slides, as we found that PEDOT:PSS or PSS significantly reduce the PL of the polymers. To calculate PL quenching efficiency, the PL efficiency of blend samples is compared to that of the pure polymers. Because PL efficiency of the pure polymers also varies for the different preparation conditions (e.g. drying temperature, solvents), a single donor and acceptor reference sample was prepared for each blend sample that was studied. For pure P3HT and P(NDI2OD-T2), we find quantum efficiencies of 7–12% and 0.09–0.2%, respectively. Measurements are performed using an integrating sphere setup (Hamamatsu C9920-02, A10094, C10027). For excitation, the EQE setup was used (see above). PL quenching of P3HT and P(NDI2OD-T2) are probed by excitation at 500 nm and 700 nm, respectively, and the entire PL spectrum up to 950 nm was integrated to obtain the number of emitted photons. Determination of the P(NDI2OD-T2) quenching was limited by the low PL quantum yield of P(NDI2OD-T2). To enhance the sensitivity of the setup, an optical density (OD) filter (OD 0.8-1.5) was used during measurement of the excitation intensity, which was removed when the PL of the films was measured. The true excitation intensity was calculated afterwards, using the measured optical density of the filter. All steps, including film preparation, sample transport and measurement were performed under inert atmosphere, as films which have been exposed to oxygen show strongly reduced PL efficiencies (up to a factor of 2).

Transient absorption spectroscopy

Transient absorption (TA) measurements were performed with a home-built pump-probe setup. To measure in the time range of 1 ps to 4 ns with a resolution of ~100 fs, the output of a commercial titanium:sapphire amplifier (Coherent LIBRA HE, 3.5 mJ, 1 kHz, 100 fs) was split into two beams independently pumping two optical parametric amplifiers (Coherent OPerA Solo). One optical parametric amplifier (OPA) was used to generate the 530 nm excitation pulse, the other OPA was used to generate a 1300 nm seed pulse for white-light generation with a sapphire window in the visible. For excitation with 800 nm the direct output of the LIBRA was used. The variable delay of up to 4 ns between pump and probe was

introduced by a broadband retroreflector mounted on a mechanical delay stage. Only reflective elements were used to guide the probe beam to the sample to minimize chirp. The excitation pulse was chopped at 500 Hz, while the white light pulses were dispersed onto a linear photodiode array which was read out at 1 kHz. Adjacent diode readings corresponding to the transmission of the sample after an excitation pulse and without an excitation pulse were used to calculate $\Delta T/T$. TA measurements were performed at room temperature under dynamic vacuum at pressures lower than 10^{-5} mbar.

Photothermal deflection spectroscopy (PDS) and IQE

For the PDS measurements monochromated light from a 100 W QTH lamp was chopped (3.333 Hz) and focused onto a photovoltaic active layer spincoated onto a quartz substrate. The temperature change caused by the de-excitation of the absorbed light was probed by emersing the sample in a deflection medium (Perfluorohexane, 3MFluorinert FC-72). The change in refractive index caused by the heating of the medium is probed by a HeNe laser (633 nm) of which the deflection is detected by a position-sensitive Si detector, connected to a Stanford Research Systems SR830 lock-in amplifier. The PDS spectra were set to absolute scale by matching the spectra with integrating sphere measurements using a Varian Cary 5000 spectrophotometer. The fraction of absorbed photons by the active layer in solar cell configureation in the weakly absorbing subgap region was calculated by the simplified assumption of the incoming light waves passing through the active layer twice owing to reflection from the metallic cathode.

Energy-filtered transmission electron microscopy

TEM measurements were performed with a Libra 200 FE (Carl Zeiss Microscopy GmbH) equipped with an in-column spectrometer. The primary electron energy was set to 200 keV. Energy-filtered (EF-) TEM images were recorded near the sulphur ionization edge (165 eV energy loss) using an energy window of 10 eV. Elemental maps were generated with the ImageJ software package and EFTEMj plugin.[70] The background was extrapolated with a power-law model from pre-edge images (acquired at 130, 140, 150 eV for **Figure 2**.a and at 110, 140 eV for **Figure 2**.b) and subtracted from the post-edge image (195 eV). Prior to processing, sub-images were carefully aligned using reference images and the TurboReg plugin for ImageJ to compensate drift and shrinking of the specimen during the measurement.[71, 72]

X-ray samples

Samples for X-ray measurements were prepared in parallel to solar cells fabrication from the same solutions and with identical protocols. To reduce the background scattering in GIWAXS,

Si wafers covered with a thin PSS (Poly(sodium 4-styrenesulfonate) aqueous solution, 4 wt%, Sigma Aldrich) layer served as substrate. For transmission experiments (scattering and microscopy), fragments of the same film were floated off the substrate by dissolving the PSS layer in water. For R-SoXS, the films were picked up from the water with 100 nm SiN windows (Norcada), while films were picked up with copper TEM grids (300 mesh, Gilder) for STXM measurements.

Resonant scattering and scanning transmission X-ray microscopy

R-SoXS measurements were performed at the 11.1.0.2 beamline of the Advanced Light Source (ALS).[73] The incident beam size of (200 μm x 150 μm) was set by collimating slits. The scattering pattern was captured by a Princeton PI-MTE CCD cooled to −45°C. For the full q-range, scattering patterns were acquired with two sample-detector distances at 190 mm and 50 mm. A modified version of the NIKA software package was used to average the data into profiles. STXM measurements were performed at the 5.3.2.2 beamline of the ALS.[74] Composition and thickness maps were extracted from the images acquired at two energies using the same procedures as previously published.[75]

Grazing-incidence wide-angle X-ray scattering

Measurements were performed at the 7.3.3 Beamline of the ALS (Beam energy at 10 keV and beam width ~1 mm).[76] A Pilatus 1M photon-counting detector array was used to measure diffraction intensities. Most of the x-ray flight path was contained by a Helium atmosphere to reduce air scatter in the signal. The edges of the substrates were cleaved to eliminate diffraction signal from the edge of the spincast films, leaving approximately the center 1 cm x 1 cm of the film. Diffraction intensities were acquired at an incident angle just above the film critical angle for maximum diffraction signal and an incident angle well above the critical angle of both film and the substrate (α=0.20˚) where intensities are linear to illuminated film volume. The results from analysis of the measurements at critical angle are presented here with their intensities scaled to those measured at the high incident angle. The intensities are additionally corrected for beam footprint (length of the sample in the beam) and film thickness.

Pole figures were constructed by integrating the intensities at each azimuth within a q-range encompassing the diffraction peak and subtracting off a linear background defined by the intensities at either end of the integrated q-range. The relative degree of crystallinity (DoC) was calculated from these pole figures by integrating the intensities over the crystallographic orientation sphere such that $\mathrm{DoC} = \int I(\omega)\sin\omega d\omega$. For measurement of crystal spacing and

coherence length, peak functions were fit to azimuthally averaged profiles I(q). The coherence length (2π/FWHM) is calculated from the first order scattering peaks. Broadening from disorder is not considered here.

Supporting Information

Supporting Information is available online from the Wiley Online Library or from the author.

Acknowledgements

The authors thank Oleksandr V. Mikhnenko and Markus Wollgarten for helpful discussions. We specifically thank Thuc-Quyen Nguyen for providing the DPP(TBFu)$_2$, and Riccardo Di Pietro, Iyad Nasrallah and Henning Sirringhaus for providing the CAS spectra. M.S. acknowledges financial support from the German Science Foundation (DFG) within the priority program SPP 1355. D.N. acknowledges a DFG travel grant. B.A.C. acknowledges financial support of the NIST-NRC postdoctoral fellowship program. The Advanced Light Source is supported by the Director, Office of Science, Office of Basic Energy Sciences, of the U.S. Department of Energy under Contract No. DE-AC02-05CH11231.

4. References

[1] Z. He, C. Zhong, S. Su, M. Xu, H. Wu, Y. Cao, *Nat. Photonics* **2012**, *6*, 591.
[2] S. H. Park, A. Roy, S. Beaupre, S. Cho, N. Coates, J. S. Moon, D. Moses, M. Leclerc, K. Lee, A. J. Heeger, *Nat. Photonics* **2009**, *3*, 297.
[3] J. Peet, J. Y. Kim, N. E. Coates, W. L. Ma, D. Moses, A. J. Heeger, G. C. Bazan, *Nat. Mater.* **2007**, *6*, 497.
[4] T. Kietzke, H. H. Horhold, D. Neher, *Chemistry of Materials* **2005**, *17*, 6532.
[5] X. M. He, F. Gao, G. L. Tu, D. Hasko, S. Huttner, U. Steiner, N. C. Greenham, R. H. Friend, W. T. S. Huck, *Nano Lett.* **2010**, *10*, 1302.
[6] E. J. Zhou, J. Z. Cong, Q. S. Wei, K. Tajima, C. H. Yang, K. Hashimoto, *Angew. Chem.-Int. Edit.* **2011**, *50*, 2799.
[7] D. Mori, H. Benten, H. Ohkita, S. Ito, K. Miyake, *ACS Appl. Mater. Interfaces* **2012**, *4*, 3325.
[8] A. Facchetti, *Materials Today* **2013**, *16*, 123.
[9] K. Vandewal, A. Gadisa, W. D. Oosterbaan, S. Bertho, F. Banishoeib, I. Van Severen, L. Lutsen, T. J. Cleij, D. Vanderzande, J. V. Manca, *Advanced Functional Materials* **2008**, *18*, 2064.
[10] C. Yin, T. Kietzke, D. Neher, H. H. Horhold, *Appl. Phys. Lett.* **2007**, *90*, 092117.
[11] C. Yin, M. Schubert, S. Bange, B. Stiller, M. Castellani, D. Neher, M. Kumke, H. H. Horhold, *J. Phys. Chem. C* **2008**, *112*, 14607.
[12] J. M. Hodgkiss, A. R. Campbell, R. A. Marsh, A. Rao, S. Albert-Seifried, R. H. Friend, *Phys. Rev. Lett.* **2010**, *104*, 177701.
[13] S. Westenhoff, I. A. Howard, J. M. Hodgkiss, K. R. Kirov, H. A. Bronstein, C. K. Williams, N. C. Greenham, R. H. Friend, *J. Am. Chem. Soc.* **2008**, *130*, 13653.
[14] C. Deibel, T. Strobel, V. Dyakonov, *Phys. Rev. Lett.* **2009**, *103*, 036402.
[15] D. H. K. Murthy, M. Gao, M. J. W. Vermeulen, L. D. A. Siebbeles, T. J. Savenije, *The Journal of Physical Chemistry C* **2012**, *116*, 9214.

[16] A. A. Bakulin, A. Rao, V. G. Pavelyev, P. H. M. van Loosdrecht, M. S. Pshenichnikov, D. Niedzialek, J. r. m. Cornil, D. Beljonne, R. H. Friend, *Science* **2012**, *335*, 1340.
[17] M. C. Heiber, A. Dhinojwala, *The Journal of Chemical Physics* **2012**, *137*, 014903.
[18] H. Tamura, I. Burghardt, *J. Am. Chem. Soc.* **2013**, *135*, 16364.
[19] P. H. Wobkenberg, D. D. C. Bradley, D. Kronholm, J. C. Hummelen, D. M. de Leeuw, M. Colle, T. D. Anthopoulos, *Synth. Met.* **2008**, *158*, 468.
[20] C.-Z. Li, C.-C. Chueh, H.-L. Yip, J. Zou, W.-C. Chen, A. K. Y. Jen, *Journal of Materials Chemistry* **2012**, *22*, 14976.
[21] C. R. McNeill, A. Abrusci, J. Zaumseil, R. Wilson, M. J. McKiernan, J. H. Burroughes, J. J. M. Halls, N. C. Greenham, R. H. Friend, *Appl. Phys. Lett.* **2007**, *90*, 193506.
[22] R. A. Marsh, C. Groves, N. C. Greenham, *Journal of Applied Physics* **2007**, *101*, 083509.
[23] H. Yan, Z. H. Chen, Y. Zheng, C. Newman, J. R. Quinn, F. Dotz, M. Kastler, A. Facchetti, *Nature* **2009**, *457*, 679.
[24] X. Guo, F. S. Kim, M. J. Seger, S. A. Jenekhe, M. D. Watson, *Chemistry of Materials* **2012**, *24*, 1434.
[25] S. Cho, J. Lee, M. Tong, J. H. Seo, C. Yang, *Advanced Functional Materials* **2011**, *21*, 1910.
[26] J. Li, Y. Zhao, H. S. Tan, Y. Guo, C.-A. Di, G. Yu, Y. Liu, M. Lin, S. H. Lim, Y. Zhou, H. Su, B. S. Ong, *Sci. Rep.* **2012**, *2*.
[27] J. H. Park, E. H. Jung, J. W. Jung, W. H. Jo, *Advanced Materials* **2013**, n/a.
[28] J. Lee, A. R. Han, H. Yu, T. J. Shin, C. Yang, J. H. Oh, *J. Am. Chem. Soc.* **2013**, *135*, 9540.
[29] R. Steyrleuthner, M. Schubert, F. Jaiser, J. C. Blakesley, Z. Chen, A. Facchetti, D. Neher, *Advanced Materials* **2010**, *22*, 2799.
[30] J. C. Blakesley, M. Schubert, R. Steyrleuthner, Z. H. Chen, A. Facchetti, D. Neher, *Appl. Phys. Lett.* **2011**, *99*, 183310.
[31] T. Schuettfort, S. Huettner, S. Lilliu, J. E. Macdonald, L. Thomsen, C. R. McNeill, *Macromolecules* **2011**, *44*, 1530.
[32] J. Rivnay, M. F. Toney, Y. Zheng, I. V. Kauvar, Z. H. Chen, V. Wagner, A. Facchetti, A. Salleo, *Advanced Materials* **2010**, *22*, 4359.
[33] J. Rivnay, R. Steyrleuthner, L. H. Jimison, A. Casadei, Z. H. Chen, M. F. Toney, A. Facchetti, D. Neher, A. Salleo, *Macromolecules* **2011**, *44*, 5246.
[34] R. Steyrleuthner, M. Schubert, I. Howard, B. Klaumünzer, K. Schilling, Z. Chen, P. Saalfrank, F. Laquai, A. Facchetti, D. Neher, *J. Am. Chem. Soc.* **2012**, *134*, 18303.
[35] J. R. Moore, S. Albert-Seifried, A. Rao, S. Massip, B. Watts, D. J. Morgan, R. H. Friend, C. R. McNeill, H. Sirringhaus, *Advanced Energy Materials* **2011**, *1*, 230.
[36] S. Fabiano, Z. Chen, S. Vahedi, A. Facchetti, B. Pignataro, M. A. Loi, *Journal of Materials Chemistry* **2011**, *21*, 5891.
[37] M. Schubert, D. Dolfen, J. Frisch, S. Roland, R. Steyrleuthner, B. Stiller, Z. H. Chen, U. Scherf, N. Koch, A. Facchetti, D. Neher, *Advanced Energy Materials* **2012**, *2*, 369.
[38] B. A. Collins, J. E. Cochran, H. Yan, E. Gann, C. Hub, R. Fink, C. Wang, T. Schuettfort, C. R. McNeill, M. L. Chabinyc, H. Ade, *Nat Mater* **2012**, *11*, 536.
[39] H. P. Yan, B. A. Collins, E. Gann, C. Wang, H. Ade, C. R. McNeill, *ACS Nano* **2012**, *6*, 677.
[40] H. Sirringhaus, P. J. Brown, R. H. Friend, M. M. Nielsen, K. Bechgaard, B. M. W. Langeveld-Voss, A. J. H. Spiering, R. A. J. Janssen, E. W. Meijer, P. Herwig, D. M. de Leeuw, *Nature* **1999**, *401*, 685.
[41] J. L. Baker, L. H. Jimison, S. Mannsfeld, S. Volkman, S. Yin, V. Subramanian, A. Salleo, A. P. Alivisatos, M. F. Toney, *Langmuir* **2010**, *26*, 9146.

[42] M. R. Hammond, R. J. Kline, A. A. Herzing, L. J. Richter, D. S. Germack, H.-W. Ro, C. L. Soles, D. A. Fischer, T. Xu, L. Yu, M. F. Toney, D. M. DeLongchamp, *ACS Nano* **2012**, *5*, 8248.
[43] R. Steyrleuthner, R. Di Pietro, B. A. Collins, F. Polzer, S. Himmelberger, M. Schubert, Z. Chen, S. Zhang, A. Salleo, H. Ade, A. Facchetti, D. Neher, *submitted*.
[44] H. W. Ro, B. Akgun, B. T. O'Connor, M. Hammond, R. J. Kline, C. R. Snyder, S. K. Satija, A. L. Ayzner, M. F. Toney, C. L. Soles, D. M. DeLongchamp, *Macromolecules* **2012**, *45*, 6587.
[45] N. S. Sariciftci, L. Smilowitz, A. J. Heeger, F. Wudl, *Science* **1992**, *258*, 1474.
[46] O. V. Mikhnenko, H. Azimi, M. Scharber, M. Morana, P. W. M. Blom, M. A. Loi, *Energy Environ. Sci.* **2012**, *5*, 6960.
[47] B. Walker, A. B. Tamayo, X.-D. Dang, P. Zalar, J. H. Seo, A. Garcia, M. Tantiwiwat, T.-Q. Nguyen, *Advanced Functional Materials* **2009**, *19*, 3063.
[48] See definition of CTS under: http://goldbook.iupac.org/C01006.html
[49] L. Goris, K. Haenen, M. Nesladek, P. Wagner, D. Vanderzande, L. De Schepper, J. D'Haen, L. Lutsen, J. V. Manca, *J. Mater. Sci.* **2005**, *40*, 1413.
[50] J. J. Benson-Smith, L. Goris, K. Vandewal, K. Haenen, J. V. Manca, D. Vanderzande, D. D. C. Bradley, J. Nelson, *Advanced Functional Materials* **2007**, *17*, 451.
[51] K. Vandewal, K. Tvingstedt, A. Gadisa, O. Inganas, J. V. Manca, *Nat. Mater.* **2009**, *8*, 904.
[52] J. Lee, K. Vandewal, S. R. Yost, M. E. Bahlke, L. Goris, M. A. Baldo, J. V. Manca, T. Van Voorhis, *J. Am. Chem. Soc.* **2010**, *132*, 11878.
[53] K. Vandewal, S. Albrecht, E. T. Hoke, K. R. Graham, J. Widmer, J. D. Douglas, M. Schubert, W. R. Mateker, J. T. Bloking, G. F. Burkhard, A. Sellinger, J. M. J. Fréchet, A. Amassian, M. K. Riede, M. D. McGehee, D. Neher, A. Salleo, *Nat. Mater.*, *DOI: 10.1038/nmat3807*.
[54] R. Di Pietro, H. Sirringhaus, *Advanced Materials* **2012**, *24*, 3367.
[55] I. A. Howard, R. Mauer, M. Meister, F. Laquai, *J. Am. Chem. Soc.* **2010**, *132*, 14866.
[56] J. M. Guo, H. Ohkita, H. Benten, S. Ito, *J. Am. Chem. Soc.* **2010**, *132*, 6154.
[57] S. Fabiano, S. Himmelberger, M. Drees, Z. Chen, R. M. Altamimi, A. Salleo, M. A. Loi, A. Facchetti, *Advanced Energy Materials* **2013**, n/a.
[58] B. P. Rand, D. Cheyns, K. Vasseur, N. C. Giebink, S. Mothy, Y. Yi, V. Coropceanu, D. Beljonne, J. Cornil, J.-L. Brédas, J. Genoe, *Advanced Functional Materials* **2012**, *22*, 2987.
[59] D. P. McMahon, D. L. Cheung, A. Troisi, *The Journal of Physical Chemistry Letters* **2011**, *2*, 2737.
[60] F. C. Jamieson, E. B. Domingo, T. McCarthy-Ward, M. Heeney, N. Stingelin, J. R. Durrant, *Chemical Science* **2012**, *3*, 485.
[61] T. J. Savenije, J. E. Kroeze, X. N. Yang, J. Loos, *Thin Solid Films* **2006**, *511*, 2.
[62] F. Piersimoni, S. Chambon, K. Vandewal, R. Mens, T. Boonen, A. Gadisa, M. Izquierdo, S. Filippone, B. Ruttens, J. D'Haen, N. Martin, L. Lutsen, D. Vanderzande, P. Adriaensens, J. V. Manca, *J. Phys. Chem. C* **2011**, *115*, 10873.
[63] G. D'Avino, S. Mothy, L. Muccioli, C. Zannoni, L. Wang, J. Cornil, D. Beljonne, F. Castet, *The Journal of Physical Chemistry C* **2013**, *117*, 12981.
[64] F. C. Spano, *J. Chem. Phys.* **2005**, *122*, 234701.
[65] S. T. Turner, P. Pingel, R. Steyrleuthner, E. J. W. Crossland, S. Ludwigs, D. Neher, *Advanced Functional Materials* **2011**, *21*, 4640.
[66] D. Caruso, A. Troisi, *Proc. Natl. Acad. Sci. U. S. A.* **2012**, *109*, 13498.
[67] H. Tamura, M. Tsukada, *Physical Review B* **2012**, *85*, 054301.
[68] R. F. Fink, J. Seibt, V. Engel, M. Renz, M. Kaupp, S. Lochbrunner, H. M. Zhao, J. Pfister, F. Wurthner, B. Engels, *J. Am. Chem. Soc.* **2008**, *130*, 12858.

[69] D. Mori, H. Benten, I. Okada, H. Ohkita, S. Ito, *Advanced Energy Materials*, *DOI: 10.1002/aenm.201301006*.
[70] https://github.com/EFTEMj
[71] P. Thevenaz, U. E. Ruttimann, M. Unser, *Image Processing, IEEE Transactions on* **1998**, *7*, 27.
[72] http://bigwww.epfl.ch/thevenaz/turboreg
[73] E. Gann, A. T. Young, B. A. Collins, H. Yan, J. Nasiatka, H. A. Padmore, H. Ade, A. Hexemer, C. Wang, *Review of Scientific Instruments* **2012**, *83*, 045110
[74] A. L. D. Kilcoyne, T. Tyliszczak, W. F. Steele, S. Fakra, P. Hitchcock, K. Franck, E. Anderson, B. Harteneck, E. G. Rightor, G. E. Mitchell, A. P. Hitchcock, L. Yang, T. Warwick, H. Ade, *Journal of Synchrotron Radiation* **2003**, *10*, 125.
[75] B. A. Collins, Z. Li, J. R. Tumbleston, E. Gann, C. R. McNeill, H. Ade, *Advanced Energy Materials* **2013**, *3*, 65.
[76] A. Hexemer, W. Bras, J. Glossinger, E. Schaible, E. Gann, R. Kirian, A. MacDowell, M. Church, B. Rude, H. Padmore, *Journal of Physics: Conference Series* **2010**, *247*, 012007.

Submitted to ADVANCED FUNCTIONAL MATERIALS

Splitting excitons into free charges can be very efficient at polymer/fullerene interfaces but it becomes a challenging task when the fullerene is replaced by a polymeric acceptor. Here, we investigate the structural origin of the photocurrent generation in all-polymer solar cells consisting of P3HT and P(NDI2OD-T2). We find that a proper orientation of the polymer crystallites is needed to enable exciton dissociation and identify the geminate recombination of electron hole pairs and the incomplete quenching of P(NDI2OD-T2) excitons as major loss channels.

Keywords: photocurrent generation, charge-transfer state recombination, polymer crystals, alternative acceptors, organic solar cells

Marcel Schubert, Brian A. Collins, Hannah Mangold, Ian A. Howard, Wolfram Schindler, Koen Vandewal, Steffen Roland, Jan Behrends, Felix Kraffert, Robert Steyrleuthner, Zhihua Chen, Konstantinos Fostiropoulos, Robert Bittl, Alberto Salleo, Antonio Facchetti, Frédéric Laquai, Harald Ade, and Dieter Neher*

Correlated Donor/Acceptor Crystal Orientation and Charge-Transfer State Recombination Controls Photocurrent Generation in All-Polymer Solar Cells

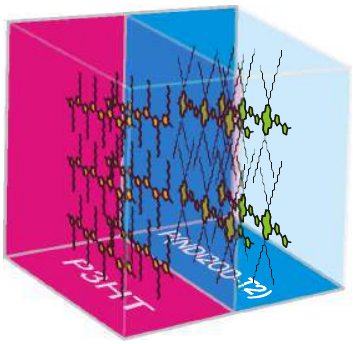

Submitted to ADVANCED FUNCTIONAL MATERIALS

Supporting Information

for *Adv. Funct. Mater.*, DOI: 10.1002/adfm.((please add manuscript number))

Correlated Donor/Acceptor Crystal Orientation and Charge-Transfer State Recombination Controls Photocurrent Generation in All-Polymer Solar Cells

*Marcel Schubert, Brian A. Collins, Hannah Mangold, Ian A. Howard, Wolfram Schindler, Koen Vandewal, Steffen Roland, Jan Behrends, Felix Kraffert, Robert Steyrleuthner, Zhihua Chen, Konstantinos Fostiropoulos, Robert Bittl, Alberto Salleo, Antonio Facchetti, Frédéric Laquai, Harald W. Ade, and Dieter Neher**

Marcel Schubert, Steffen Roland, Robert Steyrleuthner, and Prof. Dr. Dieter Neher
University of Potsdam, Institute of Physic and Astronomy, 14476 Potsdam, Germany
neher@uni-potsdam.de

Dr. Brian A. Collins, and Prof. Dr. Harald W. Ade
North Carolina State University, Department of Physics, Raleigh, NC 27695, USA

Dr. Brian A. Collins
National Institute of Standards and Technology (NIST), Gaithersburg, USA

Hannah Mangold, Dr. Ian A. Howard, and Dr. Frédéric Laquai
Max-Planck-Institute for Polymer Research (MPI-P), 55128 Mainz, Germany

Dr. Koen Vandewal, and Prof. Dr. Alberto Salleo
Stanford University, Department of Materials Science, Stanford, CA 94305-4034, USA

Dr. Wolfram Schindler and Dr. Konstantinos Fostiropoulos
Helmholtz-Zentrum Berlin (HZB), Institute for Heterogeneous Materials Systems, 14109 Berlin, Germany

Dr. Jan Behrends, Felix Kraffert, Robert Steyrleuthner, and Prof. Dr. Robert Bittl
Free University Berlin, Department of Physics, 14195 Berlin, Germany

Dr. Zhihua Chen and Prof. Dr. Antonio Facchetti
Polyera Corporation, Illinois 60077, USA

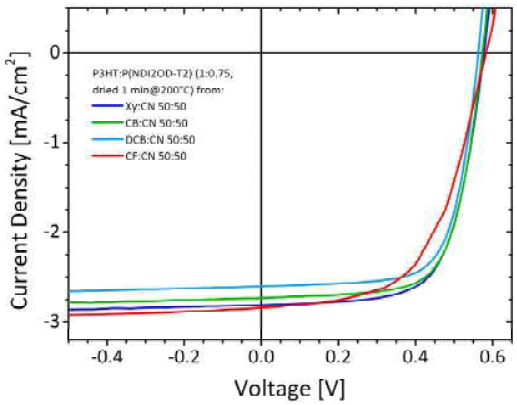

Figure S1 Effect of co-solvent on the solar cell performance.

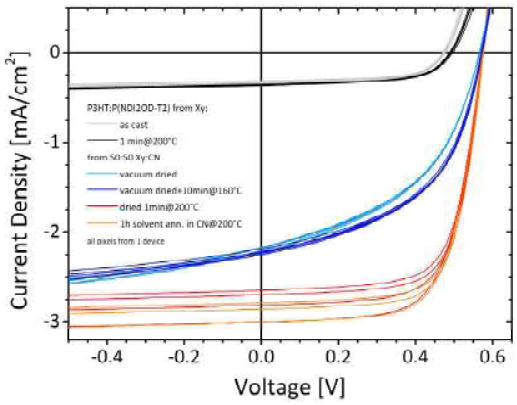

Figure S2 Influence of thermal treatment on the solar cell performance.

Scanning transmission X-ray microscopy

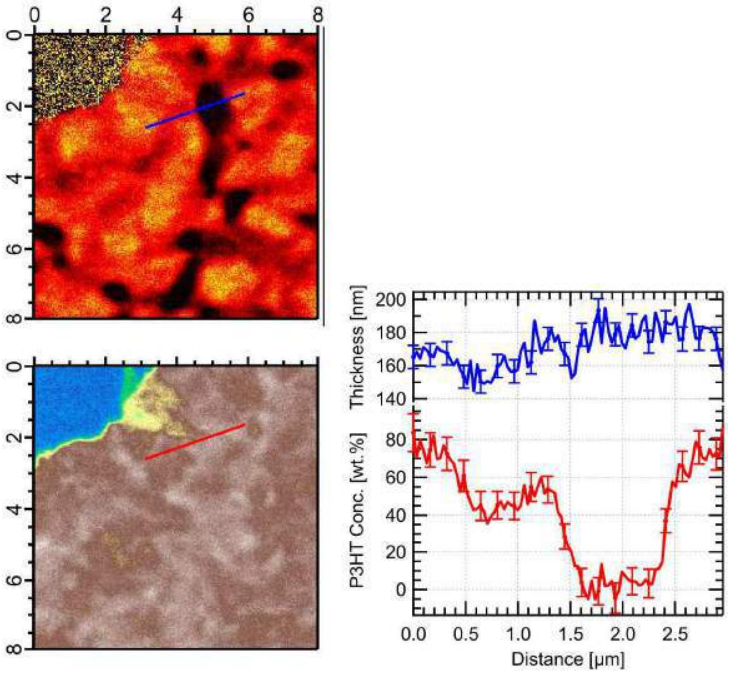

Figure S3 (left) STXM composition (top) and thickness (bottom) maps of the Xy-cast blend. (right) P3HT composition and thickness line scans.

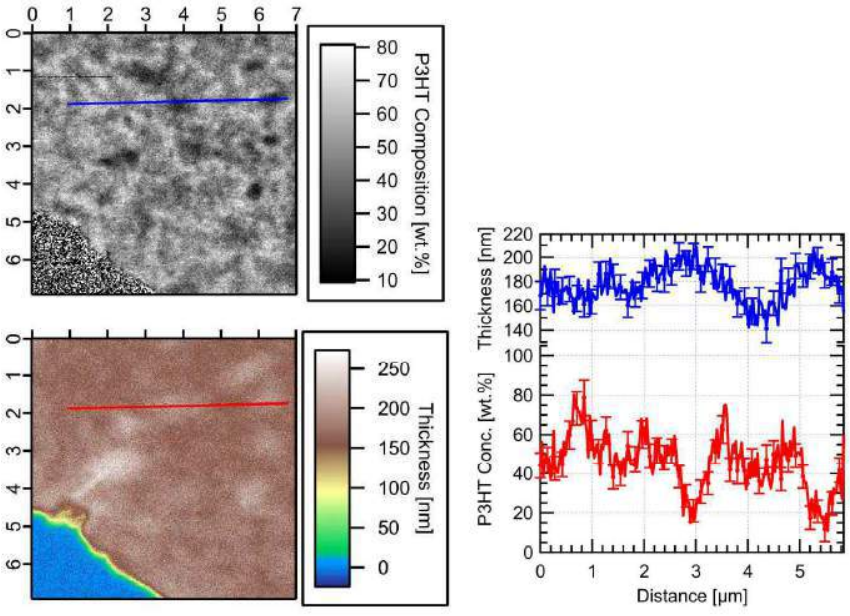

Figure S4 (left) STXM composition (top) and thickness (bottom) maps of the 95:5 Xy:CN-cast blend. (right) P3HT composition and thickness line scans.

Scanning Kelvin probe microscopy

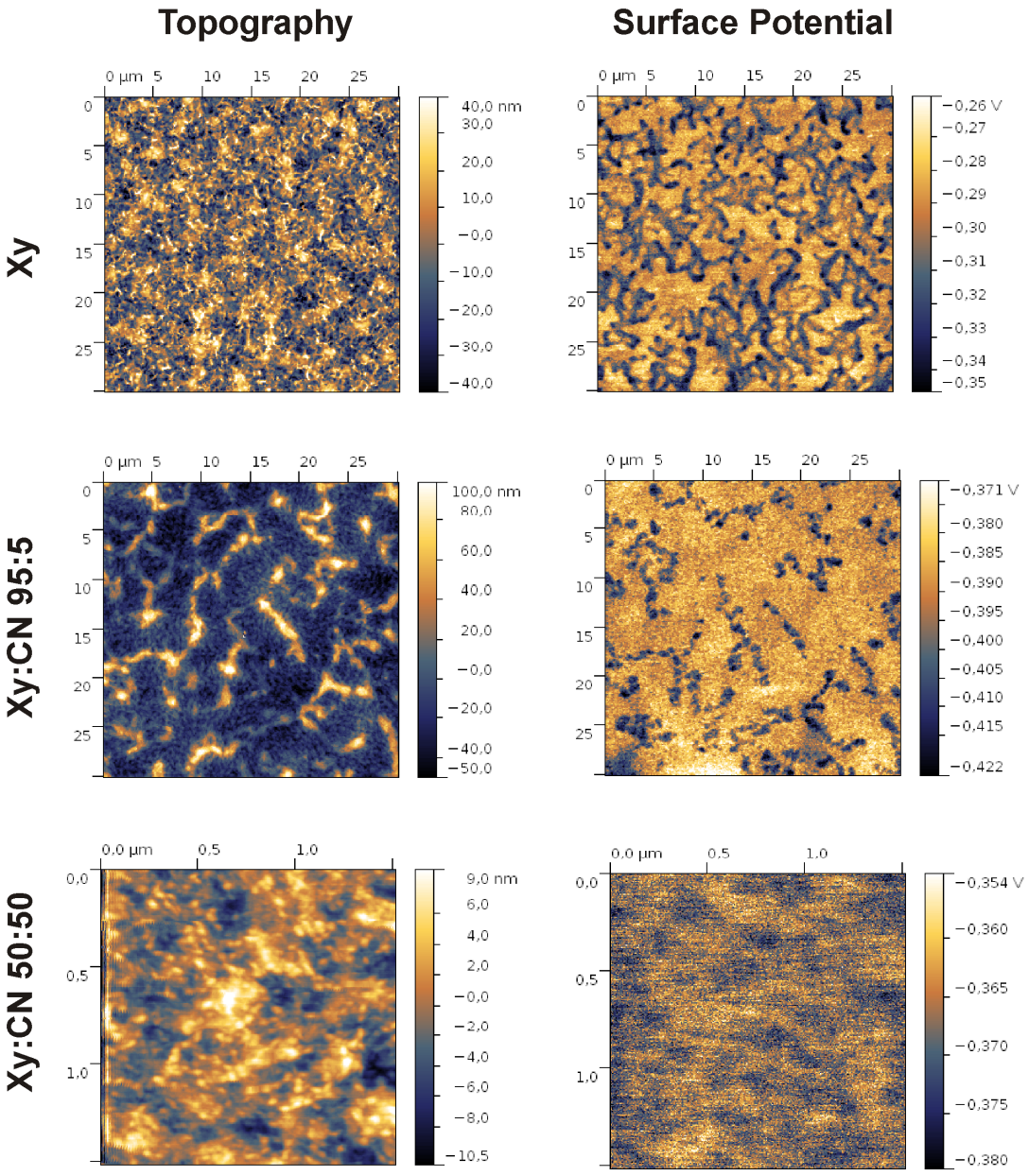

Figure S5 Surface potential (left panel) and topography (right panel) of the Xy-cast (top), the 5 vol.% (middle) and 50 vol.% (bottom) CN-cast blend films, measured with a scanning Kelvin-probe microscope (SKPM). For the surface potential maps, dark colours correspond to a low work function, which we attribute to the P(NDI2OD-T2) domains, while bright regions correspond to higher work functions, which displays the P3HT domains.

EF-TEM thickness series

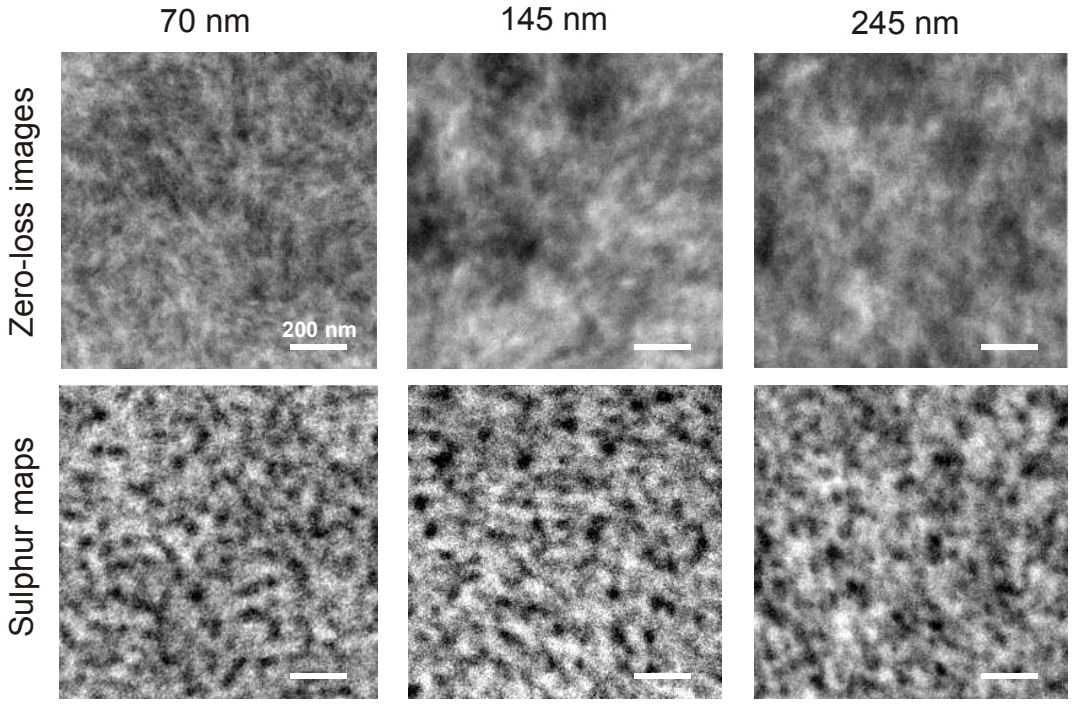

Figure S6 Energy-filtered TEM zero-loss images (top) and sulphur maps (bottom) of 50:50 Xy:CN-cast P3HT:P(NDI2OD-T2) films with an active layer thickness of about 70 nm (left), 145 nm (middle) and 245 nm (right).

Estimation of the CTS IQE

To obtain a realistic value for the internal quantum efficiency of the CTS, we first modelled the *EQE* spectra as a sum of two contributions, which are displayed in Figure 8 of the main text. The first is a Gaussian shaped band (EQE_{CT}) for the CTS and the second an exponential decaying signal (EQE_N), were we assume that it represents the decay of the absorbance at the P(NDI2OD-T2) band gap. We can now separate the CTS from the P(NDI2OD-T2) contribution and use different IQE values for both regions to model the measured absorption spectrum:

$$A(\mathrm{E}) = EQE_{CT}(\mathrm{E})/\ IQE_{CT} + EQE_N(\mathrm{E})/\ IQE_N + C.$$

For simplicity, we used a constant background C of 0.07%. Setting the constant IQE_N to 6%, the inset in Figure S7 displays the modelled absorption spectra for selected values of IQE_{CT}. While for a value of IQE_{CT} =5% the predicted absorption is much higher than the measured, a good fit is obtained for an IQE_{CT} of at least 15%, which is close to the lower boundary of 10% that was determined without the background correction. Further increasing IQE_{CT} to 35% slowly decreases the absorption, generating a broad range of reasonable conversion efficiencies. Larger values tend to underestimate the measured signal but the data does not allow to determine an upper limit of the CTS IQE.

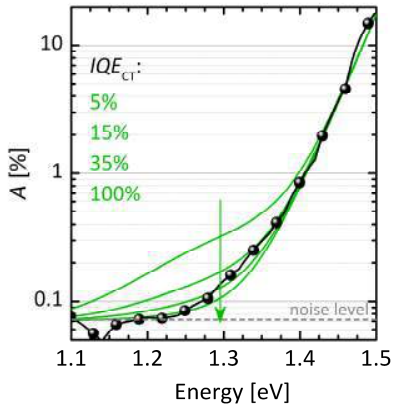

Figure S7 Enlarged CTS region of the measured absorption (black spheres) of the 50:50 Xy:CN-cast blend, and the calculated absorption (green lines) together with the IQE_{CT} values used for the calculation. The arrow points in direction of increasing IQE_{CT} values.

Transient Absorption Spectroscopy

Figure S8 displays the normalized transient absorption spectra measured at various time delays after excitation of P3HT. Two interesting features are immediately apparent upon examination of the data. First in the spectral region marked 'A' in Figure S8 we see at short time a contribution of the stimulated emission of P3HT. This decays quickly (within a few picoseconds), and leaving a net negative signal that is a superposition of the charge carrier induced absorption and the bleach of the P(NDI2OD-T2). By roughly 200 ps we see that the positive double peak at around 1.6 and 1.8 eV of the P(NDI2OD-T2) bleach is apparent; and the features from this point on are caused by long-lived charge carriers. This signal only becomes positive after several hundred picoseconds, perhaps when the charge carriers in the P(NDI2OD-T2) (negative polarons) reach the more ordered regions of the polymer. Along this line, the earliest time spectrum after P3HT excitation shows a clear shoulder in region 'B' which is known to arise from intrachain absorptions in ordered P3HT regions. As the P3HT excitons move to the interface and create charge carriers this bleach due to excited-states in an ordered P3HT region decreases. This suggests that the interfacial region is less ordered (on average) than where the P3HT excitons are created within the domains. However, on the timescale of 30 ps this bleach returns likely as there is some return of mobile charge carriers to the ordered regions of the P3HT. These interesting observations suggest that both polymers are more disordered in the interfacial regions where charge carriers are generated, a fact that could well have some influence on the charge carrier separation.

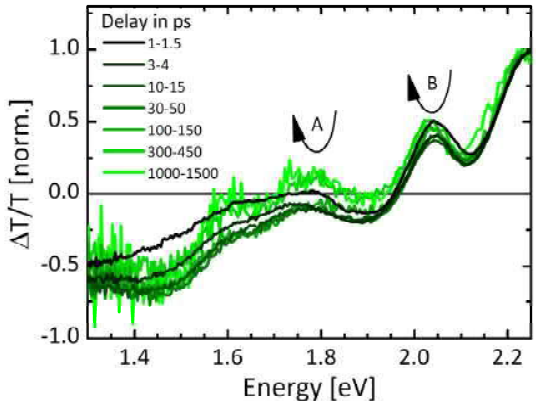

Figure S8 Evolution of the photoinduced absorption spectra (normalized to the maximum P3HT bleach) of the 50 vol.% CN-cast photovoltaic blend after excitation of the P3HT component. The region labeled A shows an initial decrease of the P3HT stimulated emission on a timescale of a few picoseconds, followed by an increase of the P(NDI2OD-T2) bleach on the long-timescale as the excitons move to more ordered regions of the polymer. A similar evolution is seen in the bleach of the ordered P3HT region marked with B. Here the P3HT excitons move from ordered phase regions to disordered interfacial regions on the same few picosecond timescale of the stimulated-emission quenching, then the bleach of the ordered P3HT regions gradually recovers, perhaps as charges move back away from the interface.

In order to get a rough estimate of the charge carrier population decay we can look at the signal kinetics in the region of photon energies less than 1.4 eV which are least affected by

the disorder-related peak shifting. We present this in Figure S9, where we show the average photoinduced absorption between 1.3 and 1.4 eV as a function of time (normalized to its value after 10 ps when charge carrier formation is complete). We see that a very significant fraction of the signal decays, indicating that a significant fraction of the charge carriers created from P3HT excitons recombine on an ultrafast timescale. In this behavior, they are similar to charge carriers created via P(NDI2OD-T2) excitons. Due to the pronounced shifting of excitons and charge carriers between ordered and disordered regions after P3HT excitation, we cannot precisely quantify the fraction of charge-carriers created from P3HT excitons that quickly recombine. We can say that, as shown in Figure S9, the PIA signal decays to 15% of its value after charge transfer is complete within a few hundred picoseconds. This is a clear indication that charge carrier dynamics are broadly similar after P3HT excitation and P(NDI2OD-T2) excitation

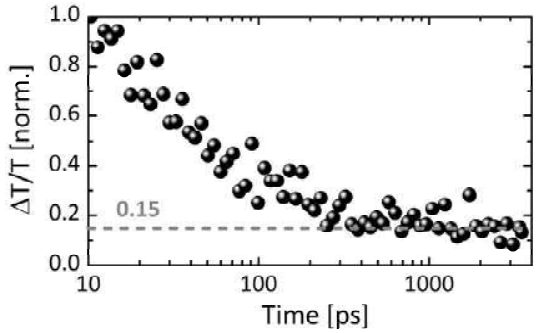

Figure S9 Evolution of the photoinduced absorption between 1.3 and 1.4 eV after excitation of the P3HT component of the blend. The signal decreases significantly, consistent with significant recombination of CTS states on the sub 200 ps timescale.

Transient EPR spectroscopy

Triplet states have been indirectly presumed before in pure films of P(NDI2OD-T2).[2] Here, we use transient electron paramagnetic resonance (trEPR) measurements for direct detection of triplet states in spin-coated films of pristine P(NDI2OD-T2) as well as in the optimized 50 vol.% CN-cast blend. Figure S10 displays low-temperature (T = 80 K) trEPR spectra of pristine P(NDI2OD-T2) and the blend after optical excitation. The spectrum of the pure film exhibits a broad signal from triplet excitons that are created by intersystem crossing from the photoexcited singlet state. The trEPR signal was modelled assuming EPR parameters typically found for triplet excitons in conjugated polymers (see details below). The intersystem crossing from singlet to triplet excitons may account for the low PL efficiency and lifetime of pure P(NDI2OD-T2) and explains the long-lived excited state species found in transient absorption measurements.[2] In contrast, the triplet signal found in the spectrum of the pristine film could not be detected in the 50:50 Xy:CN-cast blend after excitation of P3HT (excitation at 532 nm). Instead, a narrow signal with emissive/absorptive behaviour is observed that is assigned to CTS (i.e. spin-correlated polaron pairs) [Phys. Rev. B **85**, 125206 (2012)], which form upon exciton quenching at the heterojunction. These CTS are also visible upon excitation of the P(NDI2OD-T2) (excitation at 650 nm) phase of the blend film and can be detected up to several microseconds after the optical excitation at T = 80 K. Furthermore, an additional feature with an absorptive/emissive spectrum arises (marked as T'_1) that is neither a CTS, nor the bulk-triplet observed in the pristine P(NDI2OD-T2) film. The width of the spectrum identifies this signal to unambiguously arise from a triplet state, i.e. the spin-spin coupling is significantly stronger than the g-value difference between both S=1/2 species forming the strongly coupled pair. As compared to the bulk-triplet in pristine P(NDI2OD-T2), this triplet is much more *delocalized*, with the electron-hole pairs being more separated. On the other hand, it is substantially more *localized* than the CTS that give rise to the narrow component. As the T'_1 signal is neither found in pristine P(NDI2OD-T2) nor in pristine P3HT films, we suggest that it originates from a state localized at the donor-acceptor heterojunction. Such an "interface triplet" state can possibly be populated by triplet excitons formed by intersystem crossing in the P(NDI2OD-T2) domains according to the following scenario:

The PQE measurements show that only about 50% of the excitons generated in the P(NDI2OD-T2) domains are quenched at the heterojunction, indicating that the diffusion length of the singlet excitons is smaller than the average size of the P(NDI2OD-T2) domains. Part of the remaining 50% of the singlet excitons, which do not reach a heterointerface, will form triplet excitons via intersystem crossing. The presumably larger diffusion length of the triplet excitons allows them to reach the heterojunction. Whether these triplet excitons can dissociate into CTS critically depends on the energies of both types of excitations, and triplet exciton dissociation may not be energetically favourable at the P3HT:P(NDI2OD-T2) interface. Instead, the (bulk) triplet excitons, which have diffused to the heterojunction, may populate the possibly long-lived interface triplet state causing the T'_1 signal in the trEPR spectrum of the blend excited at 650 nm. Signatures of bulk triplet excitons are not observed in the blend because the diffusion towards the heterojunction likely occurs on times scales not accessible by trEPR spectroscopy. In consequence, only the long-lived interface triplet is detected. Note that while this scenario provides a credible explanation for the EPR results of

the pristine films and the blend, the assignment of the T'$_1$ signal to the interface triplet is still speculative and needs to be verified by other techniques.

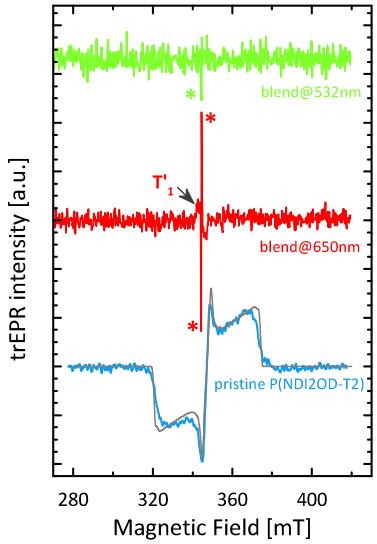

Figure S10 Transient EPR spectra for pure P(NDI2OD-T2) 800 ns after excitation (blue line) and for a 50:50 Xy:CN-cast P3HT:P(NDI2OD-T2) blend 2 µs after excitation at 532 nm (green line) and 650 nm (red line). The simulated triplet signal is also displayed (grey line). A signal from (bulk) triplet excitons in P(NDI2OD-T2) is only visible in the pristine film. The peaks marked with asterisks can be attributed to CTS (i.e. spin-correlated polaron pairs) forming upon exciton dissociation in the blend. The signal T'$_1$ is assumed to originate from an interface triplet exciton.

Triplet simulation details:

We detected the EPR signal following a laser flash as a function of time and magnetic field. The measurement is based on the fact that excitons generated by a short laser flash inherit the spin-multiplicity of the singlet ground state. Intersystem crossing transfers population from the excited singlet state to the three triplet states T_X, T_Y, T_Z energetically separated by the zero-field splitting. In a magnetic field, absorption of microwave radiation induces transitions between the triplet sublevels T_+, T_0, T_- (i.e. the eigenstates in the presence of a strong magnetic field) largely determined by the Zeeman interaction. Due to the non-equilibrium population of these triplet states (spin polarization – arising from the intersystem crossing), the trEPR spectrum immediately following exciton generation reveals both absorptive (positive) and emissive (negative) components. The specific polarization pattern of absorptive (A) and emissive (E) signal contributions is a fingerprint for the asymmetry of the intersystem crossing from the singlet precursor to the triplet state. The resulting trEPR signals are well known from detailed studies on triplet states involved in photosynthesis.[3]

The grey line in Figure S10, which is shown together with the experimental spectrum recorded for t = 800 ns, corresponds to a trEPR spectrum expected for a triplet exciton generated by intersystem crossing from a singlet state. The simulated spectrum was obtained using the EasySpin[4] toolbox for Matlab (The Mathworks, Natick, MA). The magnetic-field positions for the resonant spin transitions between the triplet energy levels were calculated for several (random) orientations of the polymer with respect to the magnetic field. These spectra were added up to yield the powder spectrum. The positions of the contributing EPR

transitions are determined by the isotropic *g*-value and the dipolar coupling tensor characterized by the zero-field splitting parameters *D* (quantifying the delocalization of the triplet wave function) and *E* (representing the deviation from axial symmetry). The dipolar contribution depends on the orientation of the triplet-state principal axes (determined by the geometry of the triplet exciton) with respect to the external magnetic field and thus differs for each individual spectrum (with fixed triplet orientation) contributing to the powder spectrum. The populations of the triplet states T_+, T_0, and T_- in the presence of a magnetic field immediately following intersystem crossing, which determine the intensities of the EPR transitions for short delays after the laser flash, are governed by the zero-field populations p_X, p_Y and p_Z of the triplet levels T_X, T_Y and T_Z in the absence of a magnetic field.[5] For the simulated spectrum shown in Figure S10 we assumed g = 2.001, the zero-field splitting parameters $|D|$ = 750 MHz, $|E|$ = 210 MHz and the relative zero-field populations p_X = 0, p_Y = 0.34, p_Z = 0.66. We further included an isotropic Gaussian line width of 2 mT in the simulation. Possible influences of spin relaxation and molecular motion on the trEPR spectrum were not taken into account.

Geometrically corrected pole figures

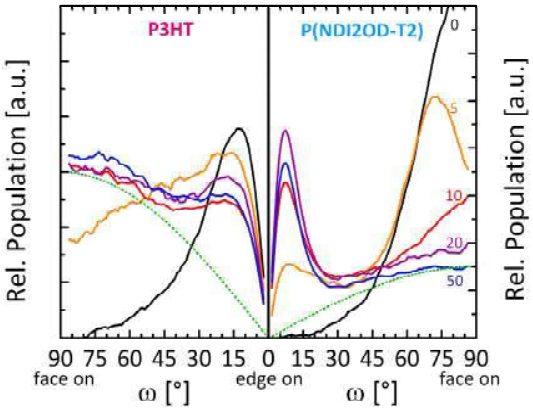

Figure S11 Geometrically corrected pole figures of the [100] lamellar stacking of P3HT (left) and P(NDI2OD-T2) (right). The dotted green line represents the intensity profile of a random crystal distribution, which is proportional to sin(ω).

References

[1] O. V. Mikhnenko, H. Azimi, M. Scharber, M. Morana, P. W. M. Blom, M. A. Loi, *Energy Environ. Sci.* **2012**, *5*, 6960.

[2] R. Steyrleuthner, M. Schubert, I. Howard, B. Klaumünzer, K. Schilling, Z. Chen, P. Saalfrank, F. Laquai, A. Facchetti, D. Neher, *J. Am. Chem. Soc.* **2012**, *134*, 18303.

[3] W. Lubitz, F. Lendzian, R. Bittl, *Accounts of Chemical Research* **2002**, *35*, 313.

[4] S. Stoll, A. Schweiger, *Journal of Magnetic Resonance* **2006**, *178*, 42.

[5] R. M. Kowalczyk, E. Schleicher, R. Bittl, S. Weber, *J. Am. Chem. Soc.* **2004**, *126*, 11393.

Danksagung

Mein größter Dank gilt Prof. Dieter Neher, für die Freiheiten die er mir während meiner Arbeit immer gewährt hat, und das Vertrauen auf welchem diese gründen, für die stundenlangen Diskusionen, die fortwährende Unterstützung und nicht zuletzt für seine gründliche und unnachgiebige Art Argumente und Ergebnisse zu hinterfragen. Ich denke ich werde erst später begreifen wie viel ich von dir gelernt habe.

Dies gilt auch für die Menschen, die mich in den vergangenen Jahren mehr als alle anderen geprägt haben. Robert, wir haben viel zusammen erlebt und mit niemandem konnte ich mich so gut austauschen wie mit dir. Mich im Stuhl umzudrehen und einfach eine Frage oder Thema in den Raum zu werfen, und darüber zu diskutieren, vermisse ich schon jetzt. Dies gilt auch für Sylvia, die mit ihrer heiteren Art jeden Tag etwas fröhlicher gemacht hat. Bleibt noch Steffen dem ich für die unzähligen Tage im Labor danken möchte, welche er durch seinen Humor gerettet hat. Darüber hinaus kann ich mir keinen besseren Assistenten vorstellen.

Ein spezieller, weil unbeschreiblich großer Dank gilt natürlich Frank. Womit ich dich nicht alles belästigt habe - und gab es jemals etwas bei dem du mir nicht helfen konntest?

Danken möchte ich auch den vielen Mitgliedern der Arbeitgruppe „Physik weicher Materie“. Besonders aber natürlich Patrick, Steve, Sahika, Apu, Sebastian, Debby und Beate. Von jedem von euch habe ich versucht etwas zu verinnerlichen.

Die Grundlage vieler Untersuchungen bildeten die sorgfältig synthetisierten Polymere der Arbeitsgruppen von Prof. Ullrich Scherf und Prof. Antonio Facchetti, wofür ich mich herzlich bedanken möchte. Die vielen verrückten Nachfragen mussten allerdings hauptsächlich Sybille Allard und Eduard Preis ausbaden, weshalb auch ihnen mein spezieller Dank gilt.

Für ihre unermüdliche Diskusionsbereitschaft und ihren Einsatz während der letzten zwei Jahre danke ich insbesondere Brian A. Collins, Koen Vandewal, Wolfram Schindler und Ian Howard.

Nach all der Unterstützung die ich durch meine Kollegen und Freunde erhalten habe würde diese Arbeit dennoch nicht existieren ohne die Liebe und den Rückhalt von Julie, meiner wundervollen Frau.

Erklärung

Hiermit erkläre ich, dass diese Arbeit selbstständig von mir verfasst wurde und ich keine anderen als die angegebenen Hilfsmittel benutzt habe. Diese Arbeit wurde an keiner anderen Hochschule eingereicht.

Potsdam, den 08.01.2014

Marcel Schubert